④

LMSC-F255516

AD-A196 275

Development of Error Criteria for
Discrete Modeling of Solids and Structures

K. C. Park and C. A. Felippa
Department of Aerospace Engineering and
Center for Space Structures and Controls
Campus Box 429
University of Colorado
Boulder, CO 80309

D. L. Flaggs, G. M. Stanley, D. S. Kang
and H. D. Cabiness
Mechanics & Materials Engineering Lab
Lockheed Palo Alto Research Laboratory
3251 Hanover St
Palo Alto, CA 94304

DTIC
S **ELECTE** **D**
JUN 1 6 1988

Final Report

N00014-86-C-0082

March 1988

88 5 09 157

Development of Error Criteria for

Discrete Modeling of Solids and Structures

K. C. Park and C. A. Felippa
Department of Aerospace Engineering and
Center for Space Structures and Controls
Campus Box 429
University of Colorado
Boulder, CO 80309

D. L. Flaggs, G. M. Stanley, D. S. Kang
and H. D. Cabiness
Mechanics & Materials Engineering Lab
Lockheed Palo Alto Research Laboratory
3251 Hanover St
Palo Alto, CA 94304

Final Report

N00014-86-C-0082

Accesion For		
NTIS CRA&I	☑	
DTIC TAB	☐	
Unannounced	☐	
Justification		
By _ltr. on file_		
Distribution /		
Availability Codes		
Dist	Avail and / or Special	
A-1		

March 1988

DTIC
COPY
INSPECTED
4

Table of Contents

i

Research Summary

1. Introduction

This final report summarizes the research activities performed at both Lockheed and at the University of Colorado on the development of advanced finite element modeling techniques for structural mechanics under ONR Contract N00014-86-C-0082. The objectives of this research were two-fold. The first was the development of *a-priori* and *a-posteriori* error estimation techniques based upon symbolic Fourier analysis techniques. The second objective was to improve the accuracy of current finite elements being used in the analysis of shell and solid structures. Significant progress was made in both research areas. A brief summary is provided below with accompanying details in the appendices.

2. Symbolic Fourier Error Estimation Techniques

In this task, an alternative to the more traditional "normed-space" approaches to finite element solution error estimation was pursued. The underlying basis of this approach is the limit differential equilibrium equations governing *intrinsic* element behavior which are symbolically derived from a representative element patch. In their own right, these limit differential equilibrium equations are used to explicitly identify intrinsic element pathologies, such as locking and spurious mechanisms, without the need to resort to numerical experimentation. Depending upon the application, both *a-priori* and *a-posteriori* local error estimates can be directly derived from these equations based upon a knowledge of the spectral content of the loading and the solution.

As a demonstration of the ability of this symbolic technique to capture complex finite element behavior, the case of the axisymmetric buckling of a cylindrical shell discretized with 4-node U1 Mindlin plate elements, as is shown in Fig. 1, was chosen. The symbolically-derived buckling load predictions, along with finite element results, are shown in Fig. 2. The continuous curves represent the symbolic results, while the symbols are used to represent actual finite element calculations. From a strictly finite element analysis standpoint, this plot graphically demonstrates the mode-switching phenomena typically encountered when modeling thin shell structures. These results also clearly show that the symbolically-derived predictions precisely capture this complex mode switching behavior. It is also significant to note that this present analysis

1
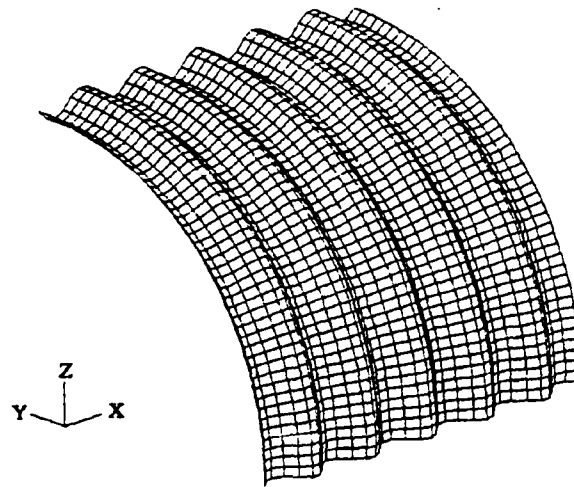
Fig. 1 – Axisymmetric buckling mode for $m = 11$ for quarter-cylinder ($R = 36$in., $L = 50.26$in., $h = .12$in., $E = 10^7$psi and $\nu = .3$) finite element model discretized with $n_{el} = 40$.
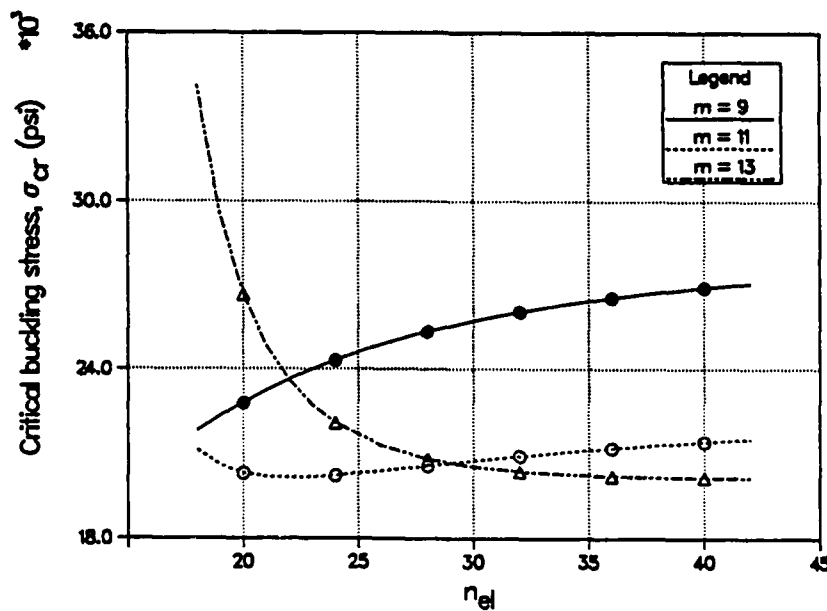

Fig. 2 – Critical buckling stress *vs.* n_{el}, for the axisymmetric buckling of the cylindrical shell shown in Fig. 1 for $m = 9$, 11 and 13 axial half-waves.

2

embodies not only the physical modeling errors associated with the different field approximations, but also the geometric errors engendered by a faceted shell approximation to the cylindrical shell.

This research effort culminated in a Stanford Ph. D. dissertation entitled *Symbolic Analysis of the Finite Element Method in Structural Mechanics* which appears as Appendix A in this report.

3. Assumed Natural Strain (ANS) Shell Elements

The theoretical formulation and implementation aspects of the ANS (Assumed Natural Strain) family of shell elements were reexamined in light of our extensive numerical experience with them over the past several years. A greatly simplified and more rigorously derived formulation resulted from this effort. This resulted in a more natural element implementation and ultimately, a more robust one. Preliminary numerical evaluation has show significant improvement in the performance of the 4-node 4-ANS shell element. In Fig. 3, results for the pinched hemisphere problem are shown where previous results for the 4-ANS and 9-ANS are directly compared with those of the new reformulated elements, 4-rANS and 9-rANS. The improved performance of the 4-rANS is remarkable. This element maintains its accuracy for mesh distortions and performs well without the need of employing reduced spatial integration. Overall, the 9-rANS appears to perform at the same level as its predecessor. It is anticipated that when their implementation is complete, the ANS family of elements will pass the patch test – a capability which has thus far eluded them in spite of their excellent performance on many problems. The details of the new ANS formulation and element implementation are found in Appendix B, *The ANS Shell Elements: Formulation*, and in Appendix C, *The ANS Shell Elements: Element Construction*.

4. Parameterized Variational Principles for Finite Element Applications

The third task of this research effort has been to develop a parameterized variational basis for comparing different finite element formulations. An important result of this study is the establishment of the interrelationships between the different variational principles which result in hybrid, mixed and free finite element formulations. This approach has permitted a reinterpretation of the classical Hu-Washizu Variational Principal and Fraeijs de Veubeke's Limitation Principle in light of parameterized variational principles. With the anticipation that future finite element development will require a simultane-
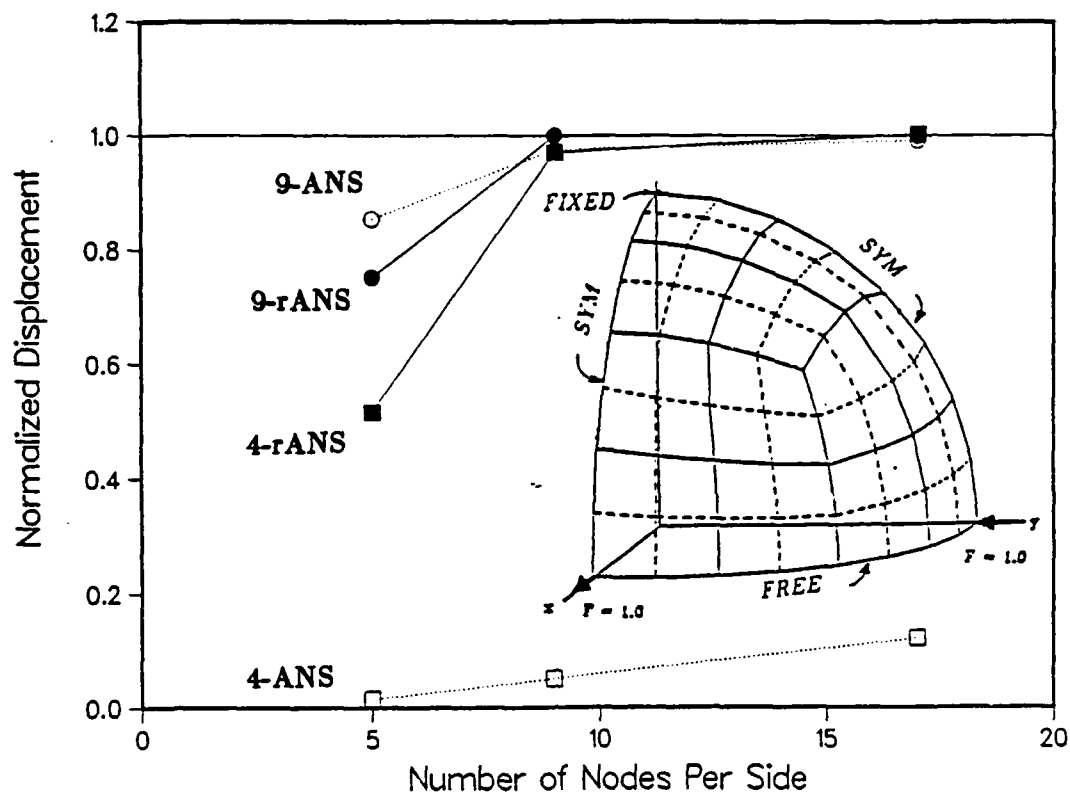
Fig. 3 – Pinched Hemisphere Element Convergence Study: Normalized Center Displacement *vs.* Grid Density.

ous approximation of the different field variables, the unifying approach to variational principles proposed here may prove beneficial to the finite element developer. The complete work entitled *Parametrized Multifield Variational Principles in Elasticity: I. Mixed Functionals, II. Hybrid Functionals and the Free Formulation* appears in Appendix D.

4

Appendix A

Symbolic Analysis of the Finite Element Method
in Structural Mechanics

A Dissertation
Submitted to the Department of Aeronautics and Astronautics
and the Committee on Graduate Studies
of Stanford University
in partial fulfillment of the requirements
for the degree of
DOCTOR OF PHILOSOPHY

by

Donald Leland Flaggs

March 1988

Symbolic Analysis of the Finite Element Method in Structural Mechanics

A Dissertation
Submitted to the Department of Aeronautics and Astronautics
and the Committee on Graduate Studies
of Stanford University
in partial fulfillment of the requirements
for the degree of
DOCTOR OF PHILOSOPHY

by

Donald Leland Flaggs

March 1988

ii

Acknowledgments

After working on this for so very long, the list of individuals and institutions to which I would like to express my gratitude is seemingly endless. To the many who I do not mention, I value your support none the less.

To my thesis advisor, Professor Thomas J. R. Hughes, I would like to express my gratitude for his guidance and assistance during the preparation of this dissertation. I would also like to thank my academic advisor, Professor Jean Mayers, for his support during my early years at Stanford.

To my Lockheed mentor and colleague, Dr. K. C. Park, I would like to express my sincere gratitude for his inspiration, guidance and support for this research effort.

To my many colleagues at Lockheed, both past and present, and in particular, Drs. Gary M. Stanley, Bahram Nour-Omid and Carlos A. Felippa, I would like to thank you for your many technical comments and suggestions, continual encouragement, and for the extra effort required to make up for what I didn't have the time to do while preoccupied with this endeavor.

To my many Lockheed managers, Drs. Richard F. Hartung, Thomas L. Geers and Frank W. Crossman, for seeing that Independent Research funding was always there, I thank you all.

Finally, I would like to express my love to Sheryl, my mother, and my family for always being there when I needed you most.

Abstract

A symbolic analysis technique is presented for determining the intrinsic behavior of a wide range of different finite element formulations. This element-independent generality stems from the fact that the analysis conceptually starts with the discrete finite element equations for an element patch, cast in symbolic form employing computer algebra. From them, the discrete formulation is recast directly back to the limit differential equilibrium equations (or strong form) governing element behavior, employing both Taylor series and discrete Fourier techniques. Comparing these equilibrium equations with the governing continuum equations establishes how well the discrete model represents the physical one, without recourse to numerical experimentation. The theoretical details of the underlying element formulation are, in essence, immaterial to the symbolic analysis since all discretization information is uniquely embodied in the discrete equations themselves. The use of nonconforming elements, special interpolation rules, reduced spatial integration rules or other numerical techniques therefore pose no obstacle to this method. As a result, this local symbolic analysis technique provides a unified approach to element evaluation presently lacking in the more mathematically precise functional analysis approach to element evaluation.

The emphasis in this work is on "structural" finite elements – bars, beams, plates and shells – whose use pose a myriad of challenges arising from working with degenerate problem domains and approximate physical geometry. Wave propagation, static loading and bifurcation buckling problems will be addressed for these different classes of elements. In particular, the causes of transverse shear element locking and spurious element mechanisms are investigated in addition to several proposed cures, such as reduced spatial integration and hourglass control techniques. For the case of curved structures, the faceted element approximation is analyzed. Local error estimates – ultimately needed for adaptive mesh refinement techniques – are determined using both Taylor series and discrete Fourier techniques. The accuracy of the discrete Fourier error predictions is numerically verified employing test cases with regular domains and periodic boundary conditions for which the error prediction is shown to be essentially exact.

Table of Contents

List of Tables

List of Figures

xii

Introduction

§1.1 Background

As with any approximate analysis technique, the question remaining after completing a finite element structural analysis is "How close is the finite element solution to the correct physical one?" More likely than not, confidence in the accuracy of the finite element solution is not based upon a fundamental understanding of the intrinsic behavior of the finite elements themselves, but rather upon the correctness of previous finite element solutions to problems where the continuum solution had been known. This solution confidence issue becomes especially severe when dealing with *thin* plate and shell structures whose myriad pathologies have always plagued the finite element developer and user alike.

In 1965, Irons introduced the idea of inferring intrinsic finite element behavior from the solution through the introduction of his patch test [1]. For the practicing engineer, the most natural extension of this idea is embodied in the sets of different structural test problems that have been proposed over the years (see e.g. MacNeal and Harder [2] and Mair [3]) as a phenomenological way of verifying element accuracy and convergence. This also facilitated a way of directly comparing one element formulation with another. These different test problems are chosen so as

to exercise both constant strain and higher-order element deformation patterns in an analogous manner to that described by Taylor et al. [4]. With this approach, two lingering difficulties remain. The first concerns defining the numerical test cases which are comprehensive enough to constitute a "complete" element patch test.[1] The second entails how a finite element developer employs the results of these tests to explicitly pinpoint potential problem areas in the underlying element formulation.

In the past, an alternative to this "solution-based" approach, favored by the engineer, has been the functional analysis-based approach employed by the applied mathematician. Excellent descriptions of research in this area may be found in the work of Strang and Fix [6], Ciarlet [7] and Oden and Reddy [8], just to name a few. As has traditionally been the case, however, progress in this area lags behind the problem-driven development of new element formulations for a number of reasons. Each new twist in formulation or numerical trick may result in mathematical complications requiring new proofs of convergence with accompanying error estimates. For this reason, the contribution in many cases is one of establishing the mathematical foundation of an existing method. As was pointed out recently by Bernadou [9], there are discretization techniques, like the faceted plate discretization of a shell, which has been used successfully for more than twenty years, for which strict proofs cannot as yet be completed. From an engineering perspective, one underlying difficulty with this approach is in relating the fidelity in which an element formulation represents physical behavior in a point-wise manner to the results of a global convergence proof.

Alternatively, this task of element evaluation may be addressed by building upon a technique that has been used for evaluating finite difference algorithms for initial-value problems employing either Taylor series or discrete Fourier anal-

---

[1] Unfortunately, "completeness" in the above sense may not provide the necessary and sufficient conditions for element convergence as has been discussed by Stummel [5] and recently refuted by Taylor et al. [4].

ysis (see e.g., [10]). This approach deals directly with the discrete finite element equations themselves instead of the solutions to them, as is the case with the different patch tests, or with the weak form from which they were derived, as is the case with the functional analysis-based approach. In a computational fluid dynamics context, the Taylor series analysis technique has been used by Hirt [11] and Warming and Hyett [12] to determine both the consistency and stability of initial value finite difference problems. Their primary interest was in characterizing the *behavior* of the discrete equations. This goal was accomplished by working with what Warming and Hyett referred to as the "modified equations". These equations were comprised of the zeroth-order and leading truncation error terms recovered from the difference equations using Taylor series expansions. From these modified equations, they were able to address the question of stability in linear problems and show the equivalence between their results and discrete Fourier (i.e., von Neumann) techniques. Going one step further, Hirt demonstrated for a two-dimensional flow problem, the general applicability of this technique even to nonlinear PDE's with variable coefficients. This approach was a fundamental departure from the restrictive local truncation error concept of consistency.

In [13], by formally viewing the finite element equations as difference equations, Walz, Fulton and Cyrus were able to apply traditional Taylor series-based finite difference techniques to evaluate the element discretization. A similar approach in the Fourier domain was investigated by Strang and Fix [14]. These pioneering investigations in the field of element evaluation were essentially limited to assessing the consistency of the resulting limit differential equilibrium equations which represent element behavior in a local manner.

In this approach to element evaluation, one works directly with the finite element difference equations which uniquely embody each step of the element formulation process. As a result, this technique shares the element-independent generality of the patch test as an element evaluation technique. Essentially all of the mathematical complications inherent in the functional analysis approach to el-

ement evaluation are thereby avoided. These complications result from variational crimes [6] resulting from employing nonconforming elements, reduced spatial integration, special interpolation rules and other numerical schemes (a.k.a. tricks). Recognizing the power of this element evaluation technique, Park and Flaggs explored the use of both Taylor series and discrete Fourier analysis techniques to evaluate the performance of different finite element discretizations [15,16,17,18].

§1.2 Objective

The objective of this dissertation is twofold. The first is to formalize the element-independent symbolic analysis procedures needed to evaluate general multi-degree-of-freedom finite element discretizations. The second is to apply these symbolic element evaluation techniques to explicitly determine the nature of several outstanding problems in the application of the finite element method to structural analysis problems.

§1.3 Approach

In order to achieve these objectives, computer algebra software [19,20] is extensively employed to recover symbolically the limit differential equilibrium equations. Starting from the finite element equations, cast in symbolic form, limit differential equations governing element *behavior* are obtained both in the physical and frequency domain. With them, a direct comparison with the strong form of the governing continuum equations is possible from which it is shown that one is able to 1) explicity identify element deficiencies, 2) infer expected element behavior and lastly, 3) compute component-wise error estimates. With this information, both the question of consistency and stability is easily verified for the case of a regular element mesh. With this information, the convergence of a particular finite element discretization can be determined without recourse to extensive numerical experimentation. By working with the matrix operator form of the discrete equations, this approach is also immediately applicable to bifurcation buckling problems. An additional benefit is the added insight into the expected behavior of

4

$$\text{Strong Form} \quad \underline{Lu = f} \quad \Leftrightarrow \quad \overbrace{\int_\Omega v(Lu - f)d\Omega = 0}^{\text{Weak Form}} \quad \Rightarrow \quad \text{Discretization} \begin{Bmatrix} \text{MWR} \\ \text{Ritz} \end{Bmatrix} \quad \Rightarrow \quad \text{Discrete Form} \quad \underline{Ku = f}$$

$$\begin{Bmatrix} \text{Virtual Work} \\ \text{Variational} \end{Bmatrix}$$

- Intrinsic element behavior
- Interior error estimate
- Element synthesis

Symbolic Analysis Procedures
Discrete Strong Form
$$L^D u^D = f^D$$
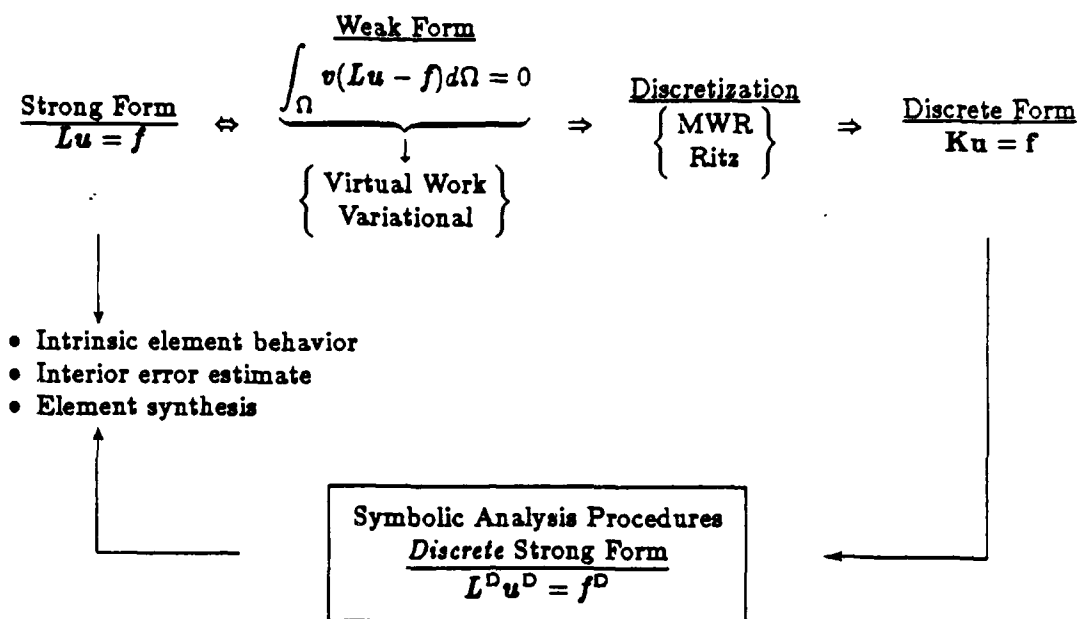
Fig. 1.1   Symbolic Analysis of Finite Element Discretization of BVP

a discrete method gained through working directly with the discrete counterpart to the continuum equilibrium equations. In essence, as a result of its generality, an element evaluation technique is being proposed which could be employed as a tool during the actual element formulation process in much the same manner as the patch test is presently used.

This symbolic approach to assessing the intrinsic behavior of a particular finite element discretization is graphically portrayed in Fig. 1.1. The symbolic analysis procedures developed here. *close the loop*[2] in order to determine how faithfully the discrete equations represent the strong (or differential) form of the governing continuum equilibrium equations. In essence, this results in what Wilkinson [21] refers to as a backward error analysis. Representative element patches for the different discrete model geometries investigated in this study are shown in Fig. 1.2. The emphasis is in the use of the different symbolic analysis techniques employed

---

[2] In actuality, each step shown in Fig. 1.1 is performed symbolically so that at the conceptual starting point of the symbolic analysis, one will have the *exact* discrete finite element equations with which to work from.

5
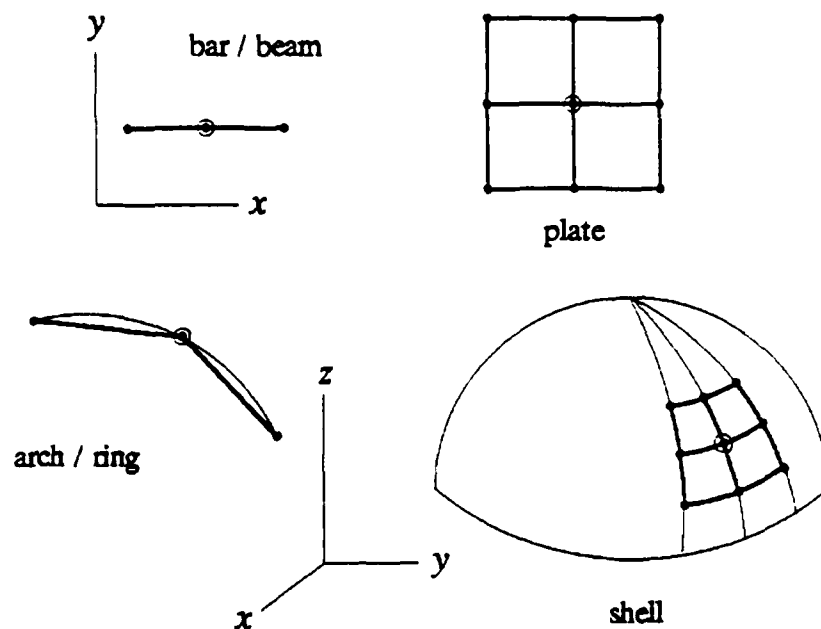
Fig. 1.2 Representative Element Patches

here to determine the effect of such aspects of element formulation as interpolation order, spatial integration rules and model geometry. In this respect, the interpretation of the symbolic analysis results differ radically from those of the underlying traditional finite difference techniques. Primary interest is directed at identifying intrinsic element *behavior* engendered by the finite element formulation and secondarily at the formal order-of-accuracy of the finite element difference equations. Using these techniques, it is possible to explicitly identify a one-to-one correspondence between element problems and deficiencies in the limit differential equilibrium equations. In particular, existing problems with present structural finite elements which are easily identified using these symbolic techniques are:

- Accuracy
- Locking
- Spurious mechanisms, i.e., stability
- Geometrical modeling errors
- Consistency with respect to particular continuum equations

This last point comes into play when dealing with finite element discretizations of thin shell structures.

§1.4 Overview

The remainder of this introduction focuses upon the technical highlights of each chapter – and of the contributions made therein.

The goal of Chapter 2 is two-fold. The first is to establish the mathematical basis for working with linear matrix differential operators in terms of fundamental matrix/vector operations suitable for computer algebra manipulation. Donnell's decoupled eighth-order cylindrical shell equilibrium equation is derived as a simple way of demonstrating the symbolic procedures to be employed using computer algebra software. This is a precursor to the primary goal of this chapter, which is the introduction of computer-aided Taylor series-based element evaluation techniques. The linear isoparametric Timoshenko beam element, with its transverse shear element locking pathology, served as the example problem. Both linear static and bifurcation buckling problems are examined. For the linear static case, the governing limit differential equilibrium equations derived from both exact and reduced spatial integration are presented. The decoupling of the w and θ limit differential equilibrium equations is found to be the key step in explicitly identifying the parasitic differential operators responsible for transverse shear locking in the exactly integrated element. For the reduced integrated element, this symbolic element analysis showed that a locking-free discretization results. Relative error estimates are then derived using the modified limit differential equilibrium equation, comprising the continuum and leading truncation terms, employing a Fourier series expansion of the distributed loading and lateral displacement. As a preliminary step, an error analysis is first performed for the one-dimensional bar element. This is to validate the element evaluation procedure for a discrete problem in which the solution is known to be nodally exact. Lastly, relative error estimates are derived for the bifurcation buckling of the linear Timoshenko beam element.

A fundamental limitation of the Taylor series technique was, however, found to be its inability to identify spurious element mechanisms. In Chapter 3, a discrete Fourier analysis technique is introduced to complement the Taylor series approach introduced in Chapter 2. Although now working in the frequency rather than the physical (or spatial) domain, the advantage of the discrete Fourier technique is in its complete representation of the discrete solution and in the resulting compact symbolic expressions. The complete representation of the discrete solution in the frequency domain permits this element evaluation technique to be used to identify spurious element mechanisms as well as to verify element consistency. Together, these two conditions constitute both the necessary and sufficient conditions for convergence of a discrete method. The example problem used to demonstrate the ability of this discrete Fourier technique to detect spurious element mechanisms is that of a linear mixed bar element. The cause of the spurious mechanism is pinpointed in a component-wise manner so that for this one-dimensional example, a remedy could be immediately identified. The linear Timoshenko beam, investigated in Chapter 2, is considered next. The same parasitic operator is identified in the frequency domain for the exactly integrated beam element. Inverse Fourier transformation is shown to yield the identical limit differential equilibrium equation in the physical domain as was derived earlier using the Taylor series technique. Error estimates for both static loading and bifurcation buckling are determined and compared to those obtained in Chapter 2 from the modified equilibrium equations. For the static solution, error estimates based upon the modified equilibrium equations proved to be reasonably close to the discrete Fourier predictions for the lower wavenumbers. For the case of bifurcation buckling, however, the Taylor series results were seen to slowly diverge from the discrete Fourier predictions, which exactly agree with finite element results. Lastly, the nonconforming element Stummel used to illustrate potential shortcomings in Irons' patch test was shown *not* to be a convergent approximation since it satisfied neither consistency nor stability requirements.

In Chapter 4, both the Taylor series and discrete Fourier techniques are used in a complementary manner to analyze different formulations of the bilinear Reissner-Mindlin plate element. Due to the ease of working with the physical variables, the Taylor series technique is employed for those problems where the question of element consistency is the sole concern. The effect of different element integration rules – exact, selectively reduced (S1), uniformly reduced (U1) and directional transverse shear – along with two alternative transverse shear interpolation techniques, are the first problems considered here. As with the case of the Timoshenko beam, the presence or absence of transverse shear element locking is explicitly identified using this symbolic element evaluation technique. Next, the way in which different spurious mode (or hourglass) control techniques manifest their effect on the governing limit differential equilibrium equations is investigated for the S1 and U1 elements. For both elements, it is observed that these hourglass control techniques reintroduce element locking, albeit in a potentially different bending deformation mode, for any nonzero w-hourglass control parameter. The results from these symbolic analyses are then verified numerically.

In the second half of Chapter 4, the discrete Fourier analysis technique is employed in a component-wise manner to construct the transformed limit differential equilibrium equations of the bilinear Reissner-Mindlin plate, as would be the case if element synthesis were the true objective. These results are then used to verify the existence of spurious mechanisms in the S1 and U1 elements, and of transverse shear locking for the exactly integrated element. Error estimates are derived for both the case of static loading and uniaxial bifurcation buckling. Comparison with numerical results for the predicted error in buckling load again demonstrates the accuracy of the present symbolic element evaluation technique.

Lastly, in Chapter 5, the symbolic analysis techniques developed thus far were employed to analyze the faceted finite element approximation of a circular arch with straight Hermitian (C^1) and Timoshenko (C^0) beams, and of the cylindrical shell with flat bilinear Reissner-Mindlin plates. Working now strictly in the

Fourier domain to take advantage of the compact symbolic notation, the straight Hermitian beam discretization of a circular arch is found to be consistent with Sanders' cylindrical shell theory specialized to the arch. For elements with a finite length, however, the geometrical modeling error resulting from the polygonal arch discretization is responsible for nonvanishing errors in displacement for the limiting case where the wave number goes to zero. In spite of the fact that this discretization is asymptotically consistent for a circular arch, the long wavelength solution components converge to the faceted arch model. For the linear Timoshenko beam discretization of the arch, the limit differential equilibrium equations were found not to be consistent with either Naghdi-Cooper or Mirsky-Herrman C^0 shell theory although in the thin-shell limit, they were shown to be consistent with Sanders' theory.

The faceted Reissner-Mindlin plate discretization of a cylindrical shell was next analyzed and compared to Naghdi-Cooper's C^0 shell theory. As was the case in the arch problem, the limit differential equilibrium equations were not found to be strictly consistent with the reference theory. Omitted terms were, however, of the order h^2/R^2 which for thin shells ($h/R > 100$) would result in a very small contribution to affected terms. By analogy with Koiter's work [22] on first approximation shell theory, expressions which differ only by such terms may in fact be equivalent with respect to the underlying C^0 assumptions. The axisymmetric buckling of cylindrical shells was used to verify the accuracy of the discrete Fourier material and buckling operators. The predicted bifurcation buckling loads derived from the symbolic analysis were found to be virtually identical with the finite element results. As a result, mode switching, which is often observed in the finite element modeling of shell buckling problems, was accurately modeled by the symbolic element analysis, even for extremely coarse finite element meshes.

Development of Symbolic Analysis Techniques:
Taylor Series Approach

In this chapter, the basic symbolic analysis techniques used to perform a computer-aided symbolic evaluation of a finite element discretization are introduced. These techniques are comprised of two essential parts. The first encompasses the fundamental operational procedures used to manipulate symbolically matrix differential operators. The second part entails defining the functional relationship between adjacent nodal degrees-of-freedom (d-o-f) needed to recover the limit differential equilibrium equations governing element behavior from the discrete equations. Two different methods are used in this regard; Taylor series expansions of the nodal d-o-f in this chapter and a discrete Fourier method in Chapter 3.

The present Taylor series analysis of boundary value problems addresses the question of finite element consistency. The emphasis and interpretation of the results from the symbolic analysis are directed toward identifying *intrinsic* element behavior from the limit differential equilibrium equations obtained from the discrete finite element equations. Of only secondary interest is the order-of-accuracy of a finite element discretization as would be the case in a formal local truncation

11

error analysis of a set of finite difference equations.

A new aspect of the present analysis is the need to symbolically manipulate the differential equations representing the coupled discrete finite element equations. With the possibility that the finite element d-o-f represent both physical and purely computational d-o-f depending upon the particular discretization, elimination of the computational d-o-f in a consistent manner is a prerequisite to recovering the governing limit differential equilibrium equations. In addition, as was found to be the case in element locking problems, decoupled limit differential equilibrium equations appear to represent the canonical form in which to identify the parasitic differential operators responsible for element locking.

The appearance of parasitic differential operators in the truncation error terms of the decoupled limit differential equilibrium equations is shown to be responsible for transverse shear element locking. These terms are found to play the dominant role in the limit differential equilibrium equations of a given finite element formulation thereby totally masking the contribution of the continuum operators. This ability to explicitly identify parasitic differential operators enables one to determine the "operational consistency" of a finite element discretization.

As a result of the generality of these symbolic analysis techniques, the symbolic analysis procedures developed for the linear static problem are immediately applicable to bifurcation buckling by the inclusion of the geometric stiffness in the symbolic analysis. Lastly, a priori error estimates for both linear static and bifurcation buckling problems are determined based upon the so-called modified equilibrium equations, which retain only leading truncation error terms, for a particular element discretization.

§2.1 Operational Procedures with Matrix Differential Operators

As was alluded to in Chapter 1, one of the key aspects of the present work will be the symbolic manipulation of linear matrix differential operators. This is necessary in order to both obtain decoupled differential expressions and to eliminate

12

purely computational degrees-of-freedom during recovery of the limit differential equilibrium equations derived from the discrete finite element equations.

In this section, the basic operational procedures used in working with matrix differential operators are described in terms of basic matrix/vector operations. An illustrative example of their application is to the derivation of Donnell's decoupled cylindrical shell equations which are succintly derived employing these procedures implemented using the computer algebra program SMP [20].

§2.1.1 Linear Matrix Differential Operators

In this investigation, attention will be focused on systems of linear partial differential operators with constant coefficients. Within this basic framework, the essential underlying theorem for dealing with linear differential matrix operators, as stated by Courant and Hilbert [23], is

from any system of linear differential equations in m unknowns with constant coefficients, a single linear differential equation with constant coefficients can be obtained for any of the unknown functions.

Hence, for example, if $u_1, u_2, \ldots, u_m$ are the unknown functions of the independent variables $x_1, x_2, \ldots, x_n$ and if L_{ij} are polynomials in the differential operators, viz.,

$$L_{ij}\left(\frac{\partial}{\partial x_1}, \frac{\partial}{\partial x_2}, \ldots\right) = \sum \alpha_{ij} \frac{\partial^{\mu_1 + \mu_2 + \cdots}}{\partial x_1^{\mu_1} \partial x_2^{\mu_2} \ldots} \tag{2.1}$$

with constant coefficients α_{ij}, then the coupled system of m independent equations in m unknown functions may be written in terms of the matrix operator notation

$$\begin{bmatrix} L_{11} & L_{12} & \cdots & L_{1m} \\ L_{21} & L_{22} & \cdots & L_{2m} \\ \vdots & \vdots & \ddots & \vdots \\ L_{m1} & L_{m2} & \cdots & L_{mm} \end{bmatrix} \begin{Bmatrix} u_1 \\ u_2 \\ \vdots \\ u_m \end{Bmatrix} = \begin{Bmatrix} f_1 \\ f_2 \\ \vdots \\ f_m \end{Bmatrix} \quad \Rightarrow \quad Lu = f \tag{2.2}$$

where $f_i = f_i(x_1, x_2, \cdots, x_n)$. Formal algebraic elimination of Eq. (2.2) using

Cramer's rule yields decoupled differential equations for each u_i given by

$$|L| \cdot u_i = |G_i| \qquad (2.3)$$

where $|\cdot|$ is used to denote the determinant of a matrix and G_i is simply L with the ith column replaced by f. The order of the system is equal to the order of the characteristic linear operator $|L|$. $|G_i|$ is likewise a linear differential operator in functions f_i, each of whose individual operators is the minor determinant of L corresponding to f_i. The determinant operations indicated by Eq. (2.3) make use of the fact that the individual operators in L are commutative resulting from their linearity, i.e., $L_1 L_2 u = L_2 L_1 u$. Also, since the symbolic calculation of $|G_i|$ is usually not performed with respect to the ith column, it will be necessary to always interpret the product of an operator, L, and f in the subsequent computer algebra runstreams as Lf, i.e., $fL \Rightarrow Lf$.

One further aspect of Eq. (2.3) which deserves comment is the case where common differential operators appear in both $|L|$ and $|G_i|$. An example of this would be

$$L_3 L_1 u = L_3 L_2 f \quad \Rightarrow \quad L_3 \underbrace{(L_1 u - L_2 f)}_{u_h} = 0 \qquad (2.4)$$

where L_i are linear operators and u_h represents the homogeneous solution. If the eigenvalues associated with L_3 are non-zero, then L_3 can be eliminated resulting in $L_1 u = L_2 f$; otherwise, $L_1 u = L_2 f + u_h$. From a computer algebra standpoint, care must be used in solving Eq. (2.2) if a direct elimination technique is used rather than Cramer's rule since L_3 would in all likelihood be lost in the solution process.

§2.1.2 Symbolic Derivation of Donnell's Cylindrical Shell Equation

Before proceeding to the discrete problems which follow, an illustrative example of some aspects of the symbolic procedures to be used will first be described here. The example problem will be the symbolic derivation of Donnell's decou-

pled eighth-order transverse equilibrium equation for the cylindrical shell. From this simple example, two important observations will emerge. The first is the straightforward way in which coupled systems of linear differential equations can be symbolically manipulated as a consequence of Eq. (2.3). The second is merely one of recognizing the ease in which symbolic algebra software – SMP in this case – can be employed to perform complex (and tedious) symbolic operations.

Donnell's "shallow" cylindrical shell equilibrium equations written in shell coordinates in terms of the displacement triad (u, v, w) are [24]

$$\frac{\partial^2 u}{\partial x^2} + \frac{1-\nu}{2}\frac{\partial^2 u}{\partial s^2} + \frac{1+\nu}{2}\frac{\partial^2 v}{\partial x \partial s} + \frac{\nu}{R}\frac{\partial w}{\partial x} = -P_x$$

$$\frac{1-\nu}{2}\frac{\partial^2 v}{\partial x^2} + \frac{\partial^2 v}{\partial s^2} + \frac{1+\nu}{2}\frac{\partial^2 u}{\partial x \partial s} + \frac{1}{R}\frac{\partial w}{\partial s} = -P_s \qquad (2.5)$$

$$\frac{h^2}{12}\nabla^4 w + \frac{1}{R}\left(\frac{w}{R} + \frac{\partial v}{\partial s} + \nu\frac{\partial u}{\partial x}\right) = P$$

where ν is the Poisson's ratio, R is the cylinder radius, h is the cylindrical shell's thickness, and $\nabla^4 = \left(\frac{\partial^2}{\partial x^2} + \frac{\partial^2}{\partial s^2}\right)^2$ with x being the axial and s the circumferential coordinates. Rewriting Eq. (2.5) in matrix differential operator form results in

$$Lu = f \qquad (2.6)$$

where the linear matrix differential operator L is given by

$$L = \begin{bmatrix} L_{uu} & L_{uv} & L_{uw} \\ L_{vu} & L_{vv} & L_{vw} \\ L_{wu} & L_{wv} & L_{ww} \end{bmatrix}$$

$$= \begin{bmatrix} \frac{\partial^2}{\partial x^2} + \frac{1-\nu}{2}\frac{\partial^2}{\partial s^2} & \frac{1+\nu}{2}\frac{\partial^2}{\partial x \partial s} & \frac{\nu}{R}\frac{\partial}{\partial x} \\ \frac{1+\nu}{2}\frac{\partial^2}{\partial x \partial s} & \frac{1-\nu}{2}\frac{\partial^2}{\partial x^2} + \frac{\partial^2}{\partial s^2} & \frac{1}{R}\frac{\partial}{\partial s} \\ \frac{\nu}{R}\frac{\partial}{\partial x} & \frac{1}{R}\frac{\partial}{\partial s} & \frac{h^2}{12}\nabla^4 + \frac{1}{R^2} \end{bmatrix} \qquad (2.7)$$

15

with

$$u = \left\{ \begin{array}{c} u \\ v \\ w \end{array} \right\} ; \qquad f = \left\{ \begin{array}{c} -P_x \\ -P_s \\ P \end{array} \right\} = \frac{(1-\nu^2)}{Eh} \left\{ \begin{array}{c} -p_x \\ -p_s \\ p \end{array} \right\} . \qquad (2.8)$$

By making use of Eq. (2.3), Donnell's decoupled w equilibrium equation is given in operator form by

$$|L| \cdot w = |G_3| = \left| \begin{array}{ccc} L_{uu} & L_{uv} & -P_x \\ L_{vu} & L_{vv} & -P_s \\ L_{wu} & L_{wv} & P \end{array} \right| , \qquad (2.9)$$

or alternatively, by

$$\frac{h^2}{12} \nabla^8 w + \frac{1-\nu^2}{R^2} \frac{\partial^4 w}{\partial x^4} =$$
$$\nabla^4 P + \frac{1}{R} \Big[\frac{\partial^3 P_s}{\partial s^3} + \nu \frac{\partial^3 P_x}{\partial x^3} + (2+\nu) \frac{\partial^3 P_s}{\partial s \partial x^2} - \frac{\partial^3 P_x}{\partial x \partial s^2} \Big] \qquad (2.10)$$

as will now be shown results from Eq. (2.9) using the computer algebra program SMP to perform the indicated determinant operations.

The sample SMP runstream, whose objective is the explicit symbolic solution of Eq. (2.9), is shown in the following program listing. The differential symbol notation

$$\frac{\partial}{\partial x} \Rightarrow \text{dx}; \quad \frac{\partial}{\partial s} \Rightarrow \text{ds}; \quad \frac{\partial^2}{\partial x^2} + \frac{\partial^2}{\partial s^2} = \nabla^2 \Rightarrow \text{del2} \qquad (2.11)$$

is used to simplify operator notation and help reduce the intermediate problem swell typical of symbolic computations. I[i]:: is used by SMP to represent an input statement while O[i]: represents the corresponding output, if any. Many of the input statements which either do not require that they be echoed as output or represent intermediate calculations which in the present context are of no interest are ended with a ";" indicating that no output is desired.

16

SMP 1.5.0

```
          /*     Donnell's cylindrical shell equations        */

#I[1]::   ueqn : dx^2 u + (1-nu)/2 ds^2 u + (1+nu)/2 dx ds v + nu/r dx w;

#I[2]::   veqn : (1-nu)/2 dx^2 v + ds^2 v + (1+nu)/2 dx ds u + ds w/r;

#I[3]::   weqn : h^2/12 del2^2 w + (w/r + ds v + nu dx u)/r;

          /*     Form differential operator matrix            */

#I[4]::   eqn : {ueqn,veqn,weqn};

#I[5]::   d   : {u,v,w};

#I[6]::   coefmatrix : Ar[ {3,3}, Coef[ d[$2], Ex[ eqn[$1]]] ];

#I[7]::   Prmat[coefmatrix]
```

$$\#O[7]: \quad \begin{array}{ccc}
-\dfrac{ds^2\ nu}{2} + \dfrac{ds^2}{2} + dx^2 & \dfrac{ds\ dx}{2} + \dfrac{ds\ dx\ nu}{2} & \dfrac{dx\ nu}{r} \\[3ex]
\dfrac{ds\ dx}{2} + \dfrac{ds\ dx\ nu}{2} & -\dfrac{dx^2\ nu}{2} + ds^2 + \dfrac{dx^2}{2} & \dfrac{ds}{r} \\[3ex]
\dfrac{dx\ nu}{r} & \dfrac{ds}{r} & \dfrac{1}{r^2} + \dfrac{del2^2\ h^2}{12}
\end{array}$$

```
          /*     Determine characteristic operator           */

#I[8]::   Ex[ 2/(1-nu) Det[coefmatrix] ];

#I[9]::   lhs : Cb[ Col[ Ex[ Fac[ S[ %, h -> 0 ]]]], dx^4 ] + \
                Ex[ h^2 S[ Ex[ Fac[ Coef[ h^2, % ]]], \
                   dx^4 -> del2^2 - ds^4 - 2 dx^2 ds^2 ]];

          /*     Form differential loading matrix             */

#I[10]::  coefmatrix[1,3]:-px; coefmatrix[2,3]:-ps; coefmatrix[3,3]:p;

          /*     Determine loading operator                   */

#I[11]::  Ex[ 2/(1-nu) Det[coefmatrix] ];
```

```
#I[12]::  rhs : Cb[ S[ p Ex[ Fac[ Coef[ p, % ]]], \
                 dx^4 -> del2^2 - ds^4 - 2 dx^2 ds^2 ], 1/r ] + \
              Fac[ S[ %, p -> 0 ]];

       /*    Donnell's transverse equilibrium equation      */

#I[13]::  lhs v = rhs

              4       2         4  2
          dx  (1 - nu )    del2  h
#O[13]:   v (------------- + --------) =
                  2             12
                 r


           3           2       2         3            2
          (ds  ps + 2ds  dx  ps - ds  dx px + dx  nu px + ds  dx  nu ps)
          ----------------------------------------------------------------

                                     r

                    2
           + del2  p
```

SMP statements I[1]-I[3] are seen to correspond to the left-hand portion
of Eq. (2.5) from which I[4]-I[6] form the *continuum operator L* subsequently
printed in matrix format by I[7]. This result should be compared to Eq. (2.7).
With L now in hand, the characteristic linear operator, $|L|$, needed in Eq. (2.9),
is symbolically calculated by I[8] and then simplified in I[9]. One step of this
simplification process is the symbolic substitution of $(\nabla^2)^2$ for $(\frac{\partial^2}{\partial x^2}+\frac{\partial^2}{\partial s^2})^2$ which,
as shown in I[9], is actually accomplished by the purely syntactic substitution
of dx^4 by del2^2 - 2 dx^2 dy^2 - ds^4. Next, G_3 is formed by I[10] followed
by I[11] which symbolically calculates $|G_3|$. I[12] simplifies that result in a
similar manner to that already described for $|L|$. Donnell's decoupled eighth-order
transverse equilibrium equation is then constructed and displayed by I[13].

It should also be pointed out that completely decoupled equilibrium equations
for both u and v could have also been obtained using this technique. In the form
originally presented by Donnell, the equilibrium equations for either u or v can be
viewed simply as partial operator factorizations of Eq. (2.6). If, for example, one

18

considers Donnell's equilibrium equation for v,

$$\nabla^4 v = -\frac{2+\nu}{R}\frac{\partial^3 w}{\partial x^2 \partial s} - \frac{1}{R}\frac{\partial^3 w}{\partial s^3} + \frac{\partial^2 P_s}{\partial s^2} + \frac{2}{1-\nu}\frac{\partial^2 P_s}{\partial x^2} - \frac{1+\nu}{1-\nu}\frac{\partial^2 P_x}{\partial x \partial s}, \quad (2.12)$$

this result could be easily obtained from Eq. (2.6) after performing the first step of a symbolic Gaussian elimination, *viz*,

$$\begin{bmatrix} L_{uu} & L_{uv} & L_{uw} \\ 0 & L_{uu}L_{vv} - L_{vu}L_{uv} & L_{uu}L_{vw} - L_{vu}L_{uw} \\ 0 & L_{uu}L_{wv} - L_{wu}L_{uv} & L_{uu}L_{ww} - L_{wu}L_{uw} \end{bmatrix} \begin{Bmatrix} u \\ v \\ w \end{Bmatrix} = \begin{Bmatrix} -P_x \\ -L_{uu}P_s + L_{vu}P_x \\ L_{uu}P + L_{wu}P_x \end{Bmatrix}$$
$$(2.13)$$

on the way to obtaining the completely decoupled w equation. Here, Eq. (2.12) would correspond to the second row of Eq. (2.13). With the next step of the elimination resulting in Eq. (2.10), L is now effectively triangularized. In this form, a very simple second-order expression for u is seen to result in lieu of Donnell's $\nabla^4 u$ expression.

§2.2 Taylor Series Technique - The Timoshenko Beam

With the basic symbolic techniques used to decouple linear matrix differential operators now in hand, the next step entails recovering the limit differential equilibrium equations corresponding to the discrete finite element equations at an interior node. These discrete finite element equations result from the assembly of an element *patch* as was portrayed in Fig. 1.1 for several different element geometries. Once an element patch has been assembled, the finite element origin of the discrete equations becomes immaterial and techniques used to examine finite difference equations may be used. The approach presented here of employing Taylor series expansions of the dependent variables is an extension of the work of Hirt [11] and Warming and Hyett [12]. The key departure from the local truncation error procedure is that the continuum solution is never formally substituted into the discrete equations in order to determine the "local truncation error." Instead, one works with the solution of the limit differential equilibrium equations correspond-

19

ing to the discrete equations. As a result, primary interest can now be directed toward identifying intrinsic element *behavior* such as spurious mechanisms and element locking which may be engendered by a particular finite element formulation. The formal order-of-accuracy of the discrete finite element equations is no longer the principal reason for performing this type of analysis. In fact, since certain element pathologies are shown to elevate the role of truncation error terms to that of playing the dominant role in the limit differential (or modified) equilibrium equations, asserting consistency based solely on local truncation error information may actually prove misleading. The limit differential equilibrium equations in this case provide the information needed to assess what one might call "operational" consistency.

The operational procedure for decoupling a set of coupled differential equilibrium equations in terms of a single dependent nodal variable, w, will be used here to first derive the decoupled continuum equilibrium equation of the Timoshenko beam for the linear dynamic, static and bifurcation buckling problems. The limit differential equations corresponding to the discrete finite element equations for the linear Timoshenko beam are then derived and compared to the continuum equilibrium equation for the cases of both exact and uniformly reduced spatial integration. For the present case, the resulting limit differential equilibrium equations expressed in a decoupled form are shown to result in a canonical representation from which one can explicitly identify the parasitic differential operator responsible for *transverse shear* element locking.

§2.2.1 Continuum Timoshenko Beam

The governing *linearized* equations of motion for the shear-deformable Timoshenko beam theory including the effects of both an inplane pre-stress and a lateral loading are derived from Hamilton's Principle,

$$\delta \int_{t_1}^{t_2} \mathcal{L} \, dt = 0 \qquad (2.14)$$

20

where the Lagrangian $\mathcal{L} = T - \Pi$ is composed of T, the kinetic energy and Π, the total potential energy which in turn is the sum of the strain energy, U, and the potential energy of the applied loads, V. The Euler-Lagrange equations resulting from Eq. (2.14) yield the strong form of the equations of motion which are of immediate interest here (while application of the Ritz procedure yields the corresponding discrete equations).

The assumed displacement field for Timoshenko beam theory is

$$
\begin{aligned}
u(x, z, t) &= -z\theta(x, t) \\
w(x, z, t) &= w(x, t)
\end{aligned}
\tag{2.15}
$$

where u and w are the inplane and transverse displacements with θ representing the counter-clockwise rotation of the beam normal. Using Eq. (2.15), the kinetic energy is given by

$$
T = \frac{1}{2} \int_0^l \int_{-h/2}^{h/2} \rho \dot{u}_i \dot{u}_i \, dz \, dx = \frac{1}{2} \int_0^l \left[\rho A \left(\frac{\partial w}{\partial t}\right)^2 + \rho I \left(\frac{\partial \theta}{\partial t}\right)^2 \right] dx
\tag{2.16}
$$

where A, I and ρ are the cross-sectional area, moment of inertia and density, respectively. The strain energy, $U = U_m + U_\sigma$, is partitioned into its separate material and stress-dependent contributions,

$$
U_m = \frac{1}{2} \int_0^l \int_{-h/2}^{h/2} [E\epsilon_x^2 + G\gamma_{xz}^2] \, dz \, dx = \frac{1}{2} \int_0^l \left[EI \left(\frac{\partial \theta}{\partial x}\right)^2 + GA \left(\frac{\partial w}{\partial x} - \theta\right)^2 \right] dx
$$

$$
U_\sigma = \int_0^l \int_{-h/2}^{h/2} \sigma \epsilon_x^{\mathrm{NL}} \, dz \, dx = \frac{1}{2} \int_0^l \left[\sigma I \left(\frac{\partial \theta}{\partial x}\right)^2 + \sigma A \left(\frac{\partial w}{\partial x}\right)^2 \right] dx
$$

$$
\tag{2.17}
$$

where E and G are the extensional and shear modulus and σ is an initial axial

stress with the nonlinear part of the total Lagrangian strain, ϵ_x, given by[1]

$$\epsilon_x^{NL} = \frac{1}{2}\Big[\Big(\frac{\partial u}{\partial x}\Big)^2 + \Big(\frac{\partial w}{\partial x}\Big)^2\Big] . \tag{2.18}$$

Lastly, the potential energy of the applied lateral load, q, is simply

$$V = -W_{ext} = -\int_0^l qw\,dx . \tag{2.19}$$

Distributed moments are neglected here in keeping with the classical derivation of these equations.

The Euler-Lagrange equations corresponding to the present functional form of $\mathcal{L} = \mathcal{L}(x, t, w, \theta, w', \theta', \dot{w}, \dot{\theta})$ are

$$\frac{\partial \mathcal{L}}{\partial u_i} - \frac{\partial}{\partial x}\Big(\frac{\partial \mathcal{L}}{\partial u_i'}\Big) - \frac{\partial}{\partial t}\Big(\frac{\partial \mathcal{L}}{\partial \dot{u}_i}\Big) = 0 \qquad i = 1, 2 \tag{2.20}$$

where $u_i = (w, \theta)$. With $\mathcal{L}$ determined, Eq. (2.20) is used to derive the governing *linearized* equations of motion for the Timoshenko beam written in the matrix differential operator form

$$L\,u = (L_{\mathrm{m}} + L_\sigma)\,u = f \tag{2.21}$$

---

[1] If the beam equivalent of von Kármán's nonlinear plate theory [25] is desired,

$$\epsilon_x^{NL} = \frac{1}{2}\Big(\frac{\partial w}{\partial x}\Big)^2$$

would instead be used in which case, the $\sigma I\big(\frac{\partial \theta}{\partial x}\big)^2$ or so-called *curvature* term [26] would be absent from Eq. (2.17). The effect on the buckling operator of including this rm will be seen in Eq. (2.28).

where

$$L_{\mathrm{m}} = \begin{bmatrix} \rho A \frac{\partial^2}{\partial t^2} - GA \frac{\partial^2}{\partial x^2} & GA \frac{\partial}{\partial x} \\ GA \frac{\partial}{\partial x} & -\rho I \frac{\partial^2}{\partial t^2} + EI \frac{\partial^2}{\partial x^2} - GA \end{bmatrix}$$

(2.22)

$$L_{\sigma} = \begin{bmatrix} -\sigma A \frac{\partial^2}{\partial x^2} & 0 \\ 0 & \sigma I \frac{\partial^2}{\partial x^2} \end{bmatrix}$$

and

$$u = \lfloor w \quad \theta \rfloor^{\mathrm{T}} \qquad f = \lfloor q \quad 0 \rfloor^{\mathrm{T}}. \tag{2.23}$$

The notation $\lfloor \cdots \rfloor$ is used to denote a row vector. The three different classes of problems which can be addressed based upon Eq. (2.21) are 1) free/forced vibration, 2) static beam bending, and 3) bifurcation buckling.

The governing equations for the first two classes of problems emanate from the material operator, L_{m}. By employing Eq. (2.3), the decoupled Timoshenko beam equation in terms of w is found from

$$|L_{\mathrm{m}}| \cdot w = \begin{vmatrix} q & GA \frac{\partial}{\partial x} \\ 0 & -\rho I \frac{\partial^2}{\partial t^2} + EI \frac{\partial^2}{\partial x^2} - GA \end{vmatrix} \tag{2.24}$$

to be

$$EI \frac{\partial^4 w}{\partial x^4} + \rho A \frac{\partial^2 w}{\partial t^2} - \rho I \left(1 + \frac{E}{G}\right) \frac{\partial^4 w}{\partial x^2 \partial t^2} + \frac{\rho^2 I}{G} \frac{\partial^4 w}{\partial t^4} = q + \frac{\rho I}{GA} \frac{\partial^2 q}{\partial t^2} - \frac{EI}{GA} \frac{\partial^2 q}{\partial x^2} \tag{2.25}$$

which agrees with Timoshenko's derivation of his C^0 beam theory [27]. For the static case (i.e., $\frac{\partial w}{\partial t} = 0$), Eq. (2.25) becomes

$$EI \frac{d^4 w}{dx^4} = q - \frac{EI}{GA} \frac{d^2 q}{dx^2} \tag{2.26}$$

which will serve as the reference continuum equation used for the identification of "transverse shear" element locking in the next section.

23

For the case of bifurcation buckling where $\frac{\partial w}{\partial t} = 0$ and $q = 0$, the reference continuum equation to be employed later in §2.2.3 is found from

$$|L_{\mathrm{m}} + L_\sigma| \cdot w = |G_1|_{q=0} \tag{2.27}$$

to be

$$\frac{I}{G}\frac{d^4w}{dx^4}\sigma^2 + [I(\frac{E}{G}+1)\frac{d^4w}{dx^4} - A\frac{d^2w}{dx^2}]\sigma + EI\frac{d^4w}{dx^4} = 0. \tag{2.28}$$

Unlike the familiar Euler-Lagrange beam equation, a quadratic eigenproblem results by including the curvature effect in conjunction with transverse shear deformation. In practice, one finds that the coefficient of the σ^2 term, $\frac{I}{G}\frac{d^4w}{dx^4} \ll 1$ with the result that Eq. (2.28) should be considered to represent a singular perturbation problem – if not formally, certainly from a numerical conditioning standpoint when solving for the flexural buckling mode.

§2.2.2 Discrete Linear Timoshenko Beam

It has been recognized for some time (see eg., [28,29]) that C^0 elements such as the exact spatially integrated linear Timoshenko beam element exhibit *transverse shear* locking when the element is thin, *ie.*, $l/h \gg 1$ where l and h are the element length and thickness, respectively. Thus, the corresponding coupled limit differential equations should also embody this locking phenomenon in some way. As will be shown shortly, the decoupled limit differential equation obtained by the present procedure plays the key role in identifying the parasitic differential operator responsible for transverse shear element locking.

The element material stiffness matrix for the linear Timoshenko beam element is determined from the second variation of the strain energy expression given by Eq. (2.17) in the usual way (see e.g. [30]) resulting in

$$\mathbf{k} = \mathbf{k}_b + \mathbf{k}_s = \int_0^l (EI\,\mathbf{B}_b^{\mathrm{T}}\mathbf{B}_b + GA\,\mathbf{B}_s^{\mathrm{T}}\mathbf{B}_s)\,dx. \tag{2.29}$$

Here, $\mathbf{B}_b$ and $\mathbf{B}_s$ are the strain-displacement matrices representing bending and

transverse shear components determined from

$$\epsilon = \left\{ \begin{array}{c} \epsilon_z \\ \gamma_{zz} \end{array} \right\} = \mathbf{B}\mathbf{d} \quad \Rightarrow \quad \mathbf{B} = \left[\begin{array}{cccc} 0 & -z\frac{\partial N_1}{\partial x} & 0 & -z\frac{\partial N_2}{\partial x} \\ \frac{\partial N_1}{\partial x} & -N_1 & \frac{\partial N_2}{\partial x} & -N_2 \end{array} \right] = \left\{ \begin{array}{c} \mathbf{B}_b \\ \mathbf{B}_s \end{array} \right\}$$

(2.30)

with the element shape functions defined by $N_i = \lfloor 1 - \frac{x}{l}, \quad \frac{x}{l} \rfloor$ and the element degree-of-freedom vector by $\mathbf{d} = \lfloor w_1 \quad \theta_1 \quad w_2 \quad \theta_2 \rfloor^T$.

Evaluation of $\mathbf{B}_b^T\mathbf{B}_b$ and $\mathbf{B}_s^T\mathbf{B}_s$, making use of Eq. (2.30), shows that the nonzero terms in the first integrand in Eq. (2.29) are constant so that the use of a 1-point Gauss-Legendre quadrature rule would exactly integrate them. Quadratic order terms are however found in the second integrand which would require a 2-point quadrature rule for an exact term-by-term spatial integration. The use of a 1-point (or reduced) quadrature rule results in the loss of these quadratic order contributions to the "$\theta_1\theta_1$", "$\theta_1\theta_2$" and "$\theta_2\theta_2$" terms of $\mathbf{k}_s$.

§2.2.2.1 Exact Spatial Integration – Transverse Shear Locking

For the case of static loading with no prestress, the finite element difference equations at an interior node "j" for an assembled element patch of exactly integrated Timoshenko beam elements, as portrayed in Fig. 2.1, are

$$-GA(\frac{w_{j-1} - 2w_j + w_{j+1}}{l^2}) + GA(\frac{-\theta_{j-1} + \theta_{j+1}}{2l}) = q_j$$

(2.31)

$$EI(\frac{\theta_{j-1} - 2\theta_j + \theta_{j+1}}{l^2}) - GA(\frac{\theta_{j-1} + 4\theta_j + \theta_{j+1}}{6}) + GA(\frac{-w_{j-1} + w_{j+1}}{2l}) = 0.$$

Written in this form, these equations are viewed simply as the set of finite difference equations used to approximate Eq. (2.21). The fact that they originated from a finite element discretization rather than a direct differencing of Eq. (2.21) is immaterial for the analysis to follow. The nodal load, q_j, in Eq. (2.31) can be represented in the functional form $\bar{q}(x)l$ where $\bar{q}(x)$ is the discrete counterpart of the distributed continuum load, $q(x)$. The present emphasis is to determine the

25
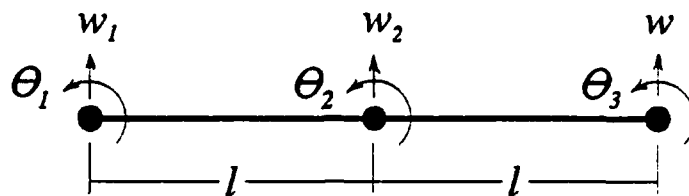
Fig. 2.1 – Timoshenko beam discretization

effect of the discretization on the homogeneous part of the continuum operator, so for now, it is convenient to assume that $q(x) = \tilde{q}(x)$. In §2.3, when the important question of discrete error estimation is introduced, the exact form of $\tilde{q}(x)$ and its role in the error estimate will be discussed.

The first, and conceptually most important step in determining the limit differential equilibrium equations corresponding to the discrete equations, Eq. (2.31), is the substitution of

$$(w, \theta) \in S_u = \{u : u \in C^\infty(x), u(x_j) = u_j\} \tag{2.32}$$

for the nodal displacements, (w_j, θ_j). Next, Taylor series expansions,

$$u(x_{j\pm1}) = u(x_j) \pm l\frac{\partial u(x_j)}{\partial x} + \frac{l^2}{2}\frac{\partial^2 u(x_j)}{\partial x^2} \pm \frac{l^3}{6}\frac{\partial^3 u(x_j)}{\partial x^3} + \cdots , \tag{2.33}$$

are used to relate the displacements at $x_{j\pm1}$ to the interior node, x_j, which when substituted into Eq. (2.31) results in the following coupled limit differential equilibrium equations,

$$-GA(\frac{d^2w}{dx^2} - \frac{d\theta}{dx}) - GA\frac{l^2}{12}(\frac{d^4w}{dx^4} - 2\frac{d^3\theta}{dx^3}) + O(l^4) = q$$

$$\tag{2.34}$$

$$EI\frac{d^2\theta}{dx^2} + GA(\frac{dw}{dx} - \theta) + EI\frac{l^2}{12}\frac{d^4\theta}{dx^4} + GA\frac{l^2}{6}(\frac{d^3w}{dx^3} - \frac{d^2\theta}{dx^2}) + O(l^4) = 0 ,$$

26

or in matrix operator form

$$L^D u = f.$$ (2.35)

These equations are representative of any interior nodal point in a uniform mesh. It is immediately apparent from these equations that this discretization is a consistent one since in the limit as $l \to 0$, the coupled continuum equilibrium equations, Eq. (2.22), are recovered, *viz.*,

$$\lim_{l \to 0} L^D = L.$$ (2.36)

It is very important to note that these equations *represent* the system for which the solution to the discrete model actually corresponds, if we ignore for the time being any discretization errors associated with q. As such, one is able to infer intrinsic element behavior by a direct term-by-term comparison with the governing strong form of the problem.

Following the symbolic procedure used for the continuum problem in the previous section, the decoupled transverse equilibrium equation is determined from Eq. (2.34) to be [2]

$$EI(1 + \frac{l^2}{12}\frac{GA}{EI}) \cdot (\frac{d^4 w}{dx^4} + \frac{l^2}{6}\frac{d^6 w}{dx^6}) = q + (\frac{l^2}{6} - \frac{EI}{GA})\frac{d^2 q}{dx^2} - \frac{l^2}{12}\frac{EI}{GA}\frac{d^4 q}{dx^4}$$

$$= (q + \frac{l^2}{6}\frac{d^2 q}{dx^2}) - \frac{EI}{GA}(\frac{d^2 q}{dx^2} + \frac{l^2}{12}\frac{d^4 q}{dx^4})$$ (2.37)

where only truncation terms of order l^2 have been retained. An equation of this form, where only leading truncation-order terms are retained, is often referred to as a *modified* equilibrium equation (see e.g., Ref. [12]).

Comparing Eq. (2.37) with its continuum counterpart, Eq. (2.26), one finds that the dominant effect of the finite element discretization manifests itself as a

---

[2] The MACSYMA runstream with associated output from which these results where obtained may be found in Appendix A.1

modification to the bending stiffness resulting from the appearance of a parasitic differential term of the same order as the primary differential operator, i.e., d^4/dx^4 The modified bending stiffness resulting from this parasitic differential operator, $\widetilde{EI}$, defined as

$$\widetilde{EI} = \left[1 + \frac{l^2}{12}\frac{GA}{EI}\right]EI \tag{2.38}$$

is the discrete counterpart of the continuum bending stiffness, EI. MacNeal [31] and Prathap and Bhashyam [32] have also identified this modified bending stiffness term working from an energy standpoint. Note that if one had prematurely stopped with Eq. (2.34), a modified bending stiffness might have mistakenly been assumed to be $(1 - \frac{l^2}{6}\frac{GA}{EI})EI$ by collecting the coefficients of $\frac{d^2\theta}{dx^2}$ from the second equation.

In order to assess the relative magnitude of $\widetilde{EI}$ with respect to EI, the case of an isotropic rectangular beam of unit width and thickness h is considered. For this simple case,

$$\widetilde{EI} = \left[1 + \frac{1}{2(1+\nu)}\left(\frac{l}{h}\right)^2\right]EI. \tag{2.39}$$

For even a moderately thin beam with $l/h = 10$ (and $\nu = .3$), one finds that

$$\widetilde{EI} = 39.5EI \tag{2.40}$$

with the immediate implication that a finite element solution of a "thin" beam problem using a linear Timoshenko beam element of this aspect ratio would result in a transverse displacement w equal to only about 2.5% of the correct solution. This problem is of course the well known *transverse shear* element locking phenomenon exhibited by C^0 beam and plate finite elements which is shown to be linked directly to deficiencies in the limit differential equilibrium equations obtained from the discrete finite element equations.

REMARK 2.1

It is important to emphasize here that element locking has been identified as

an intrinsic element property and as such does not require knowledge of boundary conditions nor any specific numerical solution. This fundamental approach to assessing intrinsic element behavior should be contrasted with the alternative technique of identifying element locking based upon the *art* of constraint counting (see e.g., [33,34]). Since locking was viewed as the result of how a particular discretization represented the thin plate limit of zero transverse shear strain, the idea of shear constraints was introduced to reflect the manner in which this condition was satisfied on the element level. If this number was larger than the number of free d-o-f per element in the global model, then mesh locking was anticipated. Tsach [34] states that *locking is not solely an element property; it is a characteristic of both the element and the boundary conditions.* Based upon the symbolic results presented here (and in the following chapters), one cannot help but conclude that this statement is misleading since the question of element locking is answered independently of any imposed boundary conditions.

§2.2.2.2 Reduced Spatial Integration – Element Unlocking

One numerical technique used to rectify the problem of transverse shear element locking is to underintegrate the transverse shear stiffness (see e.g., [28,29,35]). Doing so raises the question of element consistency since employing reduced spatial integration violates the strict variational basis of the discretization. This results in what Strang and Fix [6] refer to as a *variational crime*, from a Minimum Potential Energy standpoint. Malkus and Hughes [36] have, however, shown the equivalence between this technique and that of mixed finite element methods. This permits one to apply convergence proofs and error estimates to those cases where equivalence can be established. For the present problem of interest, Arnold [37] has shown the equivalence between reduced spatial integration and a mixed finite element implementation. In this section, the use of reduced spatial integration is shown to result in a discretization whose decoupled limit differential equilibrium equation does not contain the parasitic differential term responsible for the transverse shear element locking.

Recovery of the limit differential equilibrium equations will again begin by writing the discrete finite element equations of the linear Timoshenko beam, now derived employing one point Gaussian quadrature for the transverse shear stiffness,

at an interior node as

$$-GA(\frac{w_{j-1} - 2w_j + w_{j+1}}{l^2}) + GA(\frac{-\theta_{j-1} + \theta_{j+1}}{2l}) = q_j$$

(2.41)

$$EI(\frac{\theta_{j-1} - 2\theta_j + \theta_{j+1}}{l^2}) - GA(\frac{\theta_{j-1} + 2\theta_j + \theta_{j+1}}{4}) + GA(\frac{-w_{j-1} + w_{j+1}}{2l}) = 0$$

Comparing Eq. (2.41) with Eq. (2.31), which was obtained using exact spatial integration, one finds that they differ only in the averaging of θ in the second of these equations. Exact spatial integration resulted in a $\frac{1}{6}$(1-4-1) nodal averaging scheme versus the $\frac{1}{4}$(1-2-1) scheme seen here. By again employing Eq. (2.33), the limit differential equilibrium equations corresponding to Eq. (2.41) are found to be

$$-GA(\frac{d^2w}{dx^2} - \frac{d\theta}{dx}) - GA\frac{l^2}{12}(\frac{d^4w}{dx^4} - 2\frac{d^3\theta}{dx^3}) + O(l^4) = q$$

(2.42)

$$EI\frac{d^2\theta}{dx^2} + GA(\frac{dw}{dx} - \theta) + EI\frac{l^2}{12}\frac{d^4\theta}{dx^4} + GA\frac{l^2}{6}(\frac{d^3w}{dx^3} - \frac{3}{2}\frac{d^2\theta}{dx^2}) + O(l^4) = 0.$$

In this form, the only difference between the two sets of coupled limit differential equilibrium equations obtained from the two different integration rules is in the truncation error terms associated with approximating θ which are seen to be

$$\theta^e = \theta + \frac{l^2}{6}\frac{d^2\theta}{dx^2}$$

(2.43)

$$\theta^r = \theta + \frac{l^2}{4}\frac{d^2\theta}{dx^2}$$

where the superscripts e and r designate whether the exact or reduced spatial integration rule was used. From the traditional formal order-of-accuracy viewpoint, one may prematurely conclude at this point that the approximation engendered by the exact integration rule should result in a more accurate discrete solution which is not the case as will now be shown.

30

The decoupled limit differential equilibrium equation obtained from Eq. (2.42) is found to be

$$EI\frac{d^4w}{dx^4} + EI\frac{l^2}{6}\frac{d^6w}{dx^6} = q + \left(\frac{l^2}{4} - \frac{EI}{GA}\right)\frac{d^2q}{dx^2} - \frac{l^2}{12}\frac{EI}{GA}\frac{d^4q}{dx^4}.$$
(2.44)

It is immediately apparent that the parasitic 4th-order differential term responsible for locking has been eliminated by the reduced integration of the transverse shear stiffness. Hence, what appears to be a less accurate averaging scheme for the θ term, as shown in Eq. (2.45), plays the key role in eliminating transverse shear element locking. Examination of Eq. (2.42) shows that like Eq. (2.34), a truncation error term has a differential operator of the same order as that of the continuum operator. However, in this case, Eq. (2.44) shows that now, this effect does not propagate to the decoupled equation. Hence, it is the decoupling process which manifests the true behavior of the Timoshenko beam discretization. The results from this and the preceding sub-section show that this decoupling process results in a canonical form of the modified equilibrium equations from which intrinsic element behavior is determined.

REMARK 2.2

MacNeal's *residual bending flexibility* modification [31] of the material transverse shear stiffness is obtained from the reduced spatial integration analysis as a consequence of eliminating the second-order truncation term associated with d^2q/dx^2 in Eq. (2.44). This is accomplished by matching the coefficient associated with d^2q/dx^2 with the correct continuum coefficient. With GA only explicitly appearing here in the continuum equation, one is free to define a modified GA^* which satisfies

$$\frac{l^2}{4} - \frac{EI}{GA^*} = \frac{l^2}{6} - \frac{EI}{GA}.$$
(2.46)

This results in

$$GA^* = \left[\frac{1}{GA} + \frac{l^2}{12EI}\right]^{-1}$$
(2.47)

which is seen to be identical to MacNeal's "GA^*". Replacing GA with GA^* in the discrete finite element equations results in the following decoupled limit differential

31

equilibrium equation

$$EI\frac{d^4w}{dx^4} + EI\frac{l^2}{6}\frac{d^6w}{dx^6} = q + \left(\frac{l^2}{6} - \frac{EI}{GA}\right)\frac{d^2q}{dx^2} - \frac{l^2}{12}\frac{EI}{GA}\frac{d^4q}{dx^4}. \qquad (2.48)$$

Substitution of the continuum solution, W, results in

$$EI\frac{d^4W}{dx^4} = q - \frac{EI}{GA}\frac{d^2q}{dx^2} + \frac{l^2}{12}\frac{EI}{GA}\frac{d^4q}{dx^4} \qquad (2.49)$$

where the twice differentiated continuum equilibrium equation has been used to simplify the results. As before, only the leading truncation error terms are retained. Note that the coefficient of the last term in Eq. (2.49) can be rewritten as

$$\frac{l^2}{12}\frac{EI}{GA} = \frac{(1+\nu)}{72}l^2h^2 = \frac{(1+\nu)}{72}c^2l^4 \qquad (2.50)$$

where $c = h/l \ll 1$ for thin beam applications. Hence, the resulting finite element approximation of the Timoshenko beam by the linear element achieves a fourth-order interior accuracy for a uniform element mesh – the same order of accuracy as for the C^1 Hermitian beam.

REMARK 2.3

Penalty function techniques have been used as a method for deriving "C^1" bending elements employing C^0 displacement interpolation fields (see e.g., [30,38]). For the case of the Euler-Bernoulli beam, the constrained variational expression,

$$\Pi^* = \frac{EI}{2}\int_0^l \left(\frac{d\theta}{dx}\right)^2 dx + \alpha\int_0^l \left(\frac{dw}{dx} - \theta\right)^2 dx - \int_0^l wq\,dx, \qquad (2.51)$$

is identical to that used for the Timoshenko beam except for the interpretation of α. For the shear-flexible Timoshenko beam, the second integral represents the transverse shear energy with $\alpha = GA/2$. For the above case, however, α is the penalty parameter associated with enforcing the constraint that $\theta = dw/dx$. For the linear beam derived from Eq. (2.51) employing reduced spatial integration on the penalty term, the decoupled transverse limit differential equilibrium equation is found to be

$$EI\frac{d^4w}{dx^4} + EI\frac{l^2}{6}\frac{d^6w}{dx^6} = q + \left(\frac{l^2}{4} - \frac{EI}{2\alpha}\right)\frac{d^2q}{dx^2} - \frac{l^2}{12}\frac{EI}{2\alpha}\frac{d^4q}{dx^4}. \qquad (2.52)$$

In the context of the present penalty formulation, the expected Euler-Bernoulli

beam theory,

$$EI\frac{d^4w}{dx^4} = q + O(l^2) \tag{2.53}$$

results in the limit as the constraint that $\theta = dw/dx$ is enforced, i.e., $\alpha \to \infty$. This "C^1" beam element is seen, however, to be only second-order accurate as compared to the Hermitian beam element discussed in Remark 2.2 which achieved fourth-order accuracy by explicitly enforcing C^1 displacement continuity.

§2.2.2.3 Limit Differential Equilibrium Equations versus Local Truncation Error

In light of the two examples presented thus far where limit differential equilibrium equations have been employed to explicity identify element behavior, the differences between the type of information they provide and that of a local traditional truncation error analysis (see e.g., §1.4 of [6]) can now be easily contrasted.

Returning to the results from §2.2.2.1, the modified equilibrium equation (i.e., limit differential equilibrium equation with only leading truncation-order terms retained) for the exactly integrated Timoshenko beam element was found in to be

$$EI(1 + \frac{l^2}{12}\frac{GA}{EI}) \cdot (\frac{d^4w}{dx^4} + \frac{l^2}{6}\frac{d^6w}{dx^6}) = (q + \frac{l^2}{6}\frac{d^2q}{dx^2}) - \frac{EI}{GA}(\frac{d^2q}{dx^2} + \frac{l^2}{12}\frac{d^4q}{dx^4}), \tag{2.54}$$

or in differential operator form,

$$l^D \cdot w = r^D \cdot q. \tag{2.55}$$

Here, $w(x)$, as was defined by Eq. (2.32), is the solution of the modified equilibrium equation. The exact continuum solution, $W(x)$, does not satisfy Eq. (2.54), nor does the discrete solution, w, satisfy the continuum equilibrium equation,

$$EI\frac{d^4W}{dx^4} = q - \frac{EI}{GA}\frac{d^2q}{dx^2} \quad \Rightarrow \quad l \cdot W = r \cdot q \tag{2.56}$$

representing Timoshenko beam theory. For this very reason, Eq. (2.56) cannot be used to further simplify the limit differential equilibrium equation, Eq. (2.54).

In spite of the fact that the term "truncation error" has been applied to characterize any term in which the element length, l, explicitly appears in the limit differential equilibrium equations, they do not represent the local truncation error of the discretization from a classical finite difference standpoint. The concept of local truncation error does not arise until one formally substitutes the exact continuum solution, W, in place of the discrete solution, w, in Eq. (2.54). The differential terms remaining after the continuum equation and its differentiated forms have been employed to simplify it represent the local truncation error, τ^l, of the discretization. For the present case, the local truncation error for the Timoshenko beam discretization is found from the error equation,

$$EI(1+\frac{l^2}{12}\frac{GA}{EI})\cdot(\frac{d^4W}{dx^4}+\frac{l^2}{6}\frac{d^6W}{dx^6})-(q+\frac{l^2}{6}\frac{d^2q}{dx^2})+\frac{EI}{GA}(\frac{d^2q}{dx^2}+\frac{l^2}{12}\frac{d^4q}{dx^4})=\tau^l , \quad (2.57)$$

to be

$$\tau^l = \frac{l^2}{12}(GA\frac{\partial^4W}{\partial x^4}-\frac{EI}{GA}\frac{\partial^4q}{\partial x^4})+O(l^4) \quad (2.58)$$

Here, differentiated forms of the continuum equilibrium equation, Eq. (2.54), were employed to simplify the results. Eq. (2.58) shows that a uniform mesh of exactly integrated Timoshenko beam elements achieves a second-order interior accuracy. However, unlike the limit differential equation approach which automatically manifests element pathologies caused by parasitic differential operators, the local truncation error, per se, gives no indication of potential element trouble.

Consistency is represented in different, but equivalent, ways by these two techniques. From a limit differential equilibrium equation standpoint,

$$l^D \cdot w = r^D \cdot q \quad \rightarrow \quad l \cdot w = r \cdot q \quad \text{as} \quad l \rightarrow 0 \quad (2.59)$$

which implies that

$$w = W \quad \text{as } l \rightarrow 0 . \quad (2.60)$$

From the local truncation error standpoint,

$$\tau^l \to 0 \qquad \text{as} \quad l \to 0 \qquad\qquad (2.61)$$

with the proviso that the continuum equation was subtracted from the error equation. If the discretization is not consistent with the anticipated differential equation, the limit differential equilibrium equation reduces to the differential equation for which it is consistent (as will be seen to be important in Chapter 5).

REMARK 2.4

These results differ from the earlier work of Walz, Fulton and Cyrus [13] in several key respects. When faced with decoupling systems of coupled partial differential equations with several dependent variables, as was the case for the Hermitian beam discretization, they employed a term-by-term elimination procedure. This entailed successively substituting differentiated forms of the equations representing the displacement variables to be eliminated to cancel specific coupling terms in the retained equations. This should be contrasted with the present operational procedure whereby the decoupled w limit differential equilibrium equation is immediately obtained from $|L^D| \cdot w = |G_1|$ for the Hermitian beam problem where

$$L^D = \begin{bmatrix} -12\frac{d^2}{dx^2} - l^2\frac{d^4}{dx^4} - \frac{l^4}{30}\frac{d^6}{dx^6} - \frac{l^6}{1680}\frac{d^8}{dx^8} & 12\frac{d}{dx} + 2l^2\frac{d^3}{dx^3} + \frac{l^4}{10}\frac{d^5}{dx^5} + \frac{l^6}{420}\frac{d^7}{dx^7} \\ \frac{d}{dx} + \frac{l^2}{6}\frac{d^3}{dx^3} + \frac{l^4}{120}\frac{d^5}{dx^5} + \frac{l^6}{5040}\frac{d^7}{dx^7} & -1 - \frac{l^2}{6}\frac{d^2}{dx^2} - \frac{l^4}{72}\frac{d^4}{dx^4} - \frac{l^6}{2160}\frac{d^6}{dx^6} \end{bmatrix}$$

$$(2.62)$$

with

$$u = \lfloor w \quad \theta \rfloor^T; \qquad f = \lfloor \frac{ql^2}{EI} \quad 0 \rfloor^T.$$

The second point is more fundamental in that the distinction in [13] between w and W was overlooked. The w limit differential equilibrium equation determined from Eq. (2.62) is

$$EI\left(\frac{d^4w}{dx^4} + \frac{l^2}{6}\frac{d^6w}{dx^6} + \frac{l^4}{80}\frac{d^8w}{dx^8}\right) = q + \frac{l^2}{6}\frac{d^2q}{dx^2} + \frac{l^4}{72EI}\frac{d^4q}{dx^4} + O(l^6), \qquad (2.63)$$

where it is again stressed that w is the solution to this equation, representing the discrete problem, and not the continuum one.

The continuum equation was then mistakenly employed in [13] to simplify

Eq. (2.63) resulting in

$$\frac{d^4w}{dx^4} - \frac{l^4}{720}\frac{d^8w}{dx^8} = \frac{q}{EI} \tag{2.64}$$

which is not the modified equilibrium equation for this discretization nor does it properly represent the local truncation error which is in reality,

$$\tau^l = -\frac{l^4}{720}\frac{d^8W}{dx^8} \tag{2.65}$$

REMARK 2.5

The symbolic decoupling procedure used in Remark 2.4 has performed two important functions. The first is the obvious one of determining a decoupled equilibrium equation in terms of a single displacement variable. The second one, namely that of eliminating a purely computational d-o-f, leads us to the next comment. Strang and Fix [6] made the comment that *we can rewrite our finite element system as a set of difference equations having a very special form: one equation of the system is an accurate analogue of the original differential equation, and the other $M-1$ are completely inconsistent*[3]. In the context of the present symbolic analysis, we have shown that there are no inconsistent equations. This is a result of the decoupling process which automatically, and in a consistent manner, accounts for the coupling effects of equations corresponding to computational d-o-f on the decoupled limit differential equilibrium equation(s) corresponding to physical d-o-f.

§2.2.3 Discrete Approximation of the Buckling Operator

From a displacement-based finite element standpoint, derivation of the discrete counterpart to the continuum buckling operator, L_σ, has traditionally come about in two different ways depending upon the spectrum of problems to be addressed by the finite element developer, i.e., linear + bifurcation buckling or intrinsically nonlinear. In the first case, derivation of the so-called geometric stiffness matrix, k_σ, has either been based upon a simple extension of linear theory whereby nonlinear strain-displacement terms are selectively introduced into the strain energy, U, (or V when the inextensional membrane hypothesis is employed) as was done in Eq. (2.17) and then appropriately discretized (see e.g., [39,40,41]). In the

---

[3] see p. 170-171 of [6]

second case, an incrementally nonlinear formulation is employed from the outset where $\mathbf{k}_\sigma$ naturally evolves as one component of the tangent stiffness matrix (see e.g., [30,42,43]).

From a computational standpoint, once the global material and geometric stiffness matrices have been assembled, the structural bifurcation buckling load is determined by solving the eigenproblem

$$(\mathbf{K} + \lambda \mathbf{K}_\sigma)\mathbf{d} = 0 \qquad (2.66)$$

where λ is the load multiplier or eigenvalue at which point an adjacent equilibrium state is possible, represented by the eigenvector $\mathbf{d}$. For the present symbolic analysis where one is interested in recovering the linearized limit differential equilibrium equations governing the discrete bifurcation problem, the alternative matrix equation

$$(\mathbf{K} + \mathbf{K}_\sigma)\mathbf{d} = 0 \qquad (2.67)$$

is instead employed which leads directly to the limit differential equilibrium equations

$$(L_\mathrm{m} + L_\sigma)\mathbf{u} = 0 \qquad (2.68)$$

In this section, $\mathbf{k}_\sigma$ for the Timoshenko beam is determined by the direct discretization of the σ terms in U (see Eq. (2.17)). In a thickness-preintegrated form, the resulting $\mathbf{k}_\sigma$ is given by

$$\mathbf{k}_\sigma = \int_0^l \mathbf{B}_\sigma^\mathrm{T} \begin{bmatrix} \sigma A & 0 \\ 0 & \sigma I \end{bmatrix} \mathbf{B}_\sigma \, dx \qquad (2.69)$$

with

$$\mathbf{B}_\sigma = \begin{bmatrix} \dfrac{dN_1}{dx} & 0 & \dfrac{dN_2}{dx} & 0 \\ 0 & \dfrac{dN_1}{dx} & 0 & \dfrac{dN_2}{dx} \end{bmatrix} \qquad (2.70)$$

where the shape functions and nodal d-o-f ordering are the same as previously defined in §2.2.2. For the present case of a linear element, there is no freedom with

37

regard to spatial integration order since the individual components of the integrand are constant so that a 1-point quadrature rule exactly integrates Eq. (69). The resulting $\mathbf{k}_\sigma$ obtained employing this rule is

$$\mathbf{k}_\sigma = \frac{\sigma}{l}\begin{bmatrix} A & 0 & -A & 0 \\ 0 & I & 0 & -I \\ -A & 0 & A & 0 \\ 0 & -I & 0 & I \end{bmatrix}. \tag{2.71}$$

After the assembly of $\mathbf{K}_\sigma$ at the jth node, the now homogeneous difference equations for the reduced-integrated Timoshenko beam are[4],

$$-GA(\frac{w_{j-1} - 2w_j + w_{j+1}}{l^2}) + GA(\frac{-\theta_{j-1} + \theta_{j+1}}{2l}) - \sigma A(\frac{w_{j-1} - 2w_j + w_{j+1}}{l^2}) = 0$$

$$\tag{2.72}$$

$$EI(\frac{\theta_{j-1} - 2\theta_j + \theta_{j+1}}{l^2}) - GA(\frac{\theta_{j-1} + 2\theta_j + \theta_{j+1}}{4}) + GA(\frac{-w_{j-1} + w_{j+1}}{2l})$$

$$+\sigma I(\frac{\theta_{j-1} - 2\theta_j + \theta_{j+1}}{l^2}) = 0$$

Employing the present symbolic element evaluation procedure, the discrete counterpart of the reference continuum buckling equation, Eq. (2.28), is found to be

$$\frac{I}{G}(\frac{d^4w}{dx^4} + \frac{l^2}{6}\frac{d^6w}{dx^6})\sigma^2 + [I(\frac{E}{G} + 1)(\frac{d^4w}{dx^4} + \frac{l^2}{6}\frac{d^6w}{dx^6}) - A(\frac{d^2w}{dx^2} + \frac{l^2}{3}\frac{d^4w}{dx^4})]\sigma$$

$$+EI(\frac{d^4w}{dx^4} + \frac{l^2}{6}\frac{d^6w}{dx^6}) = 0$$

$$\tag{2.73}$$

which is the modified equilibrium equation governing the bifurcation buckling of the reduced-integrated linear Timoshenko beam element. In the next section, a priori error estimates for the bifurcation buckling load will be determined based upon this modified equilibrium equation.

---

[4] The exactly integrated Timoshenko beam will not be considered due to the locking problem.

§2.3 Error Estimates Based Upon Modified Equilibrium Equations

In the usual finite difference context, local truncation error results give no real information regarding the magnitude of the error resulting from the discrete approximation, but rather only some indication of how quickly the discrete solution approaches the exact one as the mesh is refined. This does not have to be the case, as was shown by Walz, Fulton and Cyrus [13] in their work on determining the accuracy and consistency of different finite element discretizations. They obtained a priori error estimates in the interior problem domain of a given discretization by seeking harmonic solutions of the so-called modified differential equilibrium equations comprised of the continuum operator (or zeroth-order) and leading truncation order terms. A fundamental error was, however, made by overlooking the effect that the discretization had on the loading operator which resulted in physically incorrect error predictions. In the present analysis, the discrete counterparts of both the homogeneous operator and the loading operator are consistenly treated. As will be shown, this consistent treatment results in a more realistic error estimate.

In this section, error estimates will be determined for the different discrete models considered thus far based upon the theoretical results obtained in the previous sections for both linear and bifurcation buckling problems. The present error estimates are based upon the particular solutions of the governing equilibrium equations. As such, they are valid, in general, only for the interior problem domain away from the influence of boundary conditions which would be satisfied by the homogeneous solution. For the case of periodic boundary conditions which are satisfied by the harmonic solutions, however, the error estimates will be valid for each interior nodal point in the mesh.

39

§2.3.1 Consistent Determination of Discretization Effect on Loading Operator

The case of the one-dimensional linear displacement-based bar element is a challenging way of introducing this topic since the discrete solution is nodally exact for any loading function [44,30]. The first step will be to examine the approach taken in [13] in order to see why an incorrect result was derived there. Next, the consistent way of determining the discretization effect on the loading operator will be presented which correctly results in the prediction of a nodally exact solution.

The discrete difference equation at the jth interior node, based upon a Minimum Potential Energy-based linear finite element discretization, is

$$\frac{EA}{l}(-u_{j-1} + 2u_j - u_{j+1}) = p_j \tag{2.74}$$

where p_j is the nodal load. Expanding in a Taylor series about the interior node, the modified equilibrium equation corresponding to Eq. (2.74) was determined in [13] to be

$$EA\left(\frac{\partial^2 u}{\partial x^2} + \frac{l^2}{12}\frac{\partial^4 u}{\partial x^4} + \cdots\right) + p = 0 \tag{2.75}$$

where the p_j in Eq. (2.74) was assumed to be of the functional form

$$p_j = p(x)l. \tag{2.76}$$

Fourier solutions of the form

$$u(x) = u_m \sin\frac{m\pi x}{L}; \quad m = 1, 2, \ldots \tag{2.77}$$

were then determined for

$$p(x) = p_m \sin\frac{m\pi x}{L}, \tag{2.78}$$

40

where the loading for the discrete problem was assumed to be identical to the continuum one as is reflected in Eq. (2.76). With the continuum solution given by

$$U = \frac{p_m}{EA}\left(\frac{L}{m\pi}\right)^2 \sin\frac{m\pi x}{L}, \qquad (2.79)$$

the solution to the modified equilibrium equation was written as

$$u = \frac{U}{1-\epsilon} \approx U(1+\epsilon) \qquad (2.80)$$

where

$$\epsilon = \frac{l^2}{12}\left(\frac{m\pi}{L}\right)^2. \qquad (2.81)$$

Since ϵ is always positive, it is obvious from Eq. (2.80) that $u > U$ for all m, a result which is of course inconsistent with the underlying MPE-based finite element formulation employed for this discretization. The problem with this approach results from the assumed form of Eq. (2.76) which neglects any discretization effects on the loading operator.

The consistent way to handle harmonic loading entails going back to the basic element load calculation which requires that harmonic loading be assumed from the outset. If in the following equation, ξ is used to denote the local element coordinate system and x, the global system, then the nodal load at an interior node, j, resulting from a harmonic bar loading would be

$$p_j = \int_0^l \frac{\xi}{l} p_m \sin\frac{m\pi(x_j - l + \xi)}{L}\,d\xi + \int_0^l (1 - \frac{\xi}{l}) p_m \sin\frac{m\pi(x_j + \xi)}{L}\,d\xi \quad (2.82)$$

where x_j is the position of the interior node. Performing the indicated integration, the discrete nodal load is

$$p_j = p_m \frac{4\sin^2(\frac{m\pi l}{2L})}{(\frac{m\pi}{L})^2 l} \sin\frac{m\pi x_j}{L} = \tilde{p}_m l \sin\frac{m\pi x_j}{L}. \qquad (2.83)$$

41

where $\tilde{p}_m$ is determined to be

$$\tilde{p}_m = (1 - \frac{l^2}{12}(\frac{m\pi}{L})^2 + \frac{l^4}{360}(\frac{m\pi}{L})^4 - \cdots)p_m, \qquad (2.84)$$

when $\sin(\frac{m\pi l}{2L})$ is expanded in its power series representation. Using this result, the solution to the modified equilibrium equation, Eq. (2.75), is now found to be

$$EA(\frac{m\pi}{L})^2(1 - \frac{l^2}{12}(\frac{m\pi}{L})^2 + \cdots)u_m = (1 - \frac{l^2}{12}(\frac{m\pi}{L})^2 + \cdots)p_m. \qquad (2.85)$$

Noting that the discretization of the continuum and loading terms has resulted in identical power series expansions, the discrete nodal solution is, after simplification,

$$u = \frac{p_m}{EA}(\frac{L}{m\pi})^2 \sin\frac{m\pi x_j}{L} = U, \qquad (2.86)$$

which is in fact the continuum solution; or in other words, the discrete solution is predicted to be nodally exact. This interesting result is easily verified numerically, as illustrated by a plot of both U and u *vs.* x for a 4 element bar model with

$$p(x) = p_o(\sin\frac{\pi x}{L} + \sin\frac{2\pi x}{L}), \qquad (2.87)$$

as shown in Fig. 2.2.

REMARK 2.6

It should be noted that in order to obtain the nodally exact discrete solution, exact spatial integration of Eq. (2.82) had to be employed to determine the nodal loads. This is, of course, a consequence of satisfying the requirements of the weak form of the problem which requires that the loading term,

$$\delta V = -\int_V p\,\delta u\,dV, \qquad (2.88)$$

be exactly integrated. If the same one-point spatial integration rule that was used to integrate the element stiffness had been used to evaluate the element load vector, a nodally exact discrete solution would *not* have been obtained as is also shown in Fig. 2.2. A more detailed discussion of the discretization errors which

42
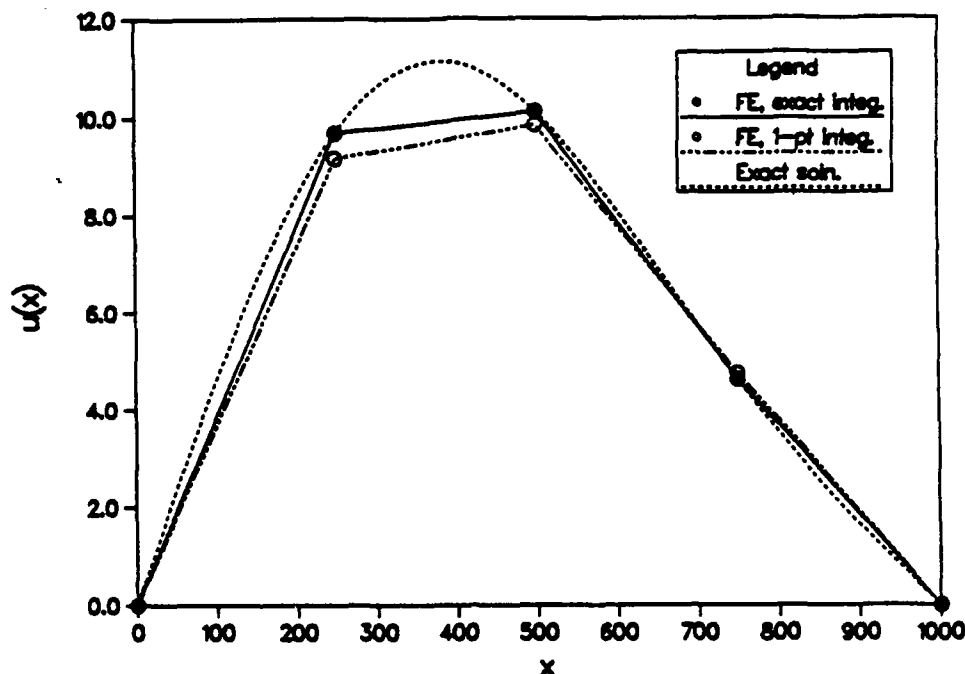
Fig. 2.2 – Exact *vs.* discrete results for 4 element bar discretization with $L = 1000$, $EA = 1$ and $p_o = 10^{-4}$.

can be introduced in the loading term through numerical quadrature can be found in Strang and Fix [6].

One might comment in passing that the common practice of integrating the loading term with the same integration rule as used for the element stiffness calculation may unintentionally introduce additional discretization errors into the finite element analysis depending upon the frequency content of the distributed load.

§2.3.2 Error Estimate for Transversely Loaded Timoshenko Beam

The bar example just examined in the previous section was rather unusual in that the discrete solution was nodally exact for any distributed loading. For the case of the linear Timoshenko beam discretization, however, this is not the case so that the solution of the modified equilibrium equation can be used to derive nodal displacement error estimates as was done in [13].

43

For this problem, harmonic solutions of the general form

$$w = w_m \sin kx \qquad (2.89)$$

will be sought corresponding to

$$q = q_m \sin kx \qquad (2.90)$$

where the Fourier coefficients, q_m and w_m, represent the frequency spectrum of the applied loading and transverse displacement. Depending upon ones perspective, k can either be viewed as the spatial frequency or in a dynamical context, the wave number. Employing the finite-length beam analogy with its discretely varying solution components, k is defined by

$$k = \frac{m\pi}{L} ; \quad m = 1, 2, \ldots . \qquad (2.91)$$

The exact solution for the mth Fourier mode is determined from Eq. (2.26) to be

$$W = \frac{(1 + \frac{EI}{GA}k^2)q_m}{EIk^4} \sin kx = W_m \sin kx . \qquad (2.92)$$

Next, using the modified equilibrium equation for the reduced integrated Timoshenko beam, Eq. (2.44), the solution to the discrete problem is

$$w = \frac{[(1 - \frac{l^2}{4}k^2) + \frac{EI}{GA}(k^2 - \frac{l^2}{12}k^4)]\tilde{q}_m}{EI(k^4 - \frac{l^2}{6}k^6)} \sin kx_j = w_m \sin kx_j \qquad (2.93)$$

where the effective distributed transverse load,

$$\tilde{q}_m = q_m \frac{4\sin^2(\frac{kl}{2})}{k^2 l^2} \qquad (2.94)$$

is identical to Eq. (2.83) since the same element shape functions are used in both cases.

As will be discussed in more detail in the next chapter dealing with discrete Fourier analysis techniques, Eq. (2.93) is not valid for all k's, or alternatively, for all solution wavelengths, λ, where $\lambda = 2\pi/k$. For the present discrete problem, solution components may only be accounted for within the bounds

$$\lambda_{\min} \leq \lambda \leq \begin{cases} \infty & \text{rigid body mode} \\ 2L & \text{first deformation mode; } m = 1 \end{cases} \qquad (2.95)$$

or alternatively,

$$k_{\max} = \frac{\pi}{l} \geq k \geq \begin{cases} 0 & \text{rigid body mode} \\ \pi/L & \text{first deformation mode; } m = 1. \end{cases} \qquad (2.96)$$

Here, $\lambda_{\min}$ is the minimum solution wavelength which the discrete mesh can represent (without aliasing) while ∞ represents the other limiting case of pure rigid body motion. The maximum m is determined from $k_{\max} = \frac{\pi}{l} = \frac{m\pi}{L}$ to be $m_{\max} = L/l = nel$ where nel is the number of elements. Based upon these results, the total displacement at the jth node would be

$$w(x_j) = \sum_{m=1}^{m_{\max}} w_m \sin k x_j \qquad (2.97)$$

while for the continuum solution,

$$W(x) = \sum_{m=1}^{\infty} W_m \sin kx \cong \sum_{m=1}^{m_{\max}} W_m \sin kx. \qquad (2.98)$$

It should be noted that the discrete model actually represents a truncated series approximation of the physical one. For now, it is convenient to assume that $\{W_m = 0 : m > m_{\max}\}$ as is indicated in Eq. (2.98).

With closed form expressions for both the continuum and discrete displacements in hand, the possibility of performing an a priori error analysis becomes a reality once the loading spectrum has been specified. From a frequency standpoint, the relative error in the magnitude of a specific Fourier solution component

45

can be simply obtained from

$$\epsilon_m = \frac{W_m - w_m}{W_m}.$$

(2.99)

A plot of ϵ_m *vs.* m is shown in Fig. 2.3 for a finite length beam discretized with 10 and 50 elements. As a result of the assumed periodicity of the solution, results are plotted only for integer m values. In spite of the fact that reduced spatial integration was employed, the displacements are seen to converge from below as $l \rightarrow 0$ since $\epsilon_m > 0 \ \forall \, m$. The "long" wavelength representation of the continuum problem by the discrete finite element solution is also quite apparent since for any number of elements, $\epsilon_{k(m)} \rightarrow 0$ as $k \rightarrow 0$ (if for a second, one views k in a continuous sense). For the case where the distributed loading is represented by a single harmonic frequency, Eq. (2.99) would represent the relative displacement error at any node where $\sin kx_j \neq 0$, i.e., points where the continuum solution is not zero.

The relative error in the total displacement at a particular node point in the mesh would be

$$\epsilon(x_j) = \frac{\sum_{m=1}^{m_{\max}} (W_m - w_m) \sin kx_j}{\sum_{m=1}^{m_{\max}} W_m \sin kx_j}$$

(2.100)

where the frequency content of the solution and hence of the error estimate is determined by the spectral density, q_m, of the loading spectrum.

REMARK 2.7

There are two possible ways in which the results from these a priori error estimates could be used by a structural engineer. The first would answer the question of what is the expected relative error for a given mesh discretization, i.e., element type and number. The second would answer the question of how many elements of a certain type are required to achieve a specified solution accuracy.

§2.3.3 Error Estimate for the Discrete Buckling Problem

Determination of the spectral error content for the discrete bifurcation buckling problem proceeds in much the same way as was done for the laterally loaded

46
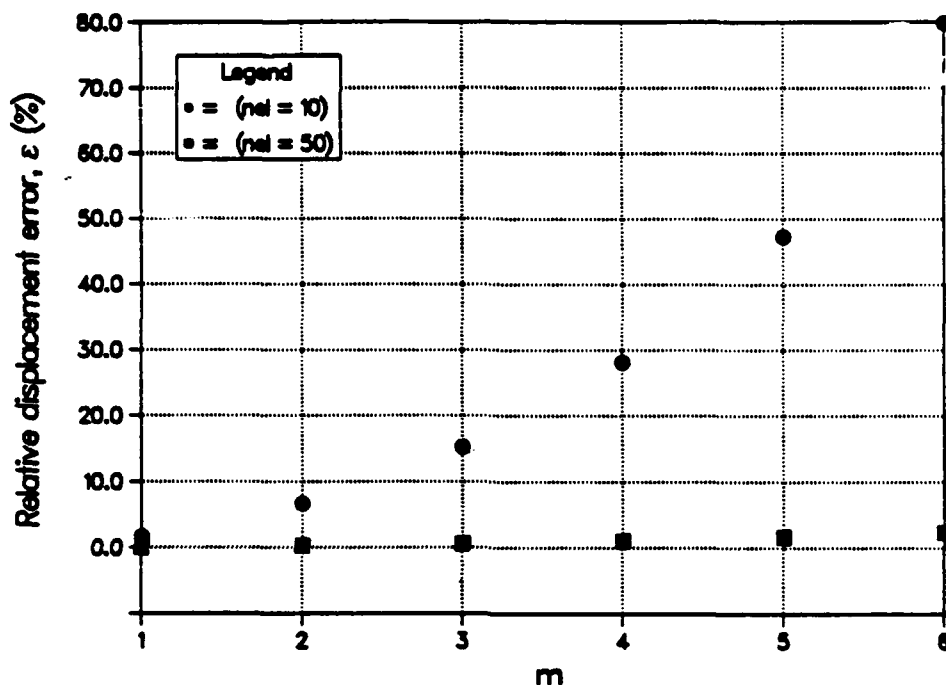
Fig. 2.3 – Relative error in Fourier solution coefficients for Timoshenko beam where $m = \frac{kL}{\pi}$; $L = 1000$, $\nu = .3$ and $h = 1$.

Timoshenko beam. For the case of external loading, error estimates were based on harmonic solutions of $Lu = f$ where the solution could be formally represented as $u = L^{-1}f$. In the present case, dealing with the homogeneous bifurcation buckling problem where $Lu = 0$, u now plays the role of eigenfunction with the buckling load determined by setting the characteristic polynomial of L equal to zero.

From Eqs. (2.28) and (2.73), a relative error estimate of the bifurcation buckling load for the Timoshenko beam may be obtained by plotting for a given buckling mode the relative error, ϵ_m, defined by

$$\epsilon_m = \frac{\sigma_m - \sigma_m^D}{\sigma_m} \tag{2.101}$$

vs. m, the number of half waves where $w = w_m \sin kx$ and $W = W_m \sin kx$. This has been done in Fig. 2.4 for the case of a Timoshenko beam discretized using 10,

47
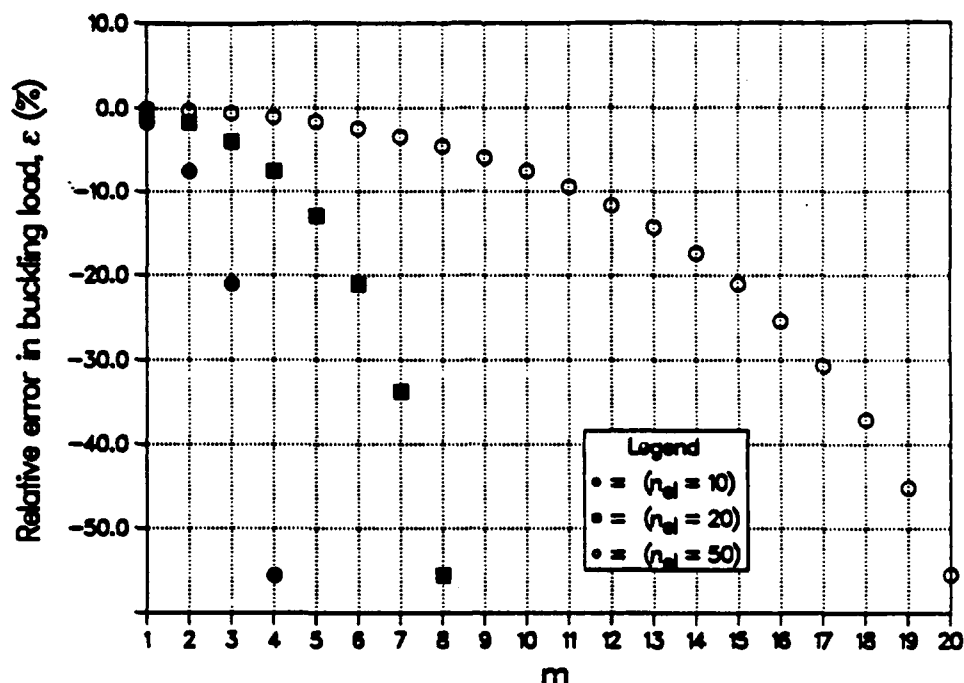
Fig. 2.4 – Relative error in Buckling Load for Timoshenko beam; $L = 1000$, $E = 10^7$, $\nu = .3$ and $h = 1$.

20 and 50 elements. While by no means a general result, the buckling loads for the discrete Timoshenko beam discretization are seen to converge monotonically from above even though reduced quadrature has been employed on the material stiffness. This behavior is consistent with the results of the static analysis where displacements were seen to converge from below. A well known, but nevertheless interesting point to note is that the relative error in buckling load for a given number of elements per half-wave $(= \lambda/2l)$ is in fact the same irrespective of element length. If we take for instance the case of 5 elements/half-wave, we see that ϵ_m is identical for $m = 2$ with $n_{el} = 10$, $m = 4$ with $n_{el} = 20$ and $m = 10$ with $n_{el} = 50$.

§2.4 Summary

In this chapter, the general symbolic operational procedures are developed

which serve as the foundation for the symbolic element evaluation techniques under investigation here. Taylor series expansions of the nodal variables in the discrete finite element equations about an interior node of an element patch are shown to result in the limit differential equilibrium equations governing *intrinsic* element behavior over the interior problem domain. One of the key aspects of this approach is the view that once the finite element discretization has produced a set of discrete equations (or from the finite difference standpoint, difference equations), the mathematical details of their origin are immaterial to the analysis to follow. Instead of relying upon specific numerical problems designed to exercise specific element deformation modes, the basis for determining *intrinsic* element behavior is to compare the decoupled limit differential equilibrium equations resulting from the finite element discretization directly with the corresponding continuum equations.

For the case of the linear Timoshenko beam element, this comparison succinctly revealed the existence of a parasitic operator in the limit differential equilibrium equation which resulted in a modified bending stiffness whose excessive stiffness effectively *locked* the solution. In essence, this symbolic element evaluation technique has identified a fundamental element characteristic which results in locking irrespective of imposed boundary conditions or loading. As such, it provides an alternative method for characterizing this type of element pathology in lieu of the heuristic notion of constraint counting. Furthermore, this example illustrates the usefulness of employing this symbolic Taylor series analysis technique to establish the consistency (i.e., legitimacy) of a particular finite element discretization resulting from employing a numerical technique such as reduced spatial integration.

With the limit differential equilibrium equations in hand, a priori interior error estimates were determined using a Fourier series approach for both the case of static and bifurcation buckling problems. For the static loading problem, a key step in the error analysis was the determination of the consistent discrete loading

49

operator. A preliminary error analysis of the one-dimensional bar problem, whose solution is nodally exact, verified the accuracy of this procedure.

Discrete Fourier Analysis Techniques

In this chapter, the symbolic analysis procedures developed in Chapter 2 using Taylor series methods will be employed in conjunction with discrete Fourier analysis techniques. The need to employ this complementary technique becomes necessary in order to address the question of solution stability for the boundary value problems of interest here.

The key aspect of the work presented in Chapter 2 was the symbolic determination of the limit differential equilibrium equations corresponding to a particular finite element discretization. From these equations, the question of the consistency of a finite element formulation can be answered. In order to ensure solution convergence, however, the question of stability also needs to be addressed. For boundary value problems, stability is not determined in the typical von Neumann sense, which is only applicable to inital value problems. Instead, one has to consider the possibility of spurious element mechanisms in a finite element formulation – a task for which the discrete Fourier technique is well suited.

The crucial difference between the Taylor series technique and the discrete Fourier technique is in the complete representation of all truncation error information resulting from working in the frequency domain. It is this characteristic

51

of the discrete Fourier analysis technique which is exploited here for the determination of spurious element mechanisms. In addition, as a consequence of the complete representation of truncation error information, a more accurate interior error estimate will result. This is in contrast to the earlier error estimates derived using the *modified* differential equilibrium equations which retained only the dominant truncation error terms. Lastly, by viewing the discrete Fourier equations as resulting from a Fourier transformation operation, limit differential equilibrium equations in the physical domain are shown to result from the inverse transformation process.

The discrete Fourier analysis procedure is presented here by way of two simple examples – wave propagation in a bar for the analysis of spurious mechanisms and wave propagation in a Timoshenko beam for the analysis of transverse shear locking.

§3.1 Identification of Spurious Element Mechanisms

In the discrete problem, spurious element mechanisms are the eigenvectors corresponding to nonphysical zero eigenvalues. The physical zero eigenvalues, of course, correspond to rigid body modes. However, an alternative definition of spurious mechanism needs to be used when approaching this problem from a differential equilibrium equation standpoint. One interesting approach [16] is that of viewing the problem from a dynamical standpoint where the needed analogies with rigid body motion occur naturally. After the symbolic recovery of the Fourier transformed limit differential equilibrium equations, examination of the characteristic differential operator will explicitly reveal the presence of non-physical "zero energy modes," if there exists admissible nonzero wave numbers corresponding to zero frequencies. It is the presence of these nonzero wave numbers which indicate the existence of spurious element mechanisms in the discrete model.

The example problem considered in this section employs one of the simplest discrete models which is known to exhibit spurious element mechanisms, namely

that of a linear bar element whose governing continuum equations are cast in their mixed form in terms of both axial displacement and stress.

§3.1.1 Continuum Fourier Analysis of Bar

The equation of motion in a mixed form for a uniform elastic bar is

$$\rho \frac{\partial^2 u}{\partial t^2} = \frac{\partial \sigma}{\partial x} \tag{3.1}$$

with the corresponding linear elastic constitutive relation given by

$$\sigma = E \frac{\partial u}{\partial x}. \tag{3.2}$$

In Eqs. (3.1) and (3.2), u is the axial displacement, σ is the axial stress, E is the extensional modulus and ρ is the density. In terms of differential matrix operator notation, Eqs. (3.1) and (3.2) may be rewritten in a symmetric form as

$$Lu = 0 \tag{3.3}$$

where

$$L = \begin{bmatrix} \rho \frac{\partial^2}{\partial t^2} & -\frac{\partial}{\partial x} \\ -\frac{\partial}{\partial x} & \frac{1}{E} \end{bmatrix} ; \qquad u = \lfloor u \quad \sigma \rfloor^{\mathrm{T}}$$

The Fourier analysis begins by transforming the problem domain from the physical (x, t) domain to the (k, ω) or so-called frequency domain by seeking a general harmonic wave solution of Eq. (3.3) of the form[1]

$$u = \hat{u}\, e^{i(kx - \omega t)} \tag{3.4}$$

---

[1] As a result of linearity, either component of the general solution

$$u = \hat{u}_1\, e^{i(kx - \omega t)} + \hat{u}_2\, e^{-i(kx + \omega t)}$$

could be employed equally well.

where $\hat{u}$ represents the generalized Fourier coefficients with ω being the circular frequency; k the wave number and $i = \sqrt{-1}$. Using this general harmonic wave solution also gives us the ability to interpret the spatial contribution to Eq. (3.4) as either one component in a complex Fourier series representation or as the integrand of the Fourier transformation in which case k would represent the continuous spatial frequency. Substitution of Eq. (3.4) into Eq. (3.3) yields

$$\hat{L}(k,\omega) \cdot \hat{u} = 0 \tag{3.5}$$

where the Fourier transformed matrix operator, $\hat{L}(k,\omega)$, is given explicitly by

$$\hat{L}(k,\omega) = \begin{bmatrix} -\rho\omega^2 & -ik \\ -ik & \frac{1}{E} \end{bmatrix} . \tag{3.6}$$

The desired relationship between frequency and wave number is obtained from the characteristic equation by setting the determinant of the Fourier matrix operator to zero, $viz.$,

$$\left(\frac{\omega}{c}\right)^2 - k^2 = 0 \tag{3.7}$$

or in the nondimemsional form,

$$\left(\frac{\omega l}{c}\right)^2 - (kl)^2 = 0 , \tag{3.8}$$

where l is a problem-dependent characteristic length and c is the wave speed defined as $c = \sqrt{E/\rho}$, which is a constant.

The characteristic equation, Eq. (3.7), indicates that for the continuum solution, the wave number is linearly proportional to the frequency, i.e., $k = \omega/c$. With c constant, each Fourier component will propagate without dispersion with the same phase velocity. For the case of pure rigid body motion, i.e., $\omega = 0$, the corresponding wave number must also be zero as is apparent from Eq. (3.7). Since this is a key result from the continuum analysis, it will be formally written as

$$\omega = 0 \quad \Rightarrow \quad k = 0 . \tag{3.9}$$

54

In the following section, a discrete counterpart of Eq. (3.8) will be derived for each numerical scheme used to approximate the governing continuum equation, Eq. (3.3). A comparison of the characteristic equation for the continuum case with that of the discrete cases will succinctly pinpoint spurious element mechanisms if present in the corresponding finite element discretization.

§3.1.2 Discrete Fourier Analysis – Mixed Linear Bar Element

In a mixed finite element formulation, for an assumed linear displacement field, the stresses must be constant in order to achieve a consistent discretization [46]. For this investigation, however, linear shape functions are purposely adopted for both displacement and stress fields since this choice introduces a spurious mechanism in the bar element. The Hellinger-Reissner mixed variational principle provides the starting point for the element derivation which for an axial bar may be written as [47]

$$\Pi_{HR} = \int_{t_1}^{t_2} \int_V \left(\frac{-\sigma^2}{2E} + \sigma \frac{\partial u}{\partial x} - \frac{\rho}{2} \left(\frac{\partial u}{\partial t} \right)^2 \right) dV \, dt. \qquad (3.10)$$

By using linear shape functions to approximate both the stress and axial displacement, one obtains the following semi-discrete equations at an interior node "j" after assembly of two elements of an equal length, l, based upon a lumped (or diagonal) mass matrix:

$$\rho \ddot{u}_j + \frac{1}{2l}(\sigma_{j-1} - \sigma_{j+1}) = 0$$

$$\qquad (3.11)$$

$$\frac{1}{6}(\sigma_{j-1} + 4\sigma_j + \sigma_{j+1}) + \frac{E}{2l}(u_{j-1} - u_{j+1}) = 0$$

where ($\ddot{}$) denotes $\partial^2 / \partial t^2$. Converting the spatial part of Eq. (3.4) to its polar form,

$$u = \hat{u} \, e^{-i\omega t}(\cos kx + i \sin kx), \qquad (3.12)$$

55

and substituting into Eq. (3.11) yields the discrete Fourier matrix operator,

$$\hat{L}^D(k,\omega) = \begin{bmatrix} -\rho\omega^2 & -\frac{i}{l}\sin kl \\ -\frac{i}{l}\sin kl & \frac{1}{E}(1 - \frac{l^2}{6}\bar{k}^2) \end{bmatrix}.$$

(3.13)

The characteristic (or frequency) equation corresponding to the semi-discrete finite element equations obtained from Eq. (3.13) is

$$|\hat{L}^D(\bar{k},\omega)| = 0 \quad \Rightarrow \quad (\frac{\omega}{c})^2 - \frac{(1 - \frac{l^2}{4}\bar{k}^2)\bar{k}^2}{(1 - \frac{l^2}{6}\bar{k}^2)} = 0$$

(3.14)

or in a nondimensional form,

$$(\frac{\omega l}{c})^2 - \frac{(1 - \frac{l^2}{4}\bar{k}^2)(\bar{k}l)^2}{(1 - \frac{l^2}{6}\bar{k}^2)} = 0.$$

(3.15)

The discrete wave number, $\bar{k}$, defined as

$$\bar{k} = \frac{\sin\frac{kl}{2}}{\frac{l}{2}},$$

(3.16)

arises naturally as a result of the discrete Fourier approximation[2] of $\frac{d^2}{dz^2}$.

Comparison of Eqs. (3.13) with (3.6) and Eqs. (3.14) with (3.7) reveals two important discrete operator approximations which will be seen over and over again in the work to follow, namely, the discrete *unity* operators

$$(1 - \frac{l^2}{4}\bar{k}^2) \quad \text{and} \quad (1 - \frac{l^2}{6}\bar{k}^2).$$

Since spurious mechanisms emanate from non-physical rigid body motions, the possibility of introducing spurious mechanisms by the preceding finite element

---

2   $\frac{d^2}{dz^2}e^{ikz}\big|_{z=0} = -k^2 \simeq \frac{e^{-ikl}-2+e^{ikl}}{l^2} = \frac{2\cos kl-2}{l^2} = -\frac{\sin^2\frac{kl}{2}}{\frac{l^2}{4}} = -\bar{k}^2$

discretization can be determined from the solution of Eq. (3.14), with $\omega = 0$. This leads to the following condition:

$$(1 - \frac{l^2}{4}\bar{k}^2)\bar{k}^2 = 0 \tag{3.17}$$

since

$$(1 - \frac{l^2}{6}\bar{k}^2) \neq 0 \ \forall \ \{k\,;\ 0 \leq k \leq k_{max}\}. \tag{3.18}$$

The roots of Eq. (3.17) are determined from both

$$\bar{k}^2 = 0 \quad \Rightarrow \quad k = \frac{2\pi n}{l}\,, \quad n = 0, 1, 2, \dots \tag{3.19}$$

and

$$(1 - \frac{l^2}{4}\bar{k}^2) = 0 \quad \Rightarrow \quad k = \frac{(2n+1)\pi}{l}\,, \quad n = 0, 1, 2, \dots. \tag{3.20}$$

Not all the wave components given by Eqs. (3.19) and (3.20) are admissible under the linear shape function approximation that has been used to discretize the wave equation. As opposed to the continuum case where all wave numbers are admissible, there is a limit in the discrete representations of admissible wave numbers within an element. Such a limit is determined by the order of the polynomial approximations adopted in the discretization process. Fig. 3.1 represents the highest admissible deformation mode shape permitted by the linear shape functions on a uniform mesh without aliasing, namely,

$$k_{max} = \frac{\pi}{l}\,. \tag{3.21}$$

In digital filtering, this is the Nyquist or folding frequency for the transformed problem (see e.g.. [48]). The nodal spacing in essence determines the spatial sampling rate. The admissible, band-limited frequency spectrum for this linear element is therefore

$$0 \leq k \leq k_{max}\,. \tag{3.22}$$

Sampling of any frequency greater than k_{max} would result in it being aliased into one of the lower admissible frequencies.
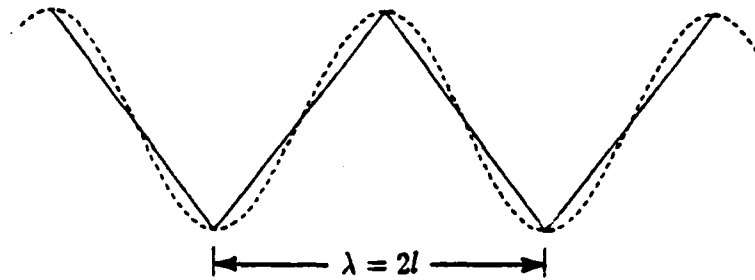
Fig. 3.1 – Piecewise linear interpolation of highest admissible Fourier component $\left(k_{max} = \frac{\pi}{l}\right)$

With the band-width of admissible spatial frequencies now defined for the bar discretization, inspection of Eqs. (3.19) and (3.20) reveals that the discrete characteristic equation, Eq. (3.14), possesses two admissible wave numbers corresponding to $\omega = 0$, namely,

$$k = \{0, \frac{\pi}{l}\} \tag{3.23}$$

As was described in §3.1.1, $k = 0$ represents physically correct rigid body motion. $k = \frac{\pi}{l}$, however, corresponds to an element deformation state with the condition of $\omega = 0$ implying that no energy is required to excite it. It therefore represents a spurious element deformation state, or a so-called spurious element mechanism.

58

§3.1.3 Component-wise Elimination of Spurious Mechanisms

There are, of course, ways to eliminate the spurious mechanism in the bar element. The cause of the spurious mechanism in this particular mixed discretization emanates from the "$(1 - l^2 \bar{k}^2/4)$" term of Eq. (3.14), which can in turn be traced to the "$\sin kl$" term in the discrete Fourier matrix operator, Eq. (3.13). This term originated from the whole-station (or central) differencing of the first derivatives appearing in the wave equation. This term results from the linear interpolation fields employed in the finite element discretization. After assembly of adjacent elements, one finds that

$$\frac{du}{dx}\Big|_j = \frac{1}{2l}(u_{j+1} - u_{j-1}) \tag{3.24}$$

and

$$\frac{d\sigma}{dx}\Big|_j = \frac{1}{2l}(\sigma_{j+1} - \sigma_{j-1}). \tag{3.25}$$

If this problem is recast from a finite difference standpoint, one way to eliminate the spurious mechanism is to adopt the so-called half-station finite difference scheme which would yield the following set of difference equations:

$$\rho \ddot{u}_j = \frac{1}{l}(\sigma_{j+1/2} - \sigma_{j-1/2})$$
$$\sigma_{j+1/2} = \frac{E}{l}(u_{j+1} - u_j) \tag{3.26}$$

where a lumped mass matrix has again been used.

The discrete Fourier characteristic equation for these difference equations, cast in nondimensional form, is

$$(\frac{\omega l}{c})^2 - (\bar{k}l)^2 = 0. \tag{3.27}$$

The half-station scheme will therefore exhibit no spurious oscillation since for

$\omega = 0$ we have

$$\bar{k}^2 = 0 \quad \Rightarrow \quad k = \frac{2\pi n}{l}, \quad n = 0, 1, 2, \dots \qquad (3.28)$$

where $k = 0$ is the only admissible wave number. Eq. (3.27) may also be obtained from the discretization of the displacement-based equations with its strong form derived by substituting Eq. (3.2) into (3.1).

Fig. 3.2 shows nondimensional frequency curves for the continuum solution and the corresponding mixed beam finite element and half-station finite difference discretizations. Note that for the mixed beam finite element discretization, the discrete frequency curve is plotted for all admissible wavenumbers even though negative discrete group velocities, i.e., $d\omega/dk < 0$, which are an artifact of the discretization process, are seen to result within the range of admissible wave numbers. The zero root at $kl = \pi$ is vividly portrayed in the figure. Lastly, wave propagation in the continuum solution is non-dispersive in contrast to both discrete approximations which are dispersive, i.e., $\omega/k \neq$constant.

The poor performance of the mixed finite element discretization, is apparent as manifested in the relative mode-by-mode frequency error,

$$\epsilon(kl) = \frac{\omega - \omega^{\mathrm{D}}}{\omega}. \qquad (3.29)$$

plotted in Fig. 3.3 where ω^{D} denotes the discrete approximation. At the Nyquist frequency (corresponding to the maximum admissible wave number), the finite element discretization performs at its worst, admitting non-physical rigid-body motion (i.e., a spurious element mechanism). On the other hand, the half-station finite difference scheme is not only more accurate, but also exhibits its maximum frequency at the maximum admissible discrete wave number ($k = \pi/l$), thus indicating the absence of spurious mechanisms for this discretization.

One particularly illuminating numerical example of the effect of spurious element mechanisms on a computed solution was presented by Underwood [49].
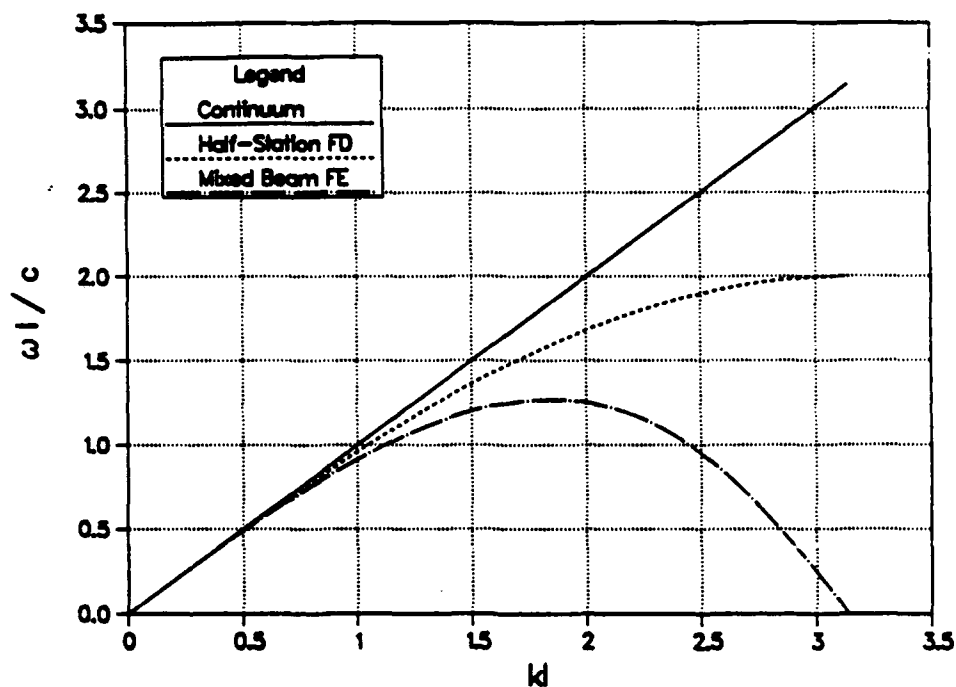
Fig. 3.2 – Frequency spectrum curves for continuum and discrete bar elements
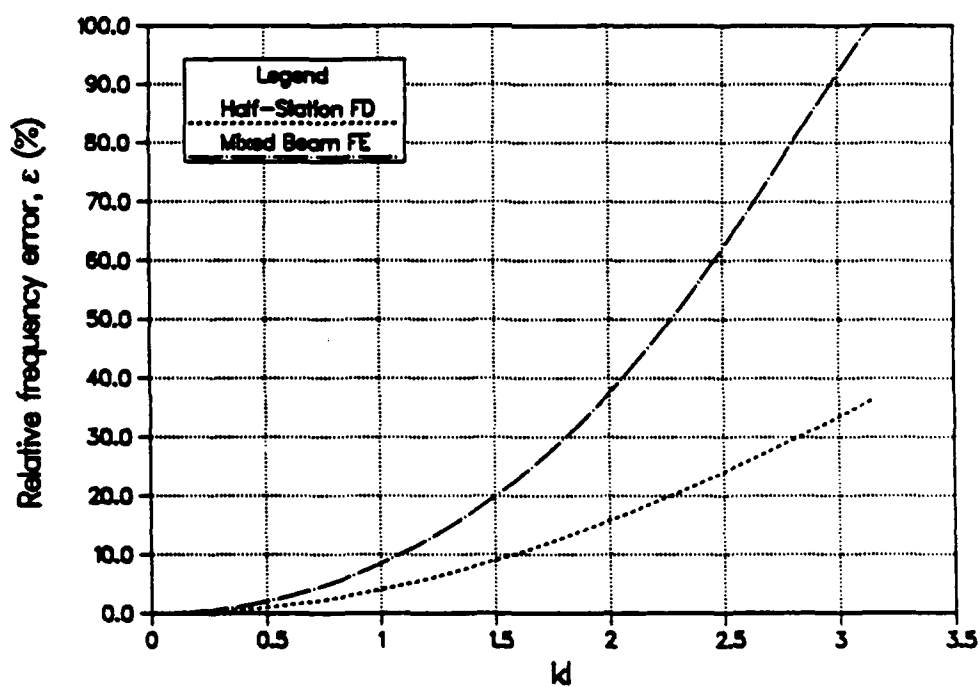
Fig. 3.3 – Relative error in frequency spectrum for each bar discretization

61
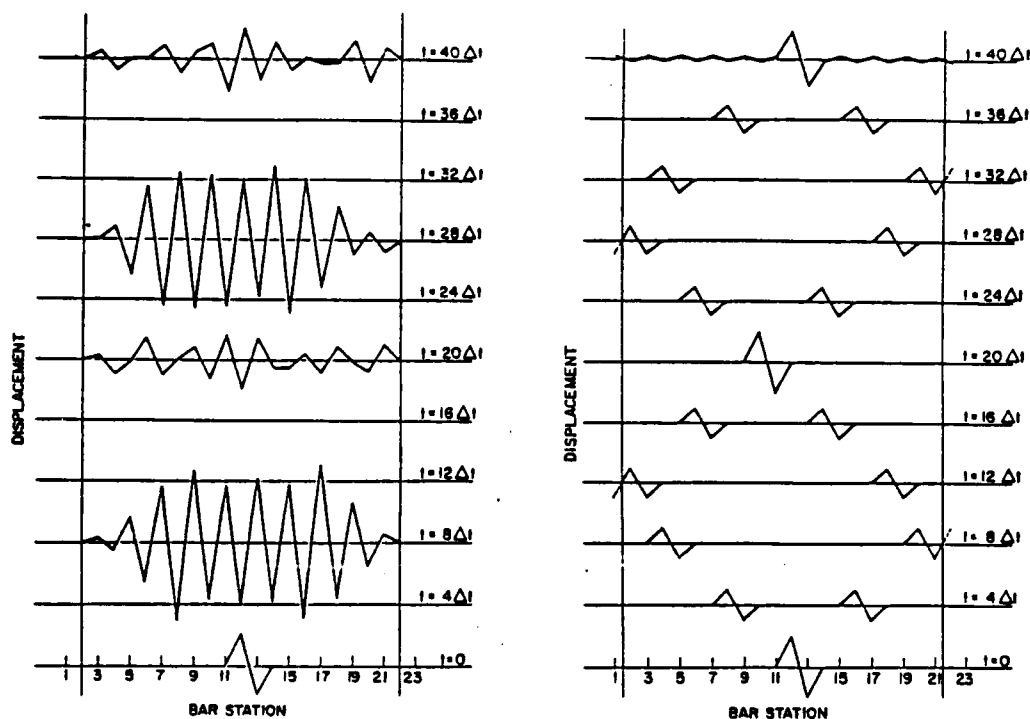
Fig. 3.4 – Wave propagation in fixed bar. (a) Whole-station; (b) Half-station [49]

Fig. 3.4 shows his results for the case of wave propagation in a fixed bar for both a whole-station (equivalent to the mixed finite element beam discretization) and half-station finite difference discretization. The initial displacement conditions are shown at the bottom for $t = 0$. The initial displacements should theoretically reappear shifted by two stations at $t = 20\Delta t$ and at $t = 40\Delta t$ where Δt is the critical time step for the explicit time integration. The whole-station results are seen to wildly distort the inital pulse at each time step while the half-station differencing results in a physically correct solution.

§3.2 Transverse Shear Locking in the Timoshenko Beam Element

In the preceding section, a technique of identifying spurious element mechanisms using a discrete Fourier analysis technique was described. The discrete Fourier matrix operator and its characteristic equation were shown to possess the necessary information needed to detect the existence of spurious element mech-

62

anisms engendered by a finite element discretization. In this section, this same Fourier analysis technique is used to identify transverse shear element locking. In the frequency domain, locking is viewed as an unrealistically high frequency state (analogous to the over-stiffening already shown in static problems) for all wavenumbers. By transforming back to the physical domain, the results of the discrete Fourier analysis in the frequency domain are shown to be identical to that presented earlier for the Taylor series techniques.

§3.2.1 Dynamic Behavior of the Continuum Timoshenko Beam

As before, the first step in the Fourier analysis involves substituting the harmonic wave solution

$$u = \hat{u}e^{i(kz - \omega t)} \tag{3.30}$$

into Eq. (2.21) which results in

$$\hat{L}(k, \omega) \cdot \hat{u} = 0 \tag{3.31}$$

where

$$\hat{L}(k, \omega) = \begin{bmatrix} -\rho A\omega^2 + GAk^2 & iGAk \\ iGAk & \rho I\omega^2 - EIk^2 - GA \end{bmatrix} ; \quad \hat{u} = \left\{ \begin{array}{c} \hat{w} \\ \hat{\theta} \end{array} \right\} \tag{3.32}$$

The reference continuum frequency equation derived from Eq. (3.32), nondimensionalized with respect to the beam's thickness, h, is then

$$\Omega^4 - \left[(r+1)(kh)^2 + 12\right]\Omega^2 + r(kh)^4 = 0 \tag{3.33}$$

where

$$\Omega = \frac{\omega h}{\sqrt{G/\rho}} ; \quad r = \frac{E}{G} . \tag{3.34}$$

Observe once again from Eq. (3.33) that the condition for rigid-body motion, i.e., $\omega = 0$, corresponds to

$$k = 0 \tag{3.35}$$

63

for the continuum Timoshenko beam.

§3.2.2 Dynamic Behavior of the Discrete Timoshenko Beam

The semi-discrete finite element equations for a uniform mesh of linear Timoshenko-beam elements at an interior node, "j", are for exact (two-point) spatial integration,

$$\rho A \ddot{w}_j = GA\left(\frac{w_{j+1} - 2w_j + w_{j-1}}{l^2}\right) - GA\left(\frac{\theta_{j+1} - \theta_{j-1}}{2l}\right) + q_j$$

$$\rho I \ddot{\theta}_j = EI\left(\frac{\theta_{j+1} - 2\theta_j + \theta_{j-1}}{l^2}\right) + GA\left(\frac{w_{j+1} - w_{j-1}}{2l}\right) - GA\left(\frac{\theta_{j+1} + 4\theta_j + \theta_{j-1}}{6}\right)$$

$$(3.36)$$

and for reduced (one-point) spatial integration,

$$\rho A \ddot{w}_j = GA\left(\frac{w_{j+1} - 2w_j + w_{j-1}}{l^2}\right) - GA\left(\frac{\theta_{j+1} - \theta_{j-1}}{2l}\right) + q_j$$

$$\rho I \ddot{\theta}_j = EI\left(\frac{\theta_{j+1} - 2\theta_j + \theta_{j-1}}{l^2}\right) + GA\left(\frac{w_{j+1} - w_{j-1}}{2l}\right) - GA\left(\frac{\theta_{j+1} + 2\theta_j + \theta_{j-1}}{4}\right)$$

$$(3.37)$$

where for simplicity, a lumped mass matrix has again been used.

As was noted in Chapter 2, the only difference between Eqs. (3.36) and (3.37) is in the way the θ-terms are averaged in these two equations. Both sets of coupled discrete finite element equations recover the continuum differential equations in the limit as $l \to 0$ and therefore are formally consistent. However, as was shown in [15], using a decoupled limit differential equation approach, the two sets of discrete equations display a radically different solution behavior as illustrated by numerical experiments [35]. The transverse shear locking phenomenon exhibited by the exactly integrated Timoshenko beam equations will now be analyzed in the frequency domain. To this end, the following discrete Fourier matrix operators corresponding to the above cases are obtained by substitution of Eq. (3.30) into

64

Eqs. (3.36) and (3.3'), resulting in

$$\hat{L}^D(\omega, k) = \begin{bmatrix} -\rho A \omega^2 + GA\bar{k}^2 & \frac{iGA}{l}\sin kl \\ \frac{iGA}{l}\sin kl & \rho I \omega^2 - EI\bar{k}^2 - GA\,\mathbf{1}^{(r,e)} \end{bmatrix} \tag{3.38}$$

where the superscripts (r, e) designate the reduced or exactly integrated cases, respectively. The discrete unity operators $\mathbf{1}^{(r,e)}$ are given explicitly by

$$\begin{aligned} \mathbf{1}^r &= 1 - \frac{l^2}{4}\bar{k}^2 \\ \mathbf{1}^e &= 1 - \frac{l^2}{6}\bar{k}^2 \, . \end{aligned} \tag{3.39}$$

where the discrete wave number, $\bar{k}$, is as defined by Eq. (3.16). In this context, the unity operators $\mathbf{1}^r$ and $\mathbf{1}^e$ can also be viewed as *averaging operators* since these quantities embody the different discrete nodal averaging schemes for θ engendered by the two different spatial integration rules. It is the difference between these two averaging operators that is shown to play the pivotal role in the transverse shear element locking phenomenon.

The frequency equations derived from Eq. (3.38) are written in the form

$$\Omega^4 - \left[(r+1)(\bar{k}h)^2 + 12\mathbf{1}^{(r,e)}\right]\Omega^2 + r(\bar{k}h)^4 + 12(\bar{k}h)^2(\mathbf{1}^{(r,e)} - \chi) = 0 \tag{3.40}$$

where the appropriate interpretation of the unity operator χ, defined by

$$\chi = 1 - \frac{l^2}{4}\bar{k}^2 \, , \tag{3.41}$$

is determined based upon the role it plays in the discretization with respect to its interaction with $\mathbf{1}^{(r,e)}$. By writing Eq. (3.40) in this general form, the interrelationships between these operators, which dictate in the present case whether there will be element locking in this finite element discretization, is succinctly shown.

The first step in identifying the source of transverse shear element locking is to compare the discrete frequency equation, Eq. (3.40), to its continuum counterpart,

Eq. (3.33). From this comparison it is immediately apparent that Eq. (3.40) contains the parasitic term

$$12(\bar{k}h)^2(1^{(r,e)} - \chi) \tag{3.42}$$

which is now shown to be responsible for element locking.

§3.2.2.1 Exact Spatial Integration

For the case of exact spatial integration, one finds that

$$1^e - \chi = \frac{(l\bar{k})^2}{12} \tag{3.43}$$

which when substituted into Eq. (3.40) results in

$$\Omega^4 - [(r+1)(\bar{k}h)^2 + 121^e]\Omega^2 + [r + (\frac{l}{h})^2](\bar{k}h)^4 = 0. \tag{3.44}$$

For thin beam applications where $(l/h) \gg 1$, the coefficient of the $(\bar{k}h)^4$ term becomes, after substituting the appropriate definitions from Eq. (3.34),

$$r + (\frac{l}{h})^2 > r \quad \Rightarrow \quad 1 + \frac{1}{2(1+\nu)}(\frac{l}{h})^2 \gg 1. \tag{3.45}$$

This term was previously identified in the earlier Taylor series analysis of transverse shear element locking in the exactly integrated Timoshenko beam (see Eq. (2.39)). From these results, χ is seen to play the role of a locking operator. It is present irrespective of the θ averaging scheme used and if not eliminated, results in a parasitic term responsible for element locking.

§3.2.2.2 Reduced Spatial Integration

For the case where reduced spatial integration is employed, the parasitic term vanishes identically since

$$1^r - \chi = 0. \tag{3.46}$$
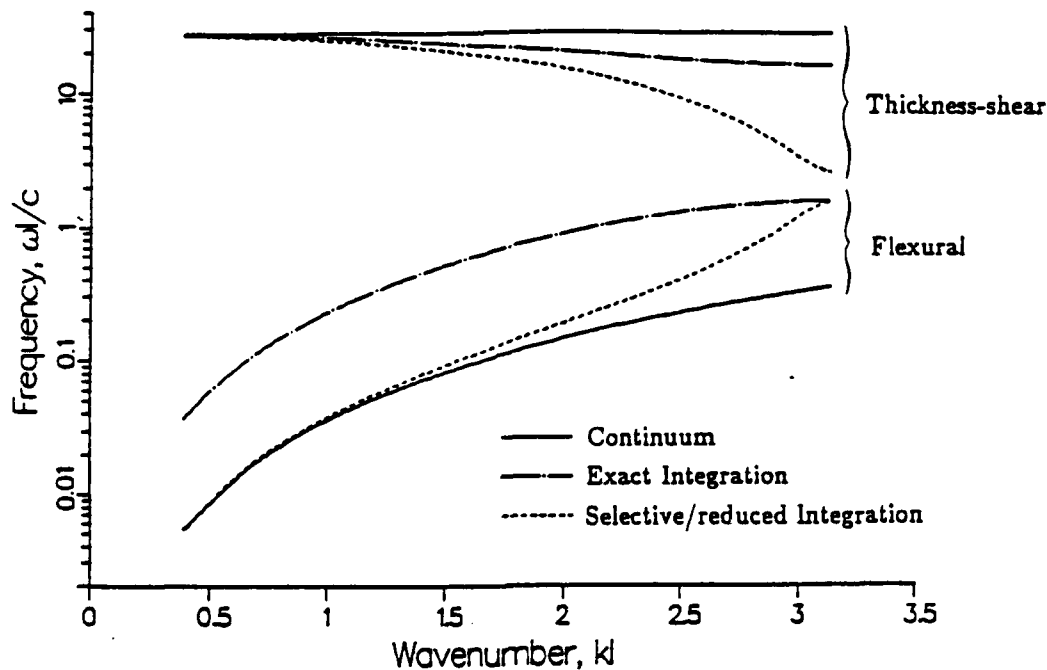
Fig. 3.5 – Frequency spectrum curves for the Timoshenko Beam

From a discrete operator standpoint, Eq. (3.46) therefore represents the correct element "unlocking" condition. In the present discretization, 1^r plays both the role of an unlocking as well as an unity operator. It should also be noted that substitution of $\omega = 0$ into Eq. (3.40) results in the correct rigid body condition, $\bar{k} = 0 \Rightarrow k = 0$. Hence, no spurious element mechanism is present in the reduced integrated beam element.

Frequency spectrum curves are shown in Fig. 3.5 for a Timoshenko beam with aspect ratio $l/h = 10$, $h = 1$ and $\nu = .3$ for both the continuum and discrete cases. The two different families of curves correspond to the flexural and thickness-shear wave branches exhibited by the Timoshenko beam. The frequency of the exactly integrated element is more than an order of magnitude higher than that for the continuum solution as well as that of the reduced integrated element at low wave numbers. This unrealistically high frequency state continues up to $k_{max} = \pi/l$ for the exact integration case. The frequency of the reduced integration case follows faithfully that of the continuum case for wave numbers up to about 1.5.

67

§3.2.3 Recovery of Limit Differential Equilibrium Equations

In §2.2, the transverse shear element locking phenomenon exhibited by exactly integrated linear Timoshenko beam elements was identified by comparison of the decoupled limit differential equilibrium equation of the discrete Timoshenko beam to that of the continuum Timoshenko beam. The operational procedure used to obtain the decoupled limit differential equations first entailed converting the discrete finite element equations to their differential form by expanding the nodal degrees-of-freedom, w and θ, in Taylor series about the interior node. The decoupled limit differential equation in terms of w was then solved by application of Cramer's rule to the resulting differential operator matrix. This same procedure can also be applied to the discrete Fourier matrix operator to obtain the decoupled equations in the frequency domain, which can then be transformed back to the physical domain.

This ability to formally view the discrete Fourier analysis technique employed thus far as a Fourier transformation operation is due to the form of the harmonic solution chosen in Eq. (3.30). The differentiation of Eq. (3.30) results in

$$\frac{d^n}{dx^n}(\hat{u}e^{ikx})\big|_{x=0} = (ik)^n\hat{u},\tag{3.47}$$

with x formally being evaluated at zero corresponding to the interior node in the discrete problem. This yields the same result as the Fourier transform of a differential operator,

$$\mathcal{F}\left[\frac{d^n g}{dx^n}\right] = (i\omega)^n\hat{g}\tag{3.48}$$

where the form of the Fourier transform pair used is (see e.g., [10])

$$\hat{g}(\omega) = \frac{1}{2\pi}\int_{-\infty}^{\infty} g(x)e^{-i\omega x}dx \; ; \quad g(x) = \int_{-\infty}^{\infty} \hat{g}(\omega)e^{i\omega x}d\omega .\tag{3.49}$$

As a result of this analogy, recovery of the limit differential equilibrium equa-

tion in the physical domain proceeds by first determining the decoupled trans-
formed equilibrium equation for $\hat{w}$ which is given in operator form as

$$\det(\hat{\boldsymbol{L}}^{D(e)}) \cdot \hat{w} = \det \begin{bmatrix} \hat{q} & \frac{iGA}{l}\sin kl \\ 0 & -EI\bar{k}^2 - GA\,\mathbf{1}^e \end{bmatrix} \tag{3.50}$$

where $\hat{\boldsymbol{L}}^{D(e)}$ denotes the discrete Fourier matrix operator corresponding to the
exactly integrated case obtained from Eq. (3.38). The solution to Eq. (3.50) is
found to be

$$EI(1 + \frac{l^2 GA}{12EI})\bar{k}^4\hat{w} = (1 - \frac{l^2}{6}\bar{k}^2)\hat{q} + \frac{EI}{GA}\bar{k}^2\hat{q}. \tag{3.51}$$

By next expanding the discrete wave number, $\bar{k}$, in the power series

$$\bar{k} = \frac{2}{l}\sin\frac{kl}{2} \cong k - \frac{l^2}{24}k^3 + \cdots \tag{3.52}$$

and substituting the result into Eq. (3.51) followed by applying the inverse Fourier
transform

$$\mathcal{F}^{-1}[(ik)^n\hat{w}] = \frac{d^n w}{dx^n} \tag{3.53}$$

to the resulting equation, one recovers the decoupled w equation in its more fa-
miliar differential form

$$EI(1 + \frac{l^2}{12}\frac{GA}{EI})(\frac{d^4 w}{dx^4} + \frac{l^2}{6}\frac{d^6 w}{dx^6}) = q + (\frac{l^2}{6} - \frac{EI}{GA})\frac{d^2 q}{dx^2} - \frac{l^2}{12}\frac{EI}{GA}\frac{d^4 q}{dx^4} + O(l^4) \tag{3.54}$$

As one would expect, this equation is identical to that previously obtained using
the Taylor series technique (see Eq. (2.37)).

The results seen in this section lead us to a very important observation re-
garding the superiority of the discrete Fourier analysis techniques over the Taylor
series techniques presented initially in Chapter 2. All truncation information is
automatically embodied in the compact Fourier-transformed expressions which
results in extremely efficient symbolic computation, as has been described, for
example, in [10].

69

§3.3 Bifurcation Buckling of the Timoshenko Beam

In this section, the discrete Fourier analysis is used to evaluate the ability of the one-point spatially integrated linear Timoshenko beam element to accurately represent continuum bifurcation buckling behavior. The continuum equations governing Timoshenko beam buckling were presented in §2.2.1.

§3.3.1 Continuum Buckling Operator

The Fourier-transformed continuum matrix operator is obtained by substituting

$$u = \hat{u}e^{ikz} \tag{3.55}$$

into Eq. (2.21) resulting in

$$\hat{L} = \begin{bmatrix} (G+\sigma)Ak^2 & iGAk \\ sym & -(E+\sigma)Ik^2 - GA \end{bmatrix} . \tag{3.56}$$

From this, the characteristic or buckling operator

$$\det \hat{L} = (kh)^2\hat{\sigma}^2 + \left[(r+1)(kh)^2 + 12\right]\hat{\sigma} + r(kh)^2 = 0 \tag{3.57}$$

is determined where the nondimensional stress, $\hat{\sigma}$, is defined by $\hat{\sigma} = \sigma/G$ and $r = E/G$. The two roots to this equation are given by

$$\hat{\sigma} = \frac{-\left[(r+1)(kh)^2 + 12\right] \pm \sqrt{\left[(r+1)(kh)^2 + 12\right]^2 - 4r(kh)^4}}{2(kh)^2} \tag{3.58}$$

$$= -\frac{1}{2}(b \mp \sqrt{b^2 - 4r})$$

with

$$b = (r+1) + \frac{12}{(kh)^2} . \tag{3.59}$$

70

The smaller root corresponds to the classical "flexural" buckling stress [26] while the larger one corresponds to a thickness-shear mode in an analogous manner to that seen in the wave propagation problem discussed earlier in §2.3.2.2.

If the von Kármán's strain-displacement approximation had instead been employed, the critical buckling load would be calculated from

$$P_{cr} = \sigma A = \frac{EIk^2}{\frac{EI}{GA}k^2 + 1}. \tag{3.60}$$

For the case of a relatively thin beam $(l/h > 50)$, there is essentially no difference in predicted flexural buckling load between Eqs. (3.58) and (3.60).

§3.3.2 Discrete Buckling Operator

The discrete counterpart to Eq. (3.56), obtained from Eq. (2.72), is found to be

$$\hat{L}_{\mathbf{D}} = \begin{bmatrix} (G + \sigma)A\bar{k}^2 & \frac{iGA}{l}\sin kl \\ sym & -(E + \sigma)I\bar{k}^2 - GA\mathbf{1}^r \end{bmatrix} \tag{3.61}$$

from which the discrete buckling operator,

$$(\bar{k}h)^2\bar{\sigma}^2 + [(r + 1)(\bar{k}h)^2 + 12\mathbf{1}^r]\bar{\sigma} + r(\bar{k}h)^2 = 0 \tag{3.62}$$

is obtained. The flexural bifurcation buckling stress corresponding to the smallest root of Eq. (3.62) is

$$\bar{\sigma}^{\mathbf{D}} = -\frac{1}{2}(b^{\mathbf{D}} - \sqrt{b^{\mathbf{D}^2} - 4r}) \tag{3.63}$$

where

$$b^{\mathbf{D}} = (r + 1) + \frac{12}{(\bar{k}h)^2}\mathbf{1}^r. \tag{3.64}$$

The critical buckling load would then simply be $P_{cr}^{\mathbf{D}} = \bar{\sigma}^{\mathbf{D}}GA$.

Employing von Kármán's strain-displacement approximation in the element

71

formulation results in the discrete counterpart to Eq. (3.60),

$$P_{cr}^{D} = \sigma^{D} A = \frac{EI\bar{k}^4}{\frac{EI}{GA}\bar{k}^4 + 1^r \bar{k}^2} \, . \tag{3.65}$$

In either case, the entire effect of the discretization process is embodied in the discrete wave number, $\bar{k}$, and the unity operator, 1^r.

§3.4 Spectral Error Estimation

In §2.3, using Taylor series techniques, a priori error estimates were calculated based upon solving the so-called modified limit differential equilibrium equations which retained only the leading truncation error terms. In this section, a priori interior error estimates will be obtained for the discrete Timoshenko beam using the discrete Fourier analysis in the frequency domain which by its very nature automatically retains all truncation information. By employing the more general Fourier transform approach, one obtains an a priori interior error estimate in the physical problem domain by inverse Fourier transformation of the results from the spectral error analysis, as will be described now.

§3.4.1 Spectral Distribution of Loading Operator

As was discussed in §2.3.1, determination of the discretization effect on the loading operator requires that the harmonic loading, which now takes the general form $q(x) = \hat{q}(k)e^{ikx}$, be used in the calculation of the nodal load from the outset. Using ξ to denote the local element coordinate system and x, the global system, as before, the nodal load corresponding to a Fourier component would be

$$q_j = \int_0^l \frac{\xi}{l}\hat{q}\,e^{ik(x_j - l + \xi)}\,d\xi + \int_0^l (1 - \frac{\xi}{l})\hat{q}\,e^{ik(x_j + \xi)}\,d\xi \tag{3.66}$$

where x_j is the position of the interior node. Performing the symbolic integration, the discrete nodal load is found to be

$$q_j = (\frac{\bar{k}}{k})^2 \hat{q}l e^{ikx_j} \tag{3.67}$$

72

so that the discrete Fourier transformed counterpart to the continuum distributed load, $\hat{q}$, is simply

$$\hat{q}^{\mathrm{D}} = (\frac{\bar{k}}{k})^2 \hat{q}\,. \tag{3.68}$$

The spectral load density itself is determined from

$$\hat{q}(k) = \frac{1}{2\pi} \int_{-\infty}^{\infty} q(x)\mathrm{e}^{-ikx} dk\,. \tag{3.69}$$

§3.4.2 Determination of Spectral Error Distribution

The Fourier transformed continuum and discrete differential operators, $\hat{L}(k)$ and $\hat{L}^{\mathrm{D}}(k)$, for the Timoshenko beam are given by

$$\hat{L}(k) = \begin{bmatrix} GAk^2 & iGAk \\ iGAk & -EIk^2 - GA \end{bmatrix} \tag{3.70}$$

and

$$\hat{L}^{\mathrm{D}}(\bar{k}) = \begin{bmatrix} GA\bar{k}^2 & \frac{iGA}{l}\sin kl \\ \frac{iGA}{l}\sin kl & -EI\bar{k}^2 - GA\,1^{(r,e)} \end{bmatrix}\,. \tag{3.71}$$

These are obtained from Eqs. (3.32) and (3.38) with $\omega = 0$. Fourier-transformed solutions are determined for the ith solution component by employing Eq. (2.3), rewritten as

$$\hat{u}_i = \frac{\det \hat{\mathbf{G}}_i}{\det \hat{\mathbf{L}}} \quad \Rightarrow \quad \hat{w} = \frac{\det \hat{\mathbf{G}}_1}{\det \hat{\mathbf{L}}}\,. \tag{3.72}$$

The relative error in a particular Fourier component is then simply

$$\hat{\epsilon}(k) = \frac{\hat{w} - \hat{w}^{\mathrm{D}}}{\hat{w}}\,. \tag{3.73}$$

For the present discrete problem, the relative error is explicitly given by

$$\hat{\epsilon}(k) = \frac{\dfrac{(1+\frac{EI}{GA}k^2)\hat{q}}{EIk^4} - \dfrac{(1^{(r,e)}+\frac{EI}{GA}\bar{k}^2)\hat{q}^{\mathrm{D}}}{EI\bar{k}^4 + GA\bar{k}^2(1^{(r,e)}-\chi)}}{\dfrac{(1+\frac{EI}{GA}k^2)\hat{q}}{EIk^4}}\,. \tag{3.74}$$

73

Fig. 3.6 shows a plot of $\hat{e}(k)$ *vs.* k for both exact and reduced integrated Timoshenko beam elements. As was discussed earlier in §2.2.2.1, only about 2.5% of the continuum solution would be expected for the exactly integrated case for an element aspect ratio of $l/h = 10$. For the present case where $l/h = 100$, $\widetilde{EI} = 3847.15EI$ with the result that the discrete solution is essentially zero, as is reflected here in the error for each Fourier mode, i.e., $\hat{e}(k) \cong 100\%$.

The question of consistency is graphically portrayed for the reduced integrated *element since* $\hat{e} \to 0$ *as* $k \to 0$ *for a finite* l*.* For the exactly integrated case, however, one must rely upon the equations themselves to verify that element consistency is satisfied since $\hat{e} \to 0$ only as $l \to 0 \quad \forall\, k$. This is a result of the modified bending stiffness which, for a specified element l and h, remains constant thus over-stiffening (i.e., locking) all modes for $k > 0$.

The results from Fig. 2.3 for the case of $n_{el} = 10$ are also plotted on this figure in order to compare the earlier Taylor series results with those from the present discrete Fourier analysis. The relationship between m and k was given by Eq. (2.90). For low wave numbers, results from the two different analyses are essentially identical. It is not until $m \geq 4$ that the predicted errors start to differ appreciably resulting from the use of the modified equilibrium equations which represent a truncated series approximation to the true discrete approximation. In essence, the result of this is the loss of higher frequency information as is seen here.

§3.4.3 Error Estimate in the Physical Domain

If one defines the absolute error in the frequency domain to be

$$\hat{e}(k) = \hat{w} - \hat{w}^{\mathbf{D}}, \qquad (3.75)$$

an a priori error estimate in the physical domain can be obtained directly frcm $\hat{e}(k)$ once the spectral load density, $\hat{q}$, is known. Based upon the observation that
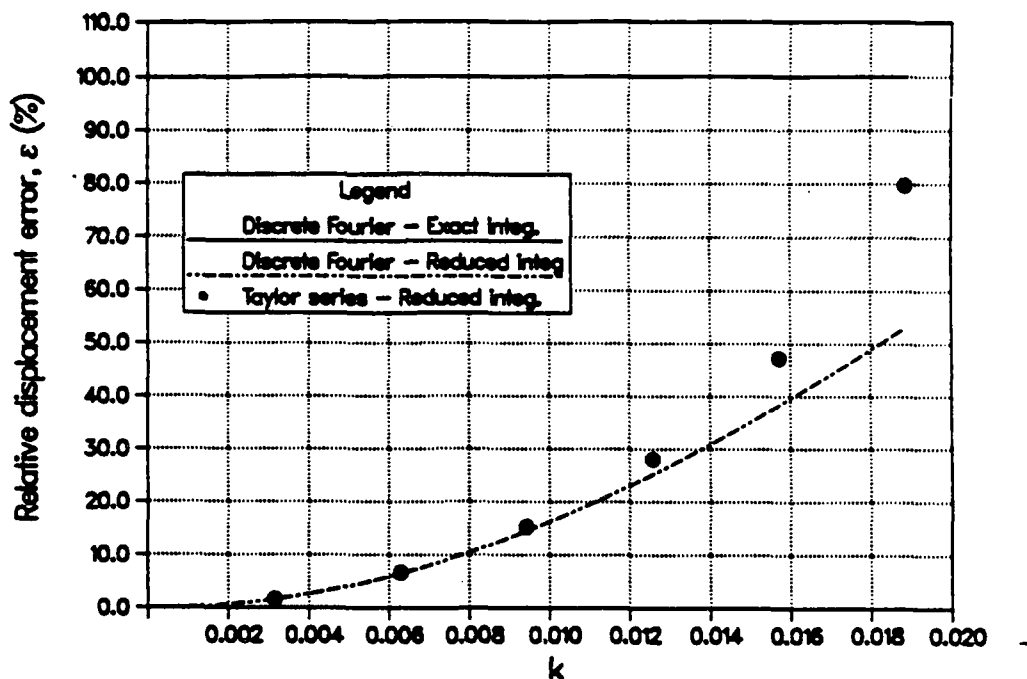
Fig. 3.6 – Relative displacement error for exactly and reduced integrated Timo-shenko beam as a function of spatial frequency, k, for $l = 100$, $h = 1$, $\nu = .3$ and $E = 10^7$.

the spatial frequency for the discrete problem is *band limited* since

$$| k | \leq k_{max}, \tag{3.76}$$

the total error in displacement at the jth node is

$$e(x_j) = \int_{-k_{max}}^{k_{max}} \hat{e}(k) e^{ikx_j} dk. \tag{3.77}$$

§3.4.4 Error Estimation for the Discrete Buckling Problem

From Eqs. (3.58) and (3.63), an a priori error estimate of the bifurcation buckling load may be obtained by plotting the relative error,

$$\epsilon = \frac{\partial - \partial^{\text{D}}}{\partial} \tag{3.78}$$

75
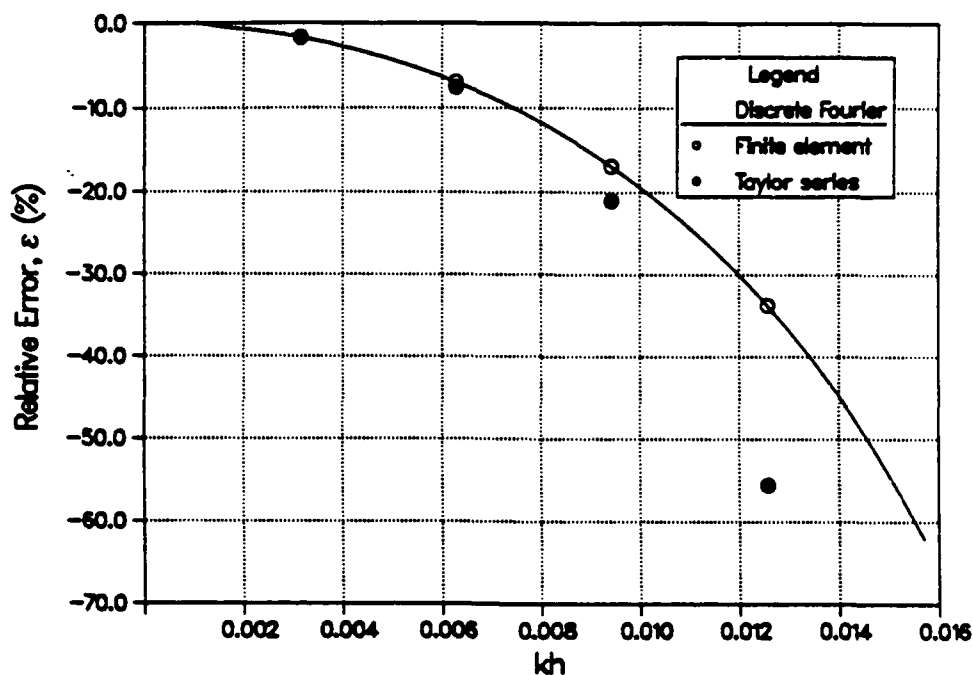
Fig. 3.7 – Relative error in buckling load for $l = 100$, $h = 1$, $E = 10^7$ and $\nu = .3$.

versus the nondimensional wavenumber, kh, for a given element geometry. This has been done in Fig. 3.7. For comparison purposes, results from both finite element analyses, and earlier Taylor series results, extracted from Fig. 2.4 for $n_{el} = 10$, are also shown. These results correspond to 1, 2, 3 and 4 axial half-waves. The domain of kh plotted is $0 \leq kh \leq .5k_{max}h$ where the maximum wavenumber represented by the discrete problem is $k_{max} = \frac{\pi}{l}$, as was described earlier in §3.1.2. While the finite element analysis employed the von Kármán's strain-displacement approximation, the difference between results where the curvature effect is included was insignificant for this case. Examination of Fig. 3.7 clearly shows that the discrete Fourier analysis exactly represents finite element behavior.

An interesting thing to notice is that eventhough reduced spatial integration is employed in the calculation of the material stiffness matrix, the buckling loads for the discrete problem are seen to monotonically converge from above. This behavior would be expected if reduced quadrature had not been employed and the discrete

equations were rigorously derived from Minimum Potential Energy. It is quite apparent that the use of the modified equilibrium equations also over-estimates the relative error in bifurcation buckling load. Unlike the results seen in Fig. 3.6 where the Taylor series predictions were resonably accurate for long wavelength behavior, the Taylor series predictions for the bifurcation buckling loads are not very accurate for any wavelength. This is perhaps not too surprising since the eigenfunctions for the Timoshenko beam buckling problem with simply-supported boundary conditions are in fact sinusoidal. This means that the truncated Taylor series expansions would not be expected to be very accurate for this case as is vividly portrayed in Fig. 3.7. This is also the reason why the discrete Fourier technique predicts the exact error in bifurcation buckling load for the discrete model, as is verified by numerical experiment, as shown in Fig. 3.8

§3.5 Stummel's Problem Revisited

In 1980, Stummel [5] presented a nonconforming element discretization of

$$-\frac{d^2u}{dx^2} + pu = f \qquad (3.79)$$

which passed Irons' patch test [1], as recast in its functional form by Strang and Fix [6], yet failed to converge in the limiting case. Recently, Taylor et al. [4] presented their interpretation of the patch test in terms of three separate tests for which Stummel's element passed the first two, but not the third. Stummel's element failed this third test as a result of a singular stiffness matrix. One might therefore conclude that the question of element convergence was answered from a stability standpoint and not from one of consistency[3]. To fulfill this need for determining intrinsic element behavior, Stummel proposed a generalized patch test [50] which would be applicable to a large class of nonconforming finite elements. In

---

[3] This is an important question to answer since in the Chapter 4, we will see that some of our "best" elements – U1 and S1 – are themselves rank deficient, hence the need for stabilization.

light of the failure of the patch test to determine element consistency for Stummel's element, the question needs to be answered as to how the present symbolic element evaluation technique would fare. As will be shown in the remainder of this section, the question of both element consistency and stability will be easily addressed with the symbolic methods proposed here.

The starting point of this analysis is the finite element equations for Stummel's element which for a single element was given in explicit symbolic form in [4] to be

$$\left(\frac{1}{l} \begin{bmatrix} 1 & -1 & 0 \\ -1 & 1 & 0 \\ 0 & 0 & 0 \end{bmatrix} + \frac{pl}{6} \begin{bmatrix} 2 & 1 & 3 \\ 1 & 2 & 3 \\ 3 & 3 & 6 \end{bmatrix} \right) \left\{ \begin{array}{c} u_i \\ u_{i+1} \\ W_i \end{array} \right\} = \left\{ \begin{array}{c} q_i \\ q_{i+1} \\ q_{W_i} \end{array} \right\} . \qquad (3.80)$$

Here, W_i is the incompatible mode which will be condensed out prior to element assembly. As was noted earlier, these equations uniquely embody all discretization details, and as such are sufficient to completely characterize the proposed finite element formulation.

From an assembly of two equal length elements, one obtains the following transformed limit differential equilibrium equation,

$$(1 + \frac{l^2}{12}p)\bar{k}^2\hat{u} = \hat{f} \qquad (3.81)$$

using the Fourier displacement field

$$u = \hat{u}\,e^{ikx} . \qquad (3.82)$$

Even without transforming Eq. (3.81) back to the physical domain, one can immediately see that the discretization embodied in these finite element equations is *not* consistent with the strong form of the problem represented by Eq. (3.79) since the "pu" term is lost as $l \rightarrow 0$. In the limit, these finite element equations will in fact represent

$$-\frac{d^2u}{dx^2} = f \qquad (3.83)$$

78

irrespective of the value of p.

The question of stability is next answered by determining if there are any zeros of the homogeneous equation,

$$(1 + \frac{l^2}{12}p)\bar{k}^2 = 0, \qquad (3.84)$$

for $k \leq k_{\max} = \pi/\iota$. Since there is one corresponding to $k = 0$, which in this problem does not correspond to a rigid-body mode due to the presence of the pu term in Eq. (3.79), one concludes that this discretization possesses one spurious mode. This is not a surprising result in light of the form of Eq. (3.83) for which one would normally expect one rigid-body mode to be present.

In summary, the convergence characteristics of Stummel's element were determined in a straightforward manner employing the present symbolic analysis technique. Further, as a result of working directly with the limit differential equilibrium equations governing intrinsic element behavior, one is able to explicitly identify the cause of the rank deficient element stiffness as resulting from the loss of the "pu" term in Eq. (3.79).

§3.6 Summary

Discrete Fourier analysis techniques were employed in this chapter in conjunction with the symbolic operational procedures developed in Chapter 2. As a result of their ability to capture complete truncation error information, this technique was used to identify spurious element mechanisms in the frequency domain. For boundary value problems, the absence of spurious mechanisms constitutes solution stability, which along with consistency guarantees convergence of a discrete technique. By transforming results in the frequency domain back to the physical domain, the question of consistency is also addressed. Transformed discrete Fourier equations were shown to result in identical limit differential equilibrium equations to those determined earlier using a Taylor series approach in Chapter 2. As a result, the present discrete Fourier technique is considered to complement

the Taylor series approach. The specific objective of a symbolic element evaluation will determine which technique is more appropriate to the problem at hand.

An approach for obtaining a priori spectral error estimates was then described and applied to both static and bifurcation buckling problems. Error estimates obtained using the modified equilibrium equations in Chapter 2 were compared to the discrete Fourier analysis results obtained in this chapter. For static problems within the accuracy regime in which one would normally be satisfied with the discrete solution, either technique works well. However, for the case of bifurcation buckling, the discrete Fourier technique exactly predicts the buckling load obtained from the finite element analysis whereas results for the modified equilibrium equations are not very accurate.

Lastly, using the discrete Fourier element evaluation technique developed here, the nonconforming element Stummel used to illustrate potential shortcomings in Irons' patch test was successfully analyzed. It was shown *not* to be a convergent approximation since it satisfied neither consistency nor stability requirements.

Symbolic Analysis of the
Bilinear Reissner-Mindlin Plate

In the two previous chapters, the different symbolic analysis techniques used to perform an evaluation of a finite element discretization have been described. In this chapter, these techniques will be employed to assess the performance of the bilinear Reissner-Mindlin plate elements for static and bifurcation buckling problems. While the symbolic procedures are identical to those employed for the earlier one-dimensional discretizations, a two-dimensional representation of the nodal d-o-f using either the Taylor series or discrete Fourier techniques is now required.

Among the different families of finite elements suitable for plate bending problems, four-noded C^0 elements appear to be extremely popular due to their simplicity and computational efficiency. This popularity has been reflected in recent activity directed at improving their performance (see e.g., [35,51,31,17,33,52,53,54,55,56,57]). Techniques to do so seem to be loosely grouped into two different schools of thought. The first one employs different reduced spatial integration rules to both eliminate transverse shear element locking and to further improve their computational efficiency. The problem of controlling the

inevitable spurious mechanisms engendered by reduced spatial integration is the subject of current research [58,59,60,61,62,63]. The second general class of techniques employs alternative interpolation schemes in order to circumvent transverse shear element locking. (see e.g., [53,52]). These elements usually employ full (2x2) spatial integration to ensure full rank.

Specific areas to be addressed are:

1) Effect of spatial integration rule on alleviating transverse shear element locking

2) Effect of different approaches for hourglass control on element performance

3) Identification of spurious element mechanisms

4) A priori assessment of interior solution accuracy for distributed static loading and bifurcation buckling load

§4.1 Continuum Reissner-Mindlin Plate Equations

In this section, the linearized coupled equilibrium equations of Reissner-Mindlin plate theory [64,65] are presented. The derivation of the decoupled transverse equilibrium equation for both the material and buckling operators follows. These equations are then Fourier-transformed to the frequency domain. In the subsequent symbolic analyses, both sets of equations will serve as the reference equations with which the properties of their corresponding discrete counterparts will be compared.

The Lagrangian for Reissner-Mindlin (or C^0) plate theory is comprised of the kinetic energy,

$$T = \frac{1}{2} \iint_A \left[\rho h \left(\frac{\partial w}{\partial t} \right)^2 + \frac{\rho h^3}{12} \left(\frac{\partial \theta_x}{\partial t} \right)^2 + \frac{\rho h^3}{12} \left(\frac{\partial \theta_y}{\partial t} \right)^2 \right] dA , \qquad (4.1)$$

the strain energy, $U = U_m + U_\sigma$, which has been partitioned here into its separate

82

material and stress-dependent contributions, given by

$$U_m = \frac{1}{2} \iint_A \left\{ D\left[\left(\frac{\partial \theta_x}{\partial x}\right)^2 + \left(\frac{\partial \theta_y}{\partial y}\right)^2 + 2\nu \frac{\partial \theta_x}{\partial x}\frac{\partial \theta_y}{\partial y} \right] + D_{11}\left(\frac{\partial \theta_x}{\partial y} + \frac{\partial \theta_y}{\partial x}\right)^2 \right.$$

$$\left. + D_s\left[\left(\frac{\partial w}{\partial x} - \theta_x\right)^2 + \left(\frac{\partial w}{\partial y} - \theta_y\right)^2 \right] \right\} dA \qquad (4.2)$$

$$U_\sigma = \iint_A \int_{-h/2}^{h/2} (\sigma_x \epsilon_x^{\mathrm{NL}} + \sigma_y \epsilon_y^{\mathrm{NL}} + \tau_{xy}\gamma_{xy}^{\mathrm{NL}})\, dz\, dA \qquad (4.3)$$

and lastly, the potential energy of external transverse loading,

$$V = - \iint_A w\, q\, dA. \qquad (4.4)$$

In these equations,

$$D = \frac{Eh^3}{12(1-\nu^2)}, \quad D_{11} = \frac{1-\nu}{2}D, \quad D_{12} = \frac{1+\nu}{2}D, \quad D_s = \kappa Gh \qquad (4.5)$$

with ρ, E, G, h, ν and κ representing the density, extensional modulus, shear modulus, plate thickness, Poisson's ratio and the shear correction factor, respectively. θ_x and θ_y are the rotations about the y and x axis and w is the transverse displacement. The in-plane displacement convention, $u = -z\theta_x$ and $v = -z\theta_y$ is used. To complete the derivation of U_σ, the assumed plate displacement field is substituted into the nonlinear part of the total Lagrangian strains given by

$$\epsilon_x^{\mathrm{NL}} = \frac{1}{2}\left[\left(\frac{\partial u}{\partial x}\right)^2 + \left(\frac{\partial v}{\partial x}\right)^2 + \left(\frac{\partial w}{\partial x}\right)^2 \right]$$

$$\epsilon_y^{\mathrm{NL}} = \frac{1}{2}\left[\left(\frac{\partial u}{\partial y}\right)^2 + \left(\frac{\partial v}{\partial y}\right)^2 + \left(\frac{\partial w}{\partial y}\right)^2 \right] \qquad (4.6)$$

$$\gamma_{xy}^{\mathrm{NL}} = \frac{\partial u}{\partial x}\frac{\partial u}{\partial y} + \frac{\partial v}{\partial x}\frac{\partial v}{\partial y} + \frac{\partial w}{\partial x}\frac{\partial w}{\partial y}.$$

That result is then substituted into Eq. (4.3), and performing the indicated thick-

83

ness integration, the following expression for U_σ,

$$U_\sigma = \frac{1}{2} \iint_A \left\{ h\left[\sigma_x\left(\frac{\partial w}{\partial x}\right)^2 + \sigma_y\left(\frac{\partial w}{\partial y}\right)^2 + 2\tau_{xy}\frac{\partial w}{\partial x}\frac{\partial w}{\partial y}\right] + \frac{h^3}{12}\left[\sigma_x\left(\left(\frac{\partial \theta_x}{\partial x}\right)^2 + \left(\frac{\partial \theta_y}{\partial x}\right)^2\right)\right.\right.$$

$$\left.\left. + \sigma_y\left(\left(\frac{\partial \theta_x}{\partial y}\right)^2 + \left(\frac{\partial \theta_y}{\partial y}\right)^2\right) + 2\tau_{xy}\left(\frac{\partial \theta_x}{\partial x}\frac{\partial \theta_x}{\partial y} + \frac{\partial \theta_y}{\partial x}\frac{\partial \theta_y}{\partial y}\right)\right]\right\} dA \,, \tag{4.7}$$

is obtained. Those terms associated with the rotational d-o-f are the plate equivalent of the so-called curvature term identified by Sun [26] for the Timoshenko beam.

The Euler-Lagrange equations determined from T, U, and V are expressed in differential matrix form as

$$Lu = (L_m + L_\sigma)u = f \tag{4.8}$$

where

$$L_m = \begin{bmatrix} \left(D\frac{\partial^2}{\partial x^2} + D_{11}\frac{\partial^2}{\partial y^2}\right. & D_{12}\frac{\partial^2}{\partial x \partial y} & D_s\frac{\partial}{\partial x} \\ \left.-D_s - \frac{\rho h^3}{12}\frac{\partial^2}{\partial t^2}\right) & & \\ & \left(D\frac{\partial^2}{\partial y^2} + D_{11}\frac{\partial^2}{\partial x^2}\right. & D_s\frac{\partial}{\partial y} \\ & \left.-D_s - \frac{\rho h^3}{12}\frac{\partial^2}{\partial t^2}\right) & \\ sym. & & -D_s\nabla^2 + \rho h\frac{\partial^2}{\partial t^2} \end{bmatrix} \tag{4.9}$$

and

$$L_\sigma = \left(\sigma_x\frac{\partial^2}{\partial x^2} + \sigma_y\frac{\partial^2}{\partial y^2} + 2\tau_{xy}\frac{\partial^2}{\partial x \partial y}\right) \begin{bmatrix} \frac{h^3}{12} & 0 & 0 \\ 0 & \frac{h^3}{12} & 0 \\ 0 & 0 & -h \end{bmatrix} \tag{4.10}$$

and

$$u = \lfloor \theta_x \quad \theta_y \quad w \rfloor^T; \qquad f = \lfloor 0 \quad 0 \quad q \rfloor^T \tag{4.11}$$

84

with the Laplacian operator, ∇^2, defined by

$$\nabla^2 = \frac{\partial^2}{\partial x^2} + \frac{\partial^2}{\partial y^2} \cdot \qquad (4.12)$$

If the nonlinear terms from the von Karman strain-displacement relations [25] were employed in place of Eq. (4.6), L_σ would take on the much simpler form,

$$L_\sigma = -(\sigma_x \frac{\partial^2}{\partial x^2} + \sigma_y \frac{\partial^2}{\partial y^2} + 2\tau_{xy} \frac{\partial^2}{\partial x \partial y}) \begin{bmatrix} 0 & 0 & 0 \\ 0 & 0 & 0 \\ 0 & 0 & h \end{bmatrix}, \qquad (4.13)$$

employed in C^1 plate theory.

§4.1.1 Linearized Transverse Equation of Motion

The first set of decoupled equations of interest here are those corresponding to the material operator, L_m. The decoupled linear equilibrium equation for the transverse displacement, w, is obtained from

$$|L_m| \cdot w = \begin{vmatrix} L_{\theta_x \theta_x} & L_{\theta_x \theta_y} & 0 \\ L_{\theta_x \theta_y} & L_{\theta_y \theta_y} & 0 \\ L_{\theta_x w} & L_{\theta_y w} & q \end{vmatrix} \qquad (4.14)$$

where the L_{ij} are the appropriate entries in Eq. (4.9). Performing the indicated symbolic operations, one obtains

$$l \cdot w = r \cdot q \qquad (4.15)$$

where the decoupled characteristic continuum operator, l, can be written as

$$l = \left[(1 - \frac{D_{11}}{D_s} \nabla^2) + \frac{\rho h^3}{12 D_s} \frac{\partial^2}{\partial t^2} \right] \cdot \left[(D \nabla^2 - \frac{\rho h^3}{12} \frac{\partial^2}{\partial t^2})(\nabla^2 - \frac{\rho h}{D_s} \frac{\partial^2}{\partial t^2}) + \rho h \frac{\partial^2}{\partial t^2} \right] \qquad (4.16)$$

with the corresponding right-hand (or loading) operator, r, given by

$$r = \left[(1 - \frac{D_{11}}{D_s} \nabla^2) + \frac{\rho h^3}{12 D_s} \frac{\partial^2}{\partial t^2} \right] \cdot \left[(1 - \frac{D}{D_s} \nabla^2) + \frac{\rho h^3}{12 D_s} \frac{\partial^2}{\partial t^2} \right] \cdot \qquad (4.17)$$

85

As is apparent from l, the Reissner-Mindlin plate equations are sixth-order, which accounts for the three families of wave motion; flexural and x- and y-direction thickness-shear. It is, however, also apparent that l and r share a common differential operator so that Eq. (4.15) may actually be written in its more familiar form (see [65]) as

$$\left[(D\nabla^2 - \frac{\rho h^3}{12}\frac{\partial^2}{\partial t^2})(\nabla^2 - \frac{\rho h}{D_s}\frac{\partial^2}{\partial t^2}) + \rho h\frac{\partial^2}{\partial t^2}\right] w = \left[(1 - \frac{D}{D_s}\nabla^2) + \frac{\rho h^3}{12 D_s}\frac{\partial^2}{\partial t^2}\right] q .$$
(4.18)

It should be noted that this simplification would *not* have been possible if distributed moments, typically neglected, were present in the distributed loading vector, f. In addition, when working with the limit differential equilibrium equations in the next section, this simplification will, in general, not be possible due to the presence of truncation terms.

The Fourier-transformed matrix operator, $\hat{L}$, is obtained by substituting the two-dimensional harmonic wave solution

$$u(x, y, t) = \hat{u}\, e^{i(k_x x + k_y y - \omega t)} ,$$
(4.19)

where k_x and k_y are the wave numbers in the x and y directions, into Eq. (4.9) yielding

$$\hat{L}_m(k_x, k_y, \omega) = \begin{bmatrix} (-Dk_x^2 - D_{11}k_y^2 & -D_{12}k_x k_y & iD_s k_x \\ -D_s + \frac{\rho h^3}{12}\omega^2) & & \\ & (-Dk_y^2 - D_{11}k_x^2 & iD_s k_y \\ & -D_s + \frac{\rho h^3}{12}\omega^2) & \\ sym. & & -D_s\hat{\nabla}^2 - \rho h\omega^2 \end{bmatrix} .$$
(4.20)

The corresponding characteristic Fourier operators are

$$\hat{l} = \left[(1 - \frac{D_{11}}{D_s}\hat{\nabla}^2) - \frac{\rho h^3}{12 D_s}\omega^2\right] \cdot \left[(D\hat{\nabla}^2 + \frac{\rho h^3}{12}\omega^2)(\hat{\nabla}^2 + \frac{\rho h}{D_s}\omega^2) - \rho h\omega^2\right]$$ (4.21)

86

and

$$\hat{r} = \left[(1 - \frac{D_{11}}{D_s} \nabla^2) - \frac{\rho h^3}{12 D_s} \omega^2 \right] \cdot \left[(1 - \frac{D}{D_s} \nabla^2) - \frac{\rho h^3}{12 D_s} \omega^2 \right] . \quad (4.22)$$

where $\hat{\nabla}^2 = -(k_x^2 + k_y^2)$.

As was discussed in Chapter 3, spurious mechanisms in the finite element method result from the presence of non-physical rigid body motion. For the present two-dimensional problems, the correct rigid body condition, which is obtained from Eq. (4.21) by setting $\omega = 0$, is

$$(1 - \frac{D_{11}}{D_s} \hat{\nabla}^2) \hat{\nabla}^4 = 0 \quad \Rightarrow \quad \hat{\nabla}^4 = 0 \quad (4.23)$$

since

$$(1 - \frac{D_{11}}{D_s} \hat{\nabla}^2) = 1 + \frac{D_{11}}{D_s} (k_x^2 + k_y^2) \neq 0 \quad \forall \; k_x, k_y \in \Re . \quad (4.24)$$

The correct rigid body conditions in the Fourier-transformed state are therefore determined from Eq. (4.23) to be

$$k_x = k_y = 0 . \quad (4.25)$$

This condition implies that if for a given finite element discretization,

$$\hat{r}^D(k_x, k_y, 0) = 0 \quad \forall \; \{k : 0 < k \leq k_{max}\} , \quad (4.26)$$

then the resulting element will exhibit the corresponding spurious mechanism(s).

§4.1.2 Linearized Buckling Equation

The linearized decoupled buckling equation in the physical domain is determined from

$$\det(L_m + L_\sigma) \cdot w = \det G_3 |_{q=0} \quad (4.27)$$

87

with $\partial^2/\partial t^2 = 0$. Due to the length of the resulting symbolic expression, however, only the case of uniaxial compression will be explicitly presented here. By assuming σ_x is the only nonzero prestress, Eq. (4.27) yields

$$(1 - \frac{D_{11}}{D_s}\nabla^2)D\nabla^4 w - \sigma_x^3\frac{hI^2}{D_s^2}\frac{\partial^6 w}{\partial x^6} + \sigma_x^2[(\frac{\nu-3}{2}\frac{D}{D_s}hI - \frac{I^2}{D_s})\nabla^2 + \frac{2hI}{D_s}]\frac{\partial^4 w}{\partial x^4}$$

$$- \sigma_x[h + (\frac{\nu-3}{2}\frac{D}{D_s}h - I)\nabla^2 + (\frac{DD_{11}}{D_s^2}h - \frac{\nu-3}{2}\frac{D}{D_s}I)\nabla^4]\frac{\partial^2 w}{\partial x^2} = 0$$
$$(4.28)$$

where $I = H^3/12$. This expression is considerably different than that for the classical C^1 plate. The solution of this equation in terms of σ_x yields three roots of which the lowest corresponds to a "flexural" buckling load. When the von Karman strain-displacement relations are instead used, a greatly simplified Eq. (4.28) results, viz.

$$(1 - \frac{D_{11}}{D_s}\nabla^2)D\nabla^4 w - \sigma_x h[1 - \frac{3-\nu}{2}\frac{D}{D_s}\nabla^2 + \frac{DD_{11}}{D_s^2}\nabla^4]\frac{\partial^2 w}{\partial x^2} = 0. \quad (4.29)$$

In the thin-plate limit, formally represented here by $D_s \to \infty$, the familiar C^1 equation governing uniaxial buckling results, given by

$$D\nabla^4 w - \sigma_x h\frac{\partial^2 w}{\partial x^2} = 0. \tag{4.30}$$

In the Fourier domain, one writes L_σ as

$$\hat{L}_\sigma = -(\sigma_x k_x^2 + \sigma_y k_y^2 + 2\tau_{xy}k_x k_y)\begin{bmatrix} I & 0 & 0 \\ 0 & I & 0 \\ 0 & 0 & -h \end{bmatrix}. \tag{4.31}$$

so that transformed counterparts of Eqs. (4.28) and (4.29) can easily be obtained from

$$\det(\hat{L}_{\mathrm{m}} + \hat{L}_\sigma) \cdot \hat{w} = \det \hat{G}_3|_{\hat{q}=0} \tag{4.32}$$

as required.

88

§4.2 Discretization of the Reissner-Mindlin Plate Equations

If one employs the bilinear isoparametric shape functions, the element material stiffness matrix for the 4-node Reissner-Mindlin plate bending element is derived from Eq. (4.2) by first substituting the element displacement interpolations

$$\mathbf{u} = \mathbf{N}_i \mathbf{d}_i \; ; \quad i = 1,4 \tag{4.33}$$

with $\mathbf{d}_i = \lfloor \theta_{x_i} \quad \theta_{y_i} \quad w_i \rfloor^T$, $\mathbf{N}_i = N_i \mathbf{I}_3$ and

$$N_i = \frac{1}{4}(1 + \xi_i \xi)(1 + \eta_i \eta) \; ; \quad \begin{cases} \xi_i = (-1,1,1,-1) \\ \eta_i = (-1,-1,1,1) \end{cases} \tag{4.34}$$

followed by setting $\delta U_m = 0$, from which the element material stiffness,

$$\mathbf{k} = \mathbf{k}_b + \mathbf{k}_s = \int\!\!\int_A (\mathbf{B}_b^T \mathbf{D}_b \mathbf{B}_b + \mathbf{B}_s^T \mathbf{D}_s \mathbf{B}_s) dA$$

$$= \int_{-1}^{1} \int_{-1}^{1} (\mathbf{B}_b^T \mathbf{D}_b \mathbf{B}_b + \mathbf{B}_s^T \mathbf{D}_s \mathbf{B}_s) |\mathbf{J}| d\xi d\eta \, . \tag{4.35}$$

is obtained. In this expression, $\mathbf{B}_b$ and $\mathbf{B}_s$ are the isoparametric strain-displacement matrices representing bending and transverse shear contributions with $\mathbf{D}_b$ and $\mathbf{D}_s$ representing the corresponding isotropic material matrices

$$\mathbf{D}_b = D \begin{bmatrix} 1 & \nu & 0 \\ \nu & 1 & 0 \\ 0 & 0 & \frac{1-\nu}{2} \end{bmatrix} \quad \text{and} \quad \mathbf{D}_s = D_s \begin{bmatrix} 1 & 0 \\ 0 & 1 \end{bmatrix} . \tag{4.36}$$

The surface Jacobian, $\mathbf{J}$, which represents the differential transformation between the physical (x,y) and isoparametric (ξ, η) coordinates, is determined from

$$\left\{ \begin{array}{c} \frac{\partial}{\partial \xi} \\ \frac{\partial}{\partial \eta} \end{array} \right\} = \mathbf{J} \left\{ \begin{array}{c} \frac{\partial}{\partial x} \\ \frac{\partial}{\partial y} \end{array} \right\} \quad \Rightarrow \quad \mathbf{J} = \begin{bmatrix} \frac{\partial x}{\partial \xi} & \frac{\partial y}{\partial \xi} \\ \frac{\partial x}{\partial \eta} & \frac{\partial y}{\partial \eta} \end{bmatrix} . \tag{4.37}$$

89

$\mathbf{B}_b$ and $\mathbf{B}_s$ are determined from the strain-displacement relations

$$\epsilon = \begin{Bmatrix} \epsilon_x \\ \epsilon_y \\ \gamma_{xy} \\ \gamma_{xz} \\ \gamma_{yz} \end{Bmatrix} = \begin{Bmatrix} \mathbf{B}_b \\ \mathbf{B}_s \end{Bmatrix} \mathbf{d} \quad \Rightarrow \quad \begin{cases} \mathbf{B}_{b_i} = \begin{bmatrix} \frac{\partial N_i}{\partial x} & 0 & 0 \\ 0 & \frac{\partial N_i}{\partial y} & 0 \\ \frac{\partial N_i}{\partial y} & \frac{\partial N_i}{\partial x} & 0 \end{bmatrix} \\[3em] \mathbf{B}_{s_i} = \begin{bmatrix} -N_i & 0 & \frac{\partial N_i}{\partial x} \\ 0 & -N_i & \frac{\partial N_i}{\partial y} \end{bmatrix} \end{cases} \quad (4.38)$$

Discretization of Eq. (4.7) results in the following geometric stiffness matrix,

$$\mathbf{k}_\sigma = \iint_A \mathbf{B}_\sigma^T \begin{bmatrix} I\mathbf{s} & 0 & 0 \\ 0 & I\mathbf{s} & 0 \\ 0 & 0 & h\mathbf{s} \end{bmatrix} \mathbf{B}_\sigma \, dA$$

$$= \int_{-1}^{1} \int_{-1}^{1} \mathbf{B}_\sigma^T \begin{bmatrix} I\mathbf{s} & 0 & 0 \\ 0 & I\mathbf{s} & 0 \\ 0 & 0 & h\mathbf{s} \end{bmatrix} \mathbf{B}_\sigma \, |\mathbf{J}| \, d\xi \, d\eta$$

$$(4.39)$$

where

$$\mathbf{s} = \begin{bmatrix} \sigma_x & \tau_{xy} \\ \tau_{xy} & \sigma_y \end{bmatrix}$$

and

$$\mathbf{B}_\sigma = \begin{bmatrix} \mathbf{J}^{-1} & 0 & 0 \\ 0 & \mathbf{J}^{-1} & 0 \\ 0 & 0 & \mathbf{J}^{-1} \end{bmatrix} \begin{bmatrix} \frac{\partial}{\partial \xi} & 0 & 0 \\ \frac{\partial}{\partial \eta} & 0 & 0 \\ 0 & \frac{\partial}{\partial \xi} & 0 \\ 0 & \frac{\partial}{\partial \eta} & 0 \\ 0 & 0 & \frac{\partial}{\partial \xi} \\ 0 & 0 & \frac{\partial}{\partial \eta} \end{bmatrix} \begin{bmatrix} \mathbf{N}_1 & \mathbf{N}_2 & \mathbf{N}_3 & \mathbf{N}_4 \end{bmatrix}$$

with $\mathbf{N}_i = N_i \mathbf{I}_3$ and the Jacobian, $\mathbf{J}$, as previously defined.

Functional evaluation of $\mathbf{B}_b^T \mathbf{D}_b \mathbf{B}_b$ and $\mathbf{B}_s^T \mathbf{D}_s \mathbf{B}_s$ shows that unlike the Timoshenko beam, both integrands contain terms of the same bi-quadratic polynomial

order. A 2x2 point quadrature rule would be required for an exact term-by-term spatial integration for the case of a rectangular (or parallelogram) element with its constant Jacobian determinant. The use of a (1x1) point (or reduced) quadrature rule would result in the loss of quadratic order contributions to both integrals introducing rank deficient stiffness matrices with the accompanying possibility of spurious oscillations appearing in the discrete solution. Thus, one of the important question to be answered in this chapter is "What is the effect of employing different spatial integration rules on Eqs. (4.35) and (4.39)?"

§4.3 Taylor Series Element Evaluation

It was noted in Chapter 3 that the Taylor series approach can not be used to detect spurious element mechanisms. Nevertheless, it is ideally suited for detecting parasitic differential operators responsible for element pathologies such as locking. In the present section, the effect of employing different spatial integration rules for the bilinear Reissner-Mindlin plate element is evaluated using the Taylor series approach outlined in Chapter 2. In the later section dealing with discrete Fourier analysis techniques, the question of spurious element mechanisms engendered by reduced spatial integration of element stiffness matrices will be addressed.

§4.3.1 Transverse Shear Locking – Exact (2x2) Spatial Integration

The most obvious place to start is to consider the exact spatial integration of Eq. (4.35) achieved by employing a (2x2) quadrature rule on both bending and transverse shear terms. Numerical convergence studies by Hughes et al. [35] have shown that the resulting element exhibits the same type of transverse shear element locking as encountered earlier for the Timoshenko beam. By using the operational procedures developed in Chapter 2, the effect of the exact spatial integration on element behavior is succinctly determined by recovering the element's governing

91

decoupled w limit differential equilibrium equation which was found to be[1]

$$[D\nabla^4 + \frac{l^2}{12}D_s(d_x^4 + d_y^4) + (\frac{l^2}{12}(4D - D_{11}) - \frac{DD_{11}}{D_s})\nabla^6$$

$$+ \frac{l^2}{12}(5D + D_{11})\nabla^2 d_x^2 d_y^2]w =$$

$$[1 + (\frac{l^2}{3} - \frac{D_{11}}{D_s} - \frac{D}{D_s})\nabla^2 + (\frac{DD_{11}}{D_s^2} - \frac{l^2}{4}(\frac{D}{D_s} + \frac{D_{11}}{D_s}))\nabla^4$$

$$+ \frac{l^2}{6}(\frac{D}{D_s} + \frac{D_{11}}{D_s})d_x^2 d_y^2]q$$

$$(4.40)$$

for a patch of square ($l \times l$) elements as shown in Fig. 4.1. Here, the compact symbolic notation $d_x = \frac{\partial}{\partial x}$ and $d_y = \frac{\partial}{\partial y}$ is used. Also, only truncation error terms that possess the same differential order as that of the continuum operators have been retained. As in the analysis of the Timoshenko beam in Chapter 2, these truncation error terms are considered to be *parasitic* differential operators. With the presence of these truncation error terms, the full sixth-order equilibrium equation must be dealt with so that Eqs. (4.16) and (4.17) with $\partial^2/\partial t^2 = 0$ will serve as the reference equations.

The possibility of transverse shear element locking is apparent due to the form of the parasitic differential operator associated with the primary differential bending term, ∇^4. By looking at these two isolated terms, one finds that

$$D\nabla^4 + \frac{l^2}{12}D_s(d_x^4 + d_y^4) = D[(1 + \frac{l^2 D_s}{12D})d_x^4 + 2d_x^2 d_y^2 + (1 + \frac{l^2 D_s}{12D})d_y^4] \quad (4.41)$$

which means that the x- and y-direction bending modes will lock for essentially any finite length plate since the bending stiffness in those directions is amplified by the factor

$$1 + \frac{l^2 D_s}{12D} = 1 + \frac{\kappa(1 - \nu)}{2}(\frac{l}{h})^2 \gg 1. \quad (4.42)$$

---

[1] The MACSYMA runstream from which the results of this analysis were obtained is shown in Appendix A.2.
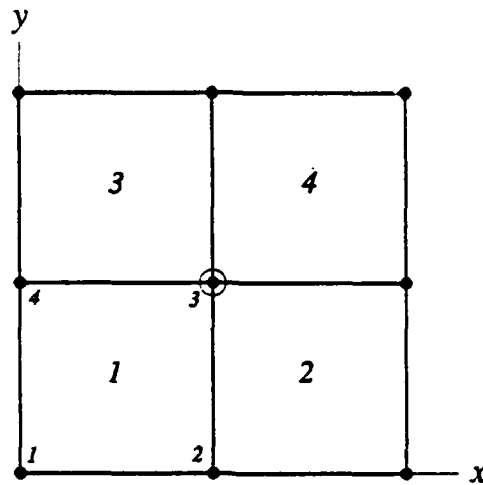
Fig. 4.1 – Element geometry for 4-node plate discretizations

Thus, in order to obtain a physically realistic solution employing this element, one must have $l \ll h$. The pure xy-twist or torsion bending mode is not effected by locking as is demonstrated by numerical example in §4.3.3.2.

The effect of truncation error terms on the secondary "thick" plate differential operator, ∇^6, are of a much less benign nature. If the parasitic transverse shear element locking terms could be eliminated, one could return to the traditional order-of-accuracy notions to evaluate this discretization.

§4.3.2 Element Unlocking – Other Spatial Integration Schemes

As far back as the early 1970's, it was independently recognized by Pawsey [28] and Zienkiewicz et al. [29] that exactly integrated thin C^0 plate (and shell) elements could be cured of their transverse shear element locking by selectively employing reduced spatial integration for the transverse shear element stiffnesses while exactly integrating the bending stiffness. The rationale for this being that, in the thin plate limit, the last two terms in the potential energy expression for the C^0 plate given by Eq. (4.2) can be considered as penalty constraint conditions enforcing the Kirchhoff constraints. With this being the case, the rank of the transverse shear stiffness, k_s, must be reduced, a condition easily achieved by

using reduced spatial integration. In this section, the effect of using different spatial integration rules to derive the element's material stiffness, as embodied in the governing limit differential equilibrium equations, is investigated.

§4.3.2.1 Selectively-Reduced Integrated S1 Element

The first Reissner-Mindlin plate element to be examined here is the S1 element [35] which employs exact (2x2) spatial integration on the bending stiffness and a reduced (1x1) integration on the transverse shear stiffness. The decoupled limit differential equilibrium equation for this element is found to be

$$[D\nabla^4 + (\frac{5l^2}{12}D - \frac{DD_{11}}{D_s})\nabla^6 + \frac{l^2}{12}(7D - D_{11})\nabla^2 d_x^2 d_y^2]w =$$
$$[1 + (\frac{l^2}{2} - \frac{D}{D_s} - \frac{D_{11}}{D_s})\nabla^2 + (\frac{DD_{11}}{D_s^2} - \frac{l^2}{3}(\frac{D}{D_s} + \frac{D_{11}}{D_s}))\nabla^4$$
$$- \frac{l^2}{6}(\frac{D}{D_s} + \frac{D_{11}}{D_s})dx^2dy^2]q.$$
(4.43)

The above equation reveals that the parasitic locking term associated with the ∇^4 operator has been eliminated through the use of reduced integration on k_s. As a result, one obtains a locking-free element discretization. Unfortunately, this reduced spatial integration of k_s results in a rank deficient element stiffness matrix which exhibits two spurious element mechanisms (see [35]). The first one, an inplane-twist mode does not propagate in an assembled mesh and hence is of little practical importance. The second one is the so-called w-hourglass mode which can be responsible for singular or near singular assembled global stiffness matrices with resulting wild solution oscillations if not controlled. The effect of employing different hourglass control techniques to stabilize this element is discussed in detail in §4.3.4.2.

§4.3.2.2 Uniformly-Reduced Integrated U1 Element

The next element to be examined is the uniformly-reduced integrated U1 element (see Refs. [33] and [56]) which employs a (1x1) spatial integration rule on

94

both the bending and transverse shear stiffnesses. This type of element is potentially quite computationally attractive since the generation of the element stiffness can essentially be "hard wired" to take advantage of the single Gauss integration point. This is provided, of course that the attendant spurious mechanisms are controlled. The decoupled limit differential equilibrium equation for this element is

$$
[D\nabla^4 + (\frac{5l^2}{12}D - \frac{DD_{11}}{D_s})\nabla^6 + \frac{2l^2}{3}D\nabla^2 d_x^2 d_y^2]w =
$$
$$
[1 + (\frac{l^2}{2} - \frac{D}{D_s} - \frac{D_{11}}{D_s})\nabla^2 + (\frac{DD_{11}}{D_s^2} - \frac{l^2}{3}(\frac{D}{D_s} + \frac{D_{11}}{D_s}))\nabla^4
$$
$$
- \frac{l^2}{3}(\frac{D}{D_s} + \frac{D_{11}}{D_s})dx^2 dy^2]q
$$
$$
(4.44)
$$

Since the same (1x1) spatial integration rule is used for k_s as for the S1 element, one would again expect that this element is locking-free. This is in fact the case due to the absence of any parasitic operators associated with the primary bending operator, ∇^4. Unfortunately, as was the case for the S1 element, reduced spatial integration also results in the presence of spurious element mechanisms; four to be exact. The two additional zero eigenvalues correspond to a θ_x-hourglass and a θ_y-hourglass mode as a result of the under-integration of k_b. The stabilization of this element will also be symbolically analyzed in the next section.

§4.3.2.3 Directionally Integrated Transverse Shear Element

The last plate bending element to be considered here is the directionally integrated transverse shear element. This element employs the (2x2) quadrature rule for k_b while further partitioning k_s into its γ_{xz} and γ_{yz} contributions and employing a (1x2) rule for the xz stiffness and a (2x1) rule for the yz stiffness. This spatial integration technique is employed by MacNeal's QUAD4 element [31] and was the focal point of the recent work by Prathap and Viswanath [54].

The rationale for the selection of these spatial integration rules lies in the inconsistent polynomial approximation inherent in using the same bilinear inter-

95

polation functions for both w, θ_x and θ_y. This point can be clarified if one considers the transverse shear strain

$$\gamma_{xz} = \frac{\partial w}{\partial x} - \theta_x. \qquad (4.45)$$

In terms of the generalized displacements,

$$w = a_0 + a_1 x + a_2 y + a_3 xy$$
$$\theta_x = b_0 + b_1 x + b_2 y + b_3 xy \qquad (4.46)$$

where (x, y) represents a centroidal-based cartesian coordinate system, one finds that

$$\gamma_{xz} = (a_1 - b_0) + (a_3 - b_2)y - b_1 x - b_3 xy. \qquad (4.47)$$

The last two terms are extraneous since they only represent θ_x contributions to γ_{xz} which are not balanced by w contributions. The easiest way to see their deleterious effect is to consider what happens in the thin plate limit where $\frac{\partial w}{\partial x} = \theta_x \Rightarrow \gamma_{xz} = 0$. Here, these terms represent nonphysical constraints on γ_{xz} which will ultimately result in element locking since $b_1 \neq 0$ and $b_3 \neq 0$.

If one now considers the calculation of the transverse shear stiffness associated with the γ_{xz} contribution, $k_{s_{xz}}$, only even polynomial functions will survive the spatial integration so that it will be sufficient to only consider the integration of the $(a_1 - b_0)^2 + (a_3 - b_2)^2 y^2 - b_1^2 x^2 - b_3^2 x^2 y^2$. To eliminate the inconsistent contribution of the b_1 and b_3 terms to $k_{s_{xz}}$, a one-point quadrature rule in the x direction may be employed while to exactly integrate the y dependence, a two-point rule is required, hence the rationale for invoking the (1x2) rule. Here, it is assumed that the Jacobian is a constant.

Similarly, it can be shown that a (2x1) quadrature rule is appropriate for $k_{s_{yz}}$. It is important to note that this element discretization is conceptually different from that for either the S1 or U1 elements in that this modified spatial integration rule is not invoked within the penalty function context of reducing the rank of k_s.

96

By selectively eliminating only the "spurious" θ_x and θ_y constraints, an element stiffness of full rank is maintained. It is this observation which has motivated research in redefining the way in which the transverse shears are handled at the element level via alternative interpolation procedures.

As expected, this spatial integration technique results in a locking-free plate bending element as is reflected in its limit differential equilibrium equation,

$$[D\nabla^4 + (\frac{l^2}{3}D - \frac{DD_{11}}{D_s})\nabla^6 + \frac{l^2}{12}(7D - D_{11})\nabla^2 d_x^2 d_y^2]w =$$

$$[1 + (\frac{5l^2}{12} - \frac{D}{D_s} - \frac{D_{11}}{D_s})\nabla^2 + (\frac{DD_{11}}{D_s^2} - \frac{l^2}{4}\frac{D}{D_s} - \frac{l^2}{3}\frac{D_{11}}{D_s}))\nabla^4 - \frac{l^2}{3}\frac{D}{D_s}dx^2 dy^2]q .$$

$$(4.48)$$

The success of this element rests solely on taking advantage of the fact that the local (x, y) and (ξ, η) coordinate systems are aligned for a rectangular element. If, however, one begins to distort the element into a parallelogram as portrayed in Fig. 4.2, the locking-free property of the discretization is lost. For this particular distortion, one finds that the (2x1) integration rule for $k_{s_{yz}}$ still works since $\xi \parallel x$ but with $\eta \nparallel y$, the (1x2) integration of $k_{s_{xz}}$ no longer eliminates the spurious constraints on γ_{xz} resulting in the reappearance of element locking. The dominant bending operator appearing in the decoupled limit differential equilibrium equation for this particular parallelogram discretization is found to be

$$D\nabla^4 + \frac{l^2 \tan^2 \beta}{12}D_s d_x^4 \qquad (4.49)$$

where β is the angle between the y and η axes as is portrayed in Fig. 4.2. The second term in this expression is the parasitic operator responsible for locking the x-direction bending mode of the parallelogram mesh. If the local (x, y) and (ξ, η) coordinate systems were not aligned at all, one would expect to see the return of element locking with the appearance of parasitic terms associated with both the d_x^4 and d_y^4 continuum operators as was the case for the exactly integrated element.
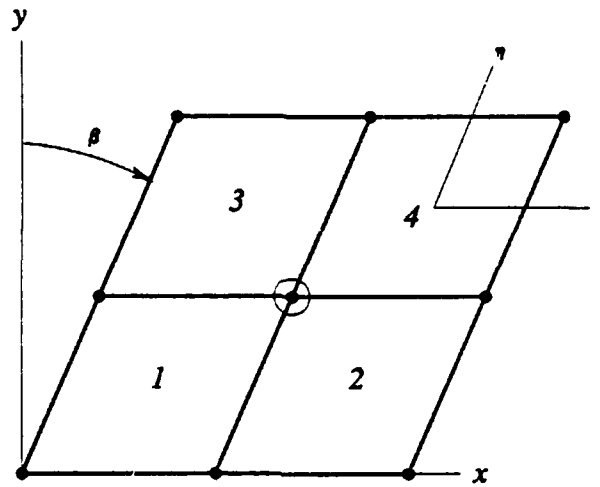
Fig. 4.2 - Element geometry for parallelogram discretization

§4.3.2.4 Alternative Transverse Shear Interpolations Schemes

In order to overcome the problem of element locking engendered through the application of the "standard" bilinear isoparametric shape functions, the technique of employing alternative interpolation schemes based upon assumed strain fields has proved quite successful (see e.g., Hughes and Tezduyar's T1 element[53] and the Bathe and Dvorkin element [52]). For a rectangular element, these alternative transverse shear interpolation schemes result in limit differential equilibrium equations identical to that determined for the directionally integrated transverse shear element discussed in the last section. This results from explicitly embedding into the element's transverse shear interpolation scheme the functional equivalent of

$$\gamma_{xz} = a_1 + b_1 y$$
$$\gamma_{yz} = a_2 + b_2 x$$

(4.50)

for the present cartesian element geometry which is identical to that achieved by employing the (1x2) and (2x1) spatial integration rules.

98

§4.4 Symbolic Evaluation of Hourglass Control Techniques

Over the years various element discretization schemes have been proposed based wholly or in part upon using reduced spatial integration techniques to alleviate different element pathologies or simply to obtain a computationally more efficient element. The inevitable spurious mechanisms engendered by such an approach can render an assembled stiffness matrix singular. Different stablization or *hourglass control* techniques have been proposed to eliminate these singularities. Except for brief excursions into functional analysis techniques (see e.g. [61,62]), the developers of hourglass control strategies have, by and large, resorted to physical considerations whereby generalized stresses and strains (or other conjugate quantities) are appropriately introduced into the analysis [58,59,60]. This physically-based approach to hourglass control, unfortunately, unnecessarily hides the intrinsic linear algebra problem of dealing with rank deficient stiffness matrices.

The present approach to understanding hourglass control is based entirely upon first viewing the problem from a linear algebraic standpoint. Once the fundamental problem is understood, the proper physical interpretation follows in a natural manner. From this starting point, the key to hourglass control or alternatively, consistent spurious element mechanism suppression, is based upon selectively shifting part of k's spectrum to remove the rank deficiency associated with the spurious mechanism(s). This entails moving eigenvectors from the null space of k to the range of an augmented element stiffness matrix, $\bar{k}$. All a priori[2] hourglass control techniques presented in the literature are based upon this basic idea.

From a physical standpoint there are two important aspects of this problem.

---

[2] Jacquotte and Oden [61] use a priori to refer to hourglass control techniques invoked prior to the global solution while a posteriori implies filtering out hourglass modes after a global solution has somehow been obtained.

The first being the obvious one of removing the spurious mechanism(s) by this shifting procedure while the second is concerned with preserving the consistency of the resulting discretization which at a minimum entails preserving the vectors spanning the rigid body and constant strain modes of k (see Ref. [58]). As will be shown here, however, there is a potential pitfall in using these techniques, namely, the reintroduction of element locking. After first briefly describing some of the underlying linear algebra details of hourglass-control in order to *motivate* their use, element evaluation of the "stabilized" S1 and U1 elements will be presented.

§4.4.1 Selected Spectral Shifting

The concept of selective spectral shifting, based upon the spectral theorem (see e.g., [66]), provides the theoretical foundation for hourglass control techniques. With the spectral theorem, the positive semi-definite element stiffness, k may be decomposed as

$$\mathbf{k} = \sum_{i=1}^{\dim(\mathbf{k})} \lambda_i \mathbf{x}_i \mathbf{x}_i^{\mathrm{T}} \tag{4.51}$$

where the λ_i's are the eigenvalues and $\mathbf{x}_i$'s are the corresponding normalized eigenvectors determined from the standard eigenproblem

$$\mathbf{k}\mathbf{x}_i = \lambda_i \mathbf{x}_i ; \quad i = 1, \ldots, \dim(\mathbf{k}) . \tag{4.52}$$

The present form of k ensures that all λ_i's are real and that the corresponding $\mathbf{x}_i$'s form an orthonormal basis such that $\mathbf{x}_i^{\mathrm{T}} \mathbf{x}_j = \delta_{ij}$. Selectively shifting one of k's eigenvalues, e.g., the jth eigenvalue, can now be accomplished by forming the augmented matrix

$$\overline{\mathbf{k}} = \mathbf{k} + \phi_j \mathbf{x}_j \mathbf{x}_j^{\mathrm{T}} \tag{4.53}$$

100

where $x_j x_j^T$ is a rank one matrix update and ϕ_j is a (positive) scalar. Now,

$$\bar{k}x_j = (k + \phi_j x_j x_j^T)x_j = kx_j + \underbrace{\phi_j x_j^T x_j}_{=\phi_j} x_j$$
$$= \underbrace{(\lambda_j + \phi_j)}_{=\bar{\lambda}_j} x_j. \tag{4.54}$$

From this, it is obvious that x_j is also an eigenvector of the augmented problem with its associated eigenvalue being $\bar{\lambda}_j$, or in other words, λ_j has been shifted by an amount ϕ_j. If one considers the remaining eigenpairs from k, they will remain unchanged since

$$x_j^T x_i = 0 \ \forall \ i \neq j \quad \Rightarrow \quad (k + \phi_j x_j x_j^T)x_i = kx_i = \lambda_i x_i. \tag{4.55}$$

These results also hold true for shifting multiple eigenvalues employing rank two and higher updates where the augmented matrix takes the form

$$\bar{k} = k + \sum_{k=1}^{v} \phi_k x_k x_k^T \tag{4.56}$$

with v denoting the number of eigenvalues to be shifted.

§4.4.2 Rank Deficient Element Matrices

When the element stiffness matrix is constructed using reduced spatial integration, the element stiffness, k, possesses one or more zero eigenvalues whose associated eigenvectors do not correspond to physical rigid-body modes. These spurious hourglass modes, along with the physical rigid body modes, span the null space of k, $\mathcal{N}(k)$, all of whose vectors satisfy the identity $kx = 0$. The remaining eigenvectors, which (should) represent the physical deformation modes, form the range of k, $\mathcal{R}(k)$. Since rank deficient element matrices can result in a singular assembled global stiffness, techniques for reducing the rank deficiency of k are of current research interest. The technique of selected spectral shifting

101

provides the needed tool for understanding exactly how the different hourglass control techniques work.

Based upon the discussion thus far, an augmented element stiffness, $\bar{k}$, would be defined by

$$\bar{k} = k + \phi v v^T \qquad (4.57)$$

where v represents the hourglass control vector and ϕ is a positive scalar. Since the x_i's form an orthonormal basis, v can be written as

$$v = \sum_{i=1}^{n} \alpha_i x_i \qquad (4.58)$$

where $n = \dim(k)$. We are now in a position to precisely define the (minimum) requirements for the successful suppression of spurious element mechanisms. First, a component of the hourglass control vector, v, must be in the direction of the eigenvector, x, corresponding to the non-physical zero eigenvalue, to ensure that this eigenvalue is shifted to a positive non-zero value. Secondly, v must be orthogonal to the rigid body and constant strain modes to ensure element consistency[3]. The one vector which automatically satisfies these conditions is the eigenvector itself corresponding to the nonphysical zero eigenvalue. It should be noted that the potential always exists to alter eigenpairs representing physical deformation and rigid body modes through an improper choice of v.

§4.4.3 Hourglass Control for the S1 Element

Hughes et al. [35] have shown that the S1 element possesses the following two

---

[3] This guarantees that the element will still pass the patch test. For higher-order elements, orthogonality with respect to higher-order strain modes would be necessary to maintain their accuracy.

spurious element mechanisms,

mode	w	θ_x	θ_y
1	h	0	0
2	0	$-y$	x

where the first mode is the w-hourglass mode and the second is the in-plane twist mode. Here, the hourglass d-o-f displacement pattern, h, is given by

$$\mathbf{h} = \lfloor x_1 y_1 \quad x_2 y_2 \quad x_3 y_3 \quad x_4 y_4 \rfloor^T \tag{4.59}$$

for the general quadrilateral, and by

$$\mathbf{h} = \lfloor 1 \quad -1 \quad 1 \quad -1 \rfloor^T \tag{4.60}$$

for a rectangular element. x and y are used to denote nodal position with respect to a local cartesian coordinate system. As was noted in [35] and symbolically verified to be the case in §4.4.3.2, the in-plane twist mode[4] is not communicable when the element is assembled in a mesh and so has typically been ignored.

In their first paper dealing with the control of hourglass modes in plate elements, Belytschko et al. [59] proposed two quite different hourglass control procedures for dealing with the w-hourglass mode of the S1 element. In the remainder of this sub-section, these two techniques will be examined in detail.

§4.4.3.1 Method 1 – Weighted Stiffness Averaging

The proposed element stiffness for method 1 was

$$\mathbf{k} = \mathbf{k}_b^{[2 \times 2]} + (1 - \epsilon)\mathbf{k}_s^{[1 \times 1]} + \epsilon \mathbf{k}_s^{[2 \times 2]} \tag{4.61}$$

---

[4] Note: This mode is the same for both the S1 and U1 elements

103

which was assumed to be comprised of the fully integrated bending stiffness (exact for rectangular elements) and a linear combination of the fully-integrated and under-integrated transverse shear stiffnesses. This expression was subsequently rewritten as

$$\mathbf{k} = \underbrace{\mathbf{k}_b^{[2\times2]} + \mathbf{k}_s^{[1\times1]}}_{\mathbf{k}_{S1}} + \epsilon\mathbf{k}_H \qquad (4.62)$$

where

$$\mathbf{k}_H = \mathbf{k}_s^{[2\times2]} - \mathbf{k}_s^{[1\times1]} \qquad (4.63)$$

represents the so-called hourglass stabilization matrix.

By making use of the spectral theorem, one can rewrite Eq. (4.62) as

$$\overline{\mathbf{k}} = \mathbf{k}_{S1} + \epsilon[\underbrace{\sum_{i=1}^{12}\phi_i\mathbf{y}_i\mathbf{y}_i^T}_{\mathbf{k}_s^{[2\times2]}} - \underbrace{\sum_{i=1}^{12}\varphi_i\mathbf{z}_i\mathbf{z}_i^T}_{\mathbf{k}_s^{[1\times1]}}]. \qquad (4.64)$$

Written in this form, it is obvious that only terms whose eigenvectors are in their respective ranges of $\mathbf{k}_s$ contribute nonzero matrix updates to $\mathbf{k}_{S1}$. The shifting of the spurious zero eigenvalues of $\mathbf{k}_{S1}$ is therefore being accomplished solely by $\mathbf{k}_s^{[2\times2]}$ whose eigenvectors in $\mathcal{R}(\mathbf{k}_s^{[2\times2]})$ have components in the direction of $\mathbf{k}_{S1}$'s w-hourglass mode – and also in that of the inplane twist mode. From a strictly hourglass control standpoint, $\mathbf{k}_s^{[1\times1]}$ plays no role since information from its null space is never used for spectral shifting.

From Eq. (4.61), it would be expected that this stabilized S1 element would perform somewhere in between the parent S1 element and the fully integrated Reissner-Mindlin plate element. The limit differential equilibrium equation corre-

sponding to this hourglass control procedure was found to be

$$[D\nabla^4 + \frac{\epsilon l^2}{12}D_s(d_x^4 + d_y^4) + (\frac{5l^2}{12}D - \frac{\epsilon l^2}{12}(D + D_{11}) - \frac{DD_{11}}{D_s})\nabla^6$$
$$+ \frac{l^2}{12}(7D - D_{11} + \frac{\epsilon l^2}{6}(D_{11} - D) + \frac{D_{11}}{D_s}))\nabla^2 d_x^2 d_y^2]w =$$

$$[1 + (\frac{l^2}{2} - \frac{\epsilon l^2}{6} - \frac{D}{D_s} - \frac{D_{11}}{D_s})\nabla^2 + (\frac{DD_{11}}{D_s^2} - \frac{l^2}{3}(\frac{D}{D_s} + \frac{D_{11}}{D_s}) + \frac{\epsilon l^2}{12}(\frac{D}{D_s} + \frac{D_{11}}{D_s}))\nabla^4$$
$$- \frac{l^2}{6}(\frac{D}{D_s} + \frac{D_{11}}{D_s})dx^2 dy^2]q.$$

$$(4.65)$$

From examining this equation, it is apparent that transverse shear element locking is an *intrinsic* element attribute of this stabilized element for any $\epsilon > 0$ since the dominant thin plate operator for this discretization is

$$D\nabla^4 + \frac{\epsilon l^2}{12}D_s(d_x^4 + d_y^4).$$

$$(4.66)$$

The potential locking deformation patterns would be the x- and y-directional bending modes as was found to be the case for the exactly integrated element. Thus, the *best* one can do is to introduce enough locking into the element formulation to suppress the spurious element mechanism. For the limiting cases when $\epsilon = 0$ or $\epsilon = 1$, Eq. (4.65) is seen to properly degenerate to the S1 element, Eq. (4.43), or the exactly integrated element, Eq. (4.40), respectively.

§4.4.3.2 Method 2 – General Rank Update

The second method proposed in [59] reduces to that of selected spectral shifting if applied to a rectangular mesh. Their augmented element stiffness was given by

$$\mathbf{k} = \mathbf{k}_{S1} + \epsilon\frac{D_s}{12A}(l_x^2 + l_y^2)\mathbf{q}_4\mathbf{q}_4^T$$

$$(4.67)$$

where $\mathbf{q}_4 = \mathbf{h}$ is the w-hourglass mode defined by Eq. (4.60). Eq. (4.67) can

immediately be rewritten in the form of Eq. (4.57), namely,

$$\mathbf{k} = \mathbf{k}_{S1} + \phi \mathbf{v}\mathbf{v}^{\mathbf{T}} \qquad (4.68)$$

where $\mathbf{v}$ represents q_4 and

$$\phi = \epsilon \frac{D_s}{12A}(l_x^2 + l_y^2) . \qquad (4.69)$$

Comparison of Eq. (4.68) with Eq. (4.64) clearly shows the differences between the two allegedly similar hourglass control schemes of Ref. [59]. For the present case, only the spurious zero eigenvalue associated with $\mathbf{v}$ is shifted while for the first scheme, essentially all the eigenpairs of $\mathbf{k}_{S1}$ are affected. Before proceeding, however, it is important to note that this choice of $\mathbf{v}$ is not an eigenvector of an arbitrarily distorted quadrilateral and therefore should not be used blindly for other than rectangular elements.

The limit differential equilibrium equation corresponding to Eq. (4.68) is

$$[D\nabla^4 + \phi l^2 d_x^2 d_y^2 + (\frac{5l^2}{12}D - \frac{DD_{11}}{D_s})\nabla^6$$
$$+ \frac{l^2}{12}(7D - D_{11} - 12\phi(\frac{D}{D_s} + \frac{D_{11}}{D_s}))\nabla^2 d_x^2 d_y^2]w =$$

$$[1 + (\frac{l^2}{2} - \frac{D}{D_s} - \frac{D_{11}}{D_s})\nabla^2 + (\frac{DD_{11}}{D_s^2} - \frac{l^2}{3}(\frac{D}{D_s} + \frac{D_{11}}{D_s}))\nabla^4$$
$$- \frac{l^2}{6}(\frac{D}{D_s} + \frac{D_{11}}{D_s})dx^2 dy^2]q .$$

$$(4.70)$$

From the limit differential equilibrium equation point-of-view, it is also quite obvious that these two element stabilization techniques are entirely different. The most obvious difference is in the form of the parasitic differential operator responsible for transverse shear locking. Instead of locking the x- and y-directional bending modes, one now finds that only the torsional bending mode is effected with the

106

Mesh	$\frac{l}{h}$	S1 Element	Method 1		Method 2	
			$r = 1$	$r = 10$	$r = 1$	$r = 10$
2x2	500	.2385	.1780	.0546	.2324	.2164
4x4	250	.2563	.1925	.0592	.2505	.2340
8x8	125	.2608	.1962	.0604	.2550	.2385
16x16	62.5	.2619	.1971	.0665	.2561	.2397
Analytical	.2636					

Table 4.1   Displacement of center edge of a laterally loaded S-S-F-F plate for $a = 200$in., $t = .1$in., $q = 10^{-5}$psi, $E = 10^7$psi and $\nu = .3$.

appearance of the parasitic differential operator

$$\phi l^2 d_x^2 d_y^2, \qquad (4.71)$$

in the discrete thin plate operator, which in retrospect is not too surprising considering the alternating ± 1 w displacement pattern. This result leads directly to the observation that if the $\mathcal{R}(\mathbf{k})$ is changed by this shifting procedure, the potential exists of reintroducing an element pathology which the reduced integration eliminated.

One interesting additional aspect is that the loading operator, r^D, is seen to remain unchanged from that of the parent S1 element in contrast to the first technique which introduces changes there also.

§4.4.3.3   Numerical Verification

The symbolic analysis of methods 1 and 2 predicts that method 2 shifts locking from the x- and y-directional bending modes to the xy mode. In Table 4.1, the simple numerical example of a laterally loaded S-S-F-F square plate which exhibits predominatly pure cylindrical bending in the x direction is used to verify this observation.

Using the same definition as in [59] for ϵ,

$$\epsilon = r\frac{h^2}{l^2}, \qquad (4.72)$$

ϕ is found to be

$$\phi = r\frac{h^2 D_s}{6l^2} \qquad (4.73)$$

where r is used to parameterize the results. Since the present boundary conditions appear sufficient to stabilize the S1 element, results for it are also presented for the different mesh discretizations. No more than a quick perusal of the results in Table 4.1 is required to see that the first stabilization technique locks the solution while the second does not. If one considers that $\epsilon = 1$ corresponds to the exactly integrated case, an $r = 10$ only results in an $\epsilon = 2.56 \times 10^{-5}$ for the (16x16) mesh. With the effective flexural stiffness for the x-directional bending mode given by

$$\tilde{D} = (1 + r\frac{(1-\nu)}{2})D = 4.5D, \qquad (4.74)$$

one would expect a computed center edge displacement of only about 22% of the analytical value based upon the stiffness modification to the thin plate operator – Table 4.1 shows that the computed finite element solution is in fact 25% of the analytical value.

§4.4.4 Hourglass Control for the U1 Element

The next element to be considered is the uniformly reduced integrated U1 element which has been shown [33] to possess four spurious element mechanisms defined by

mode	w	θ_x	θ_y
1	h	0	0
2	0	h	0
3	0	0	h
4	0	$-y$	x

Since the fourth mode does not communicate in an assembled mesh, as is subsequently symbolically verified in §4.4.3.2, Belytschko and Tsay [60] did not correct for it. For a rectangular element, hourglass control is achieved using the augmented stiffness

$$\mathbf{k} = \mathbf{k}_{U1} + \sum_{i=1}^{3} \phi_i \mathbf{v}_i \mathbf{v}_i^T \tag{4.75}$$

where the $\mathbf{v}_i$'s correspond to the first three spurious mechanisms, or hourglass modes, given above. For an assembled element mesh, the decoupled limit differential equilibrium equation is

$$[D\nabla^4 + \phi_1 l^2 d_x^2 d_y^2 + (\frac{5l^2}{12}D - \frac{DD_{11}}{D_s})\nabla^6 - (\phi_2 dx^2 + \phi_3 dy^2)l^2 dx^2 dy^2$$
$$+ \frac{l^2}{3}(2D - 3\phi_1(\frac{D}{D_s} + \frac{D_{11}}{D_s}))\nabla^2 d_x^2 d_y^2]w =$$

$$[1 + (\frac{l^2}{2} - \frac{D}{D_s} - \frac{D_{11}}{D_s})\nabla^2 + (\frac{DD_{11}}{D_s^2} - \frac{l^2}{3}(\frac{D}{D_s} + \frac{D_{11}}{D_s}))\nabla^4$$
$$- \frac{l^2}{3D_s}(D + D_{11} - (\phi_2 + \phi_3))dx^2 dy^2]q .$$
$$\tag{4.76}$$

Examination of this equation shows that locking is only associated with stabilizing the w-hourglass mode. This interesting fact was discovered by numerical experimentation in Ref. [60] when they found that (transverse shear) element locking could be reintroduced into the stabilized U1 element by what they termed as "overstabilizing the w-hourglass mode." Essentially, one again finds one's self in a Catch-22 situation: If ϕ_1 is too small, the spurious w-hourglass mode returns, while if ϕ_1 is too large, locking reappears. As they verified numerically, overstabilizing the θ-hourglass modes does not result in any form of element locking since neither mode has any components associated with ∇^4. The appropriate choice of values for ϕ_2 and ϕ_3 can therefore be made based solely upon accuracy considerations.

§4.5 Discrete Fourier Element Evaluation

The basic procedures used for performing a symbolic Fourier analysis of a finite element discretation were presented in Chapter 3. It was shown there that the finite element approximations of various terms in the governing differential equations can be transformed into simple Fourier operators whose effect on element behavior could then easily be identified. From them, the effects of different component-wise finite element approximations on intrinsic element behavior could be assessed a priori without resorting to time consuming numerical experiments. In particular, problems such as transverse shear locking, spurious mechanisms and ultimately, point-wise interior accuracy could be addressed. In this section, these techniques will be applied to the analysis of the exactly, selectively-reduced, and uniformly-reduced integrated 4-node Reissner-Mindlin plate elements.

§4.5.1 Component-Wise Analysis – Directional Participation Operators

The important question concerning how different differential operators are approximated within the Fourier domain is addressed in this section. Before looking at the different plate discretizations in their entirety, as was done for the Taylor series technique, the effect of the different spatial integration rules on individual differential operator components wil! first be examined in detail. This is an important step in pinpointing the cause of element deficiencies and at the same time prepares us for the eventual task of element synthesis[17].

As a precusor to looking at the two-dimensional finite element approximation of a differential operator at an interior node, its finite difference counterpart provides an important point-of-reference. The second-order accurate central-difference approximation of the differential operator $\frac{\partial^2}{\partial x^2}$ is given by the following

110

stencil,

$$\frac{\partial^2}{\partial x^2}\Big|_{fd} = \frac{1}{l_x^2} |1 \quad -2 \quad 1| \tag{4.77}$$

where the differencing has been performed directly on $\frac{\partial^2}{\partial x^2}$, or from the finite element viewpoint, the strong form of the operator. Discrete Fourier transforming the above expression using $e^{ik_x x}$ results in

$$\mathcal{F}\{\frac{\partial^2}{\partial x^2}\Big|_{fd}\} = \frac{1}{l_x^2}(e^{-ik_x l_x} - 2 + e^{ik_x l_x}) = -\bar{k}_x^2 \tag{4.78}$$

where $\bar{k}_x$ is the discrete wave number in the x-direction defined as

$$\bar{k}_x = \frac{\sin(\frac{k_x l_x}{2})}{\frac{l_x}{2}}. \tag{4.79}$$

The finite element discretization of $\frac{\partial^2}{\partial x^2}$ at an interior point in the problem domain is obtained from the corresponding weak form,

$$-\frac{1}{A} \int_A (\frac{\partial}{\partial x})^2 dA. \tag{4.80}$$

For the element mesh shown in Fig. 4.1, the finite element representation of $\frac{\partial^2}{\partial x^2}$ at the interior node is determined from the assembled equations where the contribution from a single element stiffness is given by

$$\int_A \frac{\partial \mathbf{N}}{\partial x} \frac{\partial \mathbf{N}^T}{\partial x} dA \tag{4.81}$$

where $\mathbf{N}$ are the bilinear element shape functions. Employing exact (2×2) spatial integration to evaluate $\mathbf{k}$, the following finite element "stencil,"

$$\frac{\partial^2}{\partial x^2}\Big|_{(2\times2)} = \frac{1}{6l_x^2} \begin{vmatrix} 1 & -2 & 1 \\ 4 & -8 & 4 \\ 1 & -2 & 1 \end{vmatrix} \tag{4.82}$$

111

is obtained for the interior node where each entry represents the nodal value corresponding to stencil position. The expected central-difference approximation embodied in the finite element equations resulting from using the bilinear element shape functions is apparent by summing the columns of Eq. (4.82). The discrete Fourier-transformed operator for this stencil is found to be

$$\mathcal{F}\{\frac{\partial^2}{\partial x^2}\big|_{2\times 2}\} = -1_y^e \bar{k}_x^2 \tag{4.83}$$

where $e^{i(k_x x + k_y y)}$ is used in the now two-dimensional transformation process. The unity operator, 1_y^e, which is engendered by the finite element discretization, is given by

$$1_y^e = 1 - \frac{l_y^2}{6} \bar{k}_y^2 \tag{4.84}$$

with $\bar{k}_y$ being the discrete wave number in the y-direction, obtained by substituting y and l_y for x and l_x in Eq. (4.79). The superscript e denotes exact (2×2) spatial integration. If the reduced (1×1) spatial integration rule is used instead of the (2×2) rule to integrate Eq. (4.81), one obtains

$$\frac{\partial^2}{\partial x^2}\big|_{(1\times 1)} = \frac{1}{4l_x^2} \begin{vmatrix} 1 & -2 & 1 \\ 2 & -4 & 2 \\ 1 & -2 & 1 \end{vmatrix} \tag{4.85}$$

with its resulting discrete Fourier-transformed operator

$$\mathcal{F}\{\frac{\partial^2}{\partial x^2}\big|_{(1\times 1)}\} = -1_y^r \bar{k}_x^2 . \tag{4.86}$$

As one might expect, a different unity operator,

$$1_y^r = 1 - \frac{l_y^2}{4} \bar{k}_y^2 \tag{4.87}$$

now appears, with the superscript r used to denote the use of reduced integration.

112

Comparing the finite difference results with those of the finite element, one explicitly sees that the interaction between adjacent nodes in the finite element equations results in the appearance of an additional operator term. At a first glance, it would seem to play only the role of a unity operator such as first encountered for the one-dimensional problems. Closer inspection, however, shows that this unity operator is also responsible for the interaction between adjacent element nodes. Because of this inherent participation from adjacent nodes, Fourier-transformed operators will appear as multiplicative combinations of the transformed fundamental operator with other *participation* operators. For the bilinear finite element representation of the differential operator $\frac{\partial^2}{\partial x^2}$, 1_y plays both the role of unity operator and of what will be called a *directional participation operator*. It embodies the degree to which cross coupling occurs between adjacent nodes in the direction orthogonal to that in which the derivative is being calculated.

Making use of results such as this, one can easily construct any of the different differential operators needed to characterize a particular finite element discretization. If, for example, the Laplacian was of interest as will be the case when considering the transverse shear term, or $\hat{L}_{ww}$ term, from the Reissner-Mindlin plate equilibrium equations, one would also need the results for $\frac{\partial^2}{\partial y^2}$ which are identical to those just discussed for $\frac{\partial^2}{\partial x^2}$, with x and y appropriately interchanged. The Fourier transformed Laplacians for the different discrete methods are shown in Table 4.2. As was described above, the only difference between the Fourier transformed operators resulting from the finite difference and the finite element approximations is in the presence of a directional participation operator in the finite element discretization.

§4.5.2 Directional Participation Operators and Spurious Mechanisms

In §3.1.2, Fig. 3.1 illustrated the saw-tooth oscillation which represents the most rapid spatial variation which linear shape functions could possibly resolve without aliasing. The corresponding Fourier wave number, k_{max}, or the *maximum*

Table 4.2 –Discrete approximation of $\hat{\nabla}^2$

Type of Discretization	$\hat{\nabla}^2 = -(k_x^2 + k_y^2)$
Central-Difference F.D.	$-(\bar{k}_x^2 + \bar{k}_y^2)$
(1x1) F.E.	$-(1_y^r \bar{k}_x^2 + 1_x^r \bar{k}_y^2)$
(2x2) F.E.	$-(1_y^e \bar{k}_x^2 + 1_x^e \bar{k}_y^2)$

admissible wave number corresponding to this saw-tooth displacement pattern is

$$k_{max} = \frac{\pi}{l}.$$
(4.88)

For the present two-dimensional problem where bilinear shape functions are used, the maximum admissible wave number in each coordinate direction is

$$k_{x_{max}} = \frac{\pi}{l_x}$$

$$k_{y_{max}} = \frac{\pi}{l_y}.$$
(4.89)

Wave numbers beyond these maximum admissible wave numbers can not be represented by a piecewise linear displacement interpolation approximation.

To examine how the directional participation operators affect $\hat{\nabla}^2$, their behavior is shown in Fig. 4.3 for the admissible nondimensional wave number range

$$0 \leq k_{(x,y)}(l_x, l_y) \leq \pi.$$
(4.90)

The key observation is that the directional participation operator for the (1x1) integrated case, $1_{(x,y)}^r$, becomes zero at the maximum admissible wave number of $k_x l_x = k_y l_y = \pi$. Since $\bar{k}_{(x,y)} > 0$ for $0 \leq k_{(x,y)}(l_x, l_y) \leq \pi$, the state at which the discrete approximations of $\hat{\nabla}^2$, denoted here by $\hat{\nabla}^2$, become zero is dictated solely by the directional participation operators. The important consequence of

114
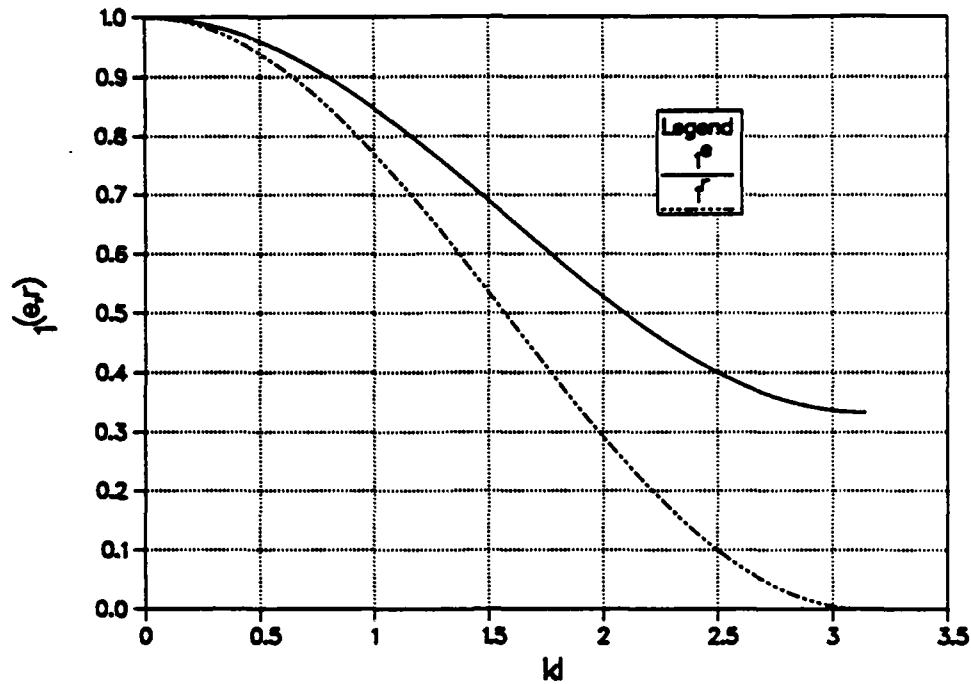
Fig. 4.3 – Behavior of *directional participation operator* as a function of nondi-
mensional wave number

$1^r_{(x,y)} = 0$ at $k_x l_x = k_y l_y = \pi$ is therefore the admission of a non-physical
rigid body motion (i.e., spurious mechanism) resulting from the (1x1) integrated
approximation of ∇^2.

§4.5.3 Symbolic Evaluation of Bilinear Reissner-Mindlin Plate Elements

In this section, a discrete Fourier analysis of both the exactly integrated and
selectively/reduced integrated (or S1) plate bending elements is performed for a
rectangular $(l_x \times l_y)$ element domain for the case of static loading only. These
two elements succinctly embody both pathologies usually associated with 4-node
Reissner-Mindlin plate elements; namely, transverse shear locking in the exactly
integrated element and spurious element mechanisms for the selectively/reduced
integrated S1 element. The approach taken here in deriving the discrete counter-
part to Eqs. (4.9) and (4.20) is different to that employed earlier for the Taylor

115

series results. Each differential component will be constructed in a component-wise manner which could potentially serve as the starting point for synthesizing a general plate bending element (see e.g., [17]).

Inspection of Eq. (4.9) shows that in order to construct the discrete Fourier-transformed material plate operator, $\hat{L}_m^D$, a total of six operator components corresponding to

$$1, \quad \frac{\partial}{\partial x}, \quad \frac{\partial}{\partial y}, \quad \frac{\partial^2}{\partial x^2}, \quad \frac{\partial^2}{\partial x \partial y}, \quad \frac{\partial^2}{\partial y^2} \tag{4.91}$$

need to be obtained for the different spatial integration rules.

When dealing with the off-diagonal terms, $\frac{\partial}{\partial x}$ and $\frac{\partial}{\partial y}$, special care needs to be exercised in order to obtain the correct algebraic sign. Depending upon which Euler equation one considers at the interior node, $\frac{\partial}{\partial x}$ may, for example, result from either

$$\frac{1}{A} \int_A \mathbf{N} \frac{\partial \mathbf{N}^T}{\partial x} dA \quad \Rightarrow \quad \frac{\partial}{\partial x} \tag{4.92}$$

or

$$\frac{1}{A} \int_A \frac{\partial \mathbf{N}}{\partial x} \mathbf{N}^T dA \quad \Rightarrow \quad -\frac{\partial}{\partial x}. \tag{4.93}$$

The finite element stencil and resulting Fourier transformed operator corresponding to Eq. (4.92) is

$$\frac{\partial}{\partial x}\bigg|_{(2\times2)} = \frac{1}{12 l_x^2} \begin{vmatrix} -1 & 0 & 1 \\ -4 & 0 & 4 \\ -1 & 0 & 1 \end{vmatrix} \quad \Rightarrow \quad \mathcal{F}\{\frac{\partial}{\partial x}\big|_{2\times2}\} = i 1_y^e \sqrt{\chi_x} \bar{k}_x \tag{4.94}$$

for exact spatial integration and

$$\frac{\partial}{\partial x}\bigg|_{(1\times1)} = \frac{1}{8 l_x^2} \begin{vmatrix} -1 & 0 & 1 \\ -2 & 0 & 2 \\ -1 & 0 & 1 \end{vmatrix} \quad \Rightarrow \quad \mathcal{F}\{\frac{\partial}{\partial x}\big|_{1\times1}\} = i 1_y^r \sqrt{\chi_x} \bar{k}_x \tag{4.95}$$

for reduced integration where $\chi_x = 1 - \frac{l_x^2}{4} \bar{k}_x^2$ is the same irrespective of the integration rule used.

116

For the case of the mixed derivative,

$$\frac{1}{A}\int_A \frac{\partial \mathbf{N}}{\partial x}\frac{\partial \mathbf{N}^T}{\partial y}dA \quad \Rightarrow \quad \frac{\partial^2}{\partial x \partial y}, \qquad (4.96)$$

the finite element stencil and resulting Fourier transformed operator,

$$\frac{\partial^2}{\partial x \partial y}\Big|_{(2\times2)} = \frac{1}{4l_x l_y}\begin{vmatrix} 1 & 0 & -1 \\ 0 & 0 & 0 \\ -1 & 0 & 1 \end{vmatrix} \quad \Rightarrow \quad \mathcal{F}\{\frac{\partial^2}{\partial x \partial y}\} = \sqrt{\chi_x}\sqrt{\chi_y}\bar{k}_x\bar{k}_y \quad (4.97)$$

are found to be identical for either integration rule.

Lastly, the finite element approximation of unity is determined from

$$\frac{1}{A}\int_A \mathbf{N}^T \mathbf{N} dA \quad \Rightarrow \quad 1 \qquad (4.98)$$

to be for the case of (2×2) integration

$$1\Big|_{(2\times2)} = \frac{1}{36}\begin{vmatrix} 1 & 4 & 1 \\ 4 & 16 & 4 \\ 1 & 4 & 1 \end{vmatrix} \quad \Rightarrow \quad \mathcal{F}\{1\big|_{(2\times2)}\} = 1_x^e 1_y^e \qquad (4.99)$$

and for (1×1) case,

$$1\Big|_{(1\times1)} = \frac{1}{20}\begin{vmatrix} 1 & 2 & 1 \\ 2 & 8 & 2 \\ 1 & 2 & 1 \end{vmatrix} \quad \Rightarrow \quad \mathcal{F}\{1\big|_{(1\times1)}\} = 1_x^r 1_y^r . \qquad (4.100)$$

The discrete Fourier transform of these two unity operators is seen to be just the product of the two directional participation operators.

With the discrete Fourier transformation for each differential component now

117

in hand, one can construct the following general discrete counterpart to Eq. (4.20),

$$
\hat{L}_m^D(\bar{k}_x, \bar{k}_y) = \begin{bmatrix} -D1_y\bar{k}_x^2 - D_{11}1_x\bar{k}_y^2 & -D_{12}\sqrt{\chi x}\sqrt{\chi y}\bar{k}_x\bar{k}_y & iD_s\sqrt{\chi x}1_y\bar{k}_x \\ -D_s1_x1_y & & \\ & -D1_x\bar{k}_y^2 - D_{11}1_y\bar{k}_x^2 & iD_s\sqrt{\chi y}1_x\bar{k}_y \\ & -D_s1_x1_y & \\ sym. & & -D_s\tilde{\nabla}^2 \end{bmatrix}
$$

$$(4.101)$$

where the direction participation operators, 1_x and 1_y, in the different terms above will assume the appropriate form depending upon which spatial integration rule is employed for each term. Examination of Eq. (4.101) reveals the interesting fact that the entire effect of spatial integration is embodied solely in the *directional participation operators*. If (1x1) spatial integration is employed for the different terms used to construct Eq. (4.101), then the directional participation operators will become $1_{(x,y)}^r$, while for the case where (2x2) integration is used, they will be $1_{(x,y)}^e$. For selective/reduced spatial integration, terms associated with D_s will be $1_{(x,y)}^r$ while the remaining bending terms will use $1_{(x,y)}^e$.

The decoupled Fourier-transformed equation for $\hat{w}$ derived from Eq. (4.101) is

$$
\hat{l}^D \cdot \hat{w} = \hat{r}^D \cdot \hat{q} \tag{4.102}
$$

where the characteristic operator, $\hat{l}^D$, is

$$
\begin{aligned}
\hat{l}^D &= (1_x1_y - \frac{D_{11}}{D_s}\tilde{\nabla}^2)D\tilde{\nabla}^4 + D_s[1_x1_y^2(1_x - \chi_x)\tilde{k}_x^2 + 1_x^21_y(1_y - \chi_y)\tilde{k}_y^2] \\
&\quad + D_{11}[1_y(1_x - \chi_x)\tilde{k}_x^4 + 2(1_x1_y - \chi_x\chi_y)\tilde{k}_x^2\tilde{k}_y^2 + 1_x(1_y - \chi_y)\tilde{k}_y^4] \\
&\quad + D(2\chi_x\chi_y - \chi_x1_y - 1_x\chi_y)\tilde{k}_x^2\tilde{k}_y^2 \\
&\quad + \frac{(D - D_{11})^2}{D_s}[2(\chi_x\chi_y1_y - 1_x1_y^2)\bar{k}_x^4\bar{k}_y^2 + 2(1_x\chi_x\chi_y - 1_x^21_y)\bar{k}_x^2\bar{k}_y^4]
\end{aligned}
$$

$$(4.103)$$

with $\tilde{\nabla}^2 = -(\bar{k}_x^2 + \bar{k}_y^2)$, and $\tilde{k}_x^2 = 1_y\bar{k}_x^2$ and $\tilde{k}_y^2 = 1_x\bar{k}_y^2$. The characteristic loading

118

operator, $\hat{r}^D$, is found to be

$$\hat{r}^D = (1_x 1_y - \frac{D_{11}}{D_s}\tilde{\nabla}^2)(1_x 1_y - \frac{D}{D_s}\tilde{\nabla}^2) + \frac{(D-D_{11})^2}{D_s^2}(\bar{k}_x^2 \bar{k}_y^2 - \chi_x \chi_y \bar{k}_x^2 \bar{k}_y^2). \quad (4.104)$$

§4.5.3.1 Transverse Shear Element Locking

Locking in the four-noded Reissner-Mindlin plate element occurs if the parasitic differential term,

$$l_{lock} = D_s[1_x 1_y^2 (1_x - \chi_x)\tilde{k}_x^2 + 1_x^2 1_y (1_y - \chi_y)\tilde{k}_y^2] \quad (4.105)$$

in Eq. (4.103) does not vanish. Hence, the *locking-free condition* is simply

$$l_{lock} = 0. \quad (4.106)$$

If (1x1) spatial integration is employed for the element stiffness, the locking-free condition is automatically satisfied since the $1_{(x,y)}$ in Eq. (4.105) become $1_{(x,y)}^r = \chi_{(x,y)}$ with the result that the terms in the parentheses vanish so that $l_{lock} = 0$.

On the other hand, if (2x2) integration is instead performed, one finds that

$$1_{(x,y)}^e - \chi_{(x,y)} = \frac{l_{(x,y)}^2}{12}\bar{k}_{(x,y)}^2. \quad (4.107)$$

Substitution of Eq. (4.107) into Eq. (4.105) provides the measure of the amount by which the locking-free condition is violated, *viz.*,

$$l_{lock} = D_s 1_x 1_y (\frac{l_x^2}{12}\tilde{k}_x^4 + \frac{l_y^2}{12}\tilde{k}_y^4). \quad (4.108)$$

Since practical considerations on element size generally requires $l_x, l_y \gg h$, the

magnitude of the coefficient in the above equation is seen to be

$$D_s \frac{l^2_{(x,y)}}{12} \gg D \quad \Rightarrow \quad \frac{\kappa(1-\nu)}{2}\left(\frac{l_{(x,y)}}{h}\right)^2 \gg 1. \qquad (4.109)$$

The dominant 4th-order part of the spatial operator, $\hat{l}^{\mathrm{D}}$, which represents the limiting thin plate behavior, is therefore modified by the amount of the locking-free violation resulting in

$$\hat{l}^{\mathrm{D}} \simeq \mathbf{1}_x \mathbf{1}_y \left[\left(1 + \frac{l^2_x D_s}{12D}\right)\tilde{k}^4_x + 2\tilde{k}^2_x \tilde{k}^2_y + \left(1 + \frac{l^2_y D_s}{12D}\right)\tilde{k}^4_y \right] \qquad (4.110)$$

Except for the rectangular element geometry, this term is identical to its counterpart in Eq. (4.41) derived using Taylor series techniques.

§4.5.3.2 Spurious Mechanisms in the U1 Element

As described in §3.3, an element will exhibit spurious mechanisms if there are non-physical rigid body motions engendered by the finite element discretization. In the context of the present symbolic element evaluation analysis, this condition corresponds to the existence of non-zero *admissible* wave numbers which satisfy the homogeneous characteristic equation. For the uniformly-reduced integrated U1 element, the homogeneous characteristic operator is given by

$$\hat{l}^{\mathrm{D}} = \left(\mathbf{1}^r_x \mathbf{1}^r_y - \frac{D_{11}}{D_s}\tilde{\nabla}^2_r\right)D\tilde{\nabla}^4_r = 0. \qquad (4.111)$$

Potential zeros for the admissible wave number range $0 \le k_{(x,y)} \le \frac{\pi}{(l_x, l_y)}$ are in turn determined from the zeros of its multiplicative components

$$\mathbf{1}^r_x \mathbf{1}^r_y - \frac{D_{11}}{D_s}\tilde{\nabla}^2_r = 0 \qquad (4.112)$$

and

$$\tilde{\nabla}^4_r = 0. \qquad (4.113)$$

120

From them, the following admissible solutions are found,

$$\bar{k}_x = \bar{k}_y = 0 \quad \Rightarrow \quad k_x = k_y = 0 \tag{4.114}$$

and

$$1_x^r = 1_y^r = 0 \quad \Rightarrow \quad k_{(x,y)} = \frac{\pi}{(l_x, l_y)}. \tag{4.115}$$

Clearly, Eq. (4.114) represents the correct rigid body motion while Eq. (4.115) corresponds to non-physical rigid body motions, i.e., spurious mechanisms. Similarly, there are two additional spurious mechanisms corresponding to the θ_x and θ_y degrees of freedom. The U1 element would therefore possess a total of three *communicable* spurious mechanisms.

REMARK 4.1

Unlike the U1 element, the S1 element employs exact (2x2) integration on the bending stiffness. As a result, it only exhibits a single communicable spurious mechanism resulting from the reduced (1x1) integration of the transverse shear stiffness. The homogeneous Fourier-transformed characteristic operator for the S1 element is

$$\hat{l}^D = (1_x^r 1_y^r - \frac{D_{11}}{D_s}\tilde{\nabla}_e^2)D\tilde{\nabla}_e^2\tilde{\nabla}_r^2 +$$

$$(D - D_{11})(21_x^r 1_y^r - 1_x^e 1_y^r - 1_x^r 1_y^e)\tilde{k}_{xr}^2\tilde{k}_{yr}^2 - \frac{(D - D_{11})^2}{D_s}(\tilde{k}_{xe}^2\tilde{k}_{ye}^2 - \tilde{k}_{xr}^2\tilde{k}_{yr}^2) \tag{4.116}$$

REMARK 4.2

The present analysis technique manifests only those spurious mechanisms which propagate across element boundaries since the analysis is performed on the assembled difference equations for an interior node. The question of whether a mechanism will communicate is therefore automatically resolved as a by-product of the present analysis. In addition, as the analysis requires no knowledge of boundary conditions, the results manifest intrinsic element behavior. In other words, suppression of spurious mechanisms by certain boundary conditions or by spurious mechanism control techniques can be viewed as a case-by-case fix rather than eradicating inherent spurious mechanisms.

§4.5.4 A priori Prediction of Interior Solution Accuracy

In §3.4, the subject of spectral error estimation was addressed for the Timoshenko beam. Those results will now be employed to provide an a priori prediction of interior accuracy for the transverse loading and bifurcation buckling of the U1 and S1 discretizations of the Reissner-Mindlin plate.

The first step in the error analysis for the transversely loaded discrete plate entails determining the nodal load at an interior node corresponding to the Fourier component

$$q(x, y) = \hat{q}\, e^{i(k_x x + k_y y)} \tag{4.117}$$

which is determined from

$$
\begin{aligned}
q_j = \int_0^{l_y} \int_0^{l_x} \Big[&\frac{\xi}{l_x}\frac{\eta}{l_y}\, e^{i[k_x(x_j - l_x + \xi) + k_y(y_j - l_y + \eta)]} \\
&+ (1 - \frac{\xi}{l_x})\frac{\eta}{l_y}\, e^{i[k_x(x_j + \xi) + k_y(y_j - l_y + \eta)]} \\
&+ (1 - \frac{\xi}{l_x})(1 - \frac{\eta}{l_y})\, e^{i[k_x(x_j + \xi) + k_y(y_j + \eta)]} \\
&+ \frac{\xi}{l_x}(1 - \frac{\eta}{l_y})\, e^{i[k_x(x_j - l_x + \xi) + k_y(y_j + \eta)]} \Big] d\xi d\eta
\end{aligned}
\tag{4.118}
$$

to be

$$q_j = \Big(\frac{\bar{k}_x \bar{k}_y}{k_x k_y}\Big)^2 \hat{q}\, l_x l_y\, e^{i(k_x x_j + k_y y_j)} \tag{4.119}$$

employing exact analytic integration. The resulting discrete Fourier transformed distributed load is then simply

$$\hat{q}^D = \Big(\frac{\bar{k}_x \bar{k}_y}{k_x k_y}\Big)^2 \hat{q}\,. \tag{4.120}$$

Alternatively, if one commits the variational crime of employing reduced (1x1) spatial integration to calculate nodal loads, $\hat{q}^D$ would have instead been found to

be

$$\hat{q}^{D} = 1_{z}^{r} 1_{y}^{r} \hat{q}. \tag{4.121}$$

Now, from Eqs. (4.16) and (4.17) for the continuum equations, and Eqs. (4.103) and (4.104) for the discrete ones, the decoupled transformed w equations are given by

$$\hat{w} = \frac{\hat{r}\hat{q}}{\hat{l}} \tag{4.122}$$

and

$$\hat{w}^{D} = \frac{\hat{r}^{D}\hat{q}^{D}}{\hat{l}^{D}} \tag{4.123}$$

so that the relative spectral displacement error is

$$\hat{\epsilon}(k_{x}, k_{y}) = \frac{\hat{w} - \hat{w}^{D}}{\hat{w}} \tag{4.124}$$

where it is the *directional participation operators* which solely determine the form of $\hat{l}^{D}$ and $\hat{r}^{D}$ in these equations.

In Figs. 4.4 and 4.5, the relative error in $\hat{w}$ is plotted for both the case where $k_{x} = k_{y}$ and $k_{x} \neq k_{y}$ for a patch of square S1 and U1 elements with $E = 10^{7}$, $\nu = .3$, $l = 100$ and $h = 1$. In Fig. 4.4, one finds the surprising result that when exact integration is used to evaluate nodal loads for the U1 element, $\hat{w}^{D}$ is seen to be essentially exact $\forall\, k$. When (1x1) spatial integration is instead used for element loads, both elements perform much worse than when exact analytic integration is used. Since there are no geometric modeling errors, all error curves in Fig. 4.4 will exhibit the same limiting behavior of $\hat{\epsilon} \rightarrow 0$ as $k \rightarrow 0$ confirming the consistency of the different discretization schemes investigated for both continuum and loading operators. The effect of cross-coupling intrinsically engendered by the finite element formulation is dramatically portrayed in Fig. 4.5 where $\hat{\epsilon}$ is plotted as a function of k_{x} for two different fixed values of k_{y}, namely, $.3k_{\max}$ and $.6k_{\max}$ with $k_{\max} = \frac{\pi}{l}$. As was discussed earlier in §4.4.1, each differential operator
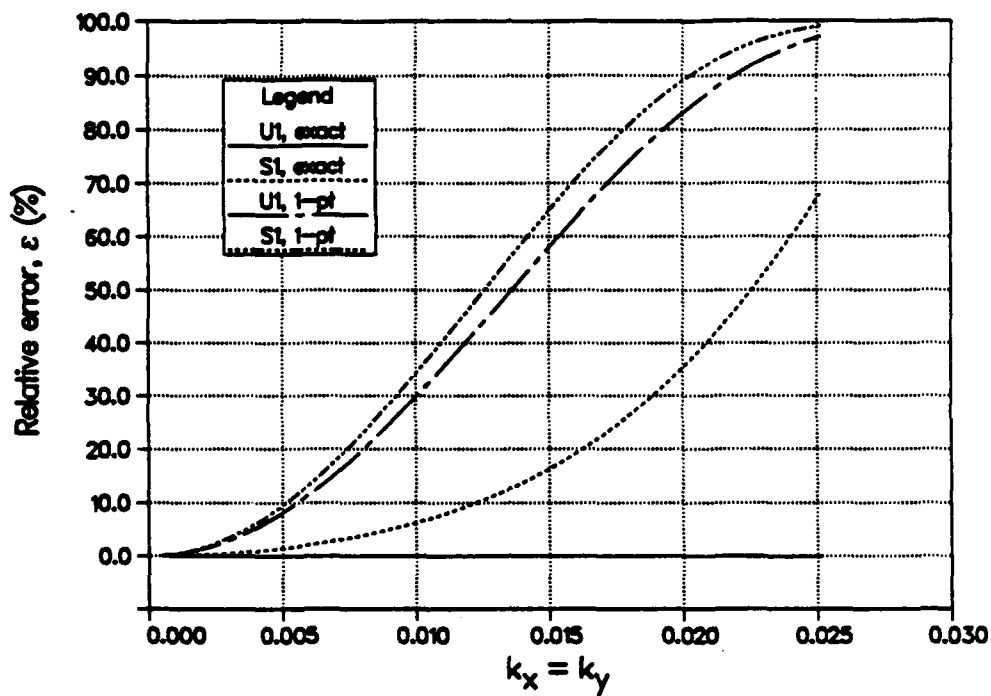
Fig. 4.4 – Relative error in $\hat{w}$ as a function of $\{k = k_x = k_y : 0 \le k \le .8 k_{max}\}$ for exactly and (1x1) integrated element loads.
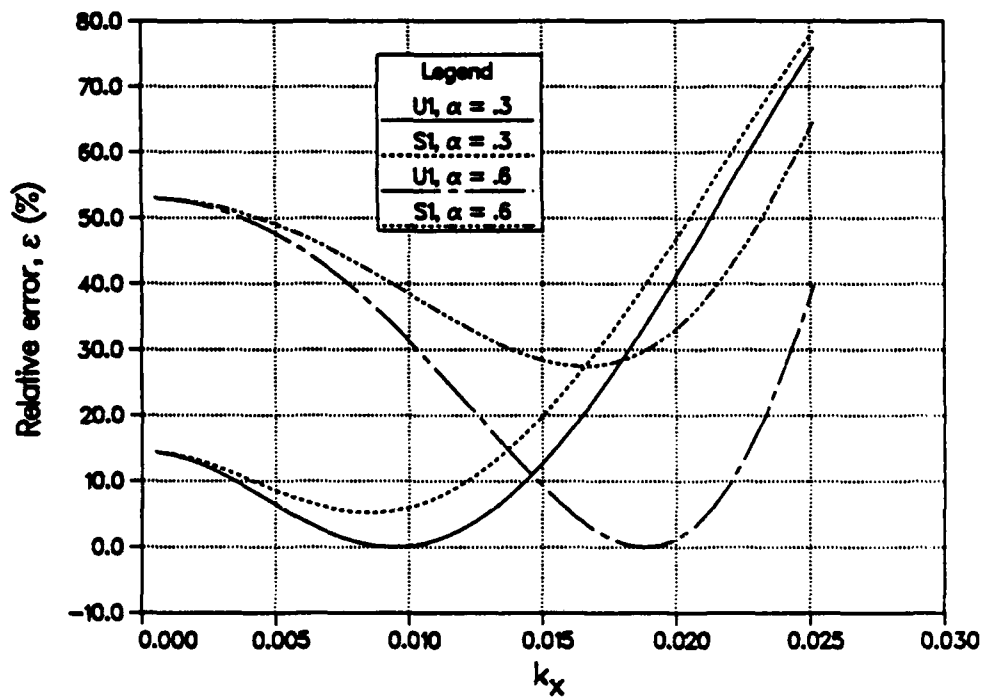
Fig. 4.5 – Relative error in $\hat{w}$ as a function of $\{k_x : 0 \le k_x \le .8 k_{x_{max}}\}$ with respect to a fixed $\{k_y : k_y = \alpha k_{y_{max}}\}$

124

in Eq. (4.101) has associated with it a *directional participation operator* which intrinsically couples differential information in one direction with each orthogonal direction. The minimum spectral error in $\hat{w}$ for the U1 element occurs at $k_x = k_y$ while for the S1 element, the minimum is shifted slightly to the left of where $k_x = k_y$. The determination of the displacement error in the physical domain would proceed as outlined in §3.4.3.

§4.5.5 Buckling of Bilinear Reissner-Mindlin Plate Elements

The symbolic analysis of the bifurcation buckling of bilinear Reissner-Mindlin plate elements proceeds in the same component-wise manner as was described earlier for the material operator. Using those results, $\hat{L}_\sigma^D$ can immediately be written as

$$\hat{L}_\sigma^D = -(\sigma_x 1_y \bar{k}_x^2 + \sigma_y 1_x \bar{k}_y^2 + 2\tau_{xy}\sqrt{\chi_x}\sqrt{\chi_y}\bar{k}_x\bar{k}_y) \begin{bmatrix} I & 0 & 0 \\ 0 & I & 0 \\ 0 & 0 & -h \end{bmatrix} \qquad (4.125)$$

where the *directional participation operators* are again determined by choice of spatial integration rule. In the next section, results for both (2x2) and (1x1) integration rules will be investigated. With $\hat{L}_m^D$ defined by Eq. (4.101), the decoupled w equation governing the bifurcation buckling of the discrete model is determined from

$$\det(\hat{L}_m^D + \hat{L}_\sigma^D)\,\hat{w} = 0 \qquad (4.126)$$

where the flexural buckling load is the smallest root corresponding to a prescribed k_x and k_y.

Based upon the discrete results represented by Eq. (4.126), a relative error estimate of the predicted bifurcation buckling load of the different possible element discretizations may be obtained by comparison with the continuum solution, Eq. (4.32). The stress field for the Reissner-Mindlin plate is comprised of three components, σ_x, σ_y and τ_{xy}. The calculated critical buckling loads presuppose proportional loading so that in reality, one is solving for the load multiplier of the

125

initial stress state,

$$\left\{ \begin{array}{c} \sigma_x \\ \sigma_y \\ \tau_{xy} \end{array} \right\}_{cr} = \alpha \left\{ \begin{array}{c} \sigma_x \\ \sigma_y \\ \tau_{xy} \end{array} \right\}_{initial} \qquad (4.127)$$

where α represents the load multiplier at which point instability occurs. The relative error in buckling load for a given k_x and k_y and initial stress field is therefore defined in terms of α by

$$\epsilon = \frac{\alpha - \alpha^D}{\alpha} \qquad (4.128)$$

The example problem to be considered is that of uniaxial σ_x compression with $k_x = k_y$ for a patch of square S1 and U1 elements where $E = 10^7$, $\nu = .3$, $l = 100$ and $h = 1$. Fig. 4.6 shows the results for both (2x2) and (1x1) integrated geometric stiffnesses where the fully integrated $\mathbf{k}_g$ is seen to be superior to the (1x1) integration for both elements. Neither the U1 nor the S1 elements are variationally consistent. Nevertheless, the buckling loads are seen to uniformly converge from above for this problem. Also shown in Fig. 4.6 are the results of finite element analyses portrayed by the plotted symbols for four different wave numbers corresponding to (5x5), (4x4), (3x3) and (2x2) mesh discretizations of a quarter-model of a simply-supported (SS2[5]) Reissner-Mindlin plate for each of the discrete models. With the constant element length, l, the wavenumber for each $(n_{el} \times n_{el})$ mesh is given by $k = \pi/2ln_{el}$. The predicted error in the finite element analysis results are essentially identical to the predicted errors in bifurcation buckling load obtained from the discrete Fourier analysis results.

For the same element geometry, Fig. 4.7 shows how the relative error in buckling load changes for fixed values of k_y with k_x allowed to vary continuously.

§4.6 Summary

Both Taylor series and discrete Fourier analysis techniques were employed

---

[5] see Hughes [67]
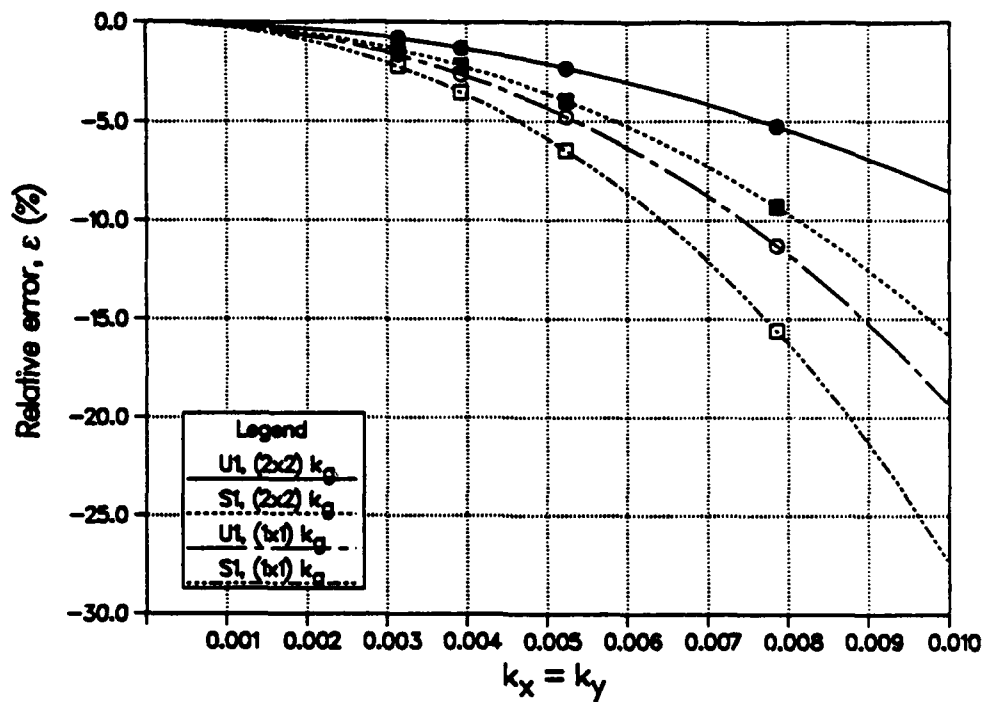
Fig. 4.6 – Relative error in $\sigma_{x_{cr}}$ as a function of $\{k = k_x = k_y : 0 \le k \le .36k_{max}\}$ for (2x2) and (1x1) integrated k_σ.
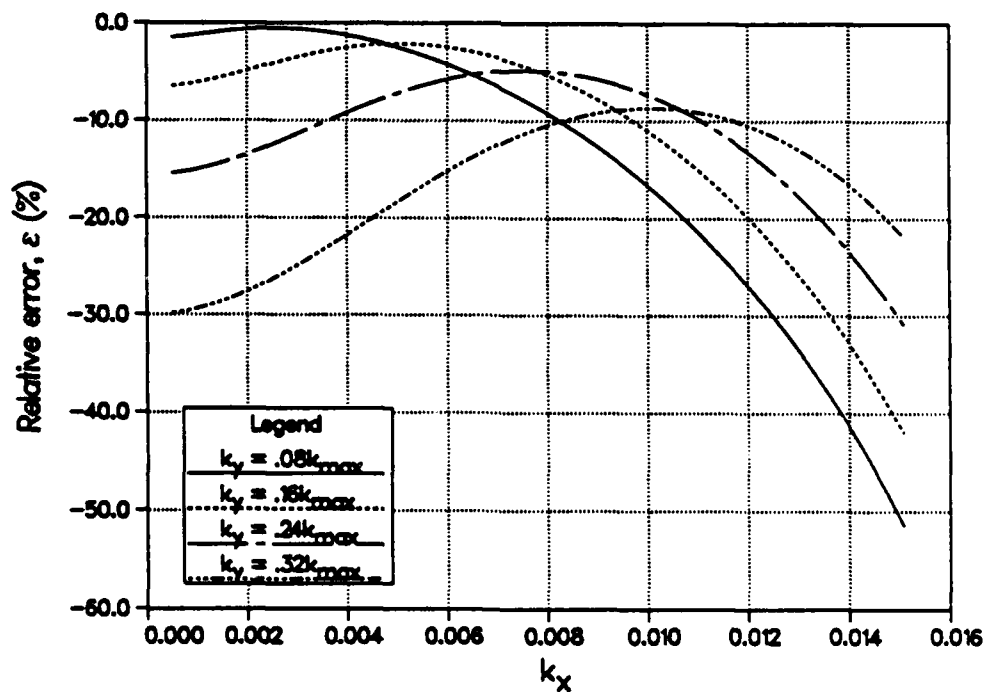
Fig. 4.7 – Relative error in $\sigma_{x_{cr}}$ as a function of $\{k_x : 0 \le k_x \le .48k_{x_{max}}\}$ with respect to a fixed $\{k_y : k_y = .08, .16, .24, .32k_{y_{max}}\}$

in this chapter for the symbolic evaluation of the bilinear Reissner-Mindlin plate element.

The first aspect considered was the effect of different spatial integration rules on element behavior. The cause of transverse shear locking in the exactly integrated element was explicitly identified as resulting from parasitic differential operators associated with the x- and y-directional bending modes. The use of alternative selectively/reduced rules was shown to result in locking-free discretizations. Next, the effect of using different hourglass control techniques to stabilize the S1 and U1 elements was addressed. The exact effect on the governing limit differential equilibrium equations of using these techniques was then determined. It was found that w-hourglass control reintroduced element locking in all cases. In addition, it was found that it was possible to switch the locking mode from the x- and y-directional bending modes to the xy-twist mode depending upon control scheme.

Employing the discrete Fourier technique, the individual differential operators comprising the transformed limit differential equilibrium equations were next determined. Unlike typical transformed finite difference stencils, transformed finite element "difference" stencils were found to be characterized by the presence of *directional participation operators*. These directional participation operators were found to couple the effect of adjacent nodal d-o-f in the orthogonal direction to that in which the differencing is taking place. Perhaps more importantly, however, these operators are found to be responsible for the spurious element mechanisms engendered by selective/reduced spatial integration. Using these results, a priori interior error estimates were determined for the case of distributed transverse pressure loading.

Lastly, the discrete respresentation of Reissner-Mindlin plate buckling was determined for the S1 and U1 elements employing (2x2) and (1x1) spatial integration rules on the geometric stiffness. A priori error estimates of the predicted bifurcation buckling loads for simply supported boundary conditions showed the

128

surprising result that the U1 element with (2x2) integration on the geometric stiffness performed by far the best. This was verified numerically to be the case. It was also shown that if the eigenfunctions of the continuum problem are harmonic, the discrete Fourier element evaluation technique exactly captures the behavior of the discrete model resulting in exact error predictions.

Symbolic Analysis of the Circular Arch and Cylindrical Shell

The analysis of a curved structure by the finite element method engenders both kinematic and physical modeling errors. The former stems from the usual polynomial approximations of the curved geometries whereas the latter are due to the discrete representations of the different field quantities. In this chapter, discrete Fourier analysis techniques are used to examine the errors from these two sources which arise due to the discretization of both the circular arch and the cylindrical shell by flat elements. It is shown that the sources of these errors can be identified from the symbolically generated discrete Fourier operators that correspond to the reference continuum equilibrium equations. From this information, both a priori estimates of the interior solution error are obtained as well as the limit differential equilibrium equations of the discrete problem.

For the case of the circular arch, discretizations using both C^1 Hermitian beam and C^0 Timoshenko beam elements will be examined. The reference equilibrium equations for the Hermitian beam discretization will be derived from Sanders cylindrical shell theory. For the Timoshenko beam discretization, however, there does not appear to be any generally agreed upon set of thick shell equations from

which to derive the corresponding arch equations. As a result, two different sets of reference equations will initially be employed, namely those of Naghdi-Cooper and Mirsky-Herrmann. As will be seen, the Timoshenko beam discretization is consistent with neither theory. It is, however, shown to be consistent in the thin shell limit with Sanders theory.

The flat Reissner-Mindlin plate discretization of the cylindrical shell is next analyzed. Naghdi-Cooper C^0 shell theory is employed as the reference theory for the material operator. For the case of bifurcation buckling, however, a buckling operator consistent with this linear theory has not been identified. As a result, buckling loads derived from the symbolic analysis results are compared directly to those from the finite element analyses for the example problem dealing with the axisymmetric bifurcation buckling of a cylindrical shell. The mode switching characteristics of finite element shell bifurcation analyses is seen to be captured by the present analysis which is able to almost exactly predict the axisymmetric bifurcation buckling load of a cylindrical shell.

§5.1 Circular Arch

With the introduction of initial curvature into the symbolic analysis, this first section serves as the fundamental starting point for the analysis of cylindrical shells to follow. The first problem to be considered is that of the thin C^1 arch. This appears to be the ideal place to start since one can make use of Sanders shell theory as the reference theory. For the case of the C^0 arch, however, the question of which shell theory to compare to becomes an important issue. Two candidate theories will be considered. Since C^0 elements are more often than not used to model relatively thin shell structures, the important question of whether the discrete C^0 model correctly models C^1 behavior in the thin-shell limit will also be discussed.

§5.1.1 Straight Hermitian (C^1) Beam Discretization

The most severe geometrical approximation encountered in a discrete analysis
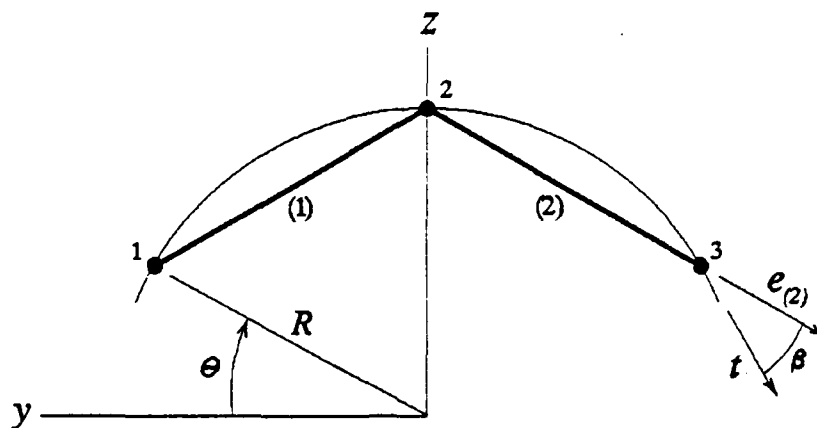
Fig. 5.1 – Arch Geometry

is the polygonal one resulting from modeling a curved structure with straight (or flat) finite elements. The simplest example of this is the 2-node C^1 (or C^0) beam discretization of an arch as portrayed in Fig. 5.1 whose analysis will serve as the precursor to the cylindrical shell problem.

Strang and Fix [6] have remarked about employing Hermitian beam bending elements with linear membrane displacement fields that *"Obviously such trial functions are inadmissible in the arch problem, but since the strain energy is also modified by the removal of R, the convergence question remains open"*. As will be shown, the results of the present analysis can be used to establish the convergence of the Hermitian beam with linear membrane displacement field to the correct governing equations.

§5.1.2 Continuum C^1 Arch

The equilibrium equations for the C^1 circular arch, cast in terms of the arclength, s, are given in the following general matrix operator form as

$$Lu = f \qquad (5.2)$$

132

with

$$L(s) = \begin{bmatrix} (EA + \frac{EI}{R^2})\frac{\partial^2}{\partial s^2} & \frac{EA}{R}\frac{\partial}{\partial s} - \frac{EI}{R}\frac{\partial^3}{\partial s^3} \\ sym & \frac{EA}{R^2} + EI\frac{\partial^4}{\partial s^4} \end{bmatrix}$$

and

$$u = \left\{ \begin{matrix} v \\ w \end{matrix} \right\} \qquad f = \left\{ \begin{matrix} -t \\ p \end{matrix} \right\}$$

where v and w are the tangential and normal displacements with t and p representing the conjugate forces. These equations were derived by Graff[68] and are identical to Sanders [69] shell equations specialized to the arch (i.e., $u = \frac{\partial}{\partial x} = \nu = 0$). The negative tangential surface traction is a result of writing L in a symmetric form.

The corresponding Fourier transformed equations result from assuming a harmonic solution of the form

$$u = \hat{u}\,e^{iks}. \tag{5.3}$$

Substitution of Eq. (5.3) into Eq. (5.2) results in

$$\hat{L}(k) = EA \begin{bmatrix} -(1 + \frac{h^2}{12R^2})k^2 & i(\frac{1}{R}k + \frac{h^2}{12R}k^3) \\ sym & \frac{1}{R^2} + \frac{h^2}{12}k^4 \end{bmatrix} \tag{5.4}$$

which will serve as the reference Fourier transformed matrix operator for the discrete analysis to follow.

§5.1.3 Discrete C^1 Arch

In previous examples (dealing with the Timoshenko beam), the goal of the decoupling procedure was the recovery of the limit differential equilibrium bending equation in terms of the lateral displacement, w. Since the structure was initially straight, no coupling existed between in-plane and bending deformation for the case of linear problems. For the case of a structure with initial curvature such as an arch, there exists an intrinsic coupling between membrane and bending

133

behavior. The operational procedure previously used for the Timoshenko beam will therefore have to be slightly modified in order to "condense" out the rotational degree-of-freedom from the discrete v and w equations which represent the discrete counterparts of the coupled membrane and bending equilibrium equations of the arch.

§5.1.3.1 Geometrical Relations for Discrete Problem

As a prelude to recovering the limit differential equations corresponding to the discrete finite element difference equations, it is necessary to first determine the transformations from the element reference frame to the local shell reference frame in which the equilibrium equations are derived with respect to. This step begins by noting that the position of any point on the arc (see Fig. 5.1) is determined by $\mathbf{r} = \lfloor R\cos\theta, \ R\sin\theta \rfloor^T$, so that the unit tangent vector at any point and hence the direction of the tangential displacement, v, in the shell reference frame is determined from

$$\mathbf{t} = \frac{d\mathbf{r}}{ds} = \frac{d\mathbf{r}}{d\theta}\frac{d\theta}{ds} = \frac{1}{R}\frac{d\mathbf{r}}{d\theta}$$

$$= \left\{ \begin{array}{c} -\sin\theta \\ \cos\theta \end{array} \right\}$$

(5.5)

where $s = R\theta$. If for example, one considers element (2), its unit orientation vector is given by

$$\mathbf{e}_{(2)} = \frac{(\mathbf{r}_3 - \mathbf{r}_2)}{l_{(2)}}$$

(5.6)

so that the angle between $\mathbf{e}_{(2)}$ and $\mathbf{t}$ at global node 3 is determined from

$$\mathbf{e}_{(2)} \cdot \mathbf{t} = \cos\beta = \frac{R}{l}\sin(\theta_3 - \theta_2)$$

$$= \frac{R}{l}\sin\Delta\theta$$

(5.7)

$$= \cos\frac{\Delta\theta}{2}$$

to be $\beta = \Delta\theta/2$ where $\Delta\theta$ is the angle subtended by the element. This result will

134

be true for each node in the mesh.

The appropriate element transformation relations from element to shell coordinate systems are given by

$$\mathbf{u} = \mathbf{T}\mathbf{u}_e, \quad \mathbf{f} = \mathbf{T}\mathbf{f}_e, \quad \mathbf{k} = \mathbf{T}\mathbf{k}_e\mathbf{T}^{\mathbf{T}} \tag{5.8}$$

where $\mathbf{u}_e$ and $\mathbf{f}_e$ represent the element displacement and force vectors and $\mathbf{k}_e$, the element stiffness matrix in the local element coordinate system with $\mathbf{u}$, $\mathbf{f}$ and $\mathbf{k}$ representing the same quantities in the shell reference frame. The 2-D nodal transformation matrix for a $\lfloor u_i \quad w_i \quad \theta_i \rfloor$ nodal *d-o-f* ordering at the ith node is

$$\Lambda_i = \begin{bmatrix} \cos\psi_i & \sin\psi_i & 0 \\ -\sin\psi_i & \cos\psi_i & 0 \\ 0 & 0 & 1 \end{bmatrix} \quad \Rightarrow \quad \mathbf{T} = \begin{bmatrix} \Lambda_1 & 0 \\ 0 & \Lambda_2 \end{bmatrix} \tag{5.9}$$

where ψ_i is the nodal transformation angle for element nodes 1 and 2. For the present case, $\psi_1 = \beta$ and $\psi_2 = -\beta$ for both elements (1) and (2).

§5.1.3.2 Discrete Fourier Analysis

The element stiffness matrix for the present case is [41]

$$\mathbf{k}_e = \begin{bmatrix} \dfrac{EA}{l_e} & 0 & 0 & -\dfrac{EA}{l_e} & 0 & 0 \\ & \dfrac{12EI}{l_e^3} & \dfrac{6EI}{l_e^2} & 0 & \dfrac{-12EI}{l_e^3} & \dfrac{6EI}{l_e^2} \\ & & \dfrac{4EI}{l_e} & 0 & \dfrac{-6EI}{l_e^2} & \dfrac{2EI}{l_e} \\ & & & \dfrac{EA}{l_e} & 0 & 0 \\ & sym & & & \dfrac{12EI}{l_e^3} & \dfrac{-6EI}{l_e^2} \\ & & & & & \dfrac{4EI}{l_e} \end{bmatrix} \tag{5.10}$$

where EA, EI and l_e represent the beam element's extensional stiffness, bending

stiffness and "computational" length[1]. The *d-o-f* ordering corresponding to $\mathbf{k}_e$ is

$$\mathbf{u} = \lfloor u_1 \quad w_1 \quad \theta_1 \quad u_2 \quad w_2 \quad \theta_2 \rfloor^T \tag{5.11}$$

where $\theta_i = \frac{dw}{dx}\big|_i$. Since $\mathbf{k}_e$ results from the superposition of a linear membrane stiffness with the Hermitian beam stiffness, no membrane/bending coupling exists on the element level. Membrane/bending coupling, however, does occurs as a consequence of element assembly on the global level.

With element transformation relations now defined by Eq. (5.8), an element patch. as portrayed in Fig. 5.1, is assembled with nodal degrees-of-freedom expressed in the shell reference frame, s. With all nodal degrees-of-freedom now expressed with respect to this common basis, Eq. (5.3) is used in its discrete form, *viz.*,

$$\mathbf{u}_1 = \hat{\mathbf{u}}\,e^{ik(s_j - s)}; \quad \mathbf{u}_2 = \hat{\mathbf{u}}\,e^{iks_j}; \quad \mathbf{u}_3 = \hat{\mathbf{u}}\,e^{ik(s_j + s)}, \tag{5.12}$$

to relate nodal degrees-of-freedom at nodes 1 and 3, back to the center (or j^{th}) node, 2, where s_j is the position of the center node and in the present context, s is now used to represent the arclength spanned by a single element. The fact that this analysis reflects a facet approximation is embodied in the discrete equations via the transformed element stiffness matrices. The discrete Fourier matrix operator at the center node is given in the symbolic form

$$\begin{bmatrix} \ell_{vv} & \ell_{vw} & \ell_{v\theta} \\ \ell_{wv} & \ell_{ww} & \ell_{w\theta} \\ \ell_{\theta v} & \ell_{\theta w} & \ell_{\theta\theta} \end{bmatrix} \begin{Bmatrix} \hat{v} \\ \hat{w} \\ \hat{\theta} \end{Bmatrix} = \begin{Bmatrix} \hat{t}^{\mathrm{D}} \\ \hat{p}^{\mathrm{D}} \\ \hat{m}^{\mathrm{D}} \end{Bmatrix} \tag{5.13}$$

where $\hat{v}$ and $\hat{w}$ are the transformed displacements in the arch (or shell) reference frame tangent and normal to the arch with $\hat{\theta}$ representing the nodal rotation; $\hat{t}^{\mathrm{D}}$, $\hat{p}^{\mathrm{D}}$ and $\hat{m}^{\mathrm{D}}$ represent the conjugate nodal forces. Relating Eq. (5.13) to its

---

[1] In light of the work by Cook and Zhao-hua [70], the question of whether l_e should be chosen as the chord or arc length will be addressed shortly.

continuum counterpart entails eliminating the computational d-o-f, θ, which has no physical significance in thin C^1 shell theory, from the v and w equilibrium equations. This step is essentially equivalent to one of *static condensation* with the result symbolically expressed as

$$\begin{bmatrix} \ell_{\theta\theta}\ell_{vv} - \ell_{v\theta}\ell_{\theta v} & \ell_{\theta\theta}\ell_{vw} - \ell_{v\theta}\ell_{\theta w} \\ \ell_{\theta\theta}\ell_{wv} - \ell_{w\theta}\ell_{\theta v} & \ell_{\theta\theta}\ell_{ww} - \ell_{w\theta}\ell_{\theta w} \end{bmatrix} \left\{ \begin{array}{c} \hat{v} \\ \hat{w} \end{array} \right\} = \left\{ \begin{array}{c} \ell_{\theta\theta}\hat{t}^{\mathrm{D}} - \ell_{v\theta}\hat{m}^{\mathrm{D}} \\ \ell_{\theta\theta}\hat{p}^{\mathrm{D}} - \ell_{w\theta}\hat{m}^{\mathrm{D}} \end{array} \right\} \qquad (5.14)$$

where again the assumption that the individual differential operators are commutative has been invoked resulting from their linearity. Note that Eq. (5.14) is not as yet written in its symmetric form.

Substitution of the polar form of $e^{\pm iks}$,

$$e^{\pm iks} = \cos ks \pm i \sin ks, \qquad (5.15)$$

into Eq. (5.14) followed by employing the geometric relations

$$\begin{aligned} \sin ks &= 2\sin\frac{ks}{2}\cos\frac{ks}{2} = s\bar{k}\sqrt{1 - \frac{s^2}{4}\bar{k}^2} \\ \cos ks &= 1 - 2\sin^2\frac{ks}{2} = 1 - \frac{s^2}{2}\bar{k}^2 \\ \sin\beta &= \frac{l}{2R} \end{aligned} \qquad (5.16)$$

with the discrete wave number,

$$\bar{k} = \frac{\sin\frac{ks}{2}}{\frac{s}{2}} \qquad (5.17)$$

now being defined with respect to the arc length, results in the discrete counterpart

137

to Eq. (5.4), namely[2],

$$
\hat{L}^{\mathrm{D}}(\bar{k}) = EA
\begin{bmatrix}
-(1_{vv}^{m} + 1_{vv}^{b}\frac{h^2}{12R^2})\bar{k}^2 & i(1_{vw}^{m}\frac{1}{R}\bar{k} + 1_{vw}^{b}\frac{h^2}{12R}\bar{k}^3) \\[2mm]
sym & 1_{ww}^{m}\frac{1}{R^2} + 1_{ww}^{\dot{v}}\frac{h^2}{12}\bar{k}^4
\end{bmatrix}
\tag{5.18}
$$

with

$$
1_{vv}^{m} = \frac{s^2}{l_e^2}\cdot\alpha_2\cdot\cos^2\beta \qquad 1_{vv}^{b} = \frac{s^2 l^2}{l_e^4}\cdot\alpha_1
$$

$$
1_{vw}^{m} = \frac{sl}{l_e^2}\cdot\sqrt{\alpha_1}\cdot\alpha_2\cdot\cos\beta \quad 1_{vw}^{b} = \frac{s^3 l}{l_e^4}\cdot\sqrt{\alpha_1}\cdot\cos\beta
$$

$$
1_{ww}^{m} = \frac{l^2}{l_e^2}\cdot\alpha_1\cdot\alpha_2 \qquad 1_{ww}^{b} = \frac{s^4}{l_e^4}\cdot\cos^2\beta
$$

and

$$
\alpha_1 = 1 - \frac{s^2}{4}\bar{k}^2; \qquad \alpha_2 = 1 - \frac{s^2}{6}\bar{k}^2 .
$$

For the loading term, one finds that

$$
\hat{f}^{\mathrm{D}} =
\begin{Bmatrix}
-\ell_{\theta\theta}\hat{t}^{\mathrm{D}} + \ell_{v\theta}\hat{m}^{\mathrm{D}} \\[2mm]
\ell_{\theta\theta}\hat{p}^{\mathrm{D}} - \ell_{w\theta}\hat{m}^{\mathrm{D}}
\end{Bmatrix}
=
\begin{Bmatrix}
-\frac{\alpha_2}{l_e}\hat{t}^{\mathrm{D}} + \frac{l}{l_e^2 R}\alpha_1\hat{m}^{\mathrm{D}} \\[2mm]
\frac{\alpha_2}{l_e}\hat{p}^{\mathrm{D}} - i\frac{s}{l_e^2}\bar{k}\cos\beta\sqrt{\alpha_1}\hat{m}^{\mathrm{D}}
\end{Bmatrix}
\tag{5.19}
$$

For these equations, l and l_e have purposely been kept separate since l represents the true geometric chord length while l_e is used to denote the element length which may be chosen so as to maximize solution accuracy (see [70]).

In an analogous manner to the beam discretizations addressed in Chapter 3, the maximum wavenumber which the present model is capable of representing without aliasing is $k_{\max} = \frac{\pi}{s}$. At $k = k_{\max}$, the point corresponding to a single half wave spanning a beam element, the terms in Eq. (5.18) representing membrane-bending coupling effects vanish since $\alpha_1 = 0$. If Eq. (5.18) is rewritten symbolically

---

[2] The symbolic analysis runstream used to obtain these results is found in Appendix A.3.

as

$$\hat{L}^D(\bar{k}) = \begin{bmatrix} -(\hat{L}_{vv}^m + \hat{L}_{vv}^b) & i(\hat{L}_{vw}^m + \hat{L}_{vw}^b) \\ sym & \hat{L}_{ww}^m + \hat{L}_{ww}^b \end{bmatrix} , \qquad (5.20)$$

then at $k_{max} = \frac{\pi}{s}$, i.e., $\bar{k} = 2/s$, one has

$$\hat{L}^D(\frac{2}{s}) = \begin{bmatrix} -\hat{L}_{vv}^m & 0 \\ 0 & \hat{L}_{ww}^b \end{bmatrix} , \qquad (5.21)$$

where only the pure membrane and bending operators $\hat{L}_{vv}^m$ and $\hat{L}_{ww}^b$ remain resulting in a degenerate uncoupled membrane-bending arch behavior. For a closed ring, however, $k_{max} = \frac{\pi}{s}$ may not in fact be the maximum wave number due to the requirement for a periodic displacement field. For this case, $k = n/R$, where n represents an integer value, so that one now has

$$k_{max} = \frac{n_{max}}{R} \leq \frac{\pi}{s} . \qquad (5.22)$$

§5.1.3.3 Calculation of Element Loads

The calculation of element loads for the straight element approximation of a curved structure usually proceeds in two general ways:

1) Calculate element loads as if they were directly applied to the facet approximation of the curved structure, or

2) Project physical loading onto discrete model based upon known physical geometry.

With the first technique being the one most commonly employed in production finite element codes, it will also be used here. The element load vector corresponding to 1) for the case of pure pressure loading on the physical structure,

$$p = \hat{p}_k e^{iks} , \qquad (5.23)$$

139

would then simply be

$$\mathbf{f}_{(1)} = \hat{p}_k \int_0^l \mathbf{N} \, e^{ik(x_j - l + \xi)} \, d\xi \qquad (5.24)$$

for element 1 (see Fig. 5.1) and

$$\mathbf{f}_{(2)} = \hat{p}_k \int_0^l \mathbf{N} \, e^{ik(x_j + \xi)} \, d\xi \qquad (5.25)$$

for element 2 where the element's Hermitian beam shape functions are

$$\mathbf{N} = \left\{ \begin{array}{c} 0 \\[1ex] 1 - \frac{3\xi^2}{l^2} + \frac{2\xi^3}{l^3} \\[1ex] \xi - \frac{2\xi^2}{l} + \frac{\xi^3}{l^2} \\[1ex] 0 \\[1ex] \frac{3\xi^2}{l^2} - \frac{2\xi^3}{l^3} \\[1ex] -\frac{\xi^2}{l} + \frac{\xi^3}{l^2} \end{array} \right\}. \qquad (5.26)$$

Once $\mathbf{f}_j$ has been calculated for each element, element contributions are then rotated into the shell reference frame and assembled into the global force vector. As a result of the spatially varying pressure loading and the w-θ shape function coupling, contributions in all three nodal load components,

$$\mathbf{f}_j = \left\{ \begin{array}{c} \hat{t}^{\mathrm{D}} \\[1ex] \hat{p}^{\mathrm{D}} \\[1ex] \hat{m}^{\mathrm{D}} \end{array} \right\} = \left\{ \begin{array}{c} i\frac{\sin\beta}{k}\left(2 + \frac{12}{k^2 l^2}(1 + \cos kl) - \frac{24}{k^3 l^3}\sin kl\right) \\[1ex] \frac{\cos\beta}{k}\left(\frac{24}{k^3 l^3}(1 - \cos kl) - \frac{12}{k^2 l^2}\sin kl\right) \\[1ex] \frac{i}{k^2}\left(\frac{4}{kl}(2 + \cos kl) - \frac{12}{k^2 l^2}\sin kl\right) \end{array} \right\} \hat{p}_k \, e^{iks_j} \qquad (5.27)$$

are seen to result. The finite element approximation corresponding to method 1, which results from letting $s_j = x_j$, is employed here.

140

§5.1.3.4 Spectral Error Estimates

From the results of the previous sections, relative error estimates in the frequency domain for each Fourier component of v and w may be determined essentially as outlined in Chapter 3. There is, however, one important new aspect of the procedure, namely that of now having to consider the $\hat{u}$ in Eq. (5.3) as complex, i.e., $\hat{u} = \hat{u}_R + i\hat{u}_I$. This change arises due to the necessity of accounting for coupling effects in the *solution* which are present in modelling curved structures due to the intrinsic bending-extensional coupling. In the past, this would have also been a problem if one had not restricted loading to that conjugate to the displacement variable for which the solution was sought. If, for example, distributed moments had been included in the load vector for the different beam and plate problems considered earlier, this complex interpretation would have also been needed there. The emphasis on *solution* should be noted since this complex intrepretation of $\hat{u}$ need only be employed when numerical solution evaluation is required as is presently the case. No changes in the earlier symbolic analysis procedures are required when addressing the question of consistency.

From Eq. (5.4), the transformed decoupled continuum equation for the lateral displacement, $\hat{w}$, is found to be

$$-(EIk^6 - \frac{2EI}{R^2}k^4 + \frac{EI}{R^4}k^2)\hat{w} = i(\frac{1}{R}k + \frac{h^2}{12R}k^3)\hat{t} - (1 + \frac{h^2}{12R^2})k^2\hat{p}. \quad (5.28)$$

Rewriting the Fourier coefficients, $\hat{w}$, $\hat{t}$ and $\hat{p}$, in complex form as[3]

$$\hat{w} = (\hat{w}_R - i\hat{w}_I)$$
$$\hat{t} = (\hat{t}_R - i\hat{t}_I) \qquad\qquad (5.29)$$
$$\hat{p} = (\hat{p}_R - i\hat{p}_I)$$

---

[3] From the analogy with $f(s) = \sum_{k=0}^{\infty}(a_k \cos ks + b_k \sin ks) = \sum_{k=-\infty}^{\infty} c_k\, e^{iks}$ where $c_k = \frac{1}{2}(a_k - ib_k)$ for $k > 0$.

141

and substituting back into Eq. (5.28) results in

$$-(EIk^6 - \frac{2EI}{R^2}k^4 + \frac{EI}{R^4}k^2)(\hat{w}_R - i\hat{w}_I) =$$

$$(\frac{1}{R}k + \frac{h^2}{12R}k^3)(i\hat{t}_R + \hat{t}_I) - (1 + \frac{h^2}{12R^2})k^2(\hat{p}_R - i\hat{p}_I) \tag{5.30}$$

where it suffices to only consider the real part[4],

$$-EI\underbrace{(k^6 - \frac{2}{R^2}k^4 + \frac{1}{R^4}k^2)}_{k^2(k^2-\frac{1}{R^2})^2}\hat{w}_R = (\frac{1}{R}k + \frac{h^2}{12R}k^3)\hat{t}_I - (1 + \frac{h^2}{12R^2})k^2\hat{p}_R \tag{5.31}$$

for error estimation purposes. A quick inspection of the continuum operator shows that in addition to $k = 0$, the solution will also have a singularity at $k = 1/R$ corresponding to a rigid body mode. Using these exact procedures, the decoupled in-plane equilibrium equation for v would also be obtained in a similiar manner.

For the Hermitian beam discretization, the decoupled $\hat{w}^D$ equilibrium equation is determined from Eqs. (5.18) and (5.19) to be

$$-EI(\frac{s^4}{l_e^3}\cos^4\beta\bar{k}^6 - \frac{s^2l^2}{l_e^3}\alpha_1\cos^2\beta\frac{2}{R^2}\bar{k}^4 + \frac{l^4}{l_e^3}\alpha_1^2\frac{1}{R^4}\bar{k}^2)\hat{w}^D =$$

$$i(\frac{l}{s}\sqrt{\alpha_1}\alpha_2\cos\beta\frac{1}{R}\bar{k} + \frac{sl}{l_e^2}\sqrt{\alpha_1}\cos\beta\frac{h^2}{12R}\bar{k}^3)\hat{t}^D$$

$$-(\alpha_2\cos^2\beta + \frac{l^2}{l_e^2}\alpha_1\frac{h^2}{12R^2})\bar{k}^2\hat{p}^D \tag{5.32}$$

$$-i(\frac{l^2}{sl_e}\sqrt[3]{\alpha_1}\cos\beta\frac{1}{R^2}\bar{k} - \frac{s}{l_e}\sqrt{\alpha_1}\cos^3\beta\bar{k}^3)\hat{m}^D$$

---

[4] In terms of the usual Fourier series representation, this is equivalent to the assumed solution $w = \hat{w}\cos ks$ with distributed loading $t = \hat{t}\sin ks$ and $p = \hat{p}\cos ks$ [71]

142

in terms of the nodal loads. For the present problem of interest, namely, that of a distributed pressure loading as described in the previous section, Eq. (5.27) gives the corresponding nodal loading which when substituted into Eq. (5.32) results in

$$-EI\bar{k}^2\left(\frac{s^2}{l_e^2}\cos^2\beta\bar{k}^2 - \frac{l^2}{l_e^2}\frac{\alpha_1}{R^2}\right)^2\hat{w}_R^D =$$

$$[-\left(\frac{l}{s}\sqrt{\alpha_1}\alpha_2\cos\beta\frac{\bar{k}}{R} + \frac{sl}{l_e^2}\sqrt{\alpha_1}\cos\beta\frac{h^2}{12R}\bar{k}^3\right)\frac{\sin\beta}{kl_e}\left(2 + \frac{12}{k^2l^2}(1+\cos kl) - \frac{24}{k^3l^3}\sin kl\right)$$

$$-\left(\alpha_2\cos^2\beta + \frac{l^2}{l_e^2}\alpha_1\frac{h^2}{12R^2}\right)\bar{k}^2\frac{\cos\beta}{kl_e}\left(\frac{24}{k^3l^3}(1-\cos kl) - \frac{12}{k^2l^2}\sin kl\right)$$

$$+\left(\frac{l^2}{sl_e}\sqrt[3]{\alpha_1}\cos\beta\frac{\bar{k}}{R^2} - \frac{s}{l_e}\sqrt{\alpha_1}\cos^3\beta\bar{k}^3\right)\frac{1}{k^2l_e}\left(\frac{4}{kl}(2+\cos kl) - \frac{12}{k^2l^2}\sin kl\right)]\hat{p}_R$$

$$\text{(5.33)}$$

With decoupled Fourier transformed expressions for both the continuum and discrete problems now available, relative spectral error estimates for both v and w would be expressed as

$$\hat{\epsilon}_v = \frac{\hat{v} - \hat{v}^D}{\hat{v}}; \quad \hat{\epsilon}_w = \frac{\hat{w} - \hat{w}^D}{\hat{w}}. \qquad \text{(5.34)}$$

Before deriving any spectral error estimates for $\hat{\epsilon}_w$, however, it is first instructive to plot the continuum solution of a circular arch with $R/h = 2000$, $h = 1$ and $E = 10^7$. This is done in Fig. 5.2 where, due to the singularity in the middle of the spectrum, $1/w$ is plotted, rather than w versus ks where the arc length, s, was chosen corresponding to $\beta = 1°$ as will be the case in the first spectral error plot to follow. It should be noted that ks values in the domain $0 < ks < \frac{1}{R}s$ are possible since the question of a closed ring versus an open arch is not an important consideration. From Eqs. (x120) and (x125), $\hat{\epsilon}_w$ vs. ks plots are determined as shown in Figs. 5.3 and 5.4 for a $\beta = 1°$ and $22.5°$ for both the case where $l_e = l$ and $l_e = s$. In order to avoid the singular behavior at $k = 1/R$, plotting is

143
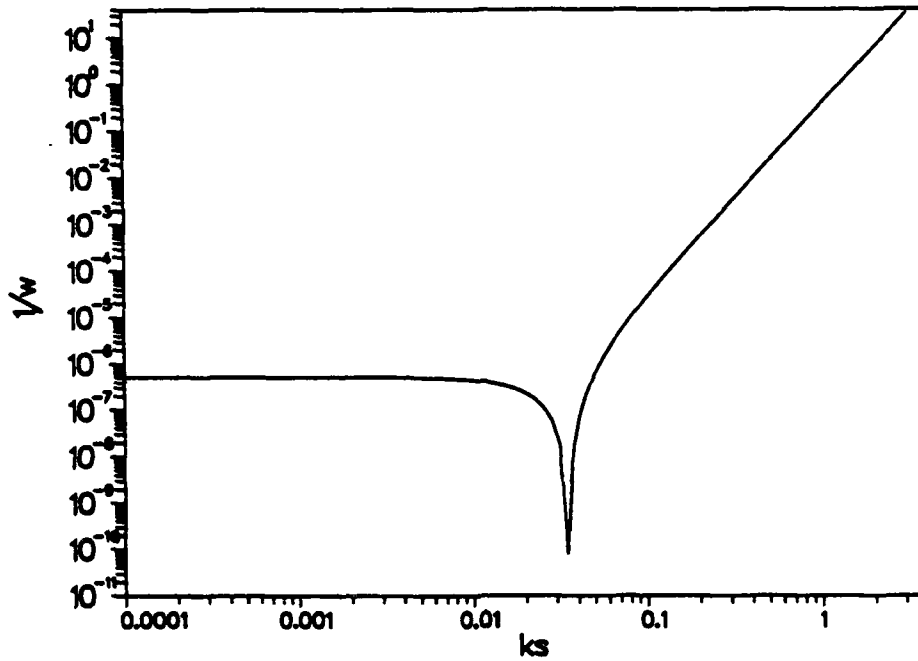
Fig. 5.2 – Continuum solution for $\hat{p}_R = 1$

started at $k = 1.5/R$ in both cases. The mathematical consistency of the straight Hermitian beam discretization of the circular arch with Sanders arch equations is graphically portrayed in these two figures since $\hat{\epsilon}_w \to 0$ as $\beta \to 0$. For the first time, however, the effect of a geometrical approximation on the finite element solution is encountered. The operational form of consistency observed for problems with exact geometry, namely, $\hat{\epsilon} \to 0$ as $k \to 0$ for finite l is unfortunately not a property of a discretization where geometrical model approximations are also employed. In the present case, one is lead to conclude that for a given k, the finite element solution corresponds to that of the faceted arch.

Cook and Zhao-Hua [70] showed by numerical experimentation that for a number of different problems, a more accurate solution resulted if the element length was defined as the arc length, s, rather than the chord length, l. Figs. 5.3 and 5.4 verify this result showing that for all wave lengths, a more accurate finite element solution will be obtained if the element length is chosen to be the arc

144

length, i.e., $l_e = s$. Lastly, one cannot help but comment on the similiarity between the results in Figs. 5.3 and 5.4 and those from comparisons between Donnell's shallow shell theory and the shell theory of Flugge-Lur'e-Byrne [24]. In both cases, the accuracy of the approximations improved for shorter wave lengths indicating that the effect of the initial curvature becomes less severe as the structure becomes *flatter* with respect to the higher frequency solution components.

§5.1.3.5 Recovery of Limit Differential Equilibrium Equations

The inverse transformation procedure described in §3.2.3 can also be employed in the present case to recover the governing limit differential equilibrium equations. In addition to the expansion of $\bar{k}$ as

$$\bar{k} = \frac{2}{l}\sin\frac{kl}{2} \cong k - \frac{l^2}{24}k^3 + \cdots \tag{5.35}$$

one also needs to use

$$\cos\beta = \sqrt{1 - \frac{l^2}{4R^2}} \cong 1 - \frac{l^2}{8R^2} - \cdots$$

$$\tag{5.36}$$

$$s = R\theta = 2R\sin^{-1}\frac{l}{2R} \cong l + \frac{l^3}{24R^2} + \cdots.$$

For the case when $l_e = l$, the limit differential equilibrium equations are found to

145
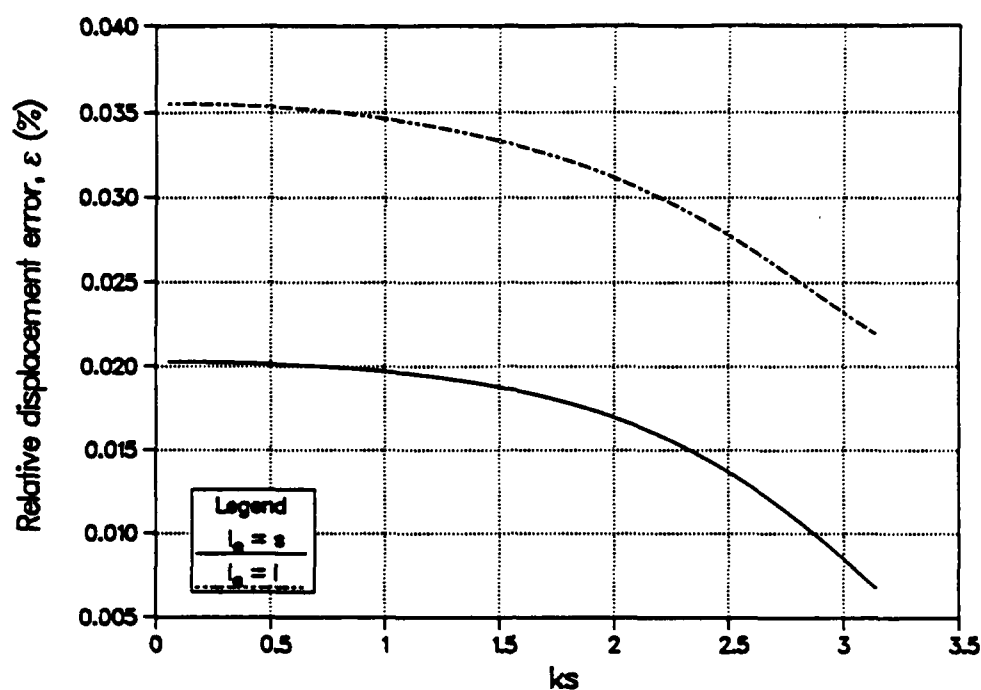
Fig. 5.3 – Relative error in $\hat{w}$ as a function of $\{ks : 1.5s/R \leq ks \leq k_{\max}s\}$ for $\beta = 1°$
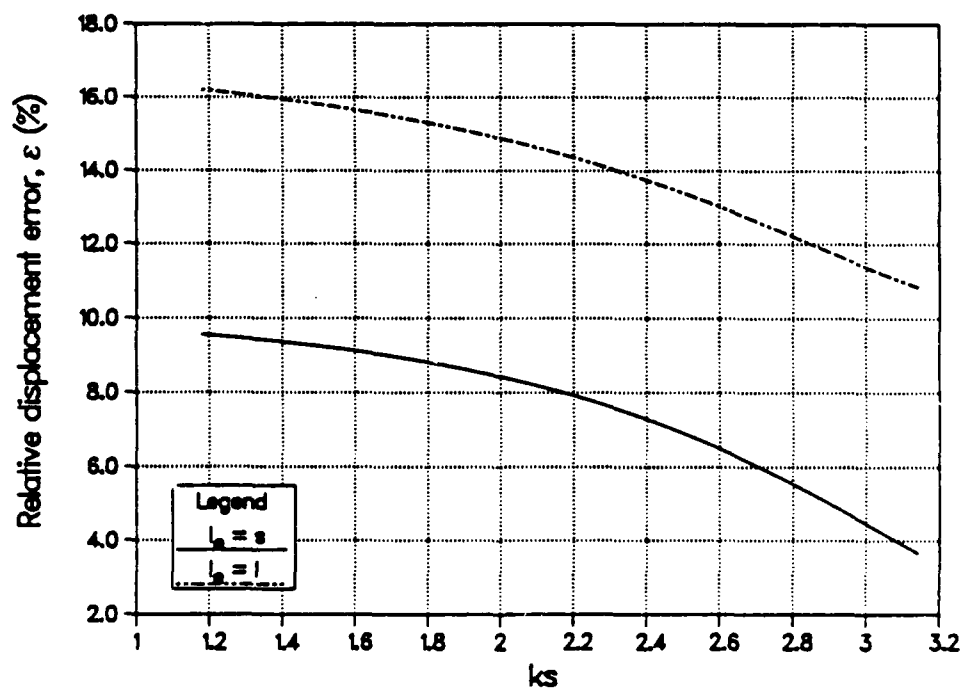
Fig. 5.4 – Relative error in $\hat{w}$ as a function of $\{ks : 1.5s/R \leq ks \leq k_{\max}s\}$ for $\beta = 22.5°$.

146

be

$$L^D = L + \mathbf{p} + \tau$$

$$
= \begin{bmatrix} (EA + \frac{EI}{R^2})\frac{\partial^2}{\partial s^2} & \frac{EA}{R}\frac{\partial}{\partial s} - \frac{EI}{R}\frac{\partial^3}{\partial s^3} \\ sym & \frac{EA}{R^2} + EI\frac{\partial^4}{\partial s^4} \end{bmatrix}
$$

$$
+ \frac{l^2}{R^2} \begin{bmatrix} -\frac{EA}{6}\frac{\partial^2}{\partial s^2} + \frac{EI}{12R^2}\frac{\partial^2}{\partial s^2} & -\frac{EA}{12R}\frac{\partial}{\partial s} \\ sym & -\frac{EI}{12}\frac{\partial^4}{\partial s^4} \end{bmatrix}
\tag{5.37}
$$

$$
+ l^2 \begin{bmatrix} \frac{EA}{4}\frac{\partial^4}{\partial s^4} + \frac{EI}{3R^2}\frac{\partial^4}{\partial s^4} & \frac{EA}{3R}\frac{\partial^3}{\partial s^3} - \frac{EI}{4R}\frac{\partial^5}{\partial s^5} \\ sym & \frac{5EA}{12R^2}\frac{\partial^2}{\partial s^2} + \frac{EI}{6}\frac{\partial^6}{\partial s^6} \end{bmatrix}
$$

where only truncation order terms through $O(l^2)$ have been retained. The first key point to note is that the present facet approximation to the circular arch is a consistent one since the correct continuum operator, L, is exactly recovered in the limit as $l \to 0$. Examination of Eq. (5.37), however, reveals the existence of parasitic operator term corresponding to L^m_{vv}, L^b_{vv}, L^m_{vw} and L^b_{ww}. Fortunately, these terms have leading coefficients equal to $\epsilon\frac{l^2}{R^2}$ ($= 4\epsilon\sin^2\beta$), with $\epsilon = 1/6$ for L^m_{vv} and $1/12$ for the other terms, which have a relatively benign effect on the solution as compared to the parasitic terms responsible for the transverse shear locking phenomena encountered earlier with the Timoshenko beam. The magnitude of the largest coefficient, namely that corresponding to L^m_{vv}, is shown in the following table,

$2\beta(= \Delta\theta)$	$\frac{l^2}{6R^2}$
90	.333
45	.098
30	.045
10	.005

147

where $\Delta\theta$ is the angle subtended by a single element. Even for the rather severe case where only 2 elements are used to discretize $90°$ of an arch, the change in apparent stiffness due to the parasitic term for L_{vv}^m is but 9.8%.

§5.1.4 Linear C^0 Beam Discretization – Continuum C^0 Arch

For the C^1 arch, Sander's shell theory seemed to truly represent what Budiansky and Sander's referred to as the "best" first-order linear shell theory [72]. When it, however, comes time to consider the C^0 circular arch, the question of which C^0 shell theory to accept as the reference theory is not at all clear. For now, C^0 arch equilibrium equations derived from two different shell theories – Naghdi-Cooper and Mirsky-Herrmann – will be presented. The reduction from the cylindrical shell equations to those of the arch was accomplished in the same manner as was described earlier for Sander's shell theory. Since C^0 elements are often used to model thin shell structures, the limiting case of no transverse shear deformation will also be examined.

The C^0 arch equilibrium equations derived from Naghdi-Cooper C^0 shell theory [73] are

$$
L = \begin{bmatrix} EA\frac{\partial^2}{\partial s^2} - \frac{\kappa GA}{R^2} & (\frac{EA}{R} + \frac{\kappa GA}{R})\frac{\partial}{\partial s} & \frac{EI}{R}\frac{\partial^2}{\partial s^2} - \frac{\kappa GA}{R} \\ & \frac{EA}{R^2} - \kappa GA\frac{\partial^2}{\partial s^2} & (\frac{EI}{R^2} + \kappa GA)\frac{\partial}{\partial s} \\ sym & & EI\frac{\partial^2}{\partial s^2} - \kappa GA \end{bmatrix} \tag{5.38}
$$

where the loading vector is given by

$$
f = \left\{ \begin{array}{c} -t \\ p \\ -m \end{array} \right\}. \tag{5.39}
$$

For the case of Mirsky-Herrmann C^0 shell theory [74], the corresponding arch equations are

$$
L = L_{\text{Naghdi-Cooper}} + L_{\text{mod}} \tag{5.40}
$$

148

where the modifying matrix differential operator is

$$
L_{\mathrm{mod}} = \begin{bmatrix} \dfrac{EI}{R^2}\dfrac{\partial^2}{\partial s^2} - \dfrac{\kappa GI}{R^4} & \left(\dfrac{EI}{R^3} + \dfrac{\kappa GI}{R^3}\right)\dfrac{\partial}{\partial s} & -\dfrac{\kappa GI}{R} \\[2ex] & \dfrac{EI}{R^4} - \dfrac{\kappa GI}{R^2}\dfrac{\partial^2}{\partial s^2} & \dfrac{\kappa GI}{R^2}\dfrac{\partial}{\partial s} \\[2ex] sym & & -\dfrac{\kappa GI}{R^2} \end{bmatrix} \tag{5.41}
$$

with f remaining the same.

§5.1.4.1 Discrete C^0 Arch

The element stiffness matrix for the present case is

$$
\mathbf{k}_e = \begin{bmatrix} \dfrac{EA}{l_e} & 0 & 0 & -\dfrac{EA}{l_e} & 0 & 0 \\[1.5ex] & \dfrac{\kappa GA}{l_e} & \dfrac{\kappa GA}{2} & 0 & \dfrac{-\kappa GA}{l_e} & \dfrac{\kappa GA}{2} \\[1.5ex] & & \dfrac{EI}{l_e} + \dfrac{\kappa GAl_e}{4} & 0 & \dfrac{-\kappa GA}{2} & -\dfrac{EI}{l_e} + \dfrac{\kappa GAl_e}{4} \\[1.5ex] & & & \dfrac{EA}{l_e} & 0 & 0 \\[1.5ex] & sym & & & \dfrac{\kappa GA}{l_e} & \dfrac{-\kappa GA}{2} \\[1.5ex] & & & & & \dfrac{EI}{l_e} + \dfrac{\kappa GAl_e}{4} \end{bmatrix} \tag{5.42}
$$

where EA, EI, κGA and l_e represent the beam element's extensional stiffness, bending stiffness, transverse shear stiffness and length. This $\mathbf{k}_e$ results from the superposition of a linear membrane stiffness with the one-point spatially integrated Timoshenko beam stiffness.

Following the same symbolic procedures as described in §5.1.3.2 for the C^1 Hermitian beam, one finds the discrete Fourier material operator to be

$$
L^{\mathrm{D}} = \begin{bmatrix} -1_{vv}^m EA\bar{k}^2 - 1_{vv}^s \dfrac{\kappa GA}{R^2} & i\left(1_{vw}^m \dfrac{\kappa GA}{R} + 1_{vw}^s \dfrac{EA}{R}\right)\bar{k} & -1_{v\theta}^s \dfrac{\kappa GA}{R} \\[2ex] & 1_{ww}^m \dfrac{EA}{R^2} + 1_{ww}^s \kappa GA\bar{k}^2 & i1_{w\theta}^s \kappa GA\bar{k} \\[2ex] sym & & -1_{\theta\theta}^b EI\bar{k}^2 - 1_{\theta\theta}^s \kappa GA \end{bmatrix} \tag{5.43}
$$

149

where

$$1^m_{vv} = \frac{s^2}{l_e^2} \cdot \cos^2 \beta \qquad\qquad 1^s_{vv} = \frac{l^2}{l_e^2} \cdot \alpha_1$$

$$1^m_{vw} = 1^s_{vw} = \frac{sl}{l_e^2} \cdot \sqrt{\alpha_1} \cdot \cos \beta$$

$$1^s_{v\theta} = \frac{l}{l_e} \cdot \alpha_1$$

$$1^m_{ww} = \frac{l^2}{l_e^2} \cdot \alpha_1 \qquad\qquad 1^s_{ww} = \frac{s^2}{l_e^2} \cdot \cos^2 \beta$$

$$1^s_{w\theta} = \frac{s}{l_e} \cdot \sqrt{\alpha_1} \cdot \cos \beta$$

$$1^b_{\theta\theta} = \frac{s^2}{l_e^2} \qquad\qquad 1^s_{\theta\theta} = \alpha_1$$

and as before,

$$\alpha_1 = 1 - \frac{s^2}{4}\bar{k}^2 \,.$$

§5.1.4.2 Recovery of Limit Differential Equilibrium Equations

For the usual case where element nodes are assumed to lie on the arch, i.e., $l_e = l$, one finds that

$$1^m_{vv} = 1^2 \cdot \alpha_2 \cdot \cos^2 \beta \qquad 1^b_{vv} = 1^2 \cdot \alpha_1$$

$$1^m_{vw} = 1 \cdot \sqrt{\alpha_1} \cdot \alpha_2 \cdot \cos \beta \quad 1^b_{vw} = 1^3 \cdot \sqrt{\alpha_1} \cdot \cos \beta \qquad (5.44)$$

$$1^m_{ww} = \alpha_1 \cdot \alpha_2 \qquad\qquad 1^b_{ww} = 1^4 \cdot \cos^2 \beta$$

with

$$1 = \frac{s}{l} \,.$$

Using these results, inverse transforming Eq. (5.x168) results in

$$
L^D = \begin{bmatrix}
EA\frac{\partial^2}{\partial s^2} - \frac{\kappa GA}{R^2} & (\frac{EA}{R} + \frac{\kappa GA}{R})\frac{\partial}{\partial s} & -\frac{\kappa GA}{R} \\[2ex]
& \frac{EA}{R^2} - \kappa GA\frac{\partial^2}{\partial s^2} & \kappa GA\frac{\partial}{\partial s} \\[2ex]
sym & & EI\frac{\partial^2}{\partial s^2} - \kappa GA
\end{bmatrix}
$$

$$
+ \frac{l^2}{R^2} \begin{bmatrix}
-\frac{EA}{6}\frac{\partial^2}{\partial s^2} & -(\frac{EA}{12} + \frac{\kappa GA}{12})\frac{\partial}{\partial s} & 0 \\[2ex]
& \frac{\kappa GA}{6}\frac{\partial^2}{\partial s^2} & -\frac{\kappa GA}{12}\frac{\partial}{\partial s} \\[2ex]
sym & & \frac{EI}{12}\frac{\partial^2}{\partial s^2}
\end{bmatrix}
$$

$$
+ l^2 \begin{bmatrix}
\frac{EA}{12}\frac{\partial^4}{\partial s^4} - \frac{\kappa GA}{4R^2}\frac{\partial^2}{\partial s^2} & (\frac{EA}{6R} + \frac{\kappa GA}{6R})\frac{\partial^3}{\partial s^3} & -\frac{\kappa GA}{4R}\frac{\partial^2}{\partial s^2} \\[2ex]
& \frac{EA}{4R^2}\frac{\partial^2}{\partial s^2} - \frac{\kappa GA}{12}\frac{\partial^4}{\partial s^4} & \frac{\kappa GA}{6}\frac{\partial^3}{\partial s^3} \\[2ex]
sym & & -\frac{\kappa GA}{4}\frac{\partial^2}{\partial s^2} + \frac{EI}{12}\frac{\partial^4}{\partial s^4}
\end{bmatrix}
$$

$$(5.45)$$

where as before, only truncation order terms through $O(l^2)$ have been retained. Comparison of Eq. (5.45) with Eqs. (5.38) and (5.41) shows that for the first time, the recovered limit differential equilibrium equations do not correspond to the reference continuum operator. The $L_{v\theta}$ and $L_{w\theta}$ terms of the recovered limit differential equations do not correspond to either reference C^0 shell theory. As in dealing with comparisons between any shell theories, the question as to what terms constitute a consistent theory is not an easy one to answer. For the case of C^1, or first approximation shell theory, Koiter [22] showed that a wide variation in shell equations are possibly consistent with the intrinsic errors introduced by employing the basic Kirchhoff-Love assumptions. In the present case, it is not at all clear whether the omission of the above mentioned terms implies a fundamentally inconsistent C^0 discretization.

§5.1.4.3 Limiting Thin Shell Behavior

Since more often than not, C^0 discretizations are used to model thin shell structures, an important question which needs to be addressed is whether in the *thin* shell limit, this approximation is a valid one. The answer to this question can be found by employing the static condensation procedure described in §5.2.2.2 to eliminate the θ *d-o-f* from Eq. (5.43). After performing this decoupling operation, the resulting Fourier transformed matrix operator equation is found to be

$$\hat{L}^{\mathrm{D}} = \hat{L}^{\mathrm{D}}_{\mathrm{Sanders}} + \hat{L}^{\mathrm{D}}_{\mathrm{Transverse\ Shear}} \cdot \tag{5.46}$$

As one might have anticipated, a valid thin shell operator is recovered, along with a "transverse shear" modifying operator. The thin shell operator turns out to be a discrete approximation to Sanders arch equations and is given by

$$\hat{L}^{\mathrm{D}}_{\mathrm{Sanders}} = EA \begin{bmatrix} -(1^m_{vv} + 1^b_{vv}\frac{h^2}{12R^2})\bar{k}^2 & i(1^m_{vw}\frac{1}{R}\bar{k} + 1^b_{vw}\frac{h^2}{12R}\bar{k}^3) \\ sym & 1^m_{ww}\frac{1}{R^2} + 1^b_{ww}\frac{h^2}{12}\bar{k}^4 \end{bmatrix} \tag{5.47}$$

where for this case,

$$1^m_{vv} = \frac{s^2}{l_e^2}\cdot\alpha_1\cdot\cos^2\beta \qquad 1^b_{vv} = \frac{s^2 l^2}{l_e^4}\cdot\alpha_1$$

$$1^m_{vw} = \frac{sl}{l_e^2}\cdot\sqrt{\alpha_1}\cdot\cos\beta \qquad 1^b_{vw} = \frac{s^3 l}{l_e^4}\cdot\sqrt{\alpha_1}\cdot\cos\beta$$

$$1^m_{ww} = \frac{l^2}{l_e^2}\cdot\alpha_1^2 \qquad\qquad 1^b_{ww} = \frac{s^4}{l_e^4}\cdot\cos^2\beta \,.$$

Except for minor differences in several of the unity operators which only effect accuracy, Eq. (5.47) is seen to be identical to Eq. (5.18). The "transverse shear" modifying matrix differential operator is found to be

$$\hat{L}^{\mathrm{D}}_{\mathrm{Transverse\ Shear}} = \epsilon\cdot EA \begin{bmatrix} -1^{\mathrm{TS}}_{vv}\bar{k}^2 & i1^{\mathrm{TS}}_{vw}\frac{1}{R}\bar{k} \\ sym & 1^{\mathrm{TS}}_{ww}\frac{1}{R^2} \end{bmatrix} \tag{5.48}$$

where the unity operators are

$$\mathbf{1}_{vv}^{\mathrm{TS}} = \frac{s^4}{l_e^4}\cos^2\beta \qquad \mathbf{1}_{vw}^{\mathrm{TS}} = \frac{ls^3}{l_e^4}\sqrt{\alpha_1}\cos\beta \qquad \mathbf{1}_{ww}^{\mathrm{TS}} = \frac{l^2 s^2}{l_e^4}\alpha_1$$

and

$$\epsilon = \frac{EI}{\kappa GA}\bar{k}^2 = \frac{(1+\nu)h^2\bar{k}^2}{6\kappa} \cong \frac{2(1+\nu)\pi^2}{3\kappa}\cdot\frac{h^2}{\lambda^2}. \qquad (5.49)$$

Here, we have made use of $\bar{k} \cong k = \frac{2\pi}{\lambda}$ where λ is the wavelength of a solution component.

In the "thin shell limit", if one adopts what Flügge calls the *theory of structures* approach [71], Eq. (5.46) becomes

$$\lim_{\gamma_{sz}\to 0 \,\Rightarrow\, G\to\infty}(\hat{L}_{\mathrm{Sanders}}^{\mathrm{D}} + \hat{L}_{\mathrm{Transverse\ Shear}}^{\mathrm{D}}) = \hat{L}_{\mathrm{Sanders}}^{\mathrm{D}}. \qquad (5.50)$$

Alternatively, by examining ϵ, one can interpret the "thin shell limit" in terms of $\frac{h^2}{\lambda^2} \to 0$ so that the two parameters governing this limiting behavior are the shell's thickness, h, and the wavelength of a solution component, λ. One can therefore conclude that in the thin shell limit, this faceted C^0 arch discretization is in fact consistent with Sanders C^1 arch equations.

§5.2 Cylindrical Shell

In this section, the faceted Reissner-Mindlin plate approximation of the cylindrical shell, as portrayed in Fig. 5.5, will be examined. One intrinsic problem with this geometric approximation, or for that matter, any finite element discretization which does not employ exact physical geometry, is in dealing with rotations about the shell normal, θ_n, engendered by the element nodal transformations employed during the assembly process. This rotational d-o-f corresponds to the "sixth" equilibrium equation representing moment equilibrium about the shell normal – which has been a continual source of trouble, even from a classical shell standpoint (see e.g., [75]). Since the usual shell (or plate) element has no stiffness associated with

153
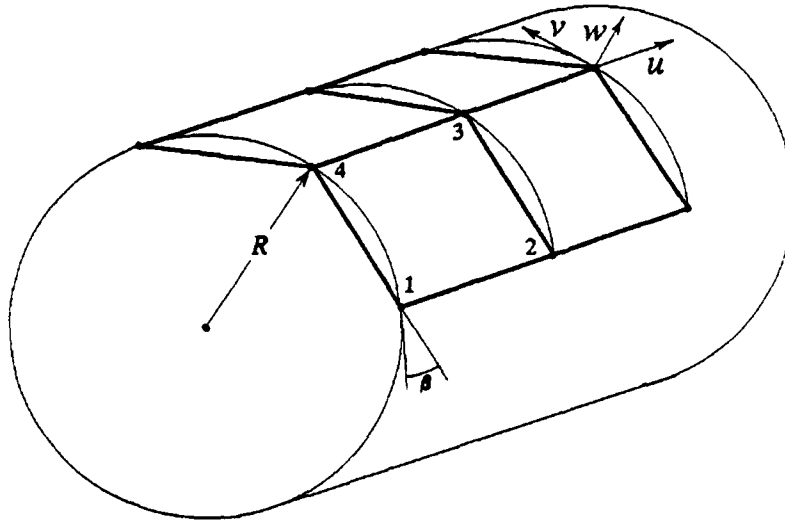
Fig. 5.5 – Faceted plate discretization of cylindrical shell

this d-o-f[5], numerical ill-conditioning may be introduced into the finite element analysis, depending upon the juncture angle, if this rotational d-o-f is retained in the global system. Common practice has therefore been to suppress θ_n in the assembled equations. In the present case of the cylindrical shell discretization, the effect of suppressing θ_n would be an overstiffening of the θ_x d-o-f due to the nodal transformation which links θ_x with θ_n.

The reference C^0 equilibrium equations to be employed here are from Naghi-Cooper's work on cylindrical shells [73] with the material operator, L_{m}, written in the following symmetric form,

$$L_{\mathrm{m}} = \begin{bmatrix} L_{mm} & L_{mb} \\ L_{mb}^{\mathrm{T}} & L_{bb} \end{bmatrix} \tag{5.51}$$

where L_{mm}, L_{mb} and L_{bb} are used to denote the following membrane, mem-

---

[5] Recent work by Bergan and Felippa [76] addresses this problem by linking θ_n to the membrane strain energy.

154

brane/bending and bending matrix differential operators

$$L_{mm} = \begin{bmatrix} Kd_x^2 + (K_{11} + \dfrac{D_{11}}{R^2})d_s^2 & K_{12}d_x d_s \\ sym & K_{11}d_x^2 + Kd_s^2 - \dfrac{\kappa GA}{R^2} \end{bmatrix}$$

$$L_{mb} = \begin{bmatrix} K\dfrac{\nu}{R}d_x & -\dfrac{D}{R}d_x^2 + \dfrac{D_{11}}{R}d_s^2 & 0 \\ (\dfrac{K}{R} + \dfrac{\kappa GA}{R})d_s & 0 & \dfrac{D}{R}d_s^2 - \dfrac{D_{11}}{R}d_x^2 - \dfrac{\kappa GA}{R} \end{bmatrix}$$

$$L_{bb} = \begin{bmatrix} -\kappa GA\nabla^2 + \dfrac{K}{R^2} & \kappa GAd_x & (\dfrac{D}{R^2} + \kappa GA)d_s \\ & Dd_x^2 + D_{11}d_s^2 - \kappa GA & D_{12}d_x d_s \\ sym & & D_{11}d_x^2 + Dd_s^2 - \kappa GA \end{bmatrix}$$
$$(5.52)$$

with

$$K = \frac{EA}{1-\nu^2} \qquad K_{11} = \frac{1-\nu}{2}K \quad K_{12} = \frac{1+\nu}{2}K$$
$$D = \frac{EA^3}{12(1-\nu^2)} \quad D_{11} = \frac{1-\nu}{2}D \quad D_{12} = \frac{1+\nu}{2}D$$

and $\nabla^2 = d_x^2 + d_s^2$. The shell displacement field and distributed load vector are
defined by

$$u = \begin{Bmatrix} u \\ v \\ w \\ \theta_x \\ \theta_y \end{Bmatrix} ; \qquad f = \begin{Bmatrix} -p_x \\ -p_s \\ p \\ 0 \\ 0 \end{Bmatrix} . \qquad (5.53)$$

Transforming Eq. (5.51) using

$$u(x,s) = \hat{u}(k_x, k_s)\, e^{i(k_x x + k_s s)} \qquad (5.54)$$

155

results in

$$\hat{L}_{mm} = \begin{bmatrix} -Kk_x^2 - (K_{11} + \frac{D_{11}}{R^2})k_s^2 & -K_{12}k_x k_s \\ sym & -K_{11}k_x^2 - Kk_s^2 - \frac{\kappa GA}{R^2} \end{bmatrix}$$

$$\hat{L}_{mb} = \begin{bmatrix} K\frac{\nu}{R}ik_x & \frac{D}{R}k_x^2 - \frac{D_{11}}{R}k_s^2 & 0 \\ (\frac{K}{R} + \frac{\kappa GA}{R})ik_s & 0 & -\frac{D}{R}k_s^2 + \frac{D_{11}}{R}k_x^2 - \frac{\kappa GA}{R} \end{bmatrix}$$

$$\hat{L}_{bb} = \begin{bmatrix} -\kappa GA\hat{\nabla}^2 + \frac{K}{R^2} & \kappa GAik_x & (\frac{D}{R^2} + \kappa GA)ik_s \\ & -Dk_x^2 - D_{11}k_s^2 - \kappa GA & -D_{12}k_x k_s \\ sym & & -D_{11}k_x^2 - Dk_s^2 - \kappa GA \end{bmatrix}$$

$$(5.55)$$

with $\hat{\nabla} = -(k_x^2 + k_s^2)$. These equations are the transformed reference equations for the material operator which will be compared to the discrete equations derived in §5.2.2.

§5.2.1 Derivation of Flat Reissner-Mindlin Plate Shell Element

In §4.2, derivation of the 12 *d-o-f* Reissner-Mindlin plate bending element was described. In this section, a bi-linear membrane stiffness will be added to this element to form a 20 *d-o-f* general plate bending element which will be used to discretize the cylindrical shell as portrayed in Fig. 5.5. As was the case for the arch analysis employing straight elements, there is no membrane/bending coupling at the element level.

By including inplane deformation effects, the plate displacement field becomes

$$u(x,y,z) = u(x,y) - z\theta_x(x,y)$$
$$v(x,y,z) = v(x,y) - z\theta_y(x,y) \qquad (5.56)$$
$$w(x,y,z) = w(x,y)$$

where x, y and z refer to a local plate-oriented coordinate system. With the addition of the in-plane displacements, u and v, the element displacement vector

is rewritten as

$$u = \mathbf{N}_i \mathbf{d}_i \,; \quad i = 1, 4 \tag{5.57}$$

with $\mathbf{d}_i = \lfloor u_i \quad v_i \quad w_i \quad \theta_{x_i} \quad \theta_{y_i} \rfloor^T$ and $\mathbf{N}_i = N_i \mathbf{I}_5$ where

$$N_i = \frac{1}{4}(1 + \xi_i \xi)(1 + \eta_i \eta) \,; \quad \begin{cases} \xi_i = (-1, 1, 1, -1) \\ \eta_i = (-1, -1, 1, 1) \,. \end{cases} \tag{5.58}$$

Based upon an isoparametric element derivation, the element's material stiffness is comprised of the following components,

$$\mathbf{k} = \underbrace{\mathbf{k}_b + \mathbf{k}_s}_{\mathbf{k}_{U1}} + \mathbf{k}_m + \mathbf{k}_{ms} \tag{5.59}$$

where $\mathbf{k}_{U1}$ is the uniformly-reduced integrated plate bending stiffness[6] from §4.2, except for the d-o-f reordering due to the changes noted above in $\mathbf{d}$. The membrane stiffness contribution is broken into two parts, $\mathbf{k}_m$, which may be either fully (2x2) or uniformly-reduced integrated (1x1), and $\mathbf{k}_{ms}$, which is usually integrated with a (1x1) rule in order to alleviate membrane shear locking [77]. The isoparametric strain-displacement matrices, $\mathbf{B}_m$ and $\mathbf{B}_{ms}$, are derived from

$$\boldsymbol{\epsilon} = \left\{ \begin{array}{c} \epsilon_x \\ \epsilon_y \\ \gamma_{xy} \end{array} \right\} = \left\{ \begin{array}{c} \mathbf{B}_m \\ \mathbf{B}_{ms} \end{array} \right\} \mathbf{d} \quad \Rightarrow \quad \begin{cases} \mathbf{B}_{m_i} = \begin{bmatrix} \frac{\partial N_i}{\partial x} & 0 & 0 & 0 & 0 \\ 0 & \frac{\partial N_i}{\partial y} & 0 & 0 & 0 \end{bmatrix} \\ \mathbf{B}_{ms_i} = \begin{bmatrix} \frac{\partial N_i}{\partial y} & \frac{\partial N_i}{\partial x} & 0 & 0 & 0 \end{bmatrix} \,. \end{cases} \tag{5.60}$$

Note that on the element level, there is no strain energy associated with a normal rotation and hence no θ_n d-o-f need appear at the element level. The isotropic membrane material matrices are

$$\mathbf{D}_m = K \begin{bmatrix} 1 & \nu \\ \nu & 1 \end{bmatrix} \quad \text{and} \quad D_{ms} = \kappa G A \,. \tag{5.61}$$

---

[6] The subsequent symbolic analysis is identical *irrespective* of which 4-node C^0 plate bending element is used here.

For the case of the element's geometric stiffness, two obvious formulation possibilities exist. The first is simply to use the plate's k_σ, Eq. (4.p220), neglecting any contributions from the membrane displacements, u and v. The second possibility is to include the nonlinear terms in k_σ associated with u and v. An interesting note by Koiter [78] discussing the buckling of short cylinders ($L^2/Rh \ll 1$) indicates that contrary to earlier work, all terms must be included, which is the approach taken here. With this approach, the geometric stiffness becomes

$$\mathbf{k}_\sigma = \iint_A \mathbf{B}_\sigma^T \begin{bmatrix} hs & 0 & 0 & 0 & 0 \\ 0 & hs & 0 & 0 & 0 \\ 0 & 0 & hs & 0 & 0 \\ 0 & 0 & 0 & Is & 0 \\ 0 & 0 & 0 & 0 & Is \end{bmatrix} \mathbf{B}_\sigma \, dA \qquad (5.62)$$

where $\mathbf{B}_\sigma$ now represents an expanded [10x20] form of $\mathbf{B}_\sigma$ found in §4.2 with

$$\mathbf{s} = \begin{bmatrix} \sigma_x & \tau_{xy} \\ \tau_{xy} & \sigma_y \end{bmatrix}$$

remaining the same.

The element transformation matrix used to transform this planar element with 5 d-o-f per node to the cylindrical shell geometry shown in Fig. 5.5 with 6 d-o-f per node is given by

$$\Lambda_i = \begin{bmatrix} 1 & 0 & 0 & 0 & 0 \\ 0 & \cos\psi_i & \sin\psi_i & 0 & 0 \\ 0 & -\sin\psi_i & \cos\psi_i & 0 & 0 \\ 0 & 0 & 0 & \cos\psi_i & 0 \\ 0 & 0 & 0 & 0 & 1 \\ 0 & 0 & 0 & \sin\psi_i & 0 \end{bmatrix} \qquad (5.63)$$

where $\psi_i = \beta$ for element nodes 1 and 2, and $\psi_i = -\beta$ for nodes 3 and 4 for each of the four elements in the patch. With this transformation operation, the 20 d-o-f plate element has now been transformed into a 24 d-o-f flat shell element, including the θ_n d-o-f which can now be eliminated at the global level, if required for numerical stability.

158

§5.2.2 Discrete Fourier Results for Material Operator

The transformed limit differential equilibrium equations for this faceted, flat plate discretization of the cylindrical shell were determined from the symbolic analysis[7] to be

$$
\hat{L}_{\mathrm{m}}^{D} = \begin{bmatrix} \begin{bmatrix} \hat{L}_{mm}^{D} & \hat{L}_{mb}^{D} \\ sym & \hat{L}_{bb}^{D} \end{bmatrix} & \begin{matrix} \hat{L}_{mn}^{D} \\ \hat{L}_{bn}^{D} \end{matrix} \\ sym & \hat{L}_{nn}^{D} \end{bmatrix}, \tag{5.65}
$$

for the case of a selective-reduced integrated membrane stiffness used in conjunction with the U1 plate bending element. In addition to the discrete approximation of the membrane, membrane/bending and bending operators, we also find ourselves with operators associated with θ_n which are included here for completeness. The individual matrix differential operators were found to be

$$
\hat{L}_{mm}^{D} = \begin{bmatrix} -1_{uu}^{(1)} K \bar{k}_x^2 - 1_{uu}^{(2)} K_{11} \bar{k}_s^2 & -1_{uv} K_{12} \bar{k}_x \bar{k}_s \\ sym & -1_{vv}^{(1)} K_{11} \bar{k}_x^2 - 1_{vv}^{(2)} K \bar{k}_s^2 - 1_{vv}^{(3)} \frac{\kappa GA}{R^2} \end{bmatrix}
$$

$$
\hat{L}_{mb}^{D} = \begin{bmatrix} 1_{uw} K \frac{\nu}{R} i \bar{k}_x & 0 & 0 \\ (1_{vw}^{(1)} \frac{K}{R} + 1_{vw}^{(2)} \frac{\kappa GA}{R}) i \bar{k}_s & 0_{v\theta_x} & -1_{v\theta_y} \frac{\kappa GA}{R} \end{bmatrix}
$$

$$
\hat{L}_{bb}^{D} = \begin{bmatrix} -1_{ww}^{(1)} \kappa GA \tilde{\nabla}^2 + 1_{ww}^{(2)} \frac{K}{R^2} & 1_{w\theta_x} \kappa GA i \bar{k}_x & 1_{w\theta_s} \kappa GA i \bar{k}_s \\ & -1_{\theta_x\theta_x}^{(1)} D \bar{k}_x^2 - 1_{\theta_x\theta_x}^{(2)} D_{11} \bar{k}_s^2 & -1_{\theta_x\theta_y} D_{12} \bar{k}_x \bar{k}_s \\ & -1_{\theta_x\theta_x}^{(3)} \kappa GA & \\ & & -1_{\theta_x\theta_x}^{(1)} D_{11} \bar{k}_x^2 \\ sym & & -1_{\theta_x\theta_x}^{(2)} D \bar{k}_s^2 \\ & & -1_{\theta_x\theta_x}^{(3)} \kappa GA \end{bmatrix}
$$

---

[7] The symbolic analysis for this faceted discretization of the cylindrical shell is shown in Appendix A.4

159

$$\hat{L}^{D}_{mn} = \begin{bmatrix} 0 \\ -\kappa GA \frac{l^2 s^2}{16R^2}\sqrt{\alpha_{z4}}\, i\bar{k}_z\bar{k}_s^2 \end{bmatrix}$$

$$\hat{L}^{D}_{bn} = \begin{bmatrix} \kappa GA \frac{ls}{4R}\cos\beta\sqrt{\alpha_{z4}}\sqrt{\alpha_{s4}}\,\bar{k}_z\bar{k}_s \\ -D\frac{s}{lR}\cos\beta\sqrt{\alpha_{s4}}\,i\bar{k}_s(\frac{1-\nu}{2} - \frac{3-\nu}{8}l^2\bar{k}_z^2) + \kappa GA\frac{ls}{4R}\cos\beta\sqrt{\alpha_{s4}}\,\alpha_{z4}i\bar{k}_s \\ -\frac{D}{R}\sqrt{\alpha_{z4}}\cos\beta\, i\bar{k}_z(\frac{1-\nu}{2} - \frac{1+\nu}{8}s^2\bar{k}_s^2) \end{bmatrix}$$

$$\hat{L}^{D}_{nn} = D\frac{l^2 s^2}{16R^2}\bar{k}_z^2\bar{k}_s^2 + \frac{D_{11}}{R^2}\alpha_{z4}\alpha_{s4} + \kappa GA\frac{l^2 s^2}{16R^2}\alpha_{z4}\bar{k}_s^2$$

where the different unity operators are defined as

$$1^{(1)}_{uu} = \alpha_{s6} \qquad\qquad 1^{(2)}_{uu} = \frac{s^2}{l^2}\alpha_{z4}$$

$$1_{uv} = \frac{s}{l}\cos\beta\sqrt{\alpha_{z4}}\sqrt{\alpha_{s4}}$$

$$1_{uw} = \sqrt{\alpha_{z4}}(1 - \frac{1+\nu}{8\nu}s^2\bar{k}_s^2)$$

$$1^{(1)}_{vv} = \cos^2\beta\,\alpha_{s4} \qquad\qquad 1^{(2)}_{vv} = \frac{s^2}{l^2}\cos^2\beta\,\alpha_{z6}$$

$$1^{(3)}_{vv} = (1 - \frac{s^2}{4}\bar{k}_s^2 - \frac{l^2}{4}\bar{k}_z^2 + \frac{s^2 l^2}{8}\bar{k}_z^2\bar{k}_s^2)$$

$$1^{(1)}_{vw} = \frac{s}{l}\cos\beta\sqrt{\alpha_{s4}}(1 - \frac{7-3\nu}{24}l^2\bar{k}_z^2) \qquad 1^{(2)}_{vw} = \frac{s}{l}\cos\beta\,\alpha_{z2}\sqrt{\alpha_{s4}}$$

$$0_{v\theta_x} = \frac{\kappa GA}{4R}ls\cos\beta\sqrt{\alpha_{z4}}\sqrt{\alpha_{s4}}\,\bar{k}_z\bar{k}_s$$

$$1_{v\theta_y} = \sqrt{\alpha_{z4}}\sqrt{\alpha_{s4}}$$

$$1^{(1)}_{ww} = \cos^2\beta \qquad\qquad 1^{(2)}_{ww} = (1 - \frac{s^2}{4}\bar{k}_s^2 - \frac{l^2}{6}\bar{k}_z^2 + \frac{7-3\nu}{96}s^2 l^2\bar{k}_z^2\bar{k}_s^2)$$

$$1_{w\theta_x} = \cos^2\beta\,\alpha_{s4}\sqrt{\alpha_{z4}}$$

$$1_{w\theta_y} = \frac{s}{l}\cos\beta\,\alpha_{z4}\sqrt{\alpha_{s4}}$$

$$1^{(1)}_{\theta_x\theta_x} = \cos^2\beta\,\alpha_{s4} \qquad\qquad 1^{(2)}_{\theta_x\theta_x} = \frac{s^2}{l^2}\cos^2\beta\,\alpha_{z4} \qquad 1^{(3)}_{\theta_x\theta_x} = \cos^2\beta\,\alpha_{z4}\alpha_{s4}$$

$$1_{\theta_x\theta_y} = \frac{s}{l}\cos\beta\sqrt{\alpha_{z4}}\sqrt{\alpha_{s4}}$$

$$1^{(1)}_{\theta_y\theta_y} = \alpha_{s4} \qquad\qquad 1^{(2)}_{\theta_y\theta_y} = \frac{s^2}{l^2}\alpha_{z4} \qquad\qquad 1^{(3)}_{\theta_y\theta_y} = \alpha_{z4}\alpha_{s4}$$

with

$$\tilde{\nabla} = -(\bar{k}_z^2 + \frac{s^2}{l^2}\alpha_{z2}\bar{k}_s^2)$$

and

$$\alpha_{(x,s)n} = 1 - \frac{(l^2 \quad s^2)}{n} \bar{k}^2_{(x,s)} \, .$$

For the case when uniform-reduced integration is also employed for the membrane stiffness, the following changes in the above unity operators are found to take place,

$$\mathbf{1}^{(1)}_{uu} = \alpha_{s4}$$

$$\mathbf{1}^{(2)}_{vv} = \frac{s^2}{l^2} \cos^2\beta \, \alpha_{x4}$$

$$\mathbf{1}^{(1)}_{vw} = \frac{s}{l} \cos\beta \sqrt{\alpha_{s4}} \left(1 - \frac{3-\nu}{8} l^2 \bar{k}^2_x\right)$$

$$\mathbf{1}^{(2)}_{ww} = \left(1 - \frac{s^2}{4}\bar{k}^2_s - \frac{l^2}{4}\bar{k}^2_x + \frac{3-\nu}{32}s^2 l^2 \bar{k}^2_x \bar{k}^2_s\right) \, .$$

Comparing Eq. (5.65) with Eq. (5.51), one observes that this discrete approximation is not consistent with Naghdi-Cooper's shell equations, which is perhaps not too surprising in light of the results from the earlier arch analysis in §5.1.4.2. Neglected terms may be insignificant if the assumption that

$$\frac{h^2}{R^2} \ll 1$$

and

$$\frac{h^3}{\lambda^2 R} \approx 0$$

holds, which would be the case in most practical applications. In the spirit of Koiter's work [22] on first approximation shell theory, these missing terms may not render this discretization inconsistent in terms of the higher-order approximation to Love's first approximation theory represented by relaxing the C^1 continuity constraint permitting transverse shear deformation to occur.

161

Integration Rule		Spurious Modes
Membrane	Bending	
f	f	no
f	sr	no
f	ur	yes
sr	f	no
sr	sr	no
sr	ur	yes
ur	f	yes
ur	sr	yes
ur	ur	yes

Table 5.1 Effect of spatial integration rule on the presence of spurious modes: f = full (2x2) integration; sr = full (2x2) integration of direct strains, reduced (1x1) on shear terms; ur = uniform reduced (1x1) integration.

An interesting aspect of the membrane/bending coupling engendered by element asssembly is the possible suppression of spurious element mechanisms. By simply determining whether $|L_m| \neq 0$ for $k_x = \pi/l$ and $k_s = \pi/s$, one can determine whether communicable spurious element mechanisms will exist for a particular choice of integration rules irrespective of the choice of boundary conditions. In the present case, nine possibilities exist if one considers full, selectively/reduced and uniformly reduced rules for the membrane and bending stiffnesses, as is shown in Table 5.1. The S1 plate bending element used in conjunction with the selectively/reduced integrated membrane stiffness is seen to become a viable analysis option for this particular physical geometry with the disappearance of the w-hourglass mode discussed in Chapter 4.

§5.2.3 Discrete Fourier Results for Buckling Operator

Employing the geometric stiffness symbolically obtained from Eq. (5.62) re-

sults in the following discrete Fourier transformed buckling operator

$$\hat{L}_\sigma = \begin{bmatrix} \hat{L}_{uu} & 0 & 0 & 0 & 0 \\ 0 & \hat{L}_{vv} & \hat{L}_{vw} & 0 & 0 \\ & & \hat{L}_{ww} & 0 & 0 \\ & & & \hat{L}_{\theta_x\theta_x} & 0 \\ & sym & & & \hat{L}_{\theta_s\theta_s} \end{bmatrix} \qquad (5.66)$$

where

$$\hat{L}_{uu} = -\alpha_{s6}h\sigma_x\bar{k}_x^2 - \frac{s^2}{l^2}\alpha_{x6}h\sigma_y\bar{k}_s^2 - 2\frac{s}{l}\sqrt{\alpha_{s4}}\sqrt{\alpha_{x4}}h\sigma_{xy}\bar{k}_x\bar{k}_s$$

$$\hat{L}_{vv} = -[\cos^2\beta\alpha_{s6} + \frac{l^2}{12R^2}(1 + \frac{s^2}{2}\bar{k}_s^2)]h\sigma_x\bar{k}_x^2$$
$$- [\frac{1}{R^2}\alpha_{s4} + \frac{s^2}{l^2}\cos^2\beta\alpha_{x6}\bar{k}_s^2 - \frac{l^2}{6R^2}\alpha_{s4}\bar{k}_x^2]h\sigma_y$$
$$- [2\frac{s}{l}\sqrt{\alpha_{s4}}\sqrt{\alpha_{x4}}\cos^2\beta - \sqrt{\alpha_{s4}}\sqrt{\alpha_{x4}}\frac{ls}{2R^2}]h\sigma_{xy}\bar{k}_x\bar{k}_s$$

$$\hat{L}_{vw} = -\frac{\sqrt{\alpha_{s4}}\cos\beta ls}{3R}i\bar{k}_x^2\bar{k}_sh\sigma_x + \frac{2s}{lR}\sqrt{\alpha_{s4}}\alpha_{x6}\cos\beta i\bar{k}_sh\sigma_y + \frac{2\alpha_{s2}\sqrt{\alpha_{x4}}\cos\beta}{R}i\bar{k}_xh\sigma_{xy}$$

$$\hat{L}_{ww} = [\alpha_{s6}\cos^2\beta + \frac{l^2}{12R^2}(1 + \frac{s^2}{2}\bar{k}_s^2)]h\sigma_x\bar{k}_x^2$$
$$+ [\frac{1}{R^2}\alpha_{s4} + \frac{s^2}{l^2}\cos^2\beta\alpha_{x6}\bar{k}_s^2 - \frac{l^2}{6R^2}\alpha_{s4}\bar{k}_x^2]h\sigma_y$$
$$+ [2\frac{s}{l}\sqrt{\alpha_{s4}}\sqrt{\alpha_{x4}}\cos^2\beta - \sqrt{\alpha_{s4}}\sqrt{\alpha_{x4}}\frac{ls}{2R^2}]h\sigma_{xy}\bar{k}_x\bar{k}_s$$

$$\hat{L}_{\theta_x\theta_x} = -\alpha_{s6}\cos^2\beta I\sigma_x\bar{k}_x^2 - \frac{s^2}{l^2}\cos^2\beta\alpha_{x6}I\sigma_y\bar{k}_s^2 - 2\frac{s}{l}\cos^2\beta\sqrt{\alpha_{s4}}\sqrt{\alpha_{x4}}I\sigma_{xy}\bar{k}_x\bar{k}_s$$

$$\hat{L}_{\theta_y\theta_y} = -\alpha_{s6}I\sigma_x\bar{k}_x^2 - \frac{s^2}{l^2}\alpha_{x6}I\sigma_y\bar{k}_s^2 - 2\frac{s}{l}\sqrt{\alpha_{s4}}\sqrt{\alpha_{x4}}I\sigma_{xy}\bar{k}_x\bar{k}_s$$

163
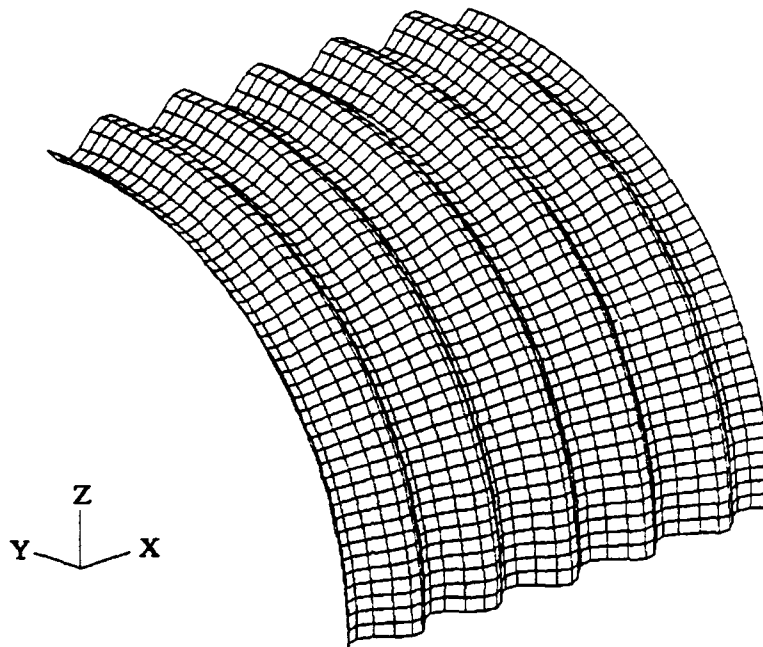
Fig. 5.6 – Axisymmetric buckling mode for $m = 11$ for quarter-cylinder ($R = 36$in., $L = 50.26$in., $h = .12$in., $E = 10^7$psi and $\nu = .3$) finite element model discretized with $n_{el} = 40$.

§5.2.4 Axisymmetric Buckling – Finite Element Validation

Having found the discrete material and buckling operators for this faceted cylindrical shell discretization, a direct comparison of predicted buckling loads derived from the symbolic analysis with finite element results can now be made. The axisymmetric buckling of a thin, axially-compressed cylinder, as is portrayed in Fig. 5.6, will be used to evaluate the ability of these discrete Fourier techniques to succinctly capture finite element behavior. Unlike earlier comparisons where the continuum equations were employed to derive error estimates, the present comparisons will be directly between symbolic predictions and finite element results.

For the case of a finite length cylinder, the displacement field for a buckling
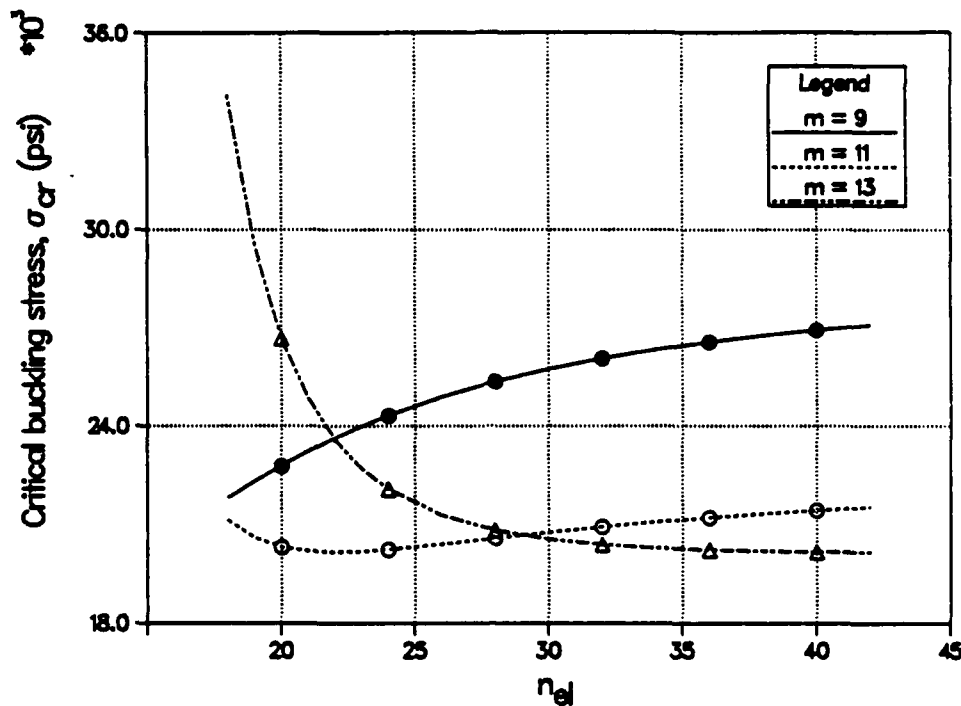
Fig. 5.7 – Critical buckling stress *vs.* n_{el}, for the axisymmetric buckling of the cylindrical shell shown in Fig. 5.6 for $m = 9$, 11 and 13 axial half-waves.

mode is represented by

$$u = \left(\hat{u}_R - i\hat{u}_I\right) e^{i\left(k_z + k_s\right)} = \left(\hat{u}_R - i\hat{u}_I\right) e^{i\left(\frac{m\pi}{L}z + n\theta\right)}, \qquad (5.67)$$

where a complex representation of $\hat{u}$ agains becomes a necessity in order to derive numerical results. For axisymmetric buckling, the following simplifications to Eqs. (5.65) and (5.66),

$$v = \theta_y = \theta_n = 0 \qquad (5.68)$$

are made prior to computing the critical buckling stresses. This same simplification was also employed for the finite element analysis.

The results of this comparison of symbolic *vs.* finite element calculated bifurcation buckling loads is shown in Fig. 5.7 where the critical buckling stess is plotted *vs.* n_{el}, the number of elements in the axial direction, for three different

integer wave numbers, $m = 9$, 11 and 13. The continuous curves represent the symbolic results for the different n_{el}, while symbols are used to represent finite element calculations. The finite element results were calculated employing a $2 \times n_{el}$ finite element mesh which exactly represents the axisymmetric buckling of the cylindrical shell. From a strictly finite element standpoint, this plot graphically demonstrates the mode-switching phenomena exhibited by finite element analyses employing successively refined mesh discretizations. The symbolically-derived predictions are seen to exactly represent this complex mode switching behavior. The fidelity to which this symbolic technique is able to capture finite element behavior is remarkable if one considers the "non-smoothness" of the discrete eigenvectors such as is shown in Fig. 5.8 for $m = 11$ and $n_{el} = 20$.
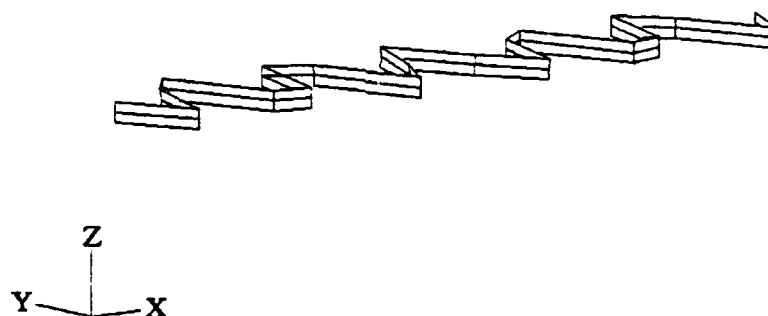
Fig. 5.8 – Axisymmetric buckling mode for $m = 11$ for finite element model with $n_{el} = 20$.

§5.3 Summary

Unlike earlier results where one had to contend only with physical modeling errors, results presented in this chapter show that the additional complexity of approximate element geometry encountered in shell analysis provides no barrier to the application of these symbolic element evaluation techniques to regular mesh

discretizations. Discretization errors originating from both sources are seen to be explicitly captured by the discrete Fourier element evaluation techniques employed here. This accuracy is particularly amazing in light of the extremely "rough" finite element solutions which in some cases, the symbolic analysis is seen to model.

Conclusions

This chapter concludes this dissertation with a summary of the technical highlights presented in this investigation, a brief synopsis of the key technical contributions made to this area of research, and lastly, describes areas of future research.

§6.1 General Comments (Technical Highlights)

The objective of this dissertation was the development of the symbolic analysis methodology and associated computer algebra procedures which would be employed to determine the *intrinsic* behavior of general multi-degree-of-freedom finite element discretizations in the interior problem domain. The scope of the present work was necessarily limited for the most part to linear, displacement-based "structural" finite elements – bars, beams, plates and shells – in order to both develop the methodology and demonstrate the symbolic analysis techniques for representative one, two and three dimensional element formulations.

This objective was accomplished by systematically extending finite difference-based analysis evaluation methods based upon both Taylor series and discrete Fourier analysis to the multi-degree-of-freedom finite element discretization problem. By adopting the finite difference view of the finite element method as simply

another way of deriving discrete difference equations, formulation details become immaterial since all aspects of the discretization process which contribute to the accuracy of the finite element solution are uniquely embodied in the resulting difference equations. Thus, the inability often times to derive global mathematical proofs of convergence for different nonconforming elements, modified interpolation schemes, spatial integration rules, numerical techniques (a.k.a. "tricks"), and miscellaneous variational crimes as they arise in practice, is thereby completely bypassed. As a result, this symbolic approach to element evaluation shares to same element-independent generality as does the patch test, albeit, it has thus far only been applied to regular mesh discretizations.

The results of these computer-aided symbolic analyses of "structural" finite elements are the limit differential equilibrium equations governing element behavior for the associated boundary-value problems from which it is shown that one is able to 1) verify formulation consistency and stability and thus solution convergence, 2) derive component-wise error estimates for the primary solution variables, and 3) open the way for improved element performance by the proper synthesis of element operators.

§6.2 Summary of Contributions

Specific technical contributions made in this dissertation were:

1) **Element-independent symbolic analysis procedures developed** – The symbolic element evaluation techniques presented herein are generally applicable to any finite element formulation – displacement-based, mixed, hybrid, solids, fluids, heat transfer, etc.

2) **Application of computer algebra to symbolic finite element evaluation procedures** – Symbolic analysis procedures were implemented for the different classes of element evaluation problems evaluated in this investigation. Both MACSYMA and SMP were used with sample runstreams shown in Appendix A.

169

3) **A priori error estimates developed using consistently derived loading operator** – The present analysis correctly handles the loading operator permitting physically correct a priori error predictions to be determined employing both Taylor series and discrete Fourier symbolic analysis techniques.

4) **Stummel's Problem** – The evaluation of Stummel's problem, which has been the source of much controversy in the finite element community, proved to be an almost trival application of the present element evaluation techniques. Stummel's nonconforming element, which passed Strang's version of the patch test yet did not converge, was shown not to be a convergent approximation since it satisfied neither consistency nor stability requirements.

5) **Symbolic analysis used to evaluate different hourglass control techniques** – The precise effect of hourglass control techniques on the limit differential equilibrium equations and hence on the discrete solution was explicitly identified without recourse to numerical experimentation.

6) **Symbolic analysis procedures extended to bifurcation buckling problems** – The present symbolic analysis procedures are shown to be directly applicable to the bifurcation buckling problem. For the case of periodic boundary conditions, a priori error estimates resulting from the discrete Fourier technique are shown to exactly predict finite element behavior.

7) **Faceted beam element approximation of arch** – Consistency of the straight beam approximation to the circular arch with Sanders' shell equations was demonstrated for both Hermitian and Timoshenko beam discretizations. The advantage of using the arc length in the element formulation *vs.* the element's actual chord length was shown to result in a more accurate finite element solution.

8) **Faceted Reissner-Mindlin plate approximation of cylindrical shell** – The transformed limit differential equilibrium equations governing this approximation were derived including the effect of the normal rotation degree-

of-freedom. It was shown that this approximation was not consistent with Naghi-Cooper cylindrical shell theory. Bifurcation buckling loads derived from the discrete Fourier results for axisymmetric buckling were found to nearly exactly reproduce finite element results including the complex mode switching phenomena encountered when using nonconverged meshes.

§6.3 Future Research

Due to the complexity of developing this element-independent analysis methodology encompassing both symbolic analysis procedures and interpretation, only a very limited subset of potential applications could be investigated in any detail. As a result, further research in a number of different areas remains to be pursued:

1) **Convergence of secondary element quantities** – The present analysis only addressed the convergence of the primary analysis variables, namely, translational and rotational displacements for the displacement-based elements investigated. Convergence of secondary variable fields, such as stress and strain fields, needs to be addressed.

2) **Higher-order element interpolation fields** – Only 2-node one dimensional elements and 4-node two dimensional element discretizations were employed in the present analysis. While these represent extremely popular element families due to their computational efficiency, higher-order elements also need to be examined for two primary reasons: a) higher-order elements offer a more exact geometric model description, and b) in some applications with rapid spatial loading variations or geometric discontinuities, increased solution accuracy may be realized by employing higher-order element interpolation fields.

3) **Effect of mesh distortion** – Employing distorted meshes is an unfortunate modeling necessity in many problems. Eventhough *h*-type adaptive mesh refinement schemes presently under development will mesh a model to the greatest extent possible with regular element geometries, there will always be

regions where distorted elements will be used. As a result, the effect of element distortion on the interpretation of the present symbolic analysis results needs to be investigated.

4) **Application to other fields** – This last item represents the ideal note on which to conclude this investigation. As a result of the generality of the present symbolic element evaluation techniques, there would appear to be no reason why they could not be employed in other fields where finite elements are being used. One extremely important area in which finite elements are just beginning to make an inroad is that of Computational Fluid Dynamics (CFD). Many of the problems encountered in Structures have their counterparts in Fluids, e.g., spurious mechanisms and incompressibility, so that extensions of the present techniques to CFD problems would appear to be a nature progression of this research.

References

[1] G. P. Bazeley, Y. K. Cheung, B. M. Irons and O. C. Zienkiewicz, "Triangular Elements in Plate Bending. Conforming and Nonconforming Solutions," Proceedings *1st Conf. Matrix Methods in Structural Mechanics*, AFFDL-TR-CC-80, Wright Patterson A. F. Base, Ohio, 1966, pp. 547-576.

[2] R. H. MacNeal and R. L. Harder, "A Proposed Standard Set of Problems to Test Finite Element Accuracy," *Finite Elements in Analysis and Design*, Vol. 1, 1985, 3-20.

[3] W. M. Mair, "The Objective of the National Agency for Finite Element Methods and Standards," *Computers & Structures*, Vol. 21, No. 5, pp. 875-879.

[4] R. L. Taylor, J. C. Simo, O. C. Zienkiewicz and A. C. H. Chan, "The Patch Test – A Condition for Assessing FEM Convergence," *International Journal for Numerical Methods in Engineering*, Vol. 22, 1986, pp. 39-62.

[5] F. Stummel, "The Limitations of the Patch Test," *International Journal for Numerical Methods in Engineering*, Vol. 15, 1980, pp. 177-188.

[6] G. Strang and G. Fix, *An Analysis of the Finite Element Method*, Prentice-Hall, 1973.

[7] P. G. Ciarlet, *The Finite Element Method for Elliptic Problems*, North-Holland, 1978.

[8] J. T. Oden and J. N. Reddy, *An Introduction to the Mathematical Theory of Finite Elements*, Wiley-Interscience, 1976.

[9] M. Bernadou, "Some Finite Element Approximations of Thin Shell Problems," *Finite Element Methods for Plate and Shell Structures*, T. J. R. Hughes and E. Hinton, eds., Pineridge Press, 1986.

[10] R. D. Richtmyer and K. W. Morton, *Difference Methods for Initial-Value Problems*, Second Edition, Interscience Publishers, New York, 1967.

[11] C. W. Hirt, "Heuristic Stability Theory for Finite-Difference Equations," *Journal of Computational Physics*, Vol. 2, 1968, pp. 339-355.

[12] R. F. Warming and B. J. Hyett, "The Modified Equation Approach to the Stability and Accuracy Analysis of Finite-Difference Methods," *Journal of Computational Physics*, Vol. 14, 1974, pp. 159-179.

[13] J. E. Walz, R. E. Fulton and N. J. Cyrus, "Accuracy and Convergence of Finite Element Approximations," Proc. of the *Second Conference on Matrix Methods in Structural Mechanics*, AFFDL TR-68-150, WPAFB, Dayton, OH, 1968, 995-1027.

[14] G. Strang and G. Fix, "A Fourier Analysis of the Finite Element Variational Method," CIME Advanced Summer Institute, Corso tenuto ad Erice dal 27 giugno al 7 luglio 1971, pp. 795-840.

[15] K. C. Park and D. L. Flaggs, "An Operational Procedure for the Symbolic Analysis of the Finite Element Method", *Computer Methods in Applied Mechanics and Engineering*, Vol. 42, 1984, pp. 37-46.

[16] K. C. Park and D. L. Flaggs, "A Fourier Analysis of Spurious Modes and Element Locking in the Finite Element Method", *Computer Methods in Applied Mechanics and Engineering*, Vol. 46, 1984, pp. 65-81.

[17] K. C. Park and D. L. Flaggs, "A Symbolic Fourier Synthesis of a One-Point Integrated Quadrilateral Plate Element", *Computer Methods in Applied Mechanics and Engineering*, Vol. 48, 1985, pp. 203-236.

[18] K. C. Park, G. M. Stanley and D. L. Flaggs, "A Uniformly Reduced, Four-Noded C^0 Shell Element with Consistent Rank Corrections", *Computers & Structures*, Vol. 20, No. 1-3, 1985, pp. 129-139.

[19] MACSYMA Reference Manual, The Mathlab Group, Laboratory for Computer Science, MIT, Version 10, Jan. 1983.

[20] SMP Reference Manual, Inference Corporation, Version 1, 1983.

[21] J. H. Wilkinson, *Rounding Errors in Algebraic Processes*, Prentice-Hall, Englewood Cliffs, N.J.

[22] W. T. Koiter, "A Consistent First Approximation in the General Theory of Thin Elastic Shells," *Proceedings of the IUTAM Symposium on the Theory of Thin Elastic Shells*, North Holland, Amsterday, 1960, pp. 12-33.

[23] R. Courant and D. Hilbert, *Methods of Mathematical Physics*, Vol. 2 - Partial Differential Equations, Interscience Publishers, John Wiley & Sons, 1962, 12-18.

[24] H. Kraus, *Thin Elastic Shells*, John Wiley & Sons, 1967.

[25] H. L. Langhaar, *Energy Methods in Applied Mechanics*, Wiley, 1962.

[26] C. T. Sun, "On the Equations for a Timoshenko Beam under Initial Stress," *J. Applied Mechanics*, March 1972, pp. 282-285.

[27] S. Timoshenko and D. H. Young, *Vibration Problems in Engineering*, Van Nostrand Reinhold, Third Edition, New York, 1955.

[28] S. F. Pawsey, "The Analysis of Moderately Thick to Thin Shells by the Finite Element Method," UCSESM 70-12, Civil Engineering Department, University of California, Berkeley, August 1970.

[29] O. C. Zienkiewicz, R. L. Taylor and J. M. Too, "Reduced Integration Techniques in the General Analysis of Plates and Shells," *International Journal for Numerical Methods in Engineering*, Vol. 3, 1971, pp. 275-290.

[30] O. C. Zienkiewicz, *The Finite Element Method*, McGraw-Hill, Third Edition, 1977.

[31] R. MacNeal, "A Simple Quadrilateral Shell Element," *Computers & Structures*, Vol. 8, 1978, pp. 175-183.

[32] G. Prathap and G. R. Bhashyam, "Reduced Integration and the Shear-Flexible Beam Element," *International Journal for Numerical Methods in Engineering*, Vol. 18, 1982, pp. 195-210.

[33] T. J. R. Hughes, M. Cohen and M. Haroun, "Reduced and Selective Integration Techniques in the Finite Element Analysis of Plates," *Nuclear Engineering and Design*, Vol. 46, No. 1, March 1978, 203-222.

[34] U. Tsach, "Locking of Thin Plate/Shell Elements," *International Journal for Numerical Methods in Engineering*, Vol. 17, 1981, pp. 633-644.

[35] T. J. R. Hughes, R. L. Taylor and W. Kanoknukulchai, "A Simple and Efficient Finite Element for Plate Bending," *International Journal for Numerical Methods in Engineering*, Vol. 11, 1977, 1529-1543.

[36] D. S. Malkus and T. J. R. Hughes, "Mixed Finite Element Methods – Reduced and Selective Integration Techniques: A Unification of Concepts," *Computer Methods in Applied Mechanics and Engineering*, Vol. 15, 1978, pp. 63-81.

[37] D. N. Arnold, "Discretization by Finite Elements of a Model Parameter Dependent Problem," *Numer. Math.*, Vol. 37, 1981, pp. 405-421.

[38] J. N. Reddy, "A Penalty Plate-Bending Element for the Analysis of Laminated Anisotropic Composite Plates," *International Journal for Numerical Methods in Engineering*, Vol. 15, 1980, pp. 1187-1206.

[39] J. S. Przemieniecki, *Theory of Matrix Structural Analysis*, McGraw-Hill, 1968.

[40] R. H. Gallagher, *Finite Element Analysis: Fundamentals*, Prentice-Hall, 1975.

[41] R. D. Cook, *Concepts and Applications of Finite Element Analysis*, Second Edition, Wiley, 1981.

[42] T. J. R. Hughes and K. S. Pister, "Consistent Linearization in Mechanics of Solids and Structures," *Computers & Structures*, Vol. 8, 1978, pp. 391-397.

[43] G. M. Stanley, "Continuum-Based Shell Elements," Ph.D. Dissertation, Stanford University, 1985.

[44] P. Tong, "Exact Solution of Certain Problems by Finite Element-Method," *AIAA J.*, January, 1969, pp. 178-180

[45] L. Collatz, *Numerical Treatment of Differential Equations*, Springer-Verlag, New York, 1966.

[46] B. F. de Veubeke, "Displacement and Equilibrium Models in the Finite Element Method," *Stress Analysis*, O. C. Zienkiewicz and G. S. Holister, eds., Wiley, 1965.

[47] K. Washizu, *Variational Methods in Elasticity & Plasticity*, Third Edition, Pergamon Press, 1982.

[48] R. W. Hamming, *Digital Filters*, Second Edition, Prentice-Hall, 1983.

[49] P. G. Underwood, "Accuracy of Finite Difference Representations for the Transient Response Analysis of Shells," *Earthquake Engineering and Structural Dynamics*, Vol. 2, 1974, pp. 219-233.

[50] F. Stummel, "The Generalized Patch Test," *SIAM J. Numerical Analysis*, Vol. 16, No. 3, 1979, pp. 449-471.

[51] A. Tessler and T. J. R. Hughes, "An Improved Treatment of Transverse Shear in the Mindlin-type Four-node Quadrilateral Element," *Computer Methods in Applied Mechanics and Engineering*, Vol. 39, 1983, pp. 311-335.

[52] K. Bathe and E. N. Dvorkin, "A Four-Node Plate Bending Element Based on Mindlin/Reissner Plate Theory and a Mixed Interpolation," *International Journal for Numerical Methods in Engineering*, Vol. 21, 1985, pp. 367-383.

[53] T. J. R. Hughes and T. E. Tezduyar, "Finite Elements Based Upon Mindlin Plate Theory with Particular Reference to the Four-Node Bilinear Isoparametric Element," *J. Applied Mechanics*, Vol. 48, September 1981, pp. 587-596.

[54] G. Prathap and S. Vawanath, "An Optimally Integrated Four-Node Quadrilateral Plate Bending Element," *International Journal for Numerical Methods in Engineering*, Vol. 19, 1983, 831-840.

[55] G. Prathap, "An Optimally Constrained 4 Node Quadrilateral Thin Plate Bending Element," *Computers & Structures*, Vol. 18, No. 5 1984, 789-794.

[56] M. Mukhopadhyay and D. K. Dinker, "Isoparametric Linear Bending Element and One-Point Integration," *Computers & Structures*, Vol. 9, 1978, 365-369.

[57] M. A. Crisfield, "A Four-Noded Thin-Plate Bending Element using Shear Constraints – A Modified Version of Lyons' Element," *Computer Methods in Applied Mechanics and Engineering*, Vol. 38, 1983, pp. 93-120.

[58] D. Kosloff and G. A. Frazier, "Treatment of Hourglass Patterns in Low Order Finite Element Codes," *International Journal for Numerical and Analytical Methods in Geomechanics*, Vol. 2, 1978, pp. 57-72.

[59] T. Belytschko, C. S. Tsay and W. K. Liu, "A Stabilization Matrix for the Bilinear Mindlin Plate Element," *Computer Methods in Applied Mechanics and Engineering*, Vol. 29, 1981, 313-327.

[60] T. Belytschko and C. S. Tsay, "A Stabilization Procedure for the Quadrilateral Plate Element with One-Point Quadrature," *International Journal for Numerical Methods in Engineering*, Vol. 19, 1970, 405-419.

[61] O. P. Jacquotte and J. T. Oden, "Analysis of Hourglass Instabilities and Control in Underintegrated Finite Element Methods," *Computer Methods in Applied Mechanics and Engineering*, Vol. 44, 1984, pp. 339-363.

[62] O. P. Jacquotte, "Stability, Accuracy, and Efficiency of Some Underintegrated Methods in Finite Element Computations," *Computer Methods in Applied Mechanics and Engineering*, Vol. 50, 1985, pp. 275-293.

[63] B. Verhegghe and G. H. Powell, "Control of Zero-Energy Modes in 9-Node Plane Element," *International Journal for Numerical Methods in Engineering*, Vol. 23, 1986, pp. 863-869.

[64] E. Reissner, "The Effects of Transverse Shear Deformation on the Bending of Elastic Plates," *Journal of Applied Mechanics*, Vol. 12, 1945, pp. 69-77.

[65] R. D. Mindlin, "Influence of Rotatory Inertia and Shear on Flexural Motions of Isotropic, Elastic Plates," J. Applied Mechanics, Vol. 18, 1951, pp. 31-38.

[66] B. N. Parlett, *The Symmetric Eigenvalue Problem*, Prentice Hall, Inc., Englewood Cliffs, N.J., 1980.

[67] T. J. R. Hughes, *The Finite Element Method: Linear Static and Dynamic Finite Element Analysis*, Prentice-Hall, Englewood Cliffs, N.J., 1987.

[68] K. F. Graff, *Wave Motion in Elastic Solids*, Ohio State University Press, 1975.

[69] J. L. Sanders, "An Improved First-Approximation Theory for Thin Shells," NASA TR R-24, 1959.

[70] R. D. Cook and Feng Zhao-Hua, "Deflection and Buckling of Rings with Straight and curved Finite Elements," *Computer & Structures*, Vol. 15, No. 6, 1982, 647-651.

[71] W. Flügge, *Stresses in Shells*, Springer-Verlag, New York, Fourth Printing, 1967.

[72] B. Budiansky and J. L. Sanders, "On the Best First-Order Linear Shell Theory," *Progress in Applied Mechanics - the Prager Anniversary Volume*, Macmillan, 1963, pp. 129-140.

[73] P. M. Naghdi and R. M. Cooper, "Propagation of Elastic Waves in Cylindrical Shells, Including the Effects of Transverse Shear and Rotatory Inertia," *The Journal of the Acoustical Society of America*, Vol. 28, No. 1, Jan. 1956, pp. 56-63.

[74] I. Mirsky and G. Herrmann, "Nonaxially Symmetric Motions of Cylindrical Shells," *The Journal of the Acoustical Society of America*, Vol. 29, No. 10, Oct. 1957, pp. 1116-1123.

[75] P. M. Naghdi, "Foundations of Elastic Shell Theory," Applied Mechnaics Technical Report No. 15, Institute of Engineering Research Series 131, Issue 15, University of California, Berkeley, January 1962.

[76] P. G. Bergan and C. A. Felippa, "A Triangular Membrane Element with Rotational Degrees of Freedom," *Computer Methods in Applied Mechanics and Engineering*, Vol. 50, 1985, pp. 25-69.

[77] W. P. Doherty, E. L. Wilson and R. L. Taylor, "Stress Analysis of Axisymmetric Solids Utilizing Higher-Order Quadrilateral Finite Elements," UCSESM 69-3, Civil Engineering Department, University of California, Berkeley, 1969.

[78] W. T. Koiter, "General Equations of Elastic Stability for Thin Shells," *Poceedings – Symposium on the Theory of Shells*, D. Muster, ed., University of Houston, Houston, Texas, 1967, pp. 187-227.

MACSYMA and SMP Runstreams

The different MACSYMA and SMP runstreams referenced in this investigation are found in this Appendix. Initial work was performed using MACSYMA (actually, UC Berkeley's VAXIMA version of MACSYMA). During the latter stages of work, SMP also became available. While not as user friendly or mature as MACSYMA, SMP was in general able to run similar problems faster using less virtual memory than MACSYMA would. Initial work was done on a VAX 11/780 and 11/785. Limited process virtual paging resources on the multi-user VAXes eventually forced the migration of all work to a SUN 3/160 with a 40MB swap partition allocation.

While syntax of the different commands used by MACSYMA and SMP are different (see [19] and [20]), there is in general a 1 : 1 correspondence between them. Hopefully, the inline comments will be sufficient to indicate what operation(s) is being performed at each step of the symbolic analysis. If not, the reader is refered to the appropriate user's manual for a complete description.

§A.1 Exactly Integrated Timoshenko Beam Discretization


```
     Vaxima 2.00

(c8) /* .
 ******************************************************************
 *                                                                *
 *                    2-Node Timoshenko Beam                      *
 *                                                                *
 ******************************************************************

     . . . . Define global dof numbering                       */

NEL    : 2$

(c9) NDOF   : 4$

(c10) NEQ    : 6$

(c11) DOF[1] : [1,2,3,4]$

(c12) DOF[2] : [3,4,5,6]$

(c13) /* . . . .  Input element lengths                        */

LNGTH : [1,1]$

(c14) /* . . . . Determine whether reduced integration is to be used on
         transverse shear stiffness                            */

REDINT : READ("Use reduced integration for shear stiffness (Y/N)?");

Use reduced integration for shear stiffness (Y/N)?


(d14)                                   n

(c15) /*
 ******************************************************************
 *                                                                *
 *            Calculate element stiffness matrices                *
 *                                                                *
 ******************************************************************

     . . . . Loop over each element                            */

FOR IEL:1 STEP 1 THRU NEL DO (

/* . . . . Define shape functions                              */

  N1 : 1-X/LNGTH[IEL],
  N2 : X/LNGTH[IEL],
```

```
/* . . . . .  Calculate  B  matrix                                        */

  B : MATRIX([         0, -DIFF(N1,X),         0, -DIFF(N2,X)],
             [DIFF(N1,X),          -N1, DIFF(N2,X),       -N2]),

/* . . . . .  Form  B transpose                                           */

  BT : TRANSPOSE(B),

/* . . . .  Calculate extensional stiffness matrix                        */

  KX : EI*COL(BT,1).ROW(B,1),

/* . . . .  Calculate transverse shear stiffness                          */

  KS : GA*COL(BT,2).ROW(B,2),

/* . . . .  Perform volume integration                                    */

  KE[IEL] : DIAGMATRIX(NDOF,0),

  FOR I:1 STEP 1 THRU 4 DO (
    FOR J:1 STEP 1 THRU 4 DO (
      IF REDINT#Y THEN (
      KE[IEL][I,J] : KX[I,J]+KS[I,J],
      KE[IEL][I,J] : INTEGRATE(KE[IEL][I,J],X,0,LNGTH[IEL]) )

/* . . . .  Reduced integration on shear terms                            */

    ELSE (
      KX[I,J] : INTEGRATE(KX[I,J],X,0,LNGTH[IEL]),
      KS[I,J] : (LNGTH[IEL]/2) * 2 * EV(KS[I,J],X:LNGTH[IEL]/2),
      KE[IEL][I,J] : KX[I,J]+KS[I,J]    )))              )$

(c16) /*
  ***********************************************************************
  *                                                                     *
  *      Perform element assembly based upon prescribed global          *
  *      degree-of-freedom (dof) number                                 *
  *                                                                     *
  ***********************************************************************

    . . . .  Loop over each element                                      */

K : DIAGMATRIX(NEQ,0)$

(c17) FOR IEL:1 STEP 1 THRU NEL DO (

/* . . . .  Assemble into global stiffness matrix                         */

  FOR I:1 STEP 1 THRU NDOF DO (
    FOR J:1 STEP 1 THRU NDOF DO (
```

181

```
        II : DOF[IEL][I], JJ : DOF[IEL][J],
        K[II,JJ]:K[II,JJ]+KE[IEL][I,J]))   )$

(c18) K;
```

$$
\begin{bmatrix}
\dfrac{ga}{1} & \dfrac{ga}{2} & -\dfrac{ga}{1} & \dfrac{ga}{2} & 0 & 0 \\[2ex]
\dfrac{ga}{2} & \dfrac{ga\,1^2 + 3\,ei}{3\,1} & -\dfrac{ga}{2} & \dfrac{ga\,1^2 - 6\,ei}{6\,1} & 0 & 0 \\[2ex]
-\dfrac{ga}{1} & -\dfrac{ga}{2} & \dfrac{2\,ga}{1} & 0 & -\dfrac{ga}{1} & \dfrac{ga}{2} \\[2ex]
\dfrac{ga}{2} & \dfrac{ga\,1^2 - 6\,ei}{6\,1} & 0 & \dfrac{2\,(ga\,1^2 + 3\,ei)}{3\,1} & -\dfrac{ga}{2} & \dfrac{ga\,1^2 - 6\,ei}{6\,1} \\[2ex]
0 & 0 & -\dfrac{ga}{1} & -\dfrac{ga}{2} & \dfrac{ga}{1} & -\dfrac{ga}{2} \\[2ex]
0 & 0 & \dfrac{ga}{2} & \dfrac{ga\,1^2 - 6\,ei}{6\,1} & -\dfrac{ga}{2} & \dfrac{ga\,1^2 + 3\,ei}{3\,1}
\end{bmatrix}
$$

(d18)

```
(c19) /*
 *****************************************************************
 *                                                               *
 *         EXPAND nodal dof about center node                    *
 *                                                               *
 *****************************************************************

    . . . . Construct 1-D Taylor Series expansion function       */

T1D(F,DX,N,XL) := SUM(XL^I*(DX**I)*F/I!,I,0,N);
```

$$
\text{(d19)} \qquad t1d(f,\ dx,\ n,\ xl) := sum\left(\frac{xl^i\ dx^i\ f}{i!},\ i,\ 0,\ n\right)
$$

```
(c20) /* . . . .  EXPAND W1,R1,W3,R3 about center node W,R         */

W1 : T1D(W,DX,8,-LNGTH[1])$

(c21) R1 : T1D(R,DX,8,-LNGTH[1])$
```

182

(c22) W3 : T1D(W,DX,8, LNGTH[2])$

(c23) R3 : T1D(R,DX,8, LNGTH[2])$

(c24) /* . . . . Create symbolic displacement vector   */

D:[W1,R1,W,R,W3,R3]$

(c25) /* . . . . Obtain "discrete" Euler equations   */

AREA : (LNGTH[1]+LNGTH[2])/2$

(c26) WEQ : RATEXPAND(SUM(K[3,I]*D[I],I,1,NEQ)/AREA=Q);

$$
\text{(d26)} \quad -\frac{dx^8\, ga^6\, l\, w}{20160} - \frac{dx^6\, ga^4\, l\, w}{360} - \frac{dx^4\, ga^2\, l\, w}{12} - dx^2\, ga\, w + \frac{dx^7\, ga^6\, l\, r}{5040}
$$

$$
+ \frac{dx^5\, ga^4\, l\, r}{120} + \frac{dx^3\, ga^2\, l\, r}{6} + dx\, ga\, r = q
$$

(c27) REQ : RATEXPAND(SUM(K[4,I]*D[I],I,1,NEQ)/AREA=0);

$$
\text{(d27)} \quad -\frac{dx^7\, ga^6\, l\, w}{5040} - \frac{dx^5\, ga^4\, l\, w}{120} - \frac{dx^3\, ga^2\, l\, w}{6} - dx\, ga\, w + \frac{dx^8\, ga^8\, l\, r}{120960}
$$

$$
+ \frac{dx^6\, ga^6\, l\, r}{2160} - \frac{dx^8\, ei\, l\, r}{20160} + \frac{dx^4\, ga^4\, l\, r}{72} - \frac{dx^6\, ei\, l\, r}{360} + \frac{dx^2\, ga^2\, l\, r}{6}
$$

$$
-\frac{dx^4\, ei\, l\, r}{12} + ga\, r - dx^2\, ei\, r = 0
$$

(c28) /*
```
************************************************************************
*                                                                      *
*            Solve for limit differential equations                    *
*                                                                      *
************************************************************************
```
 . . . . Determine coefficient matrix and determinant operator   */

CM   : COEFMATRIX([WEQ,REQ],[W,R])$

183

```
(c29) DETCM : RATEXPAND( DETERMINANT(CM) )$

(c30) /* . . . .  Continuum operator                              */

RATEXPAND( EV(DETCM,L:0) );

                                    4
(d30)                          dx  ei ga

(c31) /* . . . .  Truncation terms                               */

RATEXPAND( COEFF(DETCM,L,1) );

(d31)                               0

(c32) RATEXPAND( COEFF(DETCM,L,2) );

                              4   2       6
                            dx  ga    dx  ei ga
(d32)                       ------- + ----------
                               12         6

(c33) RATEXPAND( COEFF(DETCM,L,3) );

(d33)                               0

(c34) RATEXPAND( COEFF(DETCM,L,4) );

                              6   2       8
                            dx  ga    dx  ei ga
(d34)                       ------- + ----------
                               72         80

(c35) /* . . . .  Continuum loading operator                     */

CM[1,1] : Q$

(c36) CM[2,1] : 0$

(c37) DETCM   : RATEXPAND(DETERMINANT(CM))$

(c38) /* . . . .  Continuum operator                              */

RATEXPAND(EV(DETCM,L:0));

                                    2
(d38)                        ga q - dx  ei q

(c39) /* . . . .  Truncation terms                               */

RATEXPAND( COEFF(DETCM,L,1) );

(d39)                               0
```

```
(c40) RATEXPAND( COEFF(DETCM,L,2) );
```

$$
(d40) \qquad \frac{dx^2\ ga\ q}{6} - \frac{dx^4\ ei\ q}{12}
$$

```
(c41) RATEXPAND( COEFF(DETCM,L,3) );
```

$$
(d41) \qquad 0
$$

```
(c42) RATEXPAND( COEFF(DETCM,L,4) );
```

$$
(d42) \qquad \frac{dx^4\ ga\ q}{72} - \frac{dx^6\ ei\ q}{360}
$$

§A.2 Exactly Integrated Reissner-Mindlin Plate Discretization

```
        /* . . . .   SMP macros                                              */

#I[2]:: col[$matrix,$colnum]::Ar[Dim[$matrix][1],$matrix[$1,$colnum]];

#I[3]:: addcol[$matrix,$addcols]::Ar[Dim[$matrix][1],Cat[$matrix[$1],\
                                  $addcols[$1]]];

#I[4]:: coefmatrix[$eqns,$vars]::(%rows:Dim[$eqns][1];%cols:Dim[$vars][1];\
                          Ar[{%rows,%cols},Coef[$vars[$2],Ex[$eqns[$1]]]]);

#I[5]:: ratsubst[$old,$new,$expr,$base]::(%ans:Pqr[$expr,$old,$base];\
                                  Ex[ $new %ans[1] + %ans[2] ]);
```

```
        /*
           ***********************************************************
           *                                                         *
           *                   4-Node CO Plate                       *
           *                                                         *
           *                         S                               *
           *                         ^                               *
           *                         |                               *
           *                4----------------3                       *
           *                |        |       |                       *
           *                |        +-------|--> R                  *
           *                |        |       |                       *
           *                1----------------2                       *
           *                                                         *
           *                                                         *
           *      Degree-of-freedom ordering:  (u,v,w) -> (r1,r2,w)  *
           *                                                         *
           ***********************************************************
```

```
        . . . .   Define global equation numbers                          */

#I[6]:: eqnum  : {13,14,15};

        /* . . . .   Define element global DOF numbering                   */

#I[7]:: dof : { {1,2,3,4,5,6,13,14,15,10,11,12},\
               {4,5,6,7,8,9,16,17,18,13,14,15},\
               {10,11,12,13,14,15,22,23,24,19,20,21},\
               {13,14,15,16,17,18,25,26,27,22,23,24} };

        /* . . . .   Define shape functions in local R,S coordinates       */

#I[8]:: n1 : (1-r)*(1-s)/4;

#I[9]:: n2 : (1+r)*(1-s)/4;

#I[10]:: n3 : (1+r)*(1+s)/4;
```

186

```
#I[11]:: n4 : (1-r)*(1+s)/4;

#I[12]:: n  : { n1, n2, n3, n4 }

            (1 - r) (1 - s)  (1 + r) (1 - s)  (1 + r) (1 + s)  (1 - r) (1 + s)
#O[12]:    {---------------,---------------,---------------,---------------}
                  4                4                4                4

        /* . . . .  Determine shape function derivatives          */

#I[13]:: nderiv : { D[n,r], D[n,s] }

            -1 + s 1 - s 1 + s -1 - s   -1 + r -1 - r 1 + r 1 - r
#O[13]:    {{------,-----,-----,------},{------,------,-----,-----}}
              4      4     4      4        4      4      4     4

        /* . . . .  Define nodal coordinates                      */

#I[14]:: xy : { { 0, 0 },\
                { 1, 0 },\
                { 1, 1 },\
                { 0, 1 } };

        /* . . . .  Define 2x2 Gauss integration points           */

#I[15]:: sr3  : Sqrt[3];

#I[16]:: rint : { -1/sr3,  1/sr3, 1/sr3, -1/sr3 };

#I[17]:: sint : { -1/sr3, -1/sr3, 1/sr3,  1/sr3 };

        /* . . . .  Define "pre-integrated" DB and DS material matrices   */

#I[18]:: db : { { q11, q12,   0 },\
                { q12, q11,   0 },\
                {   0,   0, q33 }};

#I[19]:: ds : { { q44,   0 },\
                {   0, q44 }};

        /* . . . .  Determine integration rule to be used

                    f   - full spatial integration
                    sr  - reduced integration on shear
                    dsr - directional shear integration
                    ur  - uniformly reduced integration          */

#I[20]:: integrate : Rd["Integration option [f/sr/dsr/ur] ? ","/dev/tty"]

Integration option [f/sr/dsr/ur] ?

#O[20]:  f
```

187

```
/*
 ****************************************************************
 *                                                            *
 *          Calculate element stiffness matrices and          *
 *          assemble into global stiffness                    *
 *                                                            *
 ****************************************************************

      . . . .  Initialize rows of global stiffness              */

#I[21]:: k : Ar[{3,27},0];

      /* . . . .  Calculate element stiffness

           . . . . .  Calculate inverse Jacobian and Jacobian determinant */

#I[22]:: jac  : Ex[nderiv.xy];

#I[23]:: detj : Ex[ jac[1,1]*jac[2,2]-jac[1,2]*jac[2,1] ];

#I[24]:: jinv : (1/detj)*{{jac[2,2],-jac[1,2]},{-jac[2,1],jac[1,1]}};

      /* . . . . .  Loop over each nodal group to calculate element
                    B matrix                                      */

#I[25]:: Do[ inode, start:1, 4,\
             nix : jinv[1].col[nderiv,inode];\
             niy : jinv[2].col[nderiv,inode];\
             bbi : {{-nix,0,0},{0,-niy,0},{-niy,-nix,0}};\
             bsi : {{-n[inode],0,nix},{0,-n[inode],niy}};\
             If[ Match[inode,1], bb:bbi; bs:bsi,\
                                 bb:addcol[bb,bbi];bs:addcol[bs,bsi] ]\
           ];

      /* . . . . .  Calculate BT*D*B                             */

#I[26]:: ke : detj*Trans[bb].db.bb;

#I[27]:: If[ Match[integrate,dsr],\
             ks : detj*q44*bs[1]**bs[1];ksy:detj*q44*bs[2]**bs[2],\
             ks : detj*Trans[bs].ds.bs ];

      /* . . . . .  Perform volume integration of element stiffness  */

#I[28]:: If[ Match[integrate,f],\
             ke : Ar[ {12,12},\
                 Ex[ Sum[ S[ ke[$1,$2]+ks[$1,$2],r->rint[%i],s->sint[%i] ],\
                 {%i,1,4} ]]]\
             ];

#I[29]:: If[ Match[integrate,sr],\
             ke : Ar[ {12,12},\
                 Ex[ Sum[ S[ ke[$1,$2],r->rint[%i],s->sint[%i] ], {%i,1,4} ] +\
```

188

```
                    4 * S[ ks[$1,$2],r->0,s->0 ]]]\
                ];

#I[30]:: If[ Match[integrate,dsr],\
            ke : Ar[ {12,12},\
                Ex[ Sum[ S[ke[$1,$2],r->rint[%i],s->sint[%i]], {%i,1,4} ] +\
                2 * Sum[ S[ks[$1,$2],r->0,s->rint[%i]],{%i,1,2} ] + \
                2 * Sum[ S[ksy[$1,$2],r->rint[%i],s->0],{%i,1,2} ]]]\
                ];

#I[31]:: If[ Match[integrate,ur],\
            ke : Ar[ {12,12},\
                Ex[ 4 * S[ ke[$1,$2]+ks[$1,$2],r->0, s->0 ]]]\
                ];

        /* . . . . .  Update element stiffness with hourglass mode

        hg1 : {1,0,0,-1,0,0,1,0,0,-1,0,0}      /*  r1 mode */
        Ex[ke.hg1]

        hg2 : {0,1,0,0,-1,0,0,1,0,0,-1,0}      /*  r2 mode */
        Ex[ke.hg2]

        hg3 : {0,0,1,0,0,-1,0,0,1,0,0,-1}      /*  w mode  */
        Ex[ke.hg3]

        ke : ke + g1*hg1**hg1+ g2*hg2**hg2+ g3*hg3**hg3;                  */

        /* . . . . .  Perform element assembly based upon prescribed
                      global degree-of-freedom (dof) number              */

#I[32]:: Do [ iel, start:1, 4,\
            Do [ i, start:1, 12,\
              Do [ j, start:1, 12,\
                ii:dof[iel,i]; jj:dof[iel,j];\
                If [ Match[ii,eqnum[1]], k[1,jj]:k[1,jj]+ke[i,j] ];\
                If [ Match[ii,eqnum[2]], k[2,jj]:k[2,jj]+ke[i,j] ];\
                If [ Match[ii,eqnum[3]], k[3,jj]:k[3,jj]+ke[i,j] ];\
              ]]];

        /*
        ****************************************************************
        *                                                              *
        *           Expand nodal dof about center node                 *
        *                                                              *
        ****************************************************************

        . . . . .  Construct 2-D Taylor Series expansion function       */

#I[33]:: t2d[$f,$dx,$dy,$n,$xl,$yl]::\
            Sum[ Sum[ ($xl^i)*($yl^j)*($dx^i)*($dy^j)*$f/(i!*j!),\
                {j,0,$n-i} ], {i,0,$n} ];
```

189

```
          /* . . . .   Construct 1-D Taylor Series expansion function        */

#I[34]:: t1d[$f,$dx,$n,$x1]::Sum[ ($x1^i)*($dx^i)*$f/i!, {i,0,$n} ];

          /* . . . .   Construct generalized expansion function              */

#I[35]:: expn[$f,$dx,$dy,$n,$x1,$y1]::\
              If[ Match[$x1,0], t1d[$f,$dy,$n,$y1],\
              If[ Match[$y1,0], t1d[$f,$dx,$n,$x1],\
                                t2d[$f,$dx,$dy,$n,$x1,$y1] ] ];

          /* . . . .   Expand element dof's about r1,r2,w at global node 5   */

#I[36]:: xnode : { -1, 0, 1, \
                   -1, 0, 1, \
                   -1, 0, 1  };

#I[37]:: ynode : { -1, -1, -1, \
                    0,  0,  0, \
                    1,  1,  1  };

#I[38]:: Do [ inode, start:1, 9,\
            If [ Match[inode,1],\
              d : { expn[r1,dx,dy,6,xnode[inode],ynode[inode]],\
                    expn[r2,dx,dy,6,xnode[inode],ynode[inode]],\
                    expn[ w,dx,dy,6,xnode[inode],ynode[inode]] },\
              d : Cat[ d,\
                    { expn[r1,dx,dy,6,xnode[inode],ynode[inode]],\
                      expn[r2,dx,dy,6,xnode[inode],ynode[inode]],\
                      expn[ w,dx,dy,6,xnode[inode],ynode[inode]] } ] ] ];

          /* . . . .   Obtain "discrete" Euler equations                     */

#I[39]:: area : 4*detj

            2
#O[39]:   1

#I[40]:: r1eq : Ex[ k[1].d/area ]
```

$$
\#O[40]: \quad q44\ r1 - dx\ q44\ w - dx^2\ q11\ r1 - dy^2\ q33\ r1 - dx\ dy\ q12\ r2
$$

$$
- dx\ dy\ q33\ r2 + \frac{dx^2\ l^2\ q44\ r1}{6} - \frac{dx^3\ l^2\ q44\ w}{6}
$$

$$
- \frac{dx^4\ l^2\ q11\ r1}{12} + \frac{dx^4\ l^4\ q44\ r1}{72} - \frac{dx^5\ l^4\ q44\ w}{120}
$$

$$- \frac{dx^6\, l^4\, q11\, r1}{360} + \frac{dx^6\, l^6\, q44\, r1}{2160} + \frac{dy^2\, l^2\, q44\, r1}{6}$$

$$- \frac{dy^4\, l^2\, q33\, r1}{12} + \frac{dy^4\, l^4\, q44\, r1}{72} - \frac{dy^6\, l^4\, q33\, r1}{360}$$

$$+ \frac{dy^6\, l^6\, q44\, r1}{2160} - \frac{dx^2\, dy^2\, l^2\, q44\, w}{6} - \frac{dx^3\, dy^2\, l\, q12\, r2}{6}$$

$$- \frac{dx^3\, dy^2\, l\, q33\, r2}{6} - \frac{dx^4\, dy^4\, l\, q44\, w}{72} - \frac{dx^5\, dy^4\, l\, q12\, r2}{120}$$

$$- \frac{dx^5\, dy^4\, l\, q33\, r2}{120} - \frac{dx^2\, dy^2\, l^2\, q11\, r1}{6} - \frac{dx^2\, dy^2\, l^2\, q33\, r1}{6}$$

$$+ \frac{dx^2\, dy^2\, l^4\, q44\, r1}{36} - \frac{dx^2\, dy^4\, l^4\, q11\, r1}{72} - \frac{dx^2\, dy^4\, l^4\, q33\, r1}{72}$$

$$+ \frac{dx^2\, dy^4\, l^6\, q44\, r1}{432} - \frac{dx^3\, dy^2\, l\, q12\, r2}{6} - \frac{dx^3\, dy^2\, l\, q33\, r2}{6}$$

$$- \frac{dx^3\, dy^2\, l^4\, q44\, w}{36} - \frac{dx^3\, dy^3\, l^4\, q12\, r2}{36} - \frac{dx^3\, dy^3\, l^4\, q33\, r2}{36}$$

$$- \frac{dx^4\, dy^2\, l^4\, q11\, r1}{72} - \frac{dx^4\, dy^2\, l^4\, q33\, r1}{72} + \frac{dx^4\, dy^2\, l^6\, q44\, r1}{432}$$

$$- \frac{dx^5\, dy^4\, l\, q12\, r2}{120} - \frac{dx^5\, dy^4\, l\, q33\, r2}{120}$$

#I[41]:: r2eq : Ex[k[2].d/area]

$$2 \qquad\qquad 2$$

191

#0[41]: $q_{44}\, r_2 - dy\, q_{44}\, w - dx\ q_{33}\, r_2 - dy\ q_{11}\, r_2 - dx\, dy\, q_{12}\, r_1$

$$- dx\, dy\, q_{33}\, r_1 + \frac{dx^2\, l^2\, q_{44}\, r_2}{6} - \frac{dx^4\, l^2\, q_{33}\, r_2}{12}$$

$$+ \frac{dx^4\, l^4\, q_{44}\, r_2}{72} - \frac{dx^6\, l^4\, q_{33}\, r_2}{360} + \frac{dx^6\, l^6\, q_{44}\, r_2}{2160}$$

$$+ \frac{dy^2\, l^2\, q_{44}\, r_2}{6} - \frac{dy^3\, l^2\, q_{44}\, w}{6} - \frac{dy^4\, l^2\, q_{11}\, r_2}{12}$$

$$+ \frac{dy^4\, l^4\, q_{44}\, r_2}{72} - \frac{dy^5\, l^4\, q_{44}\, w}{120} - \frac{dy^6\, l^4\, q_{11}\, r_2}{360}$$

$$+ \frac{dy^6\, l^6\, q_{44}\, r_2}{2160} - \frac{dx\, dy^3\, l^2\, q_{12}\, r_1}{6} - \frac{dx\, dy^3\, l^2\, q_{33}\, r_1}{6}$$

$$- \frac{dx\, dy^5\, l^4\, q_{12}\, r_1}{120} - \frac{dx\, dy^5\, l^4\, q_{33}\, r_1}{120} - \frac{dx^2\, dy^2\, l^2\, q_{44}\, w}{6}$$

$$- \frac{dx^2\, dy^2\, l^2\, q_{11}\, r_2}{6} - \frac{dx^2\, dy^2\, l^2\, q_{33}\, r_2}{6} + \frac{dx^2\, dy^2\, l^4\, q_{44}\, r_2}{36}$$

$$- \frac{dx^2\, dy^3\, l^4\, q_{44}\, w}{36} - \frac{dx^2\, dy^4\, l^4\, q_{11}\, r_2}{72} - \frac{dx^2\, dy^4\, l^4\, q_{33}\, r_2}{72}$$

$$+ \frac{dx^2\, dy^4\, l^6\, q_{44}\, r_2}{432} - \frac{dx^3\, dy^2\, l^2\, q_{12}\, r_1}{6} - \frac{dx^3\, dy^2\, l^2\, q_{33}\, r_1}{6}$$

$$- \frac{dx^3\, dy^3\, l^4\, q_{12}\, r_1}{36} - \frac{dx^3\, dy^3\, l^4\, q_{33}\, r_1}{36} - \frac{dx^4\, dy\, l^4\, q_{44}\, w}{72}$$

$$dx^4\, dy^2\, l^4 \qquad dx^4\, dy^2\, l^4 \qquad dx^4\, dy^2\, l^6$$

$$- \frac{dx\ dy\ 1\ q11\ r2}{72} - \frac{dx\ dy\ 1\ q33\ r2}{72} + \frac{dx\ dy\ 1\ q44\ r2}{432}$$

$$- \frac{dx^5\ dy^4\ 1\ q12\ r1}{120} - \frac{dx^5\ dy^4\ 1\ q33\ r1}{120}$$

#I[42]:: weq : Ex[k[3].d/area]

#O[42]: $dx\ q44\ r1 + dy\ q44\ r2 - dx^2\ q44\ w - dy^2\ q44\ w + \dfrac{dx^3\ 1^2\ q44\ r1}{6}$

$$- \frac{dx^4\ 1^2\ q44\ w}{12} + \frac{dx^5\ 1^4\ q44\ r1}{120} - \frac{dx^6\ 1^4\ q44\ w}{360}$$

$$+ \frac{dy^3\ 1^2\ q44\ r2}{6} - \frac{dy^4\ 1^2\ q44\ w}{12} + \frac{dy^5\ 1^4\ q44\ r2}{120}$$

$$- \frac{dy^6\ 1^4\ q44\ w}{360} + \frac{dx^2\ dy^2\ 1\ q44\ r1}{6} + \frac{dx^4\ dy^4\ 1\ q44\ r1}{72}$$

$$+ \frac{dx^2\ dy^2\ 1\ q44\ r2}{6} - \frac{dx^2\ dy^2\ 1^2\ q44\ w}{3} + \frac{dx^2\ dy^3\ 1^4\ q44\ r2}{36}$$

$$- \frac{dx^2\ dy^4\ 1^4\ q44\ w}{36} + \frac{dx^3\ dy^2\ 1^4\ q44\ r1}{36} + \frac{dx^4\ dy^4\ 1\ q44\ r2}{72}$$

$$- \frac{dx^4\ dy^2\ 1^4\ q44\ w}{36}$$

```
/*
 *****************************************************************
 *                                                               *
 *           Solve for limit differential equations              *
 *                                                               *
 *****************************************************************
```

```
                . . . .   Extract continuum differential operator matrix        */

#I[43]:: continuum : coefmatrix[{Ex[ S[ r1eq, 1->0 ]],\
                                 Ex[ S[ r2eq, 1->0 ]],\
                                 Ex[ S[  weq, 1->0 ]]},\
                                 {r1,r2,w}];

        /* . . . .  Determine continuum operator                               */

#I[44]:: zerolhs : Ex[ Det[continuum] / q44 ];

#I[45]:: Ex[ S[ %, q12 -> nu mod, q33 -> ( 1 - nu ) mod / 2, q11 -> mod ]];

#I[46]:: ratsubst[ 1-nu, 2 q33 / mod, %, nu ];

#I[47]:: continuumlhs : Ex[ S[ %, mod -> q11 ]]


          4             6            4             6
#0[47]:   dx  q11 q44 - dx  q11 q33 + dy  q11 q44 - dy  q11 q33


                2   2              2   4              4   2
            + 2 dx  dy  q11 q44 - 3 dx  dy  q11 q33 - 3 dx  dy  q11 q33

        /* . . . .  Determine loading operator                                 */

#I[48]:: continuum[1,3] : 0;

#I[49]:: continuum[2,3] : 0;

#I[50]:: continuum[3,3] : 1;

#I[51]:: zerorhs : Ex[ Det[continuum] / q44 ];

#I[52]:: Ex[ S[ %, q12 -> nu mod, q33 -> ( 1 - nu ) mod / 2, q11 -> mod ]];

#I[53]:: ratsubst[ 1-nu, 2 q33 / mod, %, nu ];

#I[54]:: continuumrhs : Ex[ S[ %, mod -> q11 ]]


              4            4            2   2
            dx  q11 q33   dy  q11 q33  2 dx  dy  q11 q33      2
#0[54]:   q44 + ----------- + ----------- + ------------------ - dx  q11
              q44           q44               q44


              2         2         2
            - dx  q33 - dy  q11 - dy  q33

        /* . . . .  Extract truncation information (2nd order terms only):

              . . . . .  Differential operator first                           */

#I[55]:: discrete : coefmatrix[ {r1eq,r2eq,weq}, {r1,r2,w} ];


                                     194
```

```
#I[56]:: S[ Ex[ Det[discrete] / q44 ], 1^($n_=$n>=4)->0 ];

#I[57]:: S[ Ex[ % - zerolhs ], 1->1 ];

#I[58]:: Ex[ S[ %, q12 -> nu mod, q33 -> ( 1 - nu ) mod / 2, q11 -> mod ]];

#I[59]:: ratsubst[1-nu, 2 q33 / mod,\
                  ratsubst[ 1-nu, 2 q33 / mod, %, nu ], nu ];

#I[60]:: Ex[ S[ %, mod -> q11 ]]
```

$$
\begin{aligned}
\#O[60]: \quad & \frac{dx^4 q44^2}{12} + \frac{dy^4 q44^2}{12} + \frac{dx^2 dy^6 q11^2}{12} + \frac{dx^2 dy^6 q33^2}{12} + \frac{dx^4 dy^4 q11^2}{6} \\[2mm]
& + \frac{dx^4 dy^4 q33^2}{6} + \frac{dx^6 q11 q44^2}{3} - \frac{dx^6 q33 q44}{12} + \frac{dx^6 dy^2 q11^2}{12} \\[2mm]
& + \frac{dx^6 dy^2 q33^2}{12} - \frac{dx^8 q11 q33}{4} + \frac{dy^6 q11 q44}{3} - \frac{dy^6 q33 q44}{12} \\[2mm]
& - \frac{dy^8 q11 q33}{4} + \frac{17 dx^2 dy^4 q11 q44}{12} - \frac{dx^2 dy^4 q33 q44}{6} \\[2mm]
& - \frac{5 dx^2 dy^6 q11 q33}{3} + \frac{17 dx^4 dy^2 q11 q44}{12} - \frac{dx^4 dy^2 q33 q44}{6} \\[2mm]
& - \frac{17 dx^4 dy^4 q11 q33}{6} - \frac{5 dx^6 dy^2 q11 q33}{3}
\end{aligned}
$$

```
        /* . . . .  Loading operator                                */

#I[61]:: discrete[1,3] : 0;

#I[62]:: discrete[2,3] : 0;

#I[63]:: discrete[3,3] : 1;

#I[64]:: S[ Ex[ Det[discrete] / q44 ], 1^($n_=$n>=4)->0 ];

#I[65]:: S[ Ex[ % - zerorhs ], 1->1 ];
```

```
#I[66]:: Ex[ S[ %, q12 -> nu mod, q33 -> ( 1 - nu ) mod / 2, q11 -> mod ]];

#I[67]:: ratsubst[1-nu, 2 q33 / mod,\
                  ratsubst[ 1-nu, 2 q33 / mod, %, nu ], nu ];

#I[68]:: Ex[ S[ %, mod -> q11 ]]
```

$$
\begin{aligned}
\#O[68]: \quad &-\frac{dx^2\, dy^4\, q11^2}{12q44} - \frac{dx^2\, dy^4\, q33^2}{12q44} - \frac{dx^4\, dy^2\, q11^2}{12q44} - \frac{dx^4\, dy^2\, q33^2}{12q44} \\[2mm]
&+ \frac{dx^6\, q11\, q33}{6q44} + \frac{dy^6\, q11\, q33}{6q44} + \frac{dx^2\, dy^4\, q11\, q33}{q44} \\[2mm]
&+ \frac{dx^4\, dy^2\, q11\, q33}{q44} + \frac{dx^2\, q44}{3} - \frac{dx^4\, q11}{4} - \frac{dx^4\, q33}{4} + \frac{dy^2\, q44}{3} \\[2mm]
&- \frac{dy^4\, q11}{4} - \frac{dy^4\, q33}{4} - \frac{2\, dx^2\, dy^2\, q11}{3} - \frac{2\, dx^2\, dy^2\, q33}{3}
\end{aligned}
$$

```
#I[69]:: Exit[]
```

§A.3 Faceted Hermitian Beam Discretization of the Arch

SMP 1.6.0   (Jun 24 1987)

```
        /*
        . *********************************************************************
        *                                                                    *
        *      Static analysis of 2-Node c1 Beam discretization of arch      *
        *                                                                    *
        *********************************************************************

            . . . . . Global element/nodal numbering counter clock-wise     */

#I[6]:: dof : {{ 1, 2, 3, 4, 5, 6 },\
               { 4, 5, 6, 7, 8, 9 }};

#I[7]:: eqnum : { 4, 5, 6 };

        /* . . . . . Input appropriate element length                        */

#I[8]:: le : Rd["Effective element length ? ","/dev/tty"]

Effective element length ?

#0[8]:   le

        /*
        *********************************************************************
        *                                                                    *
        *       Assemble global stiffness matrix and load vector             *
        *                                                                    *
        *********************************************************************

            . . . . Element stiffness matrix and load vector in local
                    beam coordinates - dof ordering = {u1,w1,r1,u2,w2,r2}  */

#I[9]:: ke : {\
    { ea/le,         0,          0,   -ea/le,         0,          0 },\
    {    0, 12*ei/le^3,  6*ei/le^2,       0, -12*ei/le^3,  6*ei/le^2 },\
    {    0,  6*ei/le^2,    4*ei/le,       0,  -6*ei/le^2,    2*ei/le },\
    {-ea/le,         0,          0,    ea/le,         0,          0 },\
    {    0, -12*ei/le^3, -6*ei/le^2,      0,  12*ei/le^3, -6*ei/le^2 },\
    {    0,  6*ei/le^2,    2*ei/le,       0,  -6*ei/le^2,    4*ei/le }};

        /* . . . . . Rotate to global (shell) system                         */

#I[10]:: t : {{  csb,  snb, 0,   0,    0, 0 },\
             { -snb,  csb, 0,   0,    0, 0 },\
             {   0,    0, 1,   0,    0, 0 },\
             {   0,    0, 0, csb, -snb, 0 },\
             {   0,    0, 0, snb,  csb, 0 },\
             {   0,    0, 0,   0,    0, 1 }};
```

197

```
#I[11]:: ke : Ex[ t.ke.Trans[t] ]


                      2        2
          12ei snb  csb  ea  -csb ea snb   12csb ei snb 6ei snb
#O[11]:  {{--------- + ------- ,----------- + ------------- ,------- ,
              3        le         le             3           2
            le                                 le          le


                             2        2
                  12ei snb  csb  ea  -csb ea snb   12csb ei snb
                  --------- - ------- ,----------- - ------------- ,
                      3        le          le            3
                    le                                 le


                  6ei snb
                  -------} ,
                     2
                    le


          -csb ea snb   12csb ei snb ea snb    12  csb  ei 6csb ei
         {----------- + ------------- ,------- + ----------- ,------- ,
              le             3           le           3          2
                           le                       le         le


              csb ea snb   12csb ei snb ea snb    12 csb  ei
              ---------- + ------------- ,------- - ----------- ,
                 le             3           le           3
                               le                      le


              6csb ei
              -------} ,
                 2
                le

         6ei snb 6csb ei 4ei 6ei snb -6csb ei 2ei
         {------- ,------- ,--- ,------- ,--------- ,---} ,
             2        2    le     2        2       le
            le       le          le       le


              2        2
          12ei snb  csb  ea  csb ea snb   12csb ei snb 6ei snb
         {--------- - ------- ,---------- + ------------- ,------- ,
              3        le          le            3          2
            le                                 le          le


              2        2
          12ei snb  csb  ea  csb ea snb   12csb ei snb
         {--------- + ------- ,---------- - ------------- ,
              3        le          le            3
            le                                 le
```

198

```
                    6ei snb
                    ------}.
                       2
                      le


                                                  2                2
          -csb ea snb   12csb ei snb  ea snb    12 csb  ei  -6csb ei
         {----------- - ------------,------- - ----------,--------,
              le              3         le          3         2
                            le                     le        le


                                                 2                2
           csb ea snb   12csb ei snb  ea snb    12 csb  ei
          ---------- - ------------,------- + ----------,
              le             3         le          3
                           le                     le


            -6csb ei
            --------}.
               2
              le


          6ei snb 6csb ei 2ei 6ei snb -6csb ei 4ei
         {-------,------- ,---,------- ,-------- ,---}}
             2       2    le    2         2      le
            le      le          le       le
```

```
    /* . . . .  Perform stiffness assembly for both elements
                1 and 2 based upon prescribed global degree-of-freedom
                (dof) number                                          */

#I[12]:: k : Ar[ {3,9}, 0 ]

#O[12]:   {{0,0,0,0,0,0,0,0,0,0},{0,0,0,0,0,0,0,0,0,0},{0,0,0,0,0,0,0,0,0,0}}

#I[13]:: Do [ iel, start:1, 2,\
           Do [ i, start:1, 6,\
           Do [ j, start:1, 6,\
             ii:dof[iel,i]; jj:dof[iel,j];\
             If [ Match[ii,eqnum[1]], k[1,jj]:k[1,jj]+ke[i,j] ];\
             If [ Match[ii,eqnum[2]], k[2,jj]:k[2,jj]+ke[i,j] ];\
             If [ Match[ii,eqnum[3]], k[3,jj]:k[3,jj]+ke[i,j] ];\
           ]]];

      /*
      ***************************************************************
      *                                                             *
      *             Determine "discrete" Euler equations            *
      *                                                             *
      ***************************************************************

         . . . . .  Create transformed symbolic displacement vector   */
```

199

```
#I[14]:: Sat[ i ];  i^2 : -1;  i^4 : 1;    /*  Use "i" for imaginary unit   */

#I[15]:: d : { u*(csks-i*snks), v*(csks-i*snks), r*(csks-i*snks),\
                        u,              v,              r,\
              u*(csks+i*snks), v*(csks+i*snks), r*(csks+i*snks) };

        /* . . . . Obtain "discrete" Euler equations                      */

#I[16]:: ueq : Ex[ k[1].d ]
```

$$
\#0[16]: \quad \frac{12ei\ r\ snb}{le^2} + \frac{24ei\ snb^2\ u}{le^3} + \frac{2\ csb^2\ ea\ u}{le} + \frac{12csks\ ei\ r\ snb}{le^2}
$$

$$
+ \frac{24csks\ ei\ snb^2\ u}{le^3} - \frac{2\ csb^2\ csks\ ea\ u}{le}
$$

$$
- \frac{2csb\ ea\ i\ snb\ snks\ v}{le} - \frac{24csb\ ei\ i\ snb\ snks\ v}{le^3}
$$

```
#I[17]:: weq : Ex[ k[2].d ]
```

$$
\#0[17]: \quad \frac{2ea\ snb^2\ w}{le} + \frac{24\ csb^2\ ei\ w}{le^3} + \frac{2csks\ ea\ snb^2\ w}{le} - \frac{24\ csb^2\ csks\ ei\ w}{le^3}
$$

$$
+ \frac{12csb\ ei\ i\ r\ snks}{le^2} + \frac{2csb\ ea\ i\ snb\ snks\ u}{le}
$$

$$
+ \frac{24csb\ ei\ i\ snb\ snks\ u}{le^3}
$$

```
#I[18]:: req : Ex[ k[3].d ]
```

$$
\#0[18]: \quad \frac{8ei\ r}{le} + \frac{4csks\ ei\ r}{le} + \frac{12ei\ snb\ u}{le^2} + \frac{12csks\ ei\ snb\ u}{le^2} - \frac{12csb\ ei\ i\ snks\ w}{le^2}
$$

200

```
/*
 ****************************************************************
 *                                                            *
 *      Solve for transformed limit differential equations    *
 *                                                            *
 ****************************************************************

        . . . . Create coefficient matrix                    */

#I[19]:: cm : coefmatrix[ {ueq, weq, req}, {u,w,r} ]
```

$$
\#O[19]: \quad \left\{\left\{\frac{24ei\ snb^2}{le^3} + \frac{2\ csb^2\ ea}{le} + \frac{24csks\ ei\ snb^2}{le^3} - \frac{2\ csb^2\ csks\ ea}{le}, \right.\right.
$$

$$
\frac{-2csb\ ea\ i\ snb\ snks}{le} - \frac{24csb\ ei\ i\ snb\ snks}{le^3},
$$

$$
\left.\frac{12ei\ snb}{le^2} + \frac{12csks\ ei\ snb}{le^2}\right\},
$$

$$
\left\{\frac{2csb\ ea\ i\ snb\ snks}{le} + \frac{24csb\ ei\ i\ snb\ snks}{le^3}, \right.
$$

$$
\frac{2ea\ snb^2}{le} + \frac{24\ csb^2\ ei}{le^3} + \frac{2csks\ ea\ snb^2}{le}
$$

$$
\left.- \frac{24\ csb^2\ csks\ ei}{le^3}, \frac{12csb\ ei\ i\ snks}{le^2}\right\},
$$

$$
\left\{\frac{12ei\ snb}{le^2} + \frac{12csks\ ei\ snb}{le^2}, \frac{-12csb\ ei\ i\ snks}{le^2}, \frac{8ei}{le} + \frac{4csks\ ei}{le}\right\}\right\}
$$

```
#I[20]:: Ex[ {{ cm[3,3]*cm[1,1]-cm[1,3]*cm[3,1],\
               cm[3,3]*cm[1,2]-cm[1,3]*cm[3,2] },\
             { cm[3,3]*cm[2,1]-cm[2,3]*cm[3,1],\
               cm[3,3]*cm[2,2]-cm[2,3]*cm[3,2] }} ]
```

$$\#0[20]:\ \left\{\left\{\frac{48\ ei^2\ snb^2}{le^4} + \frac{16\ csb\ ea^2\ ei}{le^2} - \frac{48\ csks\ ei^2\ snb^2}{le^4}\right.\right.$$

$$- \frac{8\ csb^2\ csks\ ea\ ei}{le^2} - \frac{8\ csb\ csks^2\ ea\ ei}{le^2},$$

$$\frac{-48csb\ ei^2\ i\ snb\ snks}{le^4} + \frac{48csb\ csks\ ei^2\ i\ snb\ snks}{le^4}$$

$$- \frac{16csb\ ea\ ei\ i\ snb\ snks}{le^2}$$

$$\left.- \frac{8csb\ csks\ ea\ ei\ i\ snb\ snks}{le^2}\right\},$$

$$\left\{\frac{48csb\ ei^2\ i\ snb\ snks}{le^4} - \frac{48csb\ csks\ ei^2\ i\ snb\ snks}{le^4}\right.$$

$$+ \frac{16csb\ ea\ ei\ i\ snb\ snks}{le^2}$$

$$+ \frac{8csb\ csks\ ea\ ei\ i\ snb\ snks}{le^2},$$

$$\frac{192\ csb^2\ ei^2}{le^4} + \frac{16ea\ ei^2\ snb}{le^2} - \frac{96\ csb\ csks^2\ ei^2}{le^4}$$

$$96\ csb^2\ csks^2\ ei^2$$

$$- \cfrac{\cdots}{l_e^4}$$

$$\cfrac{144\ csb^2\ ei^2\ snks^2}{l_e^4}$$

$$- \cfrac{\cdots}{l_e^4}$$

$$+ \cfrac{24csks\ ea\ ei\ snb^2}{l_e^2} + \cfrac{8\ csks^2\ ea\ ei\ snb^2}{l_e^2}\}\}$$

```
#I[21]:: cm : Ex[ S[ % / (12*ei), csks -> 1-s^2*kbar^2/2,\
                     snks -> s*kbar*Sqrt[alpha1],\
                     snb  -> 1/(2*rad) ]]
```

$$\#O[21]: \{\{\cfrac{ei^2\ kbar^2\ l^2\ s^2}{l_e^4\ rad^2} - \cfrac{ei^4\ kbar^2\ l^4\ s^4}{4\ l_e^4\ rad^2} + \cfrac{csb^2\ ea\ kbar^2\ s^2}{l_e^2}$$

$$- \cfrac{csb^2\ ea\ kbar^4\ s^4}{6\ l_e^2},$$

$$\cfrac{- alpha1^{1/2}\ csb\ ea\ i\ kbar\ l\ s}{l_e^2\ rad}$$

$$+ \cfrac{alpha1^{1/2}\ csb\ ea\ i\ kbar^3\ l^3\ s^3}{6\ l_e^2\ rad}$$

$$- \cfrac{alpha1^{1/2}\ csb\ ei\ i\ kbar^3\ l^3\ s^3}{l_e^4\ rad}\},$$

$$\{\cfrac{alpha1^{1/2}\ csb\ ea\ i\ kbar\ l\ s}{\cdots}$$

203

$$le^2\ rad$$

$$-\ \frac{alpha1^{1/2}\ csb\ ea^3\ i\ kbar\ l^3\ s}{6\ le^2\ rad}$$

$$+\ \frac{alpha1^{1/2}\ csb\ ei^3\ i\ kbar\ l^3\ s}{4\ le\ rad},$$

$$\frac{ea^2\ l}{le^2\ rad^2}\ -\ \frac{5ea^2\ kbar^2\ l^2\ s}{12\ le^2\ rad^2}\ +\ \frac{ea^4\ kbar^2\ l^4\ s}{24\ le^2\ rad^2}$$

$$+\ \frac{12\ csb^2\ ei\ kbar^2\ s^2}{le^4}$$

$$-\ \frac{2\ csb^2\ ei\ kbar^4\ s^4}{le^4}$$

$$-\ \frac{12alpha1\ csb^2\ ei\ kbar^2\ s^2}{le^4}\}\}$$

§A.4 Faceted Reissner-Mindlin Plate Discretization of the Cylindrical Shell

SMP 1.6.0 (Jun 24 1987)
Sat Feb 13 16:16:29 1988

```
        /* . . . .  SMP macros                                        */

#I[1]:: col[$matrix,$colnum]::Ar[Dim[$matrix][1],$matrix[$1,$colnum]];

#I[2]:: addcol[$matrix,$addcols]::Ar[Dim[$matrix][1],Cat[$matrix[$1],\
                                  $addcols[$1]]];

#I[3]:: coefmatrix[$eqns,$vars]::(%rows:Dim[$eqns][1];%cols:Dim[$vars][1];\
                   Ar[{%rows,%cols},Coef[$vars[$2],Ex[$eqns[$1]]]]);

#I[4]:: ratsubst[$old,$new,$expr,$base]::(%ans:Pqr[$expr,$old,$base];\
                                  Ex[ $new %ans[1] + %ans[2] ]);

#I[5]:: submatrixadd[$matrix,$submatrix,$iloc,$jloc]::\
            (%nrowsub:Dim[$submatrix][1];\
             %ncolsub:Dim[$submatrix][2];\
             %mat:$matrix;\
             Do[ %i, 0, %nrowsub-1,\
               Do[ %j, 0, %ncolsub-1,\
                 %mat[$iloc+%i,$jloc+%j]:%mat[$iloc+%i,$jloc+%j] +\
                                        $submatrix[%i+1,%j+1];\
             ]];%mat);

        /*
        ****************************************************************
        *                                                            *
        *         Static analysis of c0 cylindrical shell            *
        *                                                            *
        *                          s                                 *
        *                          ^                                 *
        *                          |                                 *
        *          4----------------3                                *
        *          |               |    |                           *
        *          |               |    |                           *
        *          |        +-------|--> r                          *
        *          |               |    |                           *
        *          1----------------2                                *
        *                                                            *
        *                                                            *
        *     Degree-of-freedom ordering:  (u,v,w,rx,ry,rz)          *
        *                                                            *
        ****************************************************************

        . . . .  Global element/nodal numbering                      */

#I[6]:: dof : {{  1,  2,  3,  4,  5,  6,  7,  8,  9, 10, 11, 12,  \
             25, 26, 27, 28, 29, 30, 19, 20, 21, 22, 23, 24 },\
```

205

```
                           {  7,  8,  9, 10, 11, 12, 13, 14, 15, 16, 17, 18,  \
                             31, 32, 33, 34, 35, 36, 25, 26, 27, 28, 29, 30 },\
                           { 19, 20, 21, 22, 23, 24, 25, 26, 27, 28, 29, 30,  \
                             43, 44, 45, 46, 47, 48, 37, 38, 39, 40, 41, 42 },\
                           { 25, 26, 27, 28, 29, 30, 31, 32, 33, 34, 35, 36,  \
                             49, 50, 51, 52, 53, 54, 43, 44, 45, 46, 47, 48 }};

#I[7]:: eqnum : { 25, 26, 27, 28, 29, 30 };

        /* . . . .  Define shape functions in local r,s coordinates        */

#I[8]:: n1 : (1-r)*(1-s)/4;

#I[9]:: n2 : (1+r)*(1-s)/4;

#I[10]:: n3 : (1+r)*(1+s)/4;

#I[11]:: n4 : (1-r)*(1+s)/4;

#I[12]:: n  : { n1, n2, n3, n4 };

        /* . . . .  Determine shape function derivatives                  */

#I[13]:: nderiv : { D[n,r], D[n,s] };

        /* . . . .  Define parent element nodal coordinates                */

#I[14]:: xy : { { 0, 0 },\
                { 1, 0 },\
                { 1, 1 },\
                { 0, 1 } };

        /* . . . .  Define 2x2 Gauss integration points                    */

#I[15]:: sr3 : Sqrt[3];

#I[16]:: rint : { -1/sr3,  1/sr3, 1/sr3, -1/sr3 };

#I[17]:: sint : { -1/sr3, -1/sr3, 1/sr3,  1/sr3 };

        /* . . . .  Define "pre-integrated" material matrices              */

#I[18]:: dm  : { { m11, m12 },\
                 { m12, m11 } };

#I[19]:: dms : m33;

#I[20]:: db  : { { q11, q12,   0 },\
                 { q12, q11,   0 },\
                 {   0,   0, q33 } };

#I[21]:: ds  : { { q44,   0 },\
                 {   0, q44 } };
```

206

```
          /* . . . . . Determine integration rules to be used:

                    f   - full spatial integration
                    sr  - reduced integration on shear
                    dsr - directional shear integration
                    ur  - uniformly reduced integration          */

#I[22]:: membranerule : Rd["Integration option [f/sr/ur] ? ","/dev/tty"]

Integration option [f/sr/ur] ?

#O[22]:   sr

#I[23]:: bendingrule  : Rd["Integration option [f/sr/dsr/ur] ? ","/dev/tty"]

Integration option [f/sr/dsr/ur] ?

#O[23]:   ur

        /*
         *********************************************************************
         *                                                                   *
         *           Calculate element stiffness matrices and                *
         *           assemble into global stiffness                          *
         *                                                                   *
         *********************************************************************

             . . . . . Calculate inverse Jacobian and Jacobian determinant  */

#I[24]:: jac  : Ex[nderiv.xy];

#I[25]:: detj : Ex[ jac[1,1]*jac[2,2]-jac[1,2]*jac[2,1] ];

#I[26]:: jinv : (1/detj)*{{jac[2,2],-jac[1,2]},{-jac[2,1],jac[1,1]}};

        /* . . . . . Loop over each nodal group to calculate different
                     parts of element B matrix with 6 dof/node        */

#I[27]:: Do[ inode, start:1, 4,\
           nix  : jinv[1].col[nderiv,inode];\
           niy  : jinv[2].col[nderiv,inode];\
           bmi  : { { nix,   0, 0, 0, 0, 0 },  \
                    {   0, niy, 0, 0, 0, 0 } };\
           bmsi : { niy, nix, 0, 0, 0, 0 };\
           bbi  : { { 0, 0, 0, -nix,    0, 0 },  \
                    { 0, 0, 0,    0, -niy, 0 },  \
                    { 0, 0, 0, -niy, -nix, 0 } };\
           bsi  : { { 0, 0, nix, -n[inode],          0, 0 },  \
                    { 0, 0, niy,          0, -n[inode], 0 } };\
           If[ Match[inode,1], bm:bmi; bms:bmsi; bb:bbi; bs:bsi,\
                             bm :addcol[bm,bmi];     \
                             bms:Cat[bms,bmsi];      \
```

207

```
                                    bb  :addcol[bb,bbi];        \
                                    bs  :addcol[bs,bsi] ]       \
                ];

            /* . . . . .   Calculate BT*D*B                               */

#I[28]:: ke  : detj*Trans[bb].db.bb;

#I[29]:: km  : detj*Trans[bm].dm.bm;

#I[30]:: kms : detj*dms*bms**bms;

#I[31]:: If[ Match[bendingrule,dsr],\
                ks : detj*q44*bs[1]**bs[1];ksy:detj*q44*bs[2]**bs[2],\
                ks : detj*Trans[bs].ds.bs ];

            /* . . . . .   Perform volume integration of membrane stiffness   */

#I[32]:: If[ Match[membranerule,f],\
                km : Ar[ {24,24},\
                    Ex[ Sum[ S[ km[$1,$2]+kms[$1,$2],\
                        r->rint[%i],s->sint[%i] ], {%i,1,4} ]]]\
                ];

#I[33]:: If[ Match[membranerule,sr],\
                km : Ar[ {24,24},\
                    Ex[ Sum[ S[ km[$1,$2],r->rint[%i],s->sint[%i] ],\
                        {%i,1,4} ] +  4 * S[ kms[$1,$2],r->0,s->0 ]]]\
                ];

#I[34]:: If[ Match[membranerule,ur],\
                km : Ar[ {24,24},\
                    Ex[ 4 * S[ km[$1,$2]+kms[$1,$2],r->0,s->0 ]]]\
                ];

            /* . . . . .   Perform volume integration of plate stiffness      */

#I[35]:: If[ Match[bendingrule,f],\
                ke : Ar[ {24,24},\
                    Ex[ Sum[ S[ ke[$1,$2]+ks[$1,$2],r->rint[%i],s->sint[%i] ],\
                        {%i,1,4} ]]]\
                ];

#I[36]:: If[ Match[bendingrule,sr],\
                ke : Ar[ {24,24},\
                    Ex[ Sum[ S[ ke[$1,$2],r->rint[%i],s->sint[%i] ],\
                        {%i,1,4} ] + 4 * S[ ks[$1,$2],r->0,s->0 ]]]\
                ];

#I[37]:: If[ Match[bendingrule,dsr],\
                ke : Ar[ {24,24},\
                    Ex[ Sum[ S[ke[$1,$2],r->rint[%i],s->sint[%i]], {%i,1,4} ]+\
                    2 * Sum[ S[ks[$1,$2],r->0,s->rint[%i]],{%i,1,2} ]+\
```

208

```
                    2 * Sum[ S[ksy[$1,$2],r->rint[%i],s->0],{%i,1,2} ]]]\
            ];

#I[38]:: If[ Match[bendingrule,ur],\
            ke : Ar[ {24,24},\
                Ex[ 4 * S[ ke[$1,$2]+ks[$1,$2],r->0, s->0 ]]]\
            ];

        /* . . . . .  Complete element stiffness calculation by combining
                      membrane and bending contributions              */

#I[39]:: ke : ke + km;

#I[40]:: Set[{ bm,bms,bb,bs,km,ks,ksy,kms }];

        /* . . . . .  Rotate to global (shell) system

           . . . . . .  Nodal transformation for nodes 1 & 2          */

#I[41]:: t : Ar[{24,24},0];

        /*
        csb : 1
        snb : 0
        */

        /* . . . . . .  Translational dof                             */

#I[42]:: lambda : {{ 1,    0,    0 },\
                   { 0,  csb,  snb },\
                   { 0, -snb,  csb }};

#I[43]:: t : submatrixadd[ t, lambda, 1, 1 ];

#I[44]:: t : submatrixadd[ t, lambda, 7, 7 ];

        /* . . . . . .  Rotational dof                                */

#I[45]:: lambda : {{ csb,  0, -snb },\
                   {   0,  1,    0 },\
                   { snb,  0,  csb }};

#I[46]:: t : submatrixadd[ t, lambda,  4,  4 ];

#I[47]:: t : submatrixadd[ t, lambda, 10, 10 ];

        /* . . . . . .  Nodal transformation for nodes 3 & 4

           . . . . . .  Translational dof                             */

#I[48]:: lambda : {{ 1,    0,    0 },\
                   { 0,  csb, -snb },\
                   { 0,  snb,  csb }};
```

```
#I[49]:: t : submatrixadd[ t, lambda, 13, 13 ];

#I[50]:: t : submatrixadd[ t, lambda, 19, 19 ];

        /* . . . . . . . Rotational dof                                    */

#I[51]:: lambda : {{  csb,   0,   snb },\
                   {    0,   1,    0 },\
                   { -snb,   0,  csb }};

#I[52]:: t : submatrixadd[ t, lambda, 16, 16 ];

#I[53]:: t : submatrixadd[ t, lambda, 22, 22 ];

#I[54]:: ker : Ex[ t.ke.Trans[t] ];

        /* . . . . . Perform element assembly based upon prescribed
                     global degree-of-freedom (dof) number                 */

#I[55]:: k : Ar[{6,54},0];

#I[56]:: Do [ iel, start:1, 4,\
          Do [ i, start:1, 24,\
          Do [ j, start:1, 24,\
              ii:dof[iel,i]; jj:dof[iel,j];\
              If [ Match[ii,eqnum[1]], k[1,jj]:k[1,jj]+ker[i,j] ];\
              If [ Match[ii,eqnum[2]], k[2,jj]:k[2,jj]+ker[i,j] ];\
              If [ Match[ii,eqnum[3]], k[3,jj]:k[3,jj]+ker[i,j] ];\
              If [ Match[ii,eqnum[4]], k[4,jj]:k[4,jj]+ker[i,j] ];\
              If [ Match[ii,eqnum[5]], k[5,jj]:k[5,jj]+ker[i,j] ];\
              If [ Match[ii,eqnum[6]], k[6,jj]:k[6,jj]+ker[i,j] ];\
          ]]];

        /*
        *******************************************************************
        *                                                                 *
        *           Expand nodal dof about center node in terms of        *
        *           shell coordinates/displacements                       *
        *                                                                 *
        *******************************************************************
                . . . . Construct generalized expansion function (assuming
                        rectangular element geometry)                     */

#I[57]:: Set[ i ]; i^2 : -1; i^4 : 1;    /* Use "i" for imaginary unit   -/

#I[58]:: expn[$f,$x,$s]::\
                If[ Match[$s,0]&Match[$x,0], $f,\
                If[ Match[$s,0], $f ( cskx + Nc[$x] i snkx ),\
                If[ Match[$x,0], $f ( csks + Nc[$s] i snks ),\
                $f ( cskx + Nc[$x] i snkx )( csks + Nc[$s] i snks ) ]]];
```

210

```
                    /* . . . . .  Expand dof's about global node 5              */

#I[59]:: Set[{ r, s }];

#I[60]:: xnode : { -1, 0, 1,\
                   -1, 0, 1,\
                   -1, 0, 1 };

#I[61]:: ynode : { -s, -s, -s,\
                    0,  0,  0,\
                    s,  s,  s };

#I[62]:: Do [ inode, start:1, 9,\
              If [ Match[inode,1],\
                 d : { expn[ u,xnode[inode],ynode[inode]],\
                       expn[ v,xnode[inode],ynode[inode]],\
                       expn[ v,xnode[inode],ynode[inode]],\
                       expn[rx,xnode[inode],ynode[inode]],\
                       expn[ry,xnode[inode],ynode[inode]],\
                       expn[rz,xnode[inode],ynode[inode]] },\
                 d : Cat[ d,\
                         { expn[ u,xnode[inode],ynode[inode]],\
                           expn[ v,xnode[inode],ynode[inode]],\
                           expn[ v,xnode[inode],ynode[inode]],\
                           expn[rx,xnode[inode],ynode[inode]],\
                           expn[ry,xnode[inode],ynode[inode]],\
                           expn[rz,xnode[inode],ynode[inode]] } ] ] ];

          /*
            ******************************************************************
            *                                                                *
            *          Obtain "discrete" Euler equations and differential    *
            *          operator matrix                                       *
            *                                                                *
            ******************************************************************
                                                                            */

#I[63]:: area : 4*detj;

#I[64]:: csks : 1 - s^2 kbars^2/2;

#I[65]:: cskx : 1 - l^2 kbarx^2/2;

#I[66]:: snks : s kbars Sqrt[ as4 ];

#I[67]:: snkx : l kbarx Sqrt[ ax4 ];

#I[68]:: snb  : 1 / (2*r);

#I[69]:: ueq  : Ex[ k[1].d/area ];

#I[70]:: veq  : Ex[ k[2].d/area ];
```

211

```
#I[71]:: veq  :  Ex[ k[3].d/area ];

#I[72]:: rxeq :  Ex[ k[4].d/area ];

#I[73]:: ryeq :  Ex[ k[5].d/area ];

#I[74]:: rzeq :  Ex[ k[6].d/area ];

          /* . . . .  Extract discrete differential operator matrix     */

#I[75]:: cm : coefmatrix[ { ueq,veq,weq,rxeq,ryeq,rzeq },\
                          { u,v,w,rx,ry,rz } ]
```

$$
\#O[75]: \left\{\left\{ \frac{\text{kbars}^2\ \text{m33}\ s^2}{1^2} + \text{kbarx}^2\ \text{m11} - \frac{\text{kbars}^2\ \text{kbarx}^2\ \text{m11}\ s^2}{6} \right.\right.
$$

$$
- \frac{\text{kbars}^2\ \text{kbarx}^2\ \text{m33}\ s^2}{4},
$$

$$
\frac{\text{as4}^{1/2}\ \text{ax4}^{1/2}\ \text{csb}\ \text{kbars}\ \text{kbarx}\ \text{m12}\ s}{1}
$$

$$
+ \frac{\text{as4}^{1/2}\ \text{ax4}^{1/2}\ \text{csb}\ \text{kbars}\ \text{kbarx}\ \text{m33}\ s}{1},
$$

$$
- \frac{\text{ax4}^{1/2}\ i\ \text{kbarx}\ \text{m12}}{r}
$$

$$
+ \frac{\text{ax4}^{1/2}\ i\ \text{kbars}^2\ \text{kbarx}\ \text{m12}\ s^2}{4r}
$$

$$
+ \frac{\text{ax4}^{1/2}\ i\ \text{kbars}^2\ \text{kbarx}\ \text{m33}\ s^2}{4r},\ 0,0,0\},
$$

$$
\left\{ \frac{\text{as4}^{1/2}\ \text{ax4}^{1/2}\ \text{csb}\ \text{kbars}\ \text{kbarx}\ \text{m12}\ s}{1} \right.
$$

212

$$+ \frac{as4^{1/2} \; ax4^{1/2} \; csb \; kbars \; kbarx \; m33 \; s}{1},$$

$$\frac{q44}{r^2} - \frac{kbars^2 \; q44 \; s^2}{4 \, r^2} - \frac{kbarx^2 \; 1^2 \; q44}{4 \, r^2}$$

$$+ \frac{csb^2 \; kbars^2 \; m11 \; s^2}{1^2}$$

$$+ \frac{kbars^2 \; kbarx^2 \; 1^2 \; q44 \; s^2}{8 \, r^2} + csb^2 \; kbarx^2 \; m33$$

$$- \frac{csb^2 \; kbars^2 \; kbarx^2 \; m11 \; s^2}{6}$$

$$- \frac{csb^2 \; kbars^2 \; kbarx^2 \; m33 \; s^2}{4},$$

$$- \frac{as4^{1/2} \; csb \; i \; kbars \; m11 \; s}{1 \, r}$$

$$- \frac{as4^{1/2} \; csb \; i \; kbars \; q44 \; s}{1 \, r}$$

$$+ \frac{as4^{1/2} \; csb \; i \; kbars \; kbarx^2 \; 1 \; m11 \; s}{6r}$$

$$+ \frac{as4^{1/2} \; csb \; i \; kbars \; kbarx^2 \; 1 \; m33 \; s}{4r}$$

213

$$+ \frac{as4^{1/2} \, csb \, i \, kbars \, kbarx^2 \, l \, q44 \, s}{2r},$$

$$\frac{- as4^{1/2} \, ax4^{1/2} \, csb \, kbars \, kbarx \, l \, q44 \, s}{4r},$$

$$\frac{q44^2}{r} - \frac{kbars^2 \, q44^2 \, s}{4r} \cdot \frac{kbarx^2 \, l^2 \, q44}{4r}$$

$$+ \frac{kbars^2 \, kbarx^2 \, l^2 \, q44^2 \, s}{16r},$$

$$\frac{ax4^{1/2} \, i \, kbars^2 \, kbarx^2 \, l \, q44^2 \, s}{16 \, r^2} \Big\},$$

$$\Big\{ \frac{ax4^{1/2} \, i \, kbarx \, m12^2}{r} - \frac{ax4^{1/2} \, i \, kbars^2 \, kbarx \, m12^2 \, s}{4r}$$

$$- \frac{ax4^{1/2} \, i \, kbars^2 \, kbarx \, m33^2 \, s}{4r},$$

$$\frac{as4^{1/2} \, csb \, i \, kbars \, m11 \, s}{1 \, r}$$

$$+ \frac{as4^{1/2} \, csb \, i \, kbars \, q44 \, s}{1 \, r}$$

$$- \frac{as4^{1/2} \, csb \, i \, kbars \, kbarx^2 \, l \, m11 \, s}{6r}$$

$$as4^{1/2} \qquad\qquad 2$$

214

$$- \frac{as4 \; csb \; i \; kbars \; kbarx \; l \; m33 \; s}{4r}$$

$$- \frac{as4^{1/2} \; csb \; i \; kbars \; kbarx^2 \; l \; q44 \; s}{2r},$$

$$\frac{m11^2}{r^2} \;-\; \frac{kbars^2 \; m11 \; s}{4 \, r^2} \;-\; \frac{kbarx^2 \; l^2 \; m11}{6 \, r^2}$$

$$+ \frac{csb^2 \; kbars^2 \; q44^2 \; s}{1^2}$$

$$+ \frac{kbars^2 \; kbarx^2 \; l^2 \; m11 \; s^2}{24 \, r^2}$$

$$+ \frac{kbars^2 \; kbarx^2 \; l^2 \; m33 \; s^2}{16 \, r^2} \;+\; csb^2 \; kbarx^2 \; q44$$

$$- \frac{csb^2 \; kbars^2 \; kbarx^2 \; q44^2 \; s}{2},$$

$$ax4^{1/2} \; csb^2 \; i \; kbarx \; q44$$

$$- \frac{ax4^{1/2} \; csb^2 \; i \; kbars^2 \; kbarx^2 \; q44 \; s}{4},$$

$$- \frac{as4^{1/2} \; csb \; i \; kbars \; q44 \; s}{1}$$

$$as4^{1/2} \; csb \; i \; kbars \; kbarx^2 \; l \; q44 \; s$$

$$- \frac{-------------------------------}{4},$$

$$\frac{as4^{1/2} \; ax4^{1/2} \; csb \; kbars \; kbarx \; l \; q44 \; s}{4r} \},$$

$$\{0, \frac{- as4^{1/2} \; ax4^{1/2} \; csb \; kbars \; kbarx \; l \; q44 \; s}{4r},$$

$$- ax4^{1/2} \; csb^2 \; i \; kbarx \; q44$$

$$+ \frac{ax4^{1/2} \; csb^2 \; i \; kbars^2 \; kbarx^2 \; q44 \; s}{4},$$

$$\frac{csb^2 \; kbars^2 \; q33 \; s^2}{l^2} + csb^2 \; q44 + csb^2 \; kbarx^2 \; q11$$

$$- \frac{csb^2 \; kbars^2 \; q44 \; s^2}{4} - \frac{csb^2 \; kbarx^2 \; l^2 \; q44}{4}$$

$$- \frac{csb^2 \; kbars^2 \; kbarx^2 \; q11 \; s^2}{4}$$

$$- \frac{csb^2 \; kbars^2 \; kbarx^2 \; q33 \; s^2}{4}$$

$$+ \frac{csb^2 \; kbars^2 \; kbarx^2 \; l^2 \; q44 \; s^2}{16},$$

$$\frac{as4^{1/2} \; ax4^{1/2} \; csb \; kbars \; kbarx \; q12 \; s}{l}$$

$$as4^{1/2} \; ax4^{1/2}$$

216

$$+ \frac{as4 \quad ax4 \quad csb \; kbars \; kbarx \; q33 \; s}{1},$$

$$\frac{as4^{1/2} \; csb \; i \; kbars \; q33 \; s}{1 \; r} - \frac{as4^{1/2} \; csb \; i \; kbars \; l \; q44 \; s}{4r}$$

$$- \frac{as4^{1/2} \; csb \; i \; kbars \; kbarx^2 \; l \; q11 \; s}{4r}$$

$$- \frac{as4^{1/2} \; csb \; i \; kbars \; kbarx^2 \; l \; q33 \; s}{4r}$$

$$+ \frac{as4^{1/2} \; csb \; i \; kbars \; kbarx^2 \; l^3 \; q44 \; s}{16r}\},$$

$$\{0.\frac{q44}{r} - \frac{kbars^2 \; q44^2 \; s}{4r} - \frac{kbarx^2 \; l^2 \; q44}{4r}$$

$$+ \frac{kbars^2 \; kbarx^2 \; l^2 \; q44^2 \; s}{16r},$$

$$\frac{- as4^{1/2} \; csb \; i \; kbars \; q44 \; s}{1}$$

$$+ \frac{as4^{1/2} \; csb \; i \; kbars \; kbarx^2 \; l \; q44 \; s}{4},$$

$$\frac{as4^{1/2} \; ax4^{1/2} \; csb \; kbars \; kbarx \; q12 \; s}{1}$$

$$+ \frac{as4^{1/2} \; ax4^{1/2} \; csb \; kbars \; kbarx \; q33 \; s}{1},$$

217

$$q44 + \frac{kbars^2 \; q11 \; s^2}{l^2} + kbarx^2 \; q33 - \frac{kbars^2 \; q44 \; s^2}{4}$$

$$- \frac{kbarx^2 \; l^2 \; q44}{4} - \frac{kbars^2 \; kbarx^2 \; q11 \; s^2}{4}$$

$$- \frac{kbars^2 \; kbarx^2 \; q33 \; s^2}{4} + \frac{kbars^2 \; kbarx^2 \; l^2 \; q44 \; s^2}{16},$$

$$\frac{ax4^{1/2} \; i \; kbarx \; q33}{r} - \frac{ax4^{1/2} \; i \; kbars^2 \; kbarx \; q12 \; s^2}{4r}$$

$$- \frac{ax4^{1/2} \; i \; kbars^2 \; kbarx \; q33 \; s^2}{4r}\},$$

$$\{0, \frac{- ax4^{1/2} \; i \; kbars^2 \; kbarx^2 \; l^2 \; q44 \; s}{16 \; r^2},$$

$$\frac{as4^{1/2} \; ax4^{1/2} \; csb \; kbars \; kbarx \; l \; q44 \; s}{4r},$$

$$- \frac{as4^{1/2} \; csb \; i \; kbars \; q33 \; s}{l \; r} + \frac{as4^{1/2} \; csb \; i \; kbars \; l \; q44 \; s}{4r}$$

$$+ \frac{as4^{1/2} \; csb \; i \; kbars \; kbarx^2 \; l \; q11 \; s}{4r}$$

$$+ \frac{as4^{1/2} \; csb \; i \; kbars \; kbarx^2 \; l \; q33 \; s}{4r}$$

Appendix B

THE ANS SHELL ELEMENTS:
PART 1 - FORMULATION

by

K. C. PARK and G. M. STANLEY

The ANS Shell Elements: Part 1 – Formulation

K. C. Park
Department of Aerospace Engineering Sciences and
Center for Space Structures and Controls
University of Colorado, Campus Box 429
Boulder, Colorado 80309

and

G. M. Stanley
Computational Structural Mechanics Section
Lockheed Palo Alto Research Laboratory
3251 Hanover St., Palo Alto, CA 94304

June 1987/Revised March 1988

Report No. CU–CSSC–87–06

ABSTRACT

A formulation for the equations of motion for shells is presented, which is intended to provide a theoretical foundation for shell elements based on the assumed natural-coordinate strain (ANS-) interpolations. The present formulation can be hierarchically specialized to shells that admit normal loads and changes in the normal thickness, to shells exhibiting transverse shear deformations and to thin shells. In order to facilitate coordinate-invariant interpolations of variables, the formulation adopts an inertially fixed coordinate system for translational displacements and a shell coordinate system for changes in the normal vector. The central aspect of the present formulation is a general set of incremental strain-displacement relations that are valid for large strain and finite rotations. Hence, the present strain-displacement relations effectively replace the prevalent usage of the linear plate strain-displacement relations for constructing C^o-shell elements. An attractive feature of the present thin shell equations is that the in-plane bending strain ($\kappa_{\xi\eta}$) is akin to Sanders' correction term, hence alleviating slow convergence difficulty in doubly curved shell cases.

1. INTRODUCTION

A major motivation in the pioneering work on the finite element method (Turner, Clough, Martin and Topp, 1956) was to provide a shell analysis capability. During the ensuing three decades, several noteworthy developments have taken place in order to provide reliable and general shell analysis procedures in many of the existing general finite element analysis programs. Broadly speaking, these developments may be grouped into four schools of shell analysis approaches. In the early days of finite element applications to shell analysis, a patch of a plane stress and a plate bending element was formed and used to discretize the shell surface. While such elements are still in use today (Taig, 1961; Argyris, 1965; Klein, 1967; Albasiny and Martin, 1967; Connor and Brebbia, 1967; Greene, Strome and Weikel, 1971; Cowper, Lindberg and Olson, 1970), it is generally agreed that they can suffer from non-convergence, especially when membrane-bending coupling dominates the shell behavior.

The second approach has been to discretize the equations of motion based on classical shell theories (Kraus, 1967). This approach was extensively studied prior to the age of isoparametric shape functions (Zienkiewicz and Cheung, 1964, 1965; Haisler and Stricklin, 1967; Strickland and Loden, 1968; Cantin and Clough, 1968; Clough and Johnson, 1968; Fonder and Clough, 1973; Morris, 1976; Ashwell, 1976). A common difficulty with this approach is that the resulting discrete shell equations suffer from artificial strain states when the element undergoes arbitrarily large rigid motions (Cantin, 1970; Darve, 1972).

With the introduction of isoparametric shape functions (Irons, 1966; Ergatoudis, Irons and Zienkiewicz, 1968), many element developers adopted the isoparametric mapping in the transformation of the natural-coordinate basis into the inertially fixed orthogonal basis. An important consequence of this adoption in the context of shell elements was to implicitly abandon the metric of the shell curvature–i.e., a scalar-invariant quadratic form–in the strain-displacement representations. Instead, the second-order covariant tensor transformations that are needed in the formulation of shell elements were accomplished through the repeated use of the isoparametric Jacobian matrix which relates the parameterized natural-coordinate derivatives to the inertially fixed spatial derivatives. To a great extent, from a theoretical point of view, deficiencies in some of the existing shell elements can be traced to the inadequacy of the isoparametric Jacobian matrix to approximate the scalar-invariant metric of the space for representing the differential element of arc length for shell surfaces. This inadequacy, coupled with a set of inconsistent strain interpolations (Fræijs de Veubeke, 1965), has been shown to cause element locking (Ahmad, Irons and Zienkiewicz, 1970). Reduced integration (Zienkiewicz, Taylor and Too, 1971; Pawsey and Clough, 1971) to alleviate such locking phenomena has in turn led to spurious mechanisms (Kosloff and Frazer, 1978; Flanagan and Belytschko, 1981). Details in the preceding three approaches can be found in the text of Zienkiewicz (1971), Ashwell and Gallagher (1976), Irons (1980) and Hughes (1986).

The fourth approach has been to combine two salient features into element construction:

3

isoparametric interpolations of strain fields and second-order tensor transformations to transform the natural-coordinate strains into the strains in an inertially fixed orthogonal coordinate system, and vice versa. Shell elements (Dvorkin and Bathe, 1984; Park and Stanley, 1986; Pinsky and Jang, 1986) based on this approach have shown potential for more reliable shell analysis. A common variational framework employed in the implementation of these shell elements may be viewed as the one that bypasses classical shell theories and resorts to the basic equations of state and motion of continuum mechanics (Hughes and Liu, 1981). However, the strain-displacement relations used in the element formulations have been limited to those of plate theories due to Reissner (1945) and Mindlin (1951) that are generally considered to be valid for linear small strains only. Consequently, in order to properly capture shell behavior such as inextensional bending, membrane-bending coupling for thin shells and in-plane shear deformations within the context of continuum mechanics-based variational equations, the resulting elements have to be considerably embellished. In other words, many of the shell assumptions–i.e., Kirchhoff-Love's postulates (Love, 1927)–must be invoked in an element-level strain interpolation. It should be noted that, except in Park and Stanley (1986), element developers adopting this approach have not incorporated the two fundamental differential lengths of arc along the element edges in the strain-displacement relations.

In essence, the present paper is a first revised series of our effort on shell elements based on the assumed natural-coordinate strain (or ANS–) formulation. The basic philosophy we advocate here can be summarized as follows. First, we incorporate as much shell behavior as possible into the variational equations of motion while, in principle, we maintain some of the advantageous features in the continuum-based formulation–particularly the constitutive relations and large rotation algorithms. For this reason, we employ stresses as the conjugate variables to strain increments in our formulation rather than the resultant forces and moments that are used in most classical theories. In this way we hope to minimize the element embellishments referred to in the preceding paragraph. Second, we adhere to a set of *physical* covariant strains as our basis of strain interpolations along the natural-coordinate lines. It will be shown that these two aspects, together with an objective set of strain increments and nonlinear constitutive relations, effectively provide a general shell analysis capability that replaces the presently prevalent usage of the strains that were originally developed for linear plate bending theories. Third, we propose to employ the isoparametric shape functions both for shell surface geometries and displacements. However, we will abandon the isoparametric Jacobian matrix in the derivation of strains. Instead, we will employ appropriate second-order tensor transformations to obtain the orthogonal shell-surface strains from the natural-coordinate strains. It has been found that the resulting element strain states become invariant with respect to an arbitrary choice of the shell-coordinate system (Park and Stanley, 1986). Fourth, the present formulation starts with D'Alembert's principle from which the variational equations of motion are derived, which are valid for shell dynamics. This is in contrast with most existing shell formulations wherein the inertia force terms are retrofitted into the quasi-static shell equations, thus often leading to an inconsistent set of dynamical equations.

4

Hence, Part 1 of the present paper can be viewed as a theoretical foundation on the shell elements based on assumed natural-coordinate strain (ANS-) elements that began with the linear interpolation of membrane strains in Park (1985), the 9-ANS shell element by Park and Stanley (1986), Park, Stanley and Cabiness (1986), Stanley (1985), and Stanley, Park and Hughes (1986). We now summarize the present Part.

Section 2 describes the kinematics of the shell element for which a set of triad coordinate systems are chosen: an inertially fixed coordinate system for translational motions, an orthogonal shell-surface coordinate system for rotational motions and a natural-coordinate system for strains. The present choice of such triad coordinate systems has been shown to play a fundamental role in mitigating several element deficiencies heretofore present in many of the existing shell elements. Specifically, the translational displacements and the rotations become uncoupled in the resulting inertia force expression. Shell surface geometries are characterized in terms of the parameterized natural coordinates for general shells in Section 3. The natural covariant unit basis vectors and the two fundamental differential magnitudes along the natural coordinates are derived. These two are then used to obtain natural-coordinate derivatives that are to be employed in the derivation of the present variational strain-displacement relations.

The variational equations of motion for general shells are derived in Section 4, starting with D'Alembert's principle. The acceleration vector that was obtained in Section 2 in terms of the inertial displacements and the corotational pseudo-vectors and a contravariant stress dyadic tensor, are introduced to express Cauchy's equations of motion. The product of the variational position vector and Cauchy's equations of motion yields the D'Alembert equation. A variational manipulation of the D'Alembert equation leads us to identify the present form of *virtual* strain-displacement relations. The resulting variational equations of motion, if discretized properly, should yield a consistent set of their discrete counterparts for general shells.

In order to derive the desired incremental strain-displacement relations from the virtual strain-displacement relations, we offer the essential difference between the infinitesimal virtual variation (δ-process) and the finite incremental changes (Δ-process). This is discussed in Section 5. Recognition of this difference enables us to obtain the incremental strain-displacement relations from the virtual strain-displacement relations. It is shown that the resulting incremental strain-displacement relations remain objective for arbitrarily large rigid motions and accurate for up to moderate strain increments. Computations of the shell-coordinate strain increments are then covered in Section 6. This is accomplished by the pointwise second-order tensor transformation. These strain increments are then used to compute the corresponding stress increments. With a suitable stress update algorithm, one can compute internal force.

Thin shell approximations of the present formulation are discussed in Section 7 and the present Part concludes with a discussion on classical shell theories. It is shown that, when the transverse shear strains are negligible, the present equations appear to yield an incremental form of the nonlinear shell equations given by Sanders (1963). A major difference

5

for this special case of the present shell equations is that they are presented in terms of the inertial displacements and the finite pseudo-rotations instead of the covariant shell-surface displacements and the infinitesimal rotations. Thus, the present shell equations may implicitly have incorporated the finite rotation effects discussed in Reissner(1963, 1969, 1972), and Simmonds and Danielson (1972).

2. Kinematics of Shell

We consider here a shell element undergoing large motions and deformations as shown in Fig. 1. The position vector of the particle point P from the initial time t_0 to a later time t can be expressed as

$$r = (X + u)e_1 + (Y + v)e_2 + (Z + w)e_3 + \ell_3 b_3 \qquad (2 \cdot 1)$$

where $(u\ v\ w)$ are displacements measured in the inertial system $e = (s_1\ e_2\ e_3)$, the unit triads $b = (b_1\ b_2\ b_3)$ are attached on the deformed cross-section of the shell, and ℓ_3 is the distance of the material point P on the deformed cross section from the shell neutral surface. Therefore, we have the following unique transformation from the inertially fixed frame, e, to the body-fixed frame, b:

$$b = Re \qquad (2 \cdot 2)$$

where R is a (3×3) transformation matrix.

The angular velocity of a particle point, P, on the shell cross section is thus obtained from (2.2) as

$$\dot{b} = \tilde{\omega}^T b, \quad \tilde{\omega} = -\dot{R}R^T \qquad (2 \cdot 3)$$

where

$$\tilde{\omega} = \begin{bmatrix} 0 & -\omega_3 & \omega_2 \\ \omega_3 & 0 & -\omega_1 \\ -\omega_2 & \omega_1 & 0 \end{bmatrix} \qquad (2 \cdot 4)$$

The velocity of the particle point P can be obtained from (2.1)

$$\dot{r} = \dot{u}^T e + \dot{\ell}^T b + \ell^T \dot{b} = \dot{u}^T e + \dot{\ell}^T b + \ell^T \tilde{\omega}^T b \qquad (2 \cdot 5)$$

in which the relations of (2.2) and (2.3) have been used and

$$u^T = (u\ v\ w) \quad \text{and} \quad \ell^T = (0\ 0\ \ell_3) \qquad (2 \cdot 6)$$

Time differentiation of $\dot{\mathbf{r}}$ then yields the acceleration of the particle point P:

$$\ddot{\mathbf{r}} = \ddot{\mathbf{u}}^T \mathbf{e} + \ddot{\tilde{\ell}}_3^T \mathbf{b}_3 + 2\dot{\ell}_3^T \dot{\mathbf{b}}_3 + \boldsymbol{\ell}^T \dot{\tilde{\omega}}^T \mathbf{b} + \boldsymbol{\ell}^T \tilde{\omega}^T \tilde{\omega}^T \mathbf{b} \qquad (2 \cdot 7)$$

Finally, the variation of the position vector $\mathbf{r}$ can be obtained from (2.5)

$$\delta \mathbf{r} = \delta \mathbf{u}^T \mathbf{e} + \delta \ell_3^T \mathbf{b}_3 + \delta \alpha^T \tilde{\ell} \mathbf{b} \qquad (2 \cdot 8)$$

where $\delta \alpha$ is a pseudo-vector that is conjugate with ω such that

$$\delta \tilde{\alpha}^T = \delta \mathbf{R} \mathbf{R}^T, \qquad \omega = \lfloor \omega_1 \quad \omega_2 \quad \omega_3 \rfloor^T, \qquad \delta \alpha = \lfloor \delta \alpha_1 \quad \delta \alpha_2 \quad \delta \alpha_3 \rfloor^T \qquad (2 \cdot 9)$$

and $\tilde{\ell}$ is given by

$$\tilde{\ell} = \begin{bmatrix} 0 & -\ell_3 & 0 \\ +\ell_3 & 0 & 0 \\ 0 & 0 & 0 \end{bmatrix} \qquad (2 \cdot 10)$$

Remark 2.1: In most shell theories the following approximations are widely accepted:

$$\dot{\ell}_3^T \approx 0, \qquad \delta \ell_3^T = 0 \qquad (2 \cdot 11)$$

These approximations, however, preclude applications of the resulting equations of motion to large membrane deformations such as balloons and rubber materials under extensive stretching.

It should be noted that $\delta \alpha$ should not be confused with the variation of angles in classical mechanics. Only for the variation of infinitesimal angles, their components approach infinitesimal variations of angles.

3. Shell Geometries

To describe the shell geometries, we employ two coordinate systems: an orthogonal shell-surface coordinate system (the s-system) and a natural coordinate system, $(\xi \quad \eta \quad \varsigma)$, that is not in general orthogonal as shown in Fig. 1. In order to streamline our subsequent derivations of shell geometries, we need to express the position vector ($\mathbf{r}$) to the particle point, P, on the deformed shell cross section given by (2.1) in the shell-coordinate system. To this end, we observe that there exists a unique relation between the b-system and s-system:

$$\mathbf{b} = \mathbf{S}_{bs} \mathbf{s}, \qquad \mathbf{s} = \mathbf{T}_{sg} \mathbf{e}, \qquad \boldsymbol{\ell} = \mathbf{S}_{bs} \boldsymbol{\xi} \qquad (3 \cdot 1)$$

7

where

$$\xi^T = \lfloor 0 \quad 0 \quad \bar{\varsigma} \rfloor, \quad \bar{\varsigma} = \frac{\varsigma}{2}(h(\xi,\eta) + q(\xi,\eta)) \tag{3.2}$$

in which $h(\xi,\eta)$ is the initial shell thickness and $q(\xi,\eta)$ is the change in the shell thickness. Using the above relations we have for the second term in (2.1) as

$$\ell^T \mathbf{b} = \xi^T \mathbf{S}_{b\bullet}^T \mathbf{S}_{b\bullet} \mathbf{T}_{\bullet g} \mathbf{e} = \xi^T \mathbf{T}_{\bullet g} \mathbf{e} \tag{3.3}$$

Substituting (3.3) into (2.1), the position vector, $\mathbf{r}$, of an arbitrary point in the deformed shell is then given by

$$\mathbf{r} = \mathbf{r}^\circ + \bar{\varsigma} \mathbf{t}(\varsigma)_{\bullet g} \mathbf{e}, \qquad \mathbf{r}^\circ = x \mathbf{e}_1 + y \mathbf{e}_2 + z \mathbf{e}_3 \tag{3.4}$$

where $(x,\ y,\ z)$ refer to a current position in the neutral line of the parameterized shell surface:

$$\lfloor x(\xi,\eta) \quad y(\xi,\eta) \quad z(\xi,\eta) \rfloor = \lfloor (X+u) \quad (Y+v) \quad (Z+w) \rfloor \tag{3.5}$$

and $\mathbf{t}(\varsigma)_{\bullet g}$ is the third row of $\mathbf{T}_{\bullet g}$ given by

$$\mathbf{t}(\varsigma)_{\bullet g} = \lfloor t_{31} \quad t_{32} \quad t_{33} \rfloor \tag{3.6}$$

If the shell is sufficiently thin, a natural coordinate system whose basis vectors are attached along the neutral shell surface is adequate for the derivation of the governing equations of motion and the associated incremental strain-displacement relations. However, for general shells the natural-coordinate basis vectors and/or the differential lengths of arc may vary across the shell cross sections. Hence, we re-express $\mathbf{r}$ as

$$\mathbf{r} = \lfloor \bar{x} \quad \bar{y} \quad \bar{z} \rfloor = \lfloor (x(\xi,\eta) + \bar{\varsigma} t_{31}) \quad (y(\xi,\eta) + \bar{\varsigma} t_{32}) \quad (z(\xi,\eta) + \bar{\varsigma} t_{33}) \rfloor \tag{3.7}$$

The two fundamental magnitudes along the parameterized curves, $(\xi,\ \eta,\ \varsigma)$, away from the neutral shell surface ($\varsigma = 0$) are obtained (e.g., Kraus, 1967) as

$$\bar{g}_{\xi\xi}^2 = \frac{\partial \mathbf{r}}{\partial \xi} \cdot \frac{\partial \mathbf{r}}{\partial \xi}, \qquad \bar{g}_{\eta\eta}^2 = \frac{\partial \mathbf{r}}{\partial \eta} \cdot \frac{\partial \mathbf{r}}{\partial \eta} \tag{3.8}$$

and the covariant natural-coordinate unit vectors, $\bar{\mathbf{a}} = \lfloor \bar{\mathbf{a}}_\xi \quad \bar{\mathbf{a}}_\eta \quad \bar{\mathbf{a}}_\varsigma \rfloor^T$, are defined as

$$\bar{\mathbf{a}}_\xi = \frac{1}{\bar{g}_{\xi\xi}} \frac{\partial \mathbf{r}}{\partial \xi} = \frac{1}{\bar{g}_{\xi\xi}} (\bar{x}_{,\xi} \mathbf{e}_1 + \bar{y}_{,\xi} \mathbf{e}_2 + \bar{z}_\xi \mathbf{e}_3) \tag{3.9}$$

$$\bar{\mathbf{a}}_\eta = \frac{1}{\bar{g}_{\eta\eta}} \frac{\partial \mathbf{r}}{\partial \eta} = \frac{1}{\bar{g}_{\eta\eta}} (\bar{x}_{,\eta} \mathbf{e}_1 + \bar{y}_{,\eta} \mathbf{e}_2 + \bar{z}_{,\eta} \mathbf{e}_3) \tag{3.10}$$

$$\bar{\mathbf{a}}_\varsigma = \frac{\bar{\mathbf{a}}_\xi \times \bar{\mathbf{a}}_\eta}{|\bar{\mathbf{a}}_\xi \times \bar{\mathbf{a}}_\eta|} = (\bar{x}_{,\varsigma} \mathbf{e}_1 + \bar{y}_{,\varsigma} \mathbf{e}_2 + \bar{z}_{,\varsigma} \mathbf{e}_3) \tag{3.11}$$

8

or in a compact form

$$\bar{\mathbf{a}} = \hat{T}_{n\sigma}\mathbf{e}$$ (3 · 12)

where $(\ ),_\xi$ denotes parametric differentiation with respect to ξ.

Note that the position vector for the neutral shell surface, $\mathbf{r}^\circ(\xi, \eta)$, is expressed in an inertial coordinate system, $(\mathbf{e}_1 \ \mathbf{e}_2 \ \mathbf{e}_3)$, whereas the shell thickness vector away from the neutral surface is given in the natural–coordinate system. This is consistent with our choice of dual coordinate systems, viz, the e-system for translational motions and the ā-system for rotational motions.

Remark 3.1: If, however, the shell is sufficiently thin, the preceding relations can be considerably simplified by replacing $\mathbf{r}$ by $\mathbf{r}^\circ$ in the preceding fundamental magnitudes and covariant unit vectors.

The differential lengths of the edges along the natural–coordinate lines, dS_ξ and dS_η, are thus given by

$$dS_\xi = g_{\xi\xi}d\xi, \qquad g_{\xi\xi}^2 = A_\xi^2 + (\bar{\varsigma},_\xi)^2 + 2\bar{\varsigma}A_\xi\mathbf{a}_\xi \cdot \frac{\partial \mathbf{a}_\varsigma}{\partial \xi} + \bar{\varsigma}^2\frac{\partial \mathbf{a}_\varsigma}{\partial \xi} \cdot \frac{\partial \mathbf{a}_\varsigma}{\partial \xi}$$ (3 · 13)

$$dS_\eta = g_{\eta\eta}d\eta, \qquad g_{\eta\eta}^2 = A_\eta^2 + (\bar{\varsigma},_\eta)^2 + 2\bar{\varsigma}A_\eta\mathbf{a}_\eta \cdot \frac{\partial \mathbf{a}_\varsigma}{\partial \eta} + \bar{\varsigma}^2\frac{\partial \mathbf{a}_\varsigma}{\partial \eta} \cdot \frac{\partial \mathbf{a}_\varsigma}{\partial \eta}$$ (3 · 14)

$$dS_\varsigma = g_{\varsigma\varsigma}d\varsigma, \qquad g_{\varsigma\varsigma}^2 = A_\varsigma^2 + \bar{\varsigma}^2(\frac{\partial \mathbf{a}_\varsigma}{\partial \varsigma} \cdot \frac{\partial \mathbf{a}_\varsigma}{\partial \varsigma})$$ (3 · 15)

in which we used the following definitions:

$$A_\xi^2 = \frac{\partial \mathbf{r}^\circ}{\partial \xi} \cdot \frac{\partial \mathbf{r}^\circ}{\partial \xi}, \qquad A_\eta^2 = \frac{\partial \mathbf{r}^\circ}{\partial \eta} \cdot \frac{\partial \mathbf{r}^\circ}{\partial \eta} \qquad A_\varsigma^2 = \frac{1}{4}(h(\xi, \ \eta) + q(\xi, \eta))^2$$ (3 · 16)

Equations (3.12) - (3.14) imply

$$\frac{\partial}{\partial S_\xi} = \frac{1}{g_{\xi\xi}}\frac{\partial}{\partial \xi}$$ (3 · 17)

$$\frac{\partial}{\partial S_\eta} = \frac{1}{g_{\eta\eta}}\frac{\partial}{\partial \eta}$$ (3 · 18)

$$\frac{\partial}{\partial S_\varsigma} = \frac{1}{g_{\varsigma\varsigma}}\frac{\partial}{\partial \varsigma}$$ (3 · 19)

Equations (3.8)–(3.11) and (3.16)–(3.18) will be extensively utilized in the subsequent description of the present formulation.

4. Variational Equations of Motion for General Shells

As stated in the Introduction, we begin the derivation of the present incremental strain-displacement relations from the D'Alembert principle (Lanczos, 1970). We then cast it into a variational form in the inertial reference frame, which is then subsequently transformed via the necessary tensor transformations into another variational equation of motion expressed in a non-orthogonal natural-coordinate system. From this equation, we then identify *variational* strain-displacement relations. The physical incremental strain-displacement relations are then obtained *directly* from the variational strain-displacement relations simply by changing the infinitesimal variation, δ, by the finite increment, Δ, provided certain consistency requirements are observed.

In order to effect the derivation of the variational equations of motion, we begin with the well-known Cauchy equations of motion written in vector form in the inertial coordinate frame:

$$\rho \ddot{\mathbf{r}} = \nabla_e \cdot \overrightarrow{\sigma}_e + \mathbf{f} \qquad (4 \cdot 1)$$

in which ρ is the density, the gradient vector operator ∇ is given by

$$\nabla_e = \frac{\partial}{\partial \bar{x}} \mathbf{e}_1 + \frac{\partial}{\partial \bar{y}} \mathbf{e}_2 + \frac{\partial}{\partial \bar{z}} \mathbf{e}_3, \qquad (4 \cdot 2)$$

the Cauchy stress tensor in dyadic form, $\overrightarrow{\sigma}_e$, is given by

$$\overrightarrow{\sigma}_e = \left\{ \begin{array}{l} \sigma_{xx}\mathbf{e}_1\mathbf{e}_1 + \sigma_{xy}\mathbf{e}_1\mathbf{e}_2 + \sigma_{xz}\mathbf{e}_1\mathbf{e}_3 \\ + \sigma_{yx}\mathbf{e}_2\mathbf{e}_1 + \sigma_{yy}\mathbf{e}_2\mathbf{e}_2 + \sigma_{yz}\mathbf{e}_2\mathbf{e}_3 , \\ + \sigma_{zx}\mathbf{e}_3\mathbf{e}_1 + \sigma_{zy}\mathbf{e}_3\mathbf{e}_2 + \sigma_{zz}\mathbf{e}_3\mathbf{e}_3 \end{array} \right. \qquad (4 \cdot 3)$$

and $\mathbf{f}$ is an applied force vector.

The variational equations of motion is given by

$$\int_V \delta \mathbf{r} \cdot (\rho \ddot{\mathbf{r}} - \nabla_e \cdot \overrightarrow{\sigma}_e - \mathbf{f}) dV = 0 \qquad (4 \cdot 4)$$

10

Equation (4.4) is re-expressed as

$$\delta \mathbf{F}^I + \delta \mathbf{F}^S - \delta \mathbf{F}^T = \delta \mathbf{F}^E \qquad (4 \cdot 5)$$

in which $\delta \mathbf{F}^I$, $\delta \mathbf{F}^S$, $\delta \mathbf{F}^T$ and $\delta \mathbf{F}^E$ are referred to as the inertia force, the stiffness force, the traction boundary force and the external force operators, respectively, and are given by

$$\delta \mathbf{F}^I = \int \rho \delta \mathbf{r} \cdot \ddot{\mathbf{r}} dV \qquad (4 \cdot 6)$$

$$\delta \mathbf{F}^S + \delta \mathbf{F}^T = - \int \delta \mathbf{r} \cdot \nabla_e \cdot \vec{\sigma}_e \, dV \qquad (4 \cdot 7)$$

$$\delta \mathbf{F}^E = \int \delta \mathbf{r} \cdot \mathbf{f} dV \qquad (4 \cdot 8)$$

We will now treat the above three variational operators separately.

4.1 The Inertia Force Operator, $\delta \mathbf{F}^I$

The dot product of $\delta \mathbf{r} \cdot \ddot{\mathbf{r}}$ from (2.7) and (2.8) yields

$$\delta \mathbf{r} \cdot \ddot{\mathbf{r}} = \left\{ \begin{array}{l} \delta \mathbf{u}^T (\ddot{\tilde{\mathbf{u}}} + \mathbf{e} \cdot \mathbf{b}_3^T \ddot{\tilde{\ell}}_3 + 2\mathbf{e} \cdot \dot{\mathbf{b}}_3^T \dot{\tilde{\ell}}_3 + \mathbf{R}^T \tilde{\ell}^T \dot{\omega} + \mathbf{R}^T \tilde{\omega} \tilde{\ell}^T \omega) \\ + \delta \ell_3 (\mathbf{b}_3 \cdot \mathbf{e}^T \ddot{\tilde{\mathbf{u}}} + \ddot{\tilde{\ell}}_3 + \mathbf{b}_3 \cdot \mathbf{b}^T \tilde{\ell}^T \dot{\omega} + \mathbf{b}_3 \cdot \mathbf{b}^T \tilde{\omega} \tilde{\ell}^T \omega) \\ + \delta \alpha^T \tilde{\ell} (\mathbf{R} \ddot{\tilde{\mathbf{u}}} + \mathbf{b}^T \cdot \mathbf{b}_3^T \ddot{\tilde{\ell}}_3 + 2\mathbf{b} \cdot \dot{\mathbf{b}}_3^T \dot{\tilde{\ell}}_3 + \tilde{\ell}^T \dot{\omega} + \tilde{\omega} \tilde{\ell}^T \omega) \end{array} \right. \qquad (4 \cdot 9)$$

If we choose the origin of the (ξ, η, ς)-coordinate system to be the center of the cross-sectional area of the shell element, we have

$$\int_V \tilde{\ell} dV = \int_V \tilde{\ell}^T dV = 0 \qquad (4 \cdot 10)$$

11

Substituting (4.9) into (4.6) and making use of (4.10), we obtain for the inertia force operator:

$$\delta \mathbf{F}^I = \begin{cases} \int_V \rho(\delta \mathbf{u}^T \ddot{\mathbf{u}} + \delta \ell_3 \ddot{\bar{\ell}}_3 + \delta \alpha^T \tilde{\ell} \bar{\ell}^T \dot{\omega} + \delta \alpha^T \tilde{\ell} \tilde{\omega} \bar{\ell}^T \omega) dV \\ + \int_V \rho(\delta \mathbf{u}^T \mathbf{e} \cdot \mathbf{b}_3^T \ddot{\bar{\ell}}_3 + \delta \ell_3 \mathbf{b}_3 \cdot \mathbf{e}^T \ddot{\mathbf{u}} + 2\delta \mathbf{u} \mathbf{e} \cdot \dot{\mathbf{b}}_3^T \dot{\ell}_3) dV \end{cases} \qquad (4 \cdot 11)$$

Note that the second row of (4.11) gives rise to off-block diagonal contributions to the mass matrix. In other words, they represent the cross coupling between the $\bar{\mathbf{u}}$-components and $\bar{\ell}_3$. We will assume that the inertia force due to the through-the-thickness relative motion is small compared to the inertial motions. However, in order to prevent rank-deficiency in the resulting mass matrix, we will retain $\delta \ell_3 \bar{\ell}_3$. We thus simplify (4.11) to

$$\delta \mathbf{F}^I = \int_V \rho(\delta \mathbf{u}^T \ddot{\mathbf{u}} + \delta \ell_3 \ddot{\bar{\ell}}_3 + \delta \alpha^T \tilde{\ell} \bar{\ell}^T \dot{\omega} + \delta \alpha^T \tilde{\ell} \tilde{\omega} \bar{\ell}^T \omega) dV \qquad (4 \cdot 12)$$

Remark 4.1: It is noted that the translational displacements u are measured in e, whereas the pseudo-rotations $\delta \alpha$ are measured in b. It is the dual choices that result in the simple decoupled inertia expressions as given in (4.12).

Remark 4.2: Although the preceding inertia force operator has been derived for a general three-dimensional continuum, there exists no contribution due to ω_3-term. In other words, the inertia force due to the normal rotation is assumed to be negligible, as a direct consequence of the admissible displacement adopted in (2.1). This is somewhat akin to Naghdi's adaptation (1972) of a director vector concept of the Cosserat brothers (1909).

4.2 The Stiffness Force Operator, $\delta \mathbf{F}^S$

Computations of the stiffness force operator terms as given by (4.7) are not convenient since the stresses are measured in the inertial coordinate systems. A convenient coordinate system to facilitate computations of the stiffness force is an orthogonal corotational system

(or the shell coordinate system). However, as the element meshes are in general irregular, a more suitable system is the non-orthogonal natural-coordinate system defined on the deformed shell element, i.e., the ā-system, as introduced in Section 3. This is particularly attractive when the element is based on the assumed strain states.

Of several possible approaches, the one we will employ is based on the invariance property of the variational form of the stiffness force operator under an arbitrary choice of coordinate system. Note that (4.7) contains terms expressed in both the e and ā-coordinate systems. Instead, it can be expressed in the ā-system only. To this end, first we re-express δr in the e-system:

$$\delta \mathbf{r}_e = (\delta \mathbf{u}^T + \delta \boldsymbol{\ell}_x^T + \boldsymbol{\ell}_x^T \delta \tilde{\boldsymbol{\theta}}^T) \mathbf{e} \qquad (4 \cdot 13)$$

where

$$\boldsymbol{\ell} = \mathbf{R}\boldsymbol{\ell}_x, \qquad \delta \tilde{\boldsymbol{\theta}} = \mathbf{R}^T \cdot \delta \tilde{\boldsymbol{\alpha}} \cdot \mathbf{R} \qquad (4 \cdot 14)$$

It should be noted that the presence of $\delta \boldsymbol{\ell}_x$ admits normal loads on the shell surface.

Since our objective here is to obtain the variational expression for $\delta \mathbf{F}^S$ in the natural-coordinate system, ā, we first observe that the spatial derivatives in the e-system are related to the corresponding ones in the ā-system according to

$$\left\{ \begin{array}{c} \frac{\partial}{\partial x} \\[2mm] \frac{\partial}{\partial y} \\[2mm] \frac{\partial}{\partial z} \end{array} \right\} = \bar{T}_{ng}^{-1} \left\{ \begin{array}{c} \frac{\partial}{\partial S_\xi} \\[2mm] \frac{\partial}{\partial S_\eta} \\[2mm] \frac{\partial}{\partial S_\zeta} \end{array} \right\} \qquad (4 \cdot 15)$$

Second, the contravariant stress tensor in the ā-system is related to that in the e-system by the following tensorial transformation:

$$\begin{bmatrix} \sigma_{xx} & \sigma_{xy} & \sigma_{xz} \\ \sigma_{xy} & \sigma_{yy} & \sigma_{yz} \\ \sigma_{xz} & \sigma_{yz} & \sigma_{zz} \end{bmatrix} = \bar{T}_{ng}^T \begin{bmatrix} \sigma_{\xi\xi} & \sigma_{\xi\eta} & \sigma_{\xi\zeta} \\ \sigma_{\xi\eta} & \sigma_{\eta\eta} & \sigma_{\eta\zeta} \\ \sigma_{\xi\zeta} & \sigma_{\eta\zeta} & \sigma_{\zeta\zeta} \end{bmatrix} \bar{T}_{ng} \qquad (4 \cdot 16)$$

13

Finally, by substituting (4.15) and (4.16) into the the expression, $\delta \mathbf{r} \cdot \nabla_e \cdot \bar{\sigma}_e$, in (4.7) and performing spatial integration by parts, we obtain the desired stiffness force operator:

$$\delta \mathbf{F}^S = \int_V \frac{\partial}{\partial S_\xi} \{\delta \mathbf{u}^T + \delta \ell_x^T + \ell_x^T \delta \tilde{\theta}^T\} \bar{\mathbf{T}}^T \begin{Bmatrix} \sigma_{\xi\xi} \\ \sigma_{\xi\eta} \\ \sigma_{\xi\varsigma} \end{Bmatrix} dV$$

$$+ \int_V \frac{\partial}{\partial S_\eta} \{\delta \mathbf{u}^T + \delta \ell_x^T + \ell_x^T \delta \tilde{\theta}^T\} \bar{\mathbf{T}}^T \begin{Bmatrix} \sigma_{\eta\xi} \\ \sigma_{\eta\eta} \\ \sigma_{\eta\varsigma} \end{Bmatrix} dV \qquad (4 \cdot 17)$$

$$+ \int_V \frac{\partial}{\partial S_\varsigma} \{\delta \ell_x^T + \ell_x^T \delta \tilde{\theta}^T\} \bar{\mathbf{T}}^T \begin{Bmatrix} \sigma_{\varsigma\xi} \\ \sigma_{\varsigma\eta} \\ \sigma_{\varsigma\varsigma} \end{Bmatrix} dV$$

and the traction force operator:

$$\delta \mathbf{F}^T = \int_S (\delta \mathbf{u}^T + \delta \ell_x^T + \ell_x^T \delta \tilde{\theta}^T) \bar{\mathbf{T}}^T \begin{Bmatrix} \sigma_1 \\ \sigma_2 \\ \sigma_3 \end{Bmatrix} dS \qquad (4 \cdot 18)$$

where $(\sigma_1 \quad \sigma_2 \quad \sigma_3)$ are the surface tractions along the $(\xi \quad \eta \quad \varsigma)$-coordinates around the shell element boundaries.

It should be noted that, in the above relation, we have made use of the following intrinsic shell assumption:

$$\frac{\partial}{\partial S_\varsigma} (\delta \mathbf{u}^T) = 0 \qquad (4 \cdot 19)$$

which means that the translational displacements, $\mathbf{u}$, are independent of the corotational axis, ς.

4.3 The External Force Operator, $\delta \mathbf{F}^E$

The external force can be expressed in the inertial system as

$$\mathbf{f} = f_e^T \mathbf{e}, \qquad f_e^T = \lfloor f_1 \quad f_2 \quad f_3 \rfloor \qquad (4 \cdot 20)$$

so that from (4.8) we have

14

$$\delta \mathbf{F}^E = \int \{\delta \mathbf{u}^T + \delta \ell_x^T + \ell_x^T \delta \bar{\theta}^T\} f_e dV \qquad (4 \cdot 21)$$

It should be noted that the gravitational force and the thermal loads may be effectively accounted for by (4.21) if appropriate accommodations are made into f_e.

5. Natural–Coordinate Strain–Displacement Relations

In conventional derivations of various strain-displacement relations, a specific form of stresses is first adopted. Then, one employs either the Green strain for the Piola-Kirchhoff second stress tensor or the Euler strain when the Cauchy stress tensor is adopted. In the present formulation, we will first express the stiffness force operator, $\delta \mathbf{F}^S$, derived in the preceding section in a variational form. From the resulting variational form we will then identify the variational strains. Finally, by simply exchanging the infinitesimal variational process, δ, with the finite incremental process, Δ, we obtain the present incremental strain-displacement relations. It has been shown that the incremental strain-displacement relations derived for flexible beams by a similar approach remain objective under arbitrarily large rigid motions and large transverse shear deformations (Park, 1987).

We rewrite the variational stiffness operator, δF^S, from (4.17) in the following form:

$$\delta \mathbf{F}^S = \int_V (\delta \epsilon_{\xi\xi}\sigma_{\xi\xi} + \delta \epsilon_{\xi\eta}\sigma_{\xi\eta} + \delta \epsilon_{\xi\varsigma}\sigma_{\xi\varsigma} + \delta \epsilon_{\eta\eta}\sigma_{\eta\eta} + \delta \epsilon_{\eta\varsigma}\sigma_{\eta\varsigma} + \delta \epsilon_{\varsigma\varsigma}\sigma_{\varsigma\varsigma})dV \qquad (5 \cdot 1)$$

In order to obtain the natural-coordinate strain-displacement relations expressed in the natural-coordinate system, we recall from (4.13)

$$\delta \mathfrak{u} = \{\delta \bar{u} \quad \delta \bar{v} \quad \delta \bar{w}\}^T = \delta \mathbf{u} + \delta \ell_x + \delta \bar{\theta} \ell_x \qquad (5 \cdot 2)$$

where the subscript x denotes that the quantities are expressed in the inertial coordinate system. Eventually, we would like to compute the strains and stresses in an orthogonal shell coordinate system. To this end we recall (3.1) to express ℓ_x by

$$\ell_x = \mathbf{R}^T \ell = \mathbf{T}_{sg}^T \mathbf{S}_{bs}^T \mathbf{S}_{bs} \xi = \mathbf{T}_{sg}^T \xi, \quad \xi^T = \lfloor 0 \quad 0 \quad \bar{\varsigma} \rfloor \qquad (5 \cdot 3)$$

Therefore, $\delta \ell_x$ can be expressed as

$$\delta \ell_x = \varsigma \delta q \mathbf{t}_\varsigma^T \qquad (5 \cdot 4)$$

where $\mathbf{t}_\varsigma^T$ is the same as the third row vector of $\mathbf{T}_{sg}$.

15

Similarly, for the third term in (5.2) we obtain

$$\delta \tilde{\theta} \ell_x = \bar{\varsigma} \tilde{\mathbf{t}}_{sg}^T \delta \theta \qquad (5 \cdot 5)$$

in which

$$\tilde{\mathbf{t}}_{sg}^T = \begin{bmatrix} 0 & -t_{sg}^{33} & t_{sg}^{32} \\ t_{sg}^{33} & 0 & -t_{sg}^{31} \\ -t_{sg}^{32} & t_{sg}^{31} & 0 \end{bmatrix} \qquad (5 \cdot 6)$$

Finally, by substituting $\delta \ell_x$ and $\delta \tilde{\theta} \ell_x$ into $\delta \tilde{\mathbf{u}}$ we obtain for the virtual displacements

$$\delta \tilde{\mathbf{u}} = \{\delta \tilde{u} \quad \delta \tilde{v} \quad \delta \tilde{w}\}^T = \delta \mathbf{u} + \varsigma \delta q \mathbf{t}_{sg}^T + \bar{\varsigma} \tilde{\mathbf{t}}_{sg}^T \delta \theta \qquad (5 \cdot 7)$$

We will now derive the desired, natural-coordinate strain-displacement relations in the next section.

5.1 Virtual Strain-Displacement Relations

Equation (5.1) suggests that, by rearranging (4.17), comparing term by term between the two equations and making use of (5.7), one can identify the variational natural-coordinate strain-displacement relations as:

$$\delta \epsilon_{\xi\xi} = \bar{\mathbf{t}}_\xi^T \cdot \frac{\partial \delta \tilde{\mathbf{u}}}{\partial S_\xi} \qquad (5 \cdot 8)$$

$$\delta \epsilon_{\xi\eta} = \bar{\mathbf{t}}_\xi^T \frac{\partial \delta \tilde{\mathbf{u}}}{\partial S_\eta} + \bar{\mathbf{t}}_\eta^T \frac{\partial \delta \tilde{\mathbf{u}}}{\partial S_\xi} \qquad (5 \cdot 9)$$

$$\delta \epsilon_{\eta\eta} = \bar{\mathbf{t}}_\eta^T \cdot \frac{\partial \delta \tilde{\mathbf{u}}}{\partial S_\eta} \qquad (5 \cdot 10)$$

$$\delta \epsilon_{\xi\varsigma} = \bar{\mathbf{t}}_\varsigma^T \frac{\partial \delta \tilde{\mathbf{u}}}{\partial S_\xi} + \bar{\mathbf{t}}_\xi^T \frac{\partial \delta \tilde{\mathbf{u}}}{\partial S_\varsigma} \qquad (5 \cdot 11)$$

$$\delta \epsilon_{\eta\varsigma} = \bar{\mathbf{t}}_\varsigma^T \frac{\partial \delta \tilde{\mathbf{u}}}{\partial S_\eta} + \bar{\mathbf{t}}_\eta^T \frac{\partial \delta \tilde{\mathbf{u}}}{\partial S_\varsigma} \qquad (5 \cdot 12)$$

$$\delta \epsilon_{\varsigma\varsigma} = \bar{\mathbf{t}}_\varsigma^T \frac{\partial \delta \tilde{\mathbf{u}}}{\partial S_\varsigma} \qquad (5 \cdot 13)$$

in which

$$\bar{\mathbf{t}}_\xi^T = \frac{1}{g_{\xi\xi}} (\bar{x},_\xi \quad \bar{y},_\xi \quad \bar{z},_\xi) \qquad (5 \cdot 14)$$

16

$$\bar{\mathfrak{t}}_\eta^T = \frac{1}{g_{\eta\eta}}(\bar{x}_{,\eta} \quad \bar{y}_{,\eta} \quad \bar{z}_{,\eta}) \tag{5·15}$$

$$\bar{\mathfrak{t}}_\varsigma^T = \frac{1}{g_{\varsigma\varsigma}}(\bar{x}_{,\varsigma} \quad \bar{y}_{,\varsigma} \quad \bar{z}_{,\varsigma}) \tag{5·16}$$

$$\frac{\partial \bar{u}}{\partial S_\xi} = \frac{1}{g_{\xi\xi}}(\frac{\partial \bar{u}}{\partial \xi} \quad \frac{\partial \bar{v}}{\partial \xi} \quad \frac{\partial \bar{w}}{\partial \xi})^T \tag{5·17}$$

and similarly for other expressions.

Remark 5.1: $\bar{\mathfrak{t}}_\xi, \bar{\mathfrak{t}}_\eta$ and $\bar{\mathfrak{t}}_\varsigma$ are the directional cosines that project the derivatives or the changes in the normals onto the natural–coordinate lines. It is this feature that makes the ANS shell elements simple, robust, easy-to-incorporate, while being able to preserve physically-relevant shell behavior.

It is critical to note that the pseudo-rotation vector, $\delta\theta$, are expressed in the e-system; hence, they are inertially-based quantities and linearly dependent. This linear dependency can be observed as follows. First, we note that $\delta\tilde{\theta}\boldsymbol{\ell}_x$ can be expressed from (3.1) and (4.14) as

$$\delta\tilde{\theta}\boldsymbol{\ell}_x = \mathbf{R}^T\delta\tilde{\alpha}\mathbf{R}\boldsymbol{\ell}_x = \mathbf{T}_{sg}^T\mathbf{S}_{bs}^T\delta\tilde{\alpha}\mathbf{S}_{bs}\mathbf{T}_{sg}\mathbf{T}_{sg}^T\xi = \mathbf{T}_{sg}^T\delta\tilde{\beta}\xi \tag{5·18}$$

where the skew symmetric matrix $\delta\tilde{\beta}$ consists of the pseudo-rotation vector components in the shell-coordinate system:

$$\delta\tilde{\beta} = \mathbf{S}_{bs}^T\delta\tilde{\alpha}\mathbf{S}_{bs} \tag{5·19}$$

Multiplying out $\delta\tilde{\beta}\xi$, we obtain

$$\delta\tilde{\beta}\xi = \bar{\varsigma}\left\{\begin{array}{c} \delta\beta_2 \\ -\delta\beta_1 \\ 0 \end{array}\right\} \tag{5·20}$$

In other words, both $\delta\tilde{\alpha}$ and $\delta\tilde{\theta}$ are related to $\delta\tilde{\beta}$ by

$$\delta\tilde{\beta} = \left[\begin{array}{ccc} 0 & 0 & \delta\beta_2 \\ 0 & 0 & -\delta\beta_1 \\ -\delta\beta_2 & \delta\beta_1 & 0 \end{array}\right] = \mathbf{T}_{sg}\delta\tilde{\theta}\mathbf{T}_{sg}^T = \mathbf{S}_{bs}\delta\tilde{\alpha}\mathbf{S}_{bs}^T \tag{5·21}$$

so that we have the following linear dependency for $\delta\theta$:

$$(t_{13}t_{22} - t_{12}t_{23})\delta\theta_1 + (t_{11}t_{23} - t_{13}t_{21})\delta\theta_2 + (t_{12}t_{21} - t_{11}t_{22})\delta\theta_3 = 0 \tag{5·22}$$

Notice that the purpose of introducing $\delta\theta$ is only for strain interpolations. As they are not independent variables, one must transform them at each node into $\delta\beta$ and then perform the necessary variations. This is accomplished by the following explicit relation:

$$\left\{\begin{array}{c} \delta\theta_1 \\ \delta\theta_2 \\ \delta\theta_3 \end{array}\right\} = \hat{\mathbf{T}}_{\theta\beta}\left\{\begin{array}{c} \delta\beta_1 \\ \delta\beta_2 \end{array}\right\} = \left[\begin{array}{cc} (t_{33}t_{22} - t_{23}t_{32}) & (t_{13}t_{32} - t_{33}t_{12}) \\ (t_{23}t_{31} - t_{21}t_{33}) & (t_{11}t_{33} - t_{13}t_{31}) \\ (t_{32}t_{21} - t_{22}t_{31}) & (t_{12}t_{31} - t_{32}t_{11}) \end{array}\right]\left\{\begin{array}{c} \delta\beta_1 \\ \delta\beta_2 \end{array}\right\} \tag{5·23}$$

17

Alternatively, one may wish to eliminate one of them (say, $\delta\theta_3$), and then perform variations with $(\delta\theta_1, \quad \delta\theta_2)$ only.

Remark 5.2: When the element nodal points are placed on a skewed plane as is often the case for distorted elements on a shell surface, the present ANS formulation effectively overcomes locking difficulty as the normal vector components, $\bar{t}_\zeta^T$, can properly project the displacement derivatives on the parametrically determined skewed surface. This capability plays a key role for the modeling of the transverse shear strains, $\epsilon_{\xi\zeta}$ and $\epsilon_{\eta\zeta}$, as derived in (5.11) and (5.12). Hence, the present formulation faithfully adopts the shell geometry and the corresponding strain-displacement relations.

5.2 Derivation of Incremental Strain-Displacement Relations

As stated in Introduction, we do not rely on any predefined strain-displacement formula to derive the present incremental strain-displacement relations. Instead, we derive the desired incremental strain-displacement relations from the virtual strain-displacement relations in Section 5.1. It is emphasized that those relations are derived solely from a variational transformation of the D'Alembert principle starting from the Cauchy equations of motion.

A prerequisite for deriving the incremental strain-displacement relations from the virtual strain-displacement relations is to observe the difference between the infinitesimal variation process, δ, and the finite increment process, Δ. This is dealt with first. Second, except the strain-displacement relations, (5.8)–(5.13), involve the spatial derivatives of $\delta\beta$. A computationally tractable approximation of these derivatives is discussed in detail in Section 5.2.2. Finally, the desired incremental strain-displacement relations are derived in Section 5.2.3.

5.2.1 The δ- and Δ-Processes

In order to delineate the difference between the δ and Δ processes, let us consider the two-dimensional rotational matrix:

$$\mathbf{R} = \begin{bmatrix} \cos\theta & \sin\theta \\ -\sin\theta & \cos\theta \end{bmatrix} \tag{5 \cdot 24}$$

The variational pseudo-vector operator, $\delta\bar{\alpha}^T$, for this case is obtained by

$$\delta\bar{\alpha}^T = \delta\mathbf{R}\mathbf{R}^T = \begin{bmatrix} 0 & \delta\alpha_3 \\ -\delta\alpha_3 & 0 \end{bmatrix} = \begin{bmatrix} \delta\cos\theta & \delta\sin\theta \\ -\delta\sin\theta & \delta\cos\theta \end{bmatrix} \cdot \begin{bmatrix} \cos\theta & -\sin\theta \\ \sin\theta & \cos\theta \end{bmatrix} \tag{5 \cdot 25}$$

from which one obtains

$$\delta\alpha_3 = \delta(\sin\theta) \cdot \cos\theta - \delta(\cos\theta) \cdot \sin\theta \tag{5 \cdot 26}$$

13

If one performs the required infinitesimal variation of the above expression, the resulting expression becomes

$$\delta\alpha_3 = (\delta\theta \cdot \cos\theta)\cos\theta - (-\delta\theta \cdot \sin\theta) \cdot \sin\theta = \delta\theta \qquad (5 \cdot 27)$$

On the other hand, for the finite incremental process we have

$$\Delta\alpha_3 = \Delta(\sin\theta) \cdot \cos\theta - \Delta(\cos\theta) \cdot \sin\theta, \qquad \Delta\sin\theta = \sin\theta^{(n+1)} - \sin\theta^n \qquad (5 \cdot 28)$$

for the incremental step from n to $(n+1)$-step. Clearly, one observes

$$\delta\alpha_3 \neq \Delta\alpha_3 \qquad (5 \cdot 29)$$

We will now extensively use the Δ-process in order to derive the desired incremental strain-displacement relations from the virtual strain-displacement relations, (5.8)-(5.13).

5.2.2 Approximation of Incremental Pseudo-Vector, $\Delta\beta$

The incremental counterpart of the virtual pseudo-vector employed in (5.3b) is not computationally tractable in that form. First, we note from *Remark 4.3* that the matrix, S, is associated with the point transformation; it is a constant matrix. Hence, we have from (4.14) and (5.19)

$$\frac{\partial\delta\tilde{\theta}^T}{\partial S_\xi} = \mathbf{R}_{bg}^T \cdot \frac{\partial\delta\tilde{\alpha}^T}{\partial S_\xi} \cdot \mathbf{R}_{bg}, \qquad \frac{\partial\delta\tilde{\beta}^T}{\partial S_\eta} = \mathbf{S}_{bs}^T \cdot \frac{\partial\delta\tilde{\alpha}^T}{\partial S_\eta} \cdot \mathbf{S}_{bs} \qquad (5 \cdot 30)$$

The Δ-transformation of the above equation, provided one meticulously observes the illustration given in Section 5.2.1, yields:

$$\frac{\partial\Delta\tilde{\theta}^T}{\partial S_\xi} = \mathbf{R}_{bg}^T \cdot \frac{\partial\Delta\tilde{\alpha}^T}{\partial S_\xi} \cdot \mathbf{R}_{bg}, \qquad \frac{\partial\Delta\tilde{\beta}^T}{\partial S_\eta} = \mathbf{S}_{bs}^T \cdot \frac{\partial\Delta\tilde{\alpha}^T}{\partial S_\eta} \cdot \mathbf{S}_{bs} \qquad (5 \cdot 31)$$

Note that the matrix, $\mathbf{S}_{bs}$, relates from the s-system to the b-system solely due to transverse shear deformations. This means that, when the incremental transverse shear deformations become large, one must adhere to the above equations to update $\Delta\beta$. However, if the incremental transverse deformations are small, a reasonable approximation would be

$$\frac{\partial\Delta\tilde{\beta}}{\partial S_\xi} \approx \frac{\partial\Delta\tilde{\alpha}}{\partial S_\xi}, \qquad \frac{\partial\Delta\tilde{\beta}}{\partial S_\eta} \approx \frac{\partial\Delta\tilde{\alpha}}{\partial S_\eta} \qquad (5 \cdot 32)$$

Physically, the above approximation corresponds to remeshing of the deformed element cross sections to be normal with respect to the two natural coordinates, (ξ, η) at the end of each increment.

19

5.2.3 Incremental Strain-Displacement Relations

We now derive the incremental strain-displacement relations from (5.8)-(5.13), (5.23), (5.28) and (5.31) with the Δ-process delineated in Section 5.2.1. The resulting relations are as follows:

$$\Delta\epsilon_{\xi\xi} = \bar{t}_\xi^T \cdot \frac{\partial\Delta\bar{u}}{\partial S_\xi} \tag{5 \cdot 33}$$

$$\Delta\epsilon_{\xi\eta} = \bar{t}_\xi^T \frac{\partial\Delta\bar{u}}{\partial S_\eta} + \bar{t}_\eta^T \frac{\partial\Delta\bar{u}}{\partial S_\xi} \tag{5 \cdot 34}$$

$$\Delta\epsilon_{\eta\eta} = \bar{t}_\eta^T \cdot \frac{\partial\Delta\bar{u}}{\partial S_\eta} \tag{5 \cdot 35}$$

$$\Delta\epsilon_{\xi\varsigma} = \bar{t}_\varsigma^T \frac{\partial\Delta\bar{u}}{\partial S_\xi} + \bar{t}_\xi^T \frac{\partial\Delta\bar{u}}{\partial S_\varsigma} \tag{5 \cdot 36}$$

$$\Delta\epsilon_{\eta\varsigma} = \bar{t}_\varsigma^T \frac{\partial\Delta\bar{u}}{\partial S_\eta} + \bar{t}_\eta^T \frac{\partial\Delta\bar{u}}{\partial S_\varsigma} \tag{5 \cdot 37}$$

$$\Delta\epsilon_{\varsigma\varsigma} = \bar{t}_\varsigma^T \frac{\partial\Delta\bar{u}}{\partial S_\varsigma} \tag{5 \cdot 38}$$

in which

$$\Delta\bar{u} = \{\Delta\bar{u} \ \ \Delta\bar{v} \ \ \Delta\bar{w}\}^T = \Delta u + \varsigma\Delta q t_{sg}^T + \bar{\varsigma}\bar{t}_{sg}^T\Delta\theta \tag{5 \cdot 39}$$

Remark 5.3: When one can ignore the changes in the shell thickness, one can set

$$\Delta q = 0 \tag{5 \cdot 40}$$

which reduces to a classical shell assumption.

6. Computations of Incremental Stresses

The variational stiffness operator expressed in the natural-coordinate system (5.1), even though it is natural for constructing the assumed strain fields that are aligned along the shell element mesh shapes, presents difficulties when faced with computing the natural-coordinate stresses. This is because most constitutive relations are defined in an orthogonal coordinate system. Since a constitutive matrix is a fourth-order tensor, one must perform a fourth order point-by-point tensor transformation of each orthogonally-based constitutive matrix to obtain its counterpart in the natural coordinate-based constitutive matrix.

This conversion procedure can not only be cumbersome but also can destroy in effect the assumed constant or linear strain fields to non-uniform strain fields.

In the present formulation, we transform the natural-coordinate strain increments into a shell surface-based orthogonal system. In this way one not only performs a second-order tensor transformation but also obtains the stress increments for widely preferred shell-coordinate quantities. To compute the stresses in terms of the orthogonal shell-surface coordinate system, s, one needs to transform the natural–coordinate strain increments into the shell–coordinate strain increments. The required transformation is realized from:

$$\bar{a} = \bar{T}_{ng} \cdot T_{sg}^T s = \bar{T}_{ns} s, \qquad \text{or} \quad s = \bar{T}_{sn} \bar{a} \qquad (6 \cdot 1)$$

where s is defined as

$$s = (s_s \; s_t \; s_n), \qquad s_n = \bar{a}_\varsigma \qquad (6 \cdot 2)$$

so that not only $(s_s \; s_t)$ are chosen to form an orthogonal system that is tangent to the shell surface, but also the third unit vector, s_n, coincides with the natural-coordinate vector, $\bar{a}_\varsigma$.

The variational stiffness force operator (5.1) in the shell-surface coordinate system, i.e., s-system, can be written as

$$\delta \mathbf{F}^S = \int_V (\delta \epsilon_{ss} \sigma_{ss} + \delta \epsilon_{st} \sigma_{st} + \delta \epsilon_{sn} \sigma_{sn} + \delta \epsilon_{tt} \sigma_{tt} + \delta \epsilon_{tn} \sigma_{tn} + \delta \epsilon_{nn} \sigma_{nn}) dV \qquad (6 \cdot 3)$$

in which the shell-surface strain increments are obtained by the following tensor transformation of the natural-coordinate strain increments:

$$\begin{bmatrix} \Delta \epsilon_{ss} & \frac{1}{2} \Delta \epsilon_{st} & \frac{1}{2} \Delta \epsilon_{sn} \\ \frac{1}{2} \Delta \epsilon_{st} & \Delta \epsilon_{tt} & \frac{1}{2} \Delta \epsilon_{tn} \\ \frac{1}{2} \Delta \epsilon_{sn} & \frac{1}{2} \Delta \epsilon_{tn} & \Delta \epsilon_{nn} \end{bmatrix} = \bar{T}_{sn} \begin{bmatrix} \Delta \epsilon_{\xi\xi} & \frac{1}{2} \Delta \epsilon_{\xi\eta} & \frac{1}{2} \Delta \epsilon_{\xi\varsigma} \\ \frac{1}{2} \Delta \epsilon_{\xi\eta} & \Delta \epsilon_{\eta\eta} & \frac{1}{2} \Delta \epsilon_{\eta\varsigma} \\ \frac{1}{2} \Delta \epsilon_{\xi\varsigma} & \frac{1}{2} \Delta \epsilon_{\eta\varsigma} & \Delta \epsilon_{\varsigma\varsigma} \end{bmatrix} \bar{T}_{sn}^T \qquad (6 \cdot 4)$$

These strains are then used to compute the shell-coordinate stress increments

$$\Delta \sigma_s = \lfloor \Delta \sigma_{ss} \; \Delta \sigma_{st} \; \Delta \sigma_{sn} \; \Delta \sigma_{tt} \; \Delta \sigma_{tn} \; \Delta \sigma_{nn} \rfloor^T \qquad (6 \cdot 5)$$

by adopting a suitable constitutive relation (e.g., see [Stanley, 1985])

$$\Delta \sigma_s = \mathbf{C} \; \Delta \epsilon_s \qquad (6 \cdot 6)$$

where

$$\Delta \epsilon_s = \lfloor \Delta \epsilon_{ss} \; \Delta \epsilon_{st} \; \Delta \epsilon_{sn} \; \Delta \epsilon_{tt} \; \Delta \epsilon_{tn} \; \Delta \epsilon_{nn} \rfloor^T \qquad (6 \cdot 7)$$

Once the stress increments are calculated, the total stresses are updated by

21

$$\sigma_s^{(n+1)} = \sigma_s^{(n)} + \Delta\sigma_s^{(n+1)} \tag{6·8}$$

Finally, the virtual shell-surface strain-displacement relations are obtained from the virtual natural-coordinate strain-displacement relations by replacing Δ by δ. Specifically, for the present choice of the normal vector (6.2b), we have

$$\bar{\mathbf{T}}_{,n} = \begin{bmatrix} \bar{t}_{s\xi} & \bar{t}_{s\eta} & 0 \\ \bar{t}_{t\xi} & \bar{t}_{t\eta} & 0 \\ 0 & 0 & 1 \end{bmatrix} = \frac{1}{|\bar{\mathbf{a}}_\xi \times \bar{\mathbf{a}}_\eta|} \begin{bmatrix} \mathbf{s}_t \cdot \bar{\mathbf{a}}_\eta & -\mathbf{s}_t \cdot \bar{\mathbf{a}}_\xi & 0 \\ -\mathbf{s}_s \cdot \bar{\mathbf{a}}_\eta & \mathbf{s}_s \cdot \bar{\mathbf{a}}_\xi & 0 \\ 0 & 0 & |\bar{\mathbf{a}}_\xi \times \bar{\mathbf{a}}_\eta| \end{bmatrix} \tag{6·9}$$

Expanding (6.9) while employing (6.10), we obtain the following explicit relations:

$$\begin{pmatrix} \delta\varepsilon_{ss} \\ \delta\varepsilon_{tt} \\ \delta\varepsilon_{st} \\ \delta\varepsilon_{sn} \\ \delta\varepsilon_{tn} \end{pmatrix} = \begin{bmatrix} \bar{t}_{s\xi}^2 & \bar{t}_{s\eta}^2 & \bar{t}_{s\xi}\bar{t}_{s\eta} & 0 & 0 \\ \bar{t}_{t\xi}^2 & \bar{t}_{t\eta}^2 & \bar{t}_{t\xi}\bar{t}_{t\eta} & 0 & 0 \\ 2\bar{t}_{s\xi}\bar{t}_{t\xi} & 2\bar{t}_{s\eta}\bar{t}_{t\eta} & \bar{t}_{s\xi}\bar{t}_{t\eta} + \bar{t}_{s\eta}\bar{t}_{t\xi} & 0 & 0 \\ 0 & 0 & 0 & \bar{t}_{s\xi} & \bar{t}_{s\eta} \\ 0 & 0 & 0 & \bar{t}_{t\xi} & \bar{t}_{t\eta} \end{bmatrix} \begin{pmatrix} \delta\varepsilon_{\xi\xi} \\ \delta\varepsilon_{\eta\eta} \\ \delta\varepsilon_{\xi\eta} \\ \delta\varepsilon_{\varsigma\xi} \\ \delta\varepsilon_{\varsigma\eta} \end{pmatrix} \tag{6·10}$$

Substitutions of (6.8) and (6.11) into (6.3) and evaluation of the resulting variational operator then yield the desired internal force vector in terms of the shell-coordinate quantities.

Remark 6.1: The strains, $\Delta\epsilon_s$, are equivalent to classical strain-displacement relations for an orthogonal shell-surface coordinate system, with one major difference. In classical shell theories, the unknowns are the covariant displacements ($\mathbf{a} \cdot \Delta\mathbf{u}$ and $\Delta\beta$), and their covariant derivatives. In the present formulation, the unknowns are the inertially-based displacements ($\Delta\mathbf{u}$ and $\Delta\theta$), and their covariant derivatives. This difference plays a crucial role in the finite element discretization of the resulting variational equations.

7. Thin Shell Approximations

As in classical shell theories, care must be exercised in approximating (5.?) –(5.13) in order to obtain a consistent set of virtual (or incremental, for that matter) strain-displacement relations for thin shells. The most widely accepted approximation starts with (see Sanders (1959) and Budiansky and Sanders (1963)):

$$g_{\xi\xi} \simeq A_\xi, \qquad g_{\eta\eta} \simeq A_\eta \tag{7·1}$$

which leads to the following approximations for the covariant derivatives defined in (3.18) – (3.20):

$$\frac{\partial}{\partial S_\xi} = \frac{1}{A_\xi}\frac{\partial}{\partial \xi} \qquad \frac{\partial}{\partial S_\eta} = \frac{1}{A_\eta}\frac{\partial}{\partial \eta} \qquad \frac{\partial}{\partial S_\varsigma} = \frac{1}{A_\varsigma}\frac{\partial}{\partial \varsigma} \tag{7·2}$$

22

The second approximation is to employ

$$\frac{\partial \bar{\varsigma}}{\partial S_\varsigma} = 1, \qquad q \approx 0 \tag{7·3}$$

which means that the shell normals remain straight after deformations, and the changes in the shell thickness are negligible. We now simplify the virtual and incremental strain-displacement relations for thin shells.

With the preceding approximations, we can specialize the virtual strain-displacements for general shells, (5.8) − (5.13), to thin shells as follows:

$$\begin{Bmatrix} \delta\epsilon_{\xi\xi} \\ \delta\epsilon_{\xi\eta} \\ \delta\epsilon_{\eta\eta} \\ \delta\epsilon_{\xi\varsigma} \\ \delta\epsilon_{\eta\varsigma} \end{Bmatrix} = \begin{Bmatrix} \delta\epsilon^\circ_{\xi\xi} + \bar{\varsigma}\delta\kappa_{\xi\xi} \\ \delta\epsilon^\circ_{\xi\eta} + \bar{\varsigma}\delta\kappa_{\xi\eta} \\ \delta\epsilon^\circ_{\eta\eta} + \bar{\varsigma}\delta\kappa_{\eta\eta} \\ \delta\epsilon_{\xi\varsigma} \\ \delta\epsilon_{\eta\varsigma} \end{Bmatrix} \tag{7·4}$$

where

$$\delta\epsilon^\circ_{\xi\xi} = \mathbf{t}^T_\xi \frac{\partial\delta\mathbf{u}}{\partial S_\xi} \tag{7·5}$$

$$\delta\epsilon^\circ_{\xi\eta} = \mathbf{t}^T_\xi \frac{\partial\delta\mathbf{u}}{\partial S_\eta} + \mathbf{t}^T_\eta \frac{\partial\delta\mathbf{u}}{\partial S_\xi} \tag{7·6}$$

$$\delta\epsilon^\circ_{\eta\eta} = \mathbf{t}^T_\eta \frac{\partial\delta\mathbf{u}}{\partial S_\eta} \tag{7·7}$$

$$\delta\epsilon^\circ_{\xi\varsigma} = \mathbf{t}^T_\varsigma \frac{\partial\delta\mathbf{u}}{\partial S_\xi} + \mathbf{t}^T_\xi \delta\hat{\mathbf{u}} \tag{7·8}$$

$$\delta\epsilon^\circ_{\eta\varsigma} = \mathbf{t}^T_\varsigma \frac{\partial\delta\mathbf{u}}{\partial S_\eta} + \mathbf{t}^T_\eta \delta\hat{\mathbf{u}} \tag{7·9}$$

$$\delta\kappa_{\xi\xi} = \mathbf{t}^T_\xi \frac{\partial\delta\hat{\mathbf{u}}}{\partial S_\xi} + \left[\frac{\partial\mathbf{t}^T_\varsigma}{\partial S_\xi} - \mathbf{t}^T_\xi \frac{\partial\mathbf{t}^T_\varsigma}{\partial S_\xi} \cdot \mathbf{t}^T_\xi \right] \frac{\partial\delta\mathbf{u}}{\partial S_\xi}^\dagger \tag{7·10}$$

$$\delta\kappa_{\xi\eta} = \left(\mathbf{t}^T_\xi \frac{\partial\delta\hat{\mathbf{u}}}{\partial S_\eta} + \mathbf{t}^T_\eta \frac{\partial\delta\hat{\mathbf{u}}}{\partial S_\xi} \right)$$

$$+ \left(\frac{\partial\mathbf{t}^T_\varsigma}{\partial S_\xi} - \{\mathbf{t}^T_\xi \frac{\partial\mathbf{t}^T_\varsigma}{\partial S_\xi} + \mathbf{t}^T_\eta \frac{\partial\mathbf{t}^T_\varsigma}{\partial S_\eta} \} \cdot \mathbf{t}^T_\xi \right) \frac{\partial\delta\mathbf{u}}{\partial S_\eta}^\S \tag{7·11}$$

$$+ \left(\frac{\partial\mathbf{t}^T_\varsigma}{\partial S_\eta} - \{\mathbf{t}^T_\xi \frac{\partial\mathbf{t}^T_\varsigma}{\partial S_\xi} + \mathbf{t}^T_\eta \frac{\partial\mathbf{t}^T_\varsigma}{\partial S_\eta} \} \cdot \mathbf{t}^T_\eta \right) \frac{\partial\delta\mathbf{u}}{\partial S_\xi}^\S$$

23

$$\delta\kappa_{\eta\eta} = \mathbf{t}_\eta^T \frac{\partial \delta\hat{\mathbf{u}}}{\partial S_\eta} + \left[\frac{\partial \mathbf{t}_\zeta^T}{\partial S_\eta} - \mathbf{t}_\xi^T \frac{\partial \mathbf{t}_\zeta^T}{\partial S_\eta} \cdot \mathbf{t}_\eta^T \right] \frac{\partial \delta\mathbf{u}}{\partial S_\eta}^{\ddagger} \qquad (7 \cdot 12)$$

In the above equations we have used $\delta\hat{\mathbf{u}}$ for

$$\delta\hat{\mathbf{u}} = \bar{\mathbf{t}}_\zeta^T \delta \cdot \boldsymbol{\theta} \qquad (7 \cdot 13)$$

together with the following definitions:

$$\mathbf{t}_\xi^T = \frac{1}{A_\xi}(x_{,\xi} \quad y_{,\xi} \quad z_{,\xi}) \qquad (7 \cdot 14)$$

$$\mathbf{t}_\eta^T = \frac{1}{A_\eta}(x_{,\eta} \quad y_{,\eta} \quad z_{,\eta}) \qquad (7 \cdot 15)$$

$$\mathbf{t}_\zeta^T = (t_{31} \quad t_{31} \quad t_{33}) = (x_{,\zeta} \quad y_{,\zeta} \quad z_{,\zeta}) \qquad (7 \cdot 16)$$

$$\frac{\partial \mathbf{u}}{\partial S_\xi} = \frac{1}{A_\xi}(\frac{\partial u}{\partial \xi} \quad \frac{\partial v}{\partial \xi} \quad \frac{\partial w}{\partial \xi})^T \qquad (7 \cdot 17)$$

and similarly for other expressions.

The strain-displacement relations that are valid for finite displacement and finite rotations can be obtained simply by substituting Δ in place of δ in the preceding equations with the understanding delineated in Sections 5.2.2 and 5.2.3.

Remark 7.1: Note the modification of the in-plane bending term in (7.11) denoted by ( )§. This modification in the in-plane bending is equivalent to retaining the ζ-dependent term in $\bar{t}_{ng}(\xi)$ and $\bar{t}_{ng}(\eta)$ in (3.12), and is akin to Sanders' modification (1959) to improve the in-plane bending behavior for normal torsional rigid rotations. Specifically, its first expression represents the vector cross-product of the rate of change of the normal vector (a_ζ) along the ξ-line and the membrane strain component along η-line. Similarly, the second term represents the vector product of the change of the normal vector along the η-line and the membrane strain component along the ξ-line. Hence, taken together the modification represents a torsional behavior. It can be shown, though not elaborated here, that the present strain-displacement relations satisfy the small rigid motion relations delineated in Appendix A of Sanders (1959).

Remark 7.2: It is noteworthy to point out the consistent rotational kinematics in the present trnasverse shear strains given by (7.9) and (7.10). To appreciate this important feature, we substitute (5.23) into (7.13) to obtain

$$\Delta\hat{\mathbf{u}} = \bar{\mathbf{t}}^T(3)_{,g} \dot{\mathbf{T}}_{\theta\beta} \left\{ \begin{array}{c} \Delta\beta_1 \\ \Delta\beta_2 \end{array} \right\} = \lfloor -\mathbf{t}^T(2)_{,g} \quad \mathbf{t}^T(1)_{,g} \rfloor \left\{ \begin{array}{c} \Delta\beta_1 \\ \Delta\beta_2 \end{array} \right\} \qquad (7 \cdot 18)$$

24

where $t(i)_{,g}$ are the i-th row of $T_{,g}$ that is defined by (3.1b). This relation constitutes one of the key results of the present formulation. For moderate transverse shear one needs to update first $\Delta\alpha$ from

$$\Delta\tilde{\alpha} = \Delta\mathbf{R}\mathbf{R}^T \tag{7·19}$$

and update β by (5.31b).

8. Discussion

In this Part, we have derived the variational equations of motion for general shells based on the natural-coordinate system that is in general not orthogonal. Several features of the present formulation are worth mentioning:

- The present formulation has been motivated by the desire to incorporate as much shell behavior as possible into the basic variational equations of motion, which will be discretized subsequently by the finite element procedures.

- The translational motions are fixed on an inertial orthogonal coordinate system, whereas the rotational motions are fixed on a corotational coordinate system. This choice is in contrast with classical shell theories wherein the covariant displacements are the primary variables. Hence, many difficulties associated with the finite element discretization of the classical shell equations–i.e., preservation of rigid motions, finite rotations, etc.–are circumvented.

- The virtual strain-displacement relations have been derived from a variational transformation of the D'Alembert principle in which the Cauchy contravariant stress tensor is used in the equilibrium equations for continuum. A pointwise tensor transformation is then employed to obtain the virtual strain-displacement relations from the variational equations of motion. The incremental strain-displacement relations that are needed to compute the incremental stresses are obtained by exchanging the infinitesimal variational process (δ) with the finite incremental process (Δ). The resulting incremental strains remain valid for arbitrarily large rigid translational and rotational motions.

- In the present formulation, the strain increments are interpolated first on the natural coordinates. The shell-coordinate strain increments are then obtained by pointwise tensor tranformation. These shell-coordinate strain increments are used to compute stress increments in the shell-surface coordinates. On the other hand, the inertia terms are computed in terms of the fixed coordinate system for translations and the corotational system for rotations.

- After completing the present formulation for general shells, the strain-displacement relations are specialized to thin shells. The resulting equations of motion for thin shells will be subject to finite element discretizations in Part II. A more concrete form of the equations of motion for thick shells will then be discretized.

References

Ahmad, S., Irons, B. M. and Zienkiewicz, O. C., 1970, "Analysis of Thick and Thin Shell Structures by Curved Elements," *Int. J. Num. Meth. Engr.*, 2, 419-451.

Albasiny, E. L. and Martin. D. W., 1967, "Bending and Membrane Equilibrium in Cooling Towers," *Proc. Am. Soc. Civ. Eng.*, 93, EM3, 1-17.

Argyris, J. H., 1965, "Matrix Displacement Analysis of Anisotropic Shells by Triangular Elements," *J. Roy. Aer. Soc.*, 69, 801-805.

Argyris, J. H., 1964, *Recent Advances in Matrix Methods of Structural Analysis*, Pergamon Press, New York.

Ashwell, D. G., 1976, "Strain Elements with Applications to Arches, Rings and Cylindrical Shells," in *Finite Elements for Thin Shells and Curved Members*, Eds. D. G. Ashwell and R. H. Gallagher, John Wiley & Sons, London.

Ashwell, D. G. and Gallagher, R. H. (Editors), 1976, *Finite Elements for Thin Shells and Curved Members*, John Wiley & Sons, London.

Belytschko, T., Stolarski, H., Liu, W. K., Carpenter, N., and Ong, J. S.-J., 1985, "Stress Projection for Membrane and Shear Locking in Shell Finite Elements," *Comp. Meth. Appl. Mech. Eng.* 51, 221-258.

Budiansky, B. and Sanders, J.L., 1963, "On the Best First Order Linear Shell Theory," *Progress in Applied Mechanics*, Macmillan, New York, 129-140.

Cantin, G., 1970, "Rigid Body Motions in Curved Finite Elements," *AIAA J.*, 8, No. 7, 1252-1255.

Cantin, G. and Clough, R. W., 1968, "A Curved Cylindrical Shell Finite Element," *AIAA J.*, 6, 1057-1062.

Clough, R. W. and Johnson, C. P., 1968, "A Finite Element Approximation for the Analysis of Thin Shells," *J. Solids & Struct.*, 4, 43-60.

Connor, J. and Brebbia, C., 1967, "Stiffness Matrix for Shallow Rectangular Shell Element," *Proc. Am. Soc. Civ. Eng.*, 93, EM 43-65.

Cosserat, E. and Cosserat, F., 1909, *Téorie des corps déformables*, Hermann, Paris.

Cowper, G. R., Lindberg, G. M., Olson, M. D, 1970, "A Shallow Shell Finite Element of Triangular Shape," *Inst. J. Solids & Structs.*, 6, 1133-1156.

Darve, D. J., 1972, "Rigid Body Motions and Strain–Displacement Equations of Curved Shell Finite Elements," *Int. J. Mech. Sci.*, **14**, 569-578.

Dvorkin, E. N. and Bathe, K.J., 1984, "A Continuum Mechanics Based Four-Node Shell Element for General Nonlinear Analysis," *Int. J. for Computer-Aided Engr. & Software*, **1**, 77-88.

Ergatoudis, I., Irons, B. M. and Zienkiewicz, O. C., 1968, "Curved Isoparametric Quadrilateral Elements for Finite Element Analysis," *International Journal of Solids and Structures*, **4**, 31-42.

Flanagan, D.P. and Belytschko, T., 1981, "A Uniform Strain Hexahedron and Quadrilateral with Orthogonal Hour Glass Control," *Int. J. Num. Meth. Engrg.*, **17**, 679-706.

Fonder, G. and Clough, R. W., 1973, "Explicit Addition of Rigid Body Motions in Curved Finite Elements," *AIAA J.*, **11**, No. 3, 305–312.

Fonder, G. A., 1976, "Studies in Doubly Curved Elements for Shells of Revolution," in *Finite Elements for Thin Shells and Curved Members*, Eds. D. G. Ashwell and R. W. Gallagher, John Wiley & Sons, London, 113-130.

Fræijs de Veubeke, B., 1965, "Displacement and Equilibrium Models in the Finite Element Method", in *Stress Analysis*, Eds. O. C. Zienkiewicz and G. Holister, John Wiley & Sons, London, 145-197.

Gallagher, R. H., 1976, "Problems and Progress in Thin Shell Finite Element Analysis," in *Finite Elements for Thin Shells and Curved Members*, Eds. D. G. Ashwell and R. H. Gallagher, John Wiley & Sons, London, 1-14.

Greene, B. E., Strome, D. R., Weikel, R. C., 1971, "Application of the Stiffness Method to the Analysis of Shell Structures," *Proc. Aviation Conference, Amer. Soc. Mech. Eng.*, Los Angeles, March.

Haisler, W.E. and Stricklin, J.A., 1967, "Rigid Body Displacements of Curved Elements in the Analysis of Shells by the Matrix Displacement Method," *AIAA J.*, **5**, 1525–1527.

Hansen, J. S. and Heppler, G. R., 1985, "A Mindlin Shell Element Which Satisfies Rigid Body Requirements," *AIAA J.*, **22**, No. 2, 288–295.

Hinton, E. and Owen, D. R. J., 1984, *Finite Element Software for Plates and Shells*, Pineridge Press, Swansea, U. K.

Hughes, T. J. R., 1986, *The Finite Element Method, Linear Static and Dynamic Finite Element Analysis*, Prentice-Hall, Inc., Englewood Cliffs, N. J.

Hughes, T. J. R. and Hinton, E., 1986, *Finite Element Methods for Plate and Shell Structures, Vol. 1: Element Technology*, Pineridge Press, Swansea, U. K.

Hughes, T. J. R. and Liu, W. K., 1981, "Nonlinear Finite Element Analysis of Shells: Part I," *Comp. Meth. Appl. Mech. Engr.*, **26**, 331-362.

Irons, B., 1966, "Engineering Application of Numerical Integration in Stiffness methods," *AIAA J.*, 4, 2035-2037.

Irons, B. M., 1976, "The Semiloof Shell Element," in *Finite Elements for Thin Shells and Curved Members*, Eds. D. G. Ashwell and R. H. Gallagher, John Wiley & Sons, London, 197-222.

Irons, B. and Ahmad, S., 1980, *Techniques for Finite Elements*, John Wiley and Sons, New York.

Klein, S., 1967, "A Study of the Matrix Displacement Method as Applied to Shells of Revolution," *Matrix Methods in Structural Mechanics*, Eds. J. S. Przemieniecki, R. M. Bader, W. F. Bozich, J. R. Johnson, W. J. Mykytow, AFFDL-TR-67-80, 275-298.

Koiter, W. T. and Simmonds, J. G., 1973, "Foundations of Shell Theory," *Proc. the 13th International Congress of Theoretical and Applied Mechanics*, Eds. E. Becker and G. K. Mikhailov, Springer-Verlag, New York, 150-176.

Kosloff, D. and Frazer, G. A., 1978, "Treatment of Hour Glass Patterns in Low Order Finite Element Codes," *Int. J. Num. Meth. Engr.*, 2, 57-72.

Kraus, H. 1967, *Thin Elastic Shells*, John Wiley & Sons, Inc., 2nd ed., New York, N.Y.

Lanczos, C., 1970, *The Variational Principles of Mechanics*, Univ. of Toronto Press, 4th ed., Toronto, Canada.

Love, A.E.H., 1927, *A Treatise on the Mathematical Theory of Elasticity*, The Cambridge University Press, Cambridge, U.K.

Malvern, L.E., 1969, *Introduction to the Mechanics of a Continuous Medium*, Prentice-Hall, Inc., Englewood Cliffs, N.J., 596-606.

Mindlin, R. D., 1951, "Influence of Rotary Inertia and Shear on Flexural Motions of Elastic Plates," *J. Appl. Mech.*, 18, 31-38.

Morris, A. J., 1976, "A Summary of Appropriate Governing Equations and Functionals in the Finite Element Analysis of Thin Shells," in *Finite Elements for Thin Shells and Curved Members*, Eds. D.G. Ashwell and R. H. Gallagher, John Wiley & Sons, London, 1-14.

Naghdi, P. M., 1972, "The Theory of Shells and Plates," in: *Handbuch der Physik*, 2nd ed., Ed. W. Flugge, VI-2, Springer-Verlag.

Park, K. C., 1987, "Flexible Beam Dynamics for Space Structures: – Formulation," Center for Space Structures and Controls, University of Colorado, Report CU-CSSC-87-03.

Park, K. C., 1986, "An Improved Strain Interpolation for Curved C^0 Elements," Bruce Irons Memorial Issue, *Int. J. Num. Meth. Engr.*, 22, 281-288.

Park, K.C. and Stanley, G.M., 1986, "A Curved C^0 Shell Element Based on Assumed Natural-Coordinate Strains," *Journal of Applied Mechanics*, 108, 273-290.

Pawsey, S. F. and Clough, R. W., 1971, "Improved Numerical Integration of Thick Shell Finite Elements," *Int. J. Num. Meth. Engr.*, 3, 575–586.

Pinsky, P.M. and Jang, J., 1986, "A 9-Node Assumed Covariant Strain Element," presented at the First World Congress on Computational Mechanics, Sept. 22–26, Austin, Texas.

Pugh, E. D. L., Hinton, E. and Zienkiewicz, O. C., 1978, "A Study of Quadrilateral Plate Bending Elements with Reduced Integration," *Int. J. Num. Meth. Engr.*, 12, 1059–1079.

Reissner, E., 1945, "The Effect of Transverse Shear Deformation on the Bending of Elastic Plates, *J. Appl. Mech., Trans. ASME*, A69–A77.

Reissner, E., 1973, "On One-Dimensional Large-Displacement Finite-Strain Beam Theory," *Studies in Appl. Math.*, 2, 87-95.

Sanders, J.L, 1959, "An Improved First Approximation Theory for Thin Shells," NASA-TR-R24.

Sanders, J.L, 1963, "Nonlinear Theories for Thin Shells," *Q. Appl. Math.*, 21, 21-36.

Simmonds, J.G. and Danielson, D.A., 1972, "Nonlinear Shell Theory with Finite Rotation and Stress Function Vectors," *J. Appl. Mech.*, 39, 1085-1090.

Stanley, G. M., 1985, *Continuum-Based Shell Analysis*, PhD Thesis, Stanford University, Stanford, Calif.

Stolarski, H. and Belytschko, T., 1982, "Membrane Locking and Reduced Integration for Curved Elements," *J. Appl. Mech.*, 49, 172–176.

Stolarski, H. and Belytschko, T., 1983, "Shear and Membrane Locking in Curved C^0 Elements," *Comp. Meth. Appl. Mech. Engr.*, 41, 279-296.

Strickland, G. E. and Loden, W. A., 1968, "A Doubly Curved Triangular Shell Element," *Proc. 2nd Conf. Matrix Meth. in Struct. Mech.*, AFFDL, Wright Patterson A.F. Base, Ohio.

Taig, I. C., 1961, *Structural Analysis by the Matrix Displacement Method*, English Electric Aviation Report No. S017.

Turner, M. J., Clough, R. W., Martin, H. C. and Topp, L. J., 1956, "Stiffness and Deflection Analysis of Complex Structures," *Journal of the Aeronautical Sciences*, 23, 805-823.

Wempner, G. A., Oden, T. J. and Kross, D. A., 1968, "Finite Element Analysis of Thin Shells," *J. Eng. Mech. Div.*, ASCE, 1273-1294.

Zienkiewicz, O. C., 1971, *The Finite Element Method in Engineering Science*, McGraw-Hill, New York.

Zienkiewicz, O. C. and Cheung, Y. K., 1964, "Finite Element Method of Analysis for Arch Dam Shells and Comparison with Finite Difference Procedures," *Proc. of Symposium on Theory of Arch Dams*, Southampton Univ., Pergamon Press.

Zienkiewicz, O. C. and Cheung, Y. K., 1965, "Finite Element Procedures in the Solution of Plate and Shell Problems," in *Stress Analysis*, Chapter 8, Eds. O. C. Zienkiewicz and G. S. Holister, John Wiley & Sons.

Zienkiewicz, O. C., Taylor, R. C. and Too, J. M., 1971, "Reduced Integration Technique in General Analysis of Plates and Shells," *Int. J. Num. Meth. Engr.*, **3**, 275-290.

$$\underline{r}^{\,\circ} = x\underline{e}_1 + y\underline{e}_2 + z\underline{e}_3$$
$$(x, y, z) = \left\{ (X+u),\ (X+v),\ (Z+w) \right\}$$

Fig. 1   Deformed Shell Geometries in Terms of Inertial (e), Shell Surface (s), Natural-Coordinate (a) and Deformed Normal (b_3) Vectors.

31
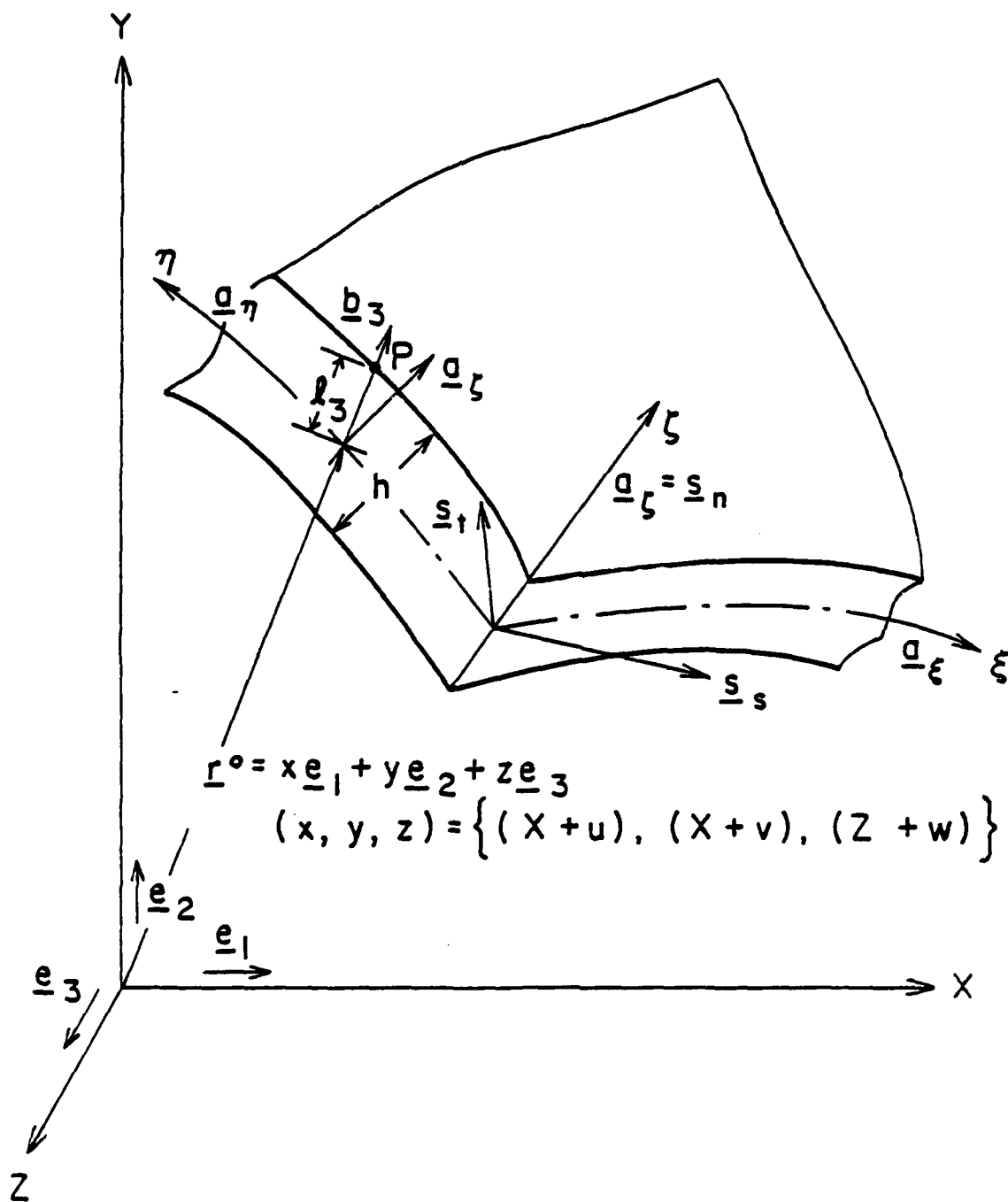
Appendix C

THE ANS SHELL ELEMENTS: PART 2 - ELEMENT CONSTRUCTION

by

K. C. PARK, G. M. STANLEY,
H. CABINESS and D. S. KANG

COLLEGE OF ENGINEERING
UNIVERSITY OF COLORADO
CAMPUS BOX 429
BOULDER, COLORADO 80309

The ANS Shell Elements: Part 2 – Element Construction

K. C. Park
Department of Aerospace Engineering Sciences and
Center for Space Structures and Controls
University of Colorado, Campus Box 429
Boulder, Colorado 80309

and

G. M. Stanley, H. A. Cabiness and D. S. Kang
Computational Structural Mechanics Section
Lockheed Palo Alto Research Laboratory
3251 Hanover St., Palo Alto, CA 94304

June 1987/Revised March 1988

Report No. CU–CSSC–87–07

ABSTRACT

Thin shell elements whose formulation is based on the assumed natural-coordinate strain(ANS) fields derived in Part I are presented. The present shell element construction offers several improvements over the ANS elements previously presented, particularly regarding the inplane shear strain, twist and transverse shear due to changes in the shell normals. These improvements have been made possible by adopting the new formulation presented in Part I and by introducing new ways of interpolating assumed strain fields. The elements thus constructed correctly preserve rigid motions, exhibiting no locking for skewed element shapes such as hemispherical geometries. In particular, the new 9-ANS element resulting from the present construction possesses a significantly improved modeling of transverse shear strains, which may be important for composite analysis.

1. INTRODUCTION

The present paper is to serve as a definitive exposition on the construction of the shell elements based on assumed natural-coordinate strains (ANS) that began with the linear interpolation of membrane strains in Park (1985), the 9-ANS shell element by Park and Stanley (1986), Park, Stanley and Cabiness (1986), Stanley (1985), and Stanley, Park and Hughes (1986). In doing so, we rely on several important corrections brought on by the theoretical formulation presented in Part I (Park and Stanley, 1987). The corrections were motivated by our desire to base our element construction on the formulation that incorporates as much shell behavior as possible from the outset into the variational equations of motion to be discretized, to improve the curvature effects, and to directly incorporate into the assumed strain-displacement relations a thick-shell capability. The present exposition may therefore be regarded as our earnest effort to effect a "marriage a la mode" between the finite element method and shell theories.

The impetus for developing the previous ANS shell elements was to improve the element performance when the elements become progressively distorted. This was in essence accomplished by abandoning the standard isoparametric mapping that is used to transform the natural-coordinate derivatives into their inertially fixed Cartesian counterparts. In addition, concepts such as the Hrennikoff grid (1941), a series of consistent interpolations on the natural-coordinate strain terms (Park, 1985), a tensorial transformation of the natural-coordinate strains into the corresponding Cartesian strains and directionally selective reduced-integration were blended to avoid element locking and spurious mechanisms. The resulting elements thus have acquired one important theoretical property: the strains remain invariant for an arbitrary choice of the local coordinate system, hence improving the element performance for distorted grids. Subsequent numerical evaluations of the ANS elements indicated that the 9-noded ANS element (or 9-ANS element) manifested no ostensible deficiency for production-level applications. The 9-ANS element then was used to analyze the post-buckling problem of a curved composite panel with a cutout (Stanley, 1985), which increased our confidence in the element.

As we turned our attention to more rigorous theoretical aspects of both the 9-ANS and 4-ANS elements, there emerged two hard evidences. First, the 4-ANS element almost locks the solution for a pinched hemispherical problem unless the reduced one-point integration is invoked instead of the full four-point integration. Second, the 9-ANS element, when put to the patch test, exhibited an oscillation on the constant strain state with an amplitude of about one-tenth of a percent of the constant strains. While the first pathology is avoidable and the second is harmless in practice, these two pathologies motivated us to reconstruct the ANS elements to eradicate such isolated pathologies (Salmon, 1987), thus making the ANS shell elements free from "exceptions" in performance. In what follows we will refer to the original ANS element construction as "the old construction" and to the present ANS element construction as the "the new construction."

In the old construction of the ANS shell elements, the Hrennikoff lattice lines were chosen.

In the 4-ANS element, the four grid edges were chosen to be the Hrennikoff lines. In the 9-ANS element, the four edge lines and the two natural-coordinate lines, $\xi = 0$ and $\eta = 0$, were chosen to be the Hrennikoff lines. Then the derivatives of the covariant displacements along the Hrennikoff lines were interpolated, which were termed as the covariant strains along the Hrennikoff lines. The natural-coordinate strains in the element interior were then obtained by interpolating the appropriate covariant displacement derivatives along the Hrennikoff lines according to the isoparametric interpolation weights. The orthogonal shell-coordinate or inertial-coordinate strains at any point in the element were finally obtained by tensorial transformation of the natural-coordinate strains. This meant two consequences. First, there must be a congruency between the directions of the natural-coordinate strains and those of the natural-coordinate basis vectors. Second, we had to abandon the isoparametric transformation of the natural-coordinate derivatives (Irons, 1966) into the Cartesian ones.

A closer examination of the interpolated natural-coordinate strains has revealed that the above congruency requirements are met only "in the large," even though the level of the incongruency quickly diminished as the grids were refined. A pathology of the 4-ANS element manifested for skewed grids, because the errors committed in interpolating the normal vectors become significant enough to lock the solution. Of several avenues we have explored to mitigate this incongruency, we have chosen the following as the basis for the new ANS element construction.

The most fundamental aspect of the new formulation presented in Part I (Park and Stanley, 1987) is in the choice of its coordinate system: an inertially fixed coordinate system for translational motions, an orthogonal shell-surface coordinate system for rotational motions and a natural-coordinate system for strains. The proper use of such triad coordinate systems has led to the mitigation of several element deficiencies heretofore present in many of the existing shell elements.

The incremental strain-displacement relations we will employ are expressed on the deformed shell geometries. However, they remain valid for finite-strain and finite-rotation increments, and hence they can be used both for linearized and nonlinear analyses. In particular, the present element construction based on the strain increments can be easily interfaced with an element-independent corotational procedure (Rankin and Brogan, 1984) to effect an efficient nonlinear analysis procedure.

In the construction of the new ANS shell elements, we preserve the two essential ingredients in the old ones: the natural-coordinate strains and the tensorial transformation of the natural-coordinate strains into any desirable orthogonal components. However, in constructing the natural-coordinate strains, we have abandoned the old way of interpolating the covariant displacements that vary their directions along the natural-coordinate lines. Instead, we have chosen to interpolate the inertial Cartesian displacement components to obtain the natural-coordinate covariant strains, since the displacements expressed in the inertial coordinate system do not vary their directions along the natural-coordinate lines.

4

In other words, the covariant strains are expressed directly in terms of the inertial displacement components and their derivatives along the natural-coordinate lines. Finally, the locking-free and mechanism-free measures adopted in the old construction are carried over almost intact into the new construction. We will now describe the new construction of ANS-shell elements in full detail.

2. Theoretical Preliminaries for Thin Shells

We summarize the equations of motion for thin shells derived in Part I (Park and Stanley, 1987) and the associated strain-displacement relations.

2.1 Kinematics and Shell Geometries

The position vector of the particle point P (see Fig. 1) on the deformed shell is given by

$$\mathbf{r} = \mathbf{r}^\circ + \ell_3 \mathbf{b}_3 \qquad (2 \cdot 1)$$

where

$$\mathbf{r}^\circ = x\mathbf{e}_1 + y\mathbf{e}_2 + z\mathbf{e}_3, \quad (x \ y \ z) = \{(X + u) \ (Y + v) \ (Z + w)\} \qquad (2 \cdot 2)$$

in which $(x \ y \ z)$ are the *deformed* neutral shell surface position coordinates, $(u \ v \ w)$ are the displacements measured in the inertial e-system, ℓ_3 is the distance of the material point P from the shell neutral surface measured in the b-system that is attached on the deformed cross-section of the shell, and the vector $\mathbf{b}$ is related to the vector $\mathbf{e}$ by

$$\mathbf{b} = \mathbf{R}\mathbf{e} \qquad \qquad (2 \cdot 3)$$

The angular velocity of a particle point, P, on the shell cross section is thus given as

$$\tilde{\omega} = -\dot{\mathbf{R}}\mathbf{R}^T = \begin{bmatrix} 0 & -\omega_3 & \omega_2 \\ \omega_3 & 0 & -\omega_1 \\ -\omega_2 & \omega_1 & 0 \end{bmatrix} \qquad (2 \cdot 4)$$

The variational pseudo-vector, $\delta\alpha$, that is conjugate with ω, is given by

$$\delta\tilde{\alpha}^T = \delta\mathbf{R}\mathbf{R}^T, \qquad \omega = \lfloor \omega_1 \ \ \omega_2 \ \ \omega_3 \rfloor^T, \qquad \delta\alpha = \lfloor \delta\alpha_1 \ \ \delta\alpha_2 \ \ \delta\alpha_3 \rfloor^T \qquad (2 \cdot 5)$$

The displacement variational quantities have been derived in Part I in the form:

$$\delta\mathbf{r} = \delta\mathbf{u}^T\mathbf{e} + \zeta\delta\hat{\mathbf{u}} \qquad (2 \cdot 6)$$

where the pseudo-rotation vector, $\delta\hat{\mathbf{u}}$, is related to the shell-surface pseudo-rotation quantities, $\delta\beta$ according to

$$\delta\hat{\mathbf{u}} = \lfloor -\mathbf{t}_{\wedge y}^T(2) \ \ \mathbf{t}_{\wedge y}^T(1) \rfloor \begin{Bmatrix} \delta\beta_1 \\ \delta\beta_2 \end{Bmatrix}, \quad \delta\tilde{\beta} = \mathbf{T}_{b,\wedge}^T \delta\tilde{\alpha}\mathbf{T}_{b\wedge} \qquad (2 \cdot 7)$$

5

in which $t_{sg}^T(i)$ represents the i-th row of the transformation matrix, T_{sg}, defined by

$$s = T_{sg}e \qquad (2 \cdot 8)$$

that are attached to the deformed shell surface; and, T_{bs} relates the shell-surface basis vectors, s, to the inertial basis vectors according to

$$b = T_{bs}s \qquad (2 \cdot 9)$$

The covariant natural-coordinate unit vectors are then obtained by

$$a_\xi = \frac{1}{A_\xi}\frac{\partial r^o}{\partial \xi} = \frac{1}{A_\xi}(x_{,\xi}e_1 + y_{,\xi}e_2 + z_\xi e_3) = t_\xi^T e \qquad (2 \cdot 10)$$

$$a_\eta = \frac{1}{A_\eta}\frac{\partial r^o}{\partial \eta} = \frac{1}{A_\eta}(x_{,\eta}e_1 + y_{,\eta}e_2 + z_\eta e_3) = t_\eta^T e \qquad (2 \cdot 11)$$

$$a_\varsigma = \frac{a_\xi \times a_\eta}{|a_\xi \times a_\eta|} = (x_{,\varsigma}e_1 + y_{,\varsigma}e_2 + z_{,\varsigma}e_3) = t_\varsigma^T e \qquad (2 \cdot 12)$$

where the two fundamental shell surface quantities, A_ξ and A_η, are given by

$$A_\xi^2 = \frac{\partial r^o}{\partial \xi} \cdot \frac{\partial r^o}{\partial \xi}, \qquad A_\eta^2 = \frac{\partial r^o}{\partial \eta} \cdot \frac{\partial r^o}{\partial \eta} \qquad (2 \cdot 13)$$

For subsequent applications, we express the above relation in a compact form:

$$a = T_{n\vartheta}e = \begin{Bmatrix} t_\xi^T \\ t_\eta^T \\ t_\varsigma^T \end{Bmatrix} e \qquad (2 \cdot 14)$$

Finally, the covariant partial derivatives are given by

$$\frac{\partial}{\partial S_\xi} = \frac{1}{A_\xi}\frac{\partial}{\partial \xi} \qquad \frac{\partial}{\partial S_\eta} = \frac{1}{A_\eta}\frac{\partial}{\partial \eta} \qquad \frac{\partial}{\partial S_\varsigma} = \frac{1}{A_\varsigma}\frac{\partial}{\partial \varsigma} \qquad A_\varsigma = h(\xi, \eta)/2 \qquad (2 \cdot 15)$$

where $h(\xi, \eta)$ is the shell thickness.

6

2.2 Variational Equations of Motion for Thin Shells

The variational equations of motion derived in Section 4 of Part I are recalled for convenience:

$$\delta \mathcal{F}^I + \delta \mathcal{F}^S = \delta \mathcal{F}^T + \delta \mathcal{F}^E \tag{2·16}$$

in which $\delta \mathcal{F}^I$, $\delta \mathcal{F}^S$, $\delta \mathcal{F}^T$ and $\delta \mathcal{F}^E$ are referred to as the inertia force, the stiffness force, the traction boundary force and the external force operators, respectively, given by

$$\delta \mathcal{F}^I = \int_V \rho(\delta \mathbf{u}^T \ddot{\mathbf{u}} + \delta \alpha^T \tilde{\ell}\tilde{\ell}^T \dot{\omega} + \delta \alpha^T \tilde{\ell}\tilde{\omega}\tilde{\ell}^T \omega) dV \tag{2·17}$$

$$\delta \mathcal{F}^S = \int_V (\delta \epsilon_{\xi\xi} \sigma_{\xi\xi} + \delta \epsilon_{\xi\eta} \sigma_{\xi\eta} + \delta \epsilon_{\eta\eta} \sigma_{\eta\eta} + \delta \epsilon_{\xi\varsigma} \sigma_{\xi\varsigma} + \delta \epsilon_{\eta\varsigma} \sigma_{\eta\varsigma}) dV \tag{2·18}$$

$$\delta \mathcal{F}^T = \int_S (\delta \mathbf{u}^T \bar{\mathbf{T}}^T + \delta \alpha^T \tilde{\ell}\mathbf{S}) \left\{ \begin{array}{c} \sigma_1 \\ \sigma_2 \\ \sigma_3 \end{array} \right\} dS \tag{2·19}$$

$$\delta \mathcal{F}^E = \int (\delta \mathbf{u}^T f_e + \delta \mathbf{u}^T \mathbf{R}^T f_a + \delta \mathbf{q}^T \mathbf{R}^T f_e + \delta \mathbf{q}^T f_a + \delta \alpha^T \tilde{\ell}\mathbf{R} f_e + \delta \alpha^T \tilde{\ell} f_a) dV \tag{2·20}$$

$$\mathbf{f} = f_e^T \mathbf{e} + f_a^T \mathbf{a} \tag{2·21}$$

where $(\sigma_1 \ \sigma_2 \ \sigma_3)$ are the surface tractions along the $(\xi \ \eta \ \varsigma)$-coordinates around the shell element boundaries, and $\mathbf{f}_e$ are the inertially applied load and $\mathbf{f}_a$ are the follow-on force, respectively.

2.3 Variational Natural-Coordinate Strains

The variational natural-coordinate strains specialized for thin shells from Section 7 of Part I are recalled:

$$\left\{ \begin{array}{c} \delta \epsilon_{\xi\xi} \\ \delta \epsilon_{\xi\eta} \\ \delta \epsilon_{\eta\eta} \\ \delta \epsilon_{\xi\varsigma} \\ \delta \epsilon_{\eta\varsigma} \end{array} \right\} = \left\{ \begin{array}{c} \delta \epsilon^{\circ}_{\xi\xi} + \bar{\varsigma}\delta \kappa_{\xi\xi} \\ \delta \epsilon^{\circ}_{\xi\eta} + \bar{\varsigma}\delta \kappa_{\xi\eta} \\ \delta \epsilon^{\circ}_{\eta\eta} + \bar{\varsigma}\delta \kappa_{\eta\eta} \\ \delta \gamma_\xi \\ \delta \gamma_\eta \end{array} \right\} \tag{2·22}$$

where

$$\delta \epsilon^{\circ}_{\xi\xi} = \mathbf{t}_\xi^T \frac{\partial \delta \mathbf{u}}{\partial S_\xi} \tag{2·23}$$

7

$$\delta\epsilon^{\text{o}}_{\xi\eta} = \mathbf{t}^T_\xi \frac{\partial\delta\mathbf{u}}{\partial S_\eta} + \mathbf{t}^T_\eta \frac{\partial\delta\mathbf{u}}{\partial S_\xi} \tag{2·24}$$

$$\delta\epsilon^{\text{o}}_{\eta\eta} = \mathbf{t}^T_\eta \frac{\partial\delta\mathbf{u}}{\partial S_\eta} \tag{2·25}$$

$$\delta\gamma_\xi = \mathbf{t}^T_\varsigma \frac{\partial\delta\mathbf{u}}{\partial S_\xi} + \mathbf{t}^T_\xi \delta\hat{\mathbf{u}} \tag{2·26}$$

$$\delta\gamma_\eta = \mathbf{t}^T_\varsigma \frac{\partial\delta\mathbf{u}}{\partial S_\eta} + \mathbf{t}^T_\eta \delta\hat{\mathbf{u}} \tag{2·27}$$

$$\delta\kappa_{\xi\xi} = \mathbf{t}^T_\xi \frac{\partial\delta\hat{\mathbf{u}}}{\partial S_\xi} + \left[\frac{\partial\mathbf{t}^T_\varsigma}{\partial S_\xi} - \mathbf{t}^T_\xi \frac{\partial\mathbf{t}_\varsigma}{\partial S_\xi}\cdot\mathbf{t}^T_\xi\right]\frac{\partial\delta\mathbf{u}}{\partial S_\xi}^\dagger \tag{2·28}$$

$$\delta\kappa_{\xi\eta} = \left(\mathbf{t}^T_\xi \frac{\partial\delta\hat{\mathbf{u}}}{\partial S_\eta} + \mathbf{t}^T_\eta \frac{\partial\delta\hat{\mathbf{u}}}{\partial S_\xi}\right)$$

$$+\left(\frac{\partial\mathbf{t}^T_\varsigma}{\partial S_\xi} - \{\mathbf{t}^T_\xi \frac{\partial\mathbf{t}_\varsigma}{\partial S_\xi} + \mathbf{t}^T_\eta \frac{\partial\mathbf{t}_\varsigma}{\partial S_\eta}\}\cdot\mathbf{t}^T_\xi\right)\frac{\partial\delta\mathbf{u}}{\partial S_\eta}^\S \tag{2·29}$$

$$+\left(\frac{\partial\mathbf{t}^T_\varsigma}{\partial S_\eta} - \{\mathbf{t}^T_\xi \frac{\partial\mathbf{t}_\varsigma}{\partial S_\xi} + \mathbf{t}^T_\eta \frac{\partial\mathbf{t}_\varsigma}{\partial S_\eta}\}\cdot\mathbf{t}^T_\eta\right)\frac{\partial\delta\mathbf{u}}{\partial S_\eta}^\S \tag{2·30}$$

$$\delta\kappa_{\eta\eta} = \mathbf{t}^T_\eta \frac{\partial\delta\hat{\mathbf{u}}}{\partial S_\eta} + \left[\frac{\partial\mathbf{t}^T_\varsigma}{\partial S_\eta} - \mathbf{t}^T_\xi \frac{\partial\mathbf{t}_\varsigma}{\partial S_\eta}\cdot\mathbf{t}^T_\eta\right]\frac{\partial\delta\mathbf{u}}{\partial S_\eta}^\ddagger \tag{2·31}$$

in which

$$\frac{\partial\mathbf{u}}{\partial S_\xi} = \frac{1}{A_\xi}\left(\frac{\partial u}{\partial\xi} \quad \frac{\partial v}{\partial\xi} \quad \frac{\partial w}{\partial\xi}\right)^T \tag{2·32}$$

$$\hat{\mathbf{u}} = (\hat{u} \quad \hat{v} \quad \hat{w})^T \tag{2·33}$$

$$\delta\hat{\mathbf{u}} = \tilde{\mathbf{T}}^T_{,g}\left\{\begin{array}{c} \delta\beta_\eta \\ -\delta\beta_\xi \\ 0 \end{array}\right\} \tag{2·34}$$

It should be noted that the incremental strain-displacement relations are obtained by replacing δ simply by Δ in the preceding equations. The terms designated by $(\ )^\perp$ and $(\ )^\ddagger$ in the bending strains of $\delta\kappa_{\xi\xi}$ and $\delta\kappa_{\eta\eta}$ usually remain small for thin shells, and they may be neglected in most applications. However, as noted in Part I, the term designated by

8

( )§ in the in-plane bending term, $\delta\kappa_{\xi\eta}$, must be retained to satisfy rigid-body motions as discussed in Sanders (1959).

2.4 Shell-Coordinate Strains and Stress Increments

The shell-surface coordinate system, s, is related to the inertial system, e, by

$$s = T_{sg}e \qquad (2 \cdot 35)$$

Hence, the natural-coordinate system, a, is related to the shell-coordinate system, s, by

$$a = T_{ng} \cdot T_{sg}^T s = T_{ns}s, \qquad \text{or} \quad s = T_{sn}a \qquad (2 \cdot 36)$$

where s is defined as

$$s = (s_s \ s_t \ s_n), \qquad s_n = a_\varsigma \qquad (2 \cdot 37)$$

so that not only $(s_s \ s_t)$ are chosen to form an orthogonal system that is tangent to the shell surface but also the normal shell-surface vector, s_n, coincides with that of the natural-coordinate vector, a_ς.

The variational stiffness force operator (2.16) in the shell-surface coordinate system–i.e., s-system–can be written as

$$\delta \mathcal{F}^S = \int_V (\delta\epsilon_{ss}\sigma_{ss} + \delta\epsilon_{st}\sigma_{st} + \delta\epsilon_{sn}\sigma_{sn} + \delta\epsilon_{tt}\sigma_{tt} + \delta\epsilon_{tn}\sigma_{tn})dV \qquad (2 \cdot 38)$$

in which the variational shell-surface strains are obtained by the following tensor transformation of the variational natural-coordinate strains:

$$\begin{bmatrix} \delta\epsilon_{ss} & \delta\epsilon_{st} & \delta\epsilon_{sn} \\ \delta\epsilon_{st} & \delta\epsilon_{tt} & \delta\epsilon_{tn} \\ \delta\epsilon_{sn} & \delta\epsilon_{tn} & 0 \end{bmatrix} = T_{sn} \begin{bmatrix} \delta\epsilon_{\xi\xi} & \delta\epsilon_{\xi\eta} & \delta\epsilon_{\xi\varsigma} \\ \delta\epsilon_{\xi\eta} & \delta\epsilon_{\eta\eta} & \delta\epsilon_{\eta\varsigma} \\ \delta\epsilon_{\xi\varsigma} & \delta\epsilon_{\eta\varsigma} & 0 \end{bmatrix} T_{sn}^T \qquad (2 \cdot 39)$$

These strains are then used to compute the shell-coordinate stress increments

$$\Delta\sigma_s = \lfloor \Delta\sigma_{ss} \ \Delta\sigma_{st} \ \Delta\sigma_{sn} \ \Delta\sigma_{tt} \ \Delta\sigma_{tn} \rfloor^T \qquad (2 \cdot 40)$$

by adopting a suitable constitutive relation (e.g., see [Stanley, 1985])

$$\Delta\sigma_s = C \ \Delta\epsilon_s \qquad (2 \cdot 41)$$

where

$$\Delta\epsilon_s = \lfloor \Delta\epsilon_{ss} \ \ \Delta\epsilon_{st} \ \ \Delta\epsilon_{sn} \ \ \Delta\epsilon_{tt} \ \ \Delta\epsilon_{tn} \rfloor^T \qquad (2 \cdot 42)$$

Once the stress increments are calculated, the total stresses are updated by

9

$$\sigma_s^{(n+1)} = \sigma_s^{(n)} + \Delta\sigma_s^{(n+1)} \tag{2.43}$$

The incremental shell-surface strain-displacement relations are obtained from the incremental natural-coordinate strain-displacement relations by the same tensor transformation.

Specifically, for the present choice of the normal vector (2.34), we have

$$\mathbf{T}_{sn} = \begin{bmatrix} t_{s\xi} & t_{s\eta} & 0 \\ t_{t\xi} & t_{t\eta} & 0 \\ 0 & 0 & 1 \end{bmatrix} = \frac{1}{|\mathbf{a}_\xi \times \mathbf{a}_\eta|} \begin{bmatrix} \mathbf{s}_t \cdot \mathbf{a}_\eta & -\mathbf{s}_t \cdot \mathbf{a}_\xi & 0 \\ -\mathbf{s}_s \cdot \mathbf{a}_\eta & \mathbf{s}_s \cdot \mathbf{a}_\xi & 0 \\ 0 & 0 & |\mathbf{a}_\xi \times \mathbf{a}_\eta| \end{bmatrix} \tag{2.44}$$

Expanding (2.42) while employing (2.36), we obtain the following explicit relation:

$$\begin{pmatrix} \delta\varepsilon_{ss} \\ \delta\varepsilon_{tt} \\ \delta\varepsilon_{st} \\ \delta\varepsilon_{sn} \\ \delta\varepsilon_{tn} \end{pmatrix} = \begin{bmatrix} t_{s\xi}^2 & t_{s\eta}^2 & t_{s\xi}t_{s\eta} & 0 & 0 \\ t_{t\xi}^2 & t_{t\eta}^2 & t_{t\xi}t_{t\eta} & 0 & 0 \\ 2t_{s\xi}t_{t\xi} & 2t_{s\eta}t_{t\eta} & t_{s\xi}t_{t\eta} + t_{s\eta}t_{t\xi} & 0 & 0 \\ 0 & 0 & 0 & t_{s\xi} & t_{s\eta} \\ 0 & 0 & 0 & t_{t\xi} & t_{t\eta} \end{bmatrix} \begin{pmatrix} \delta\varepsilon_{\xi\xi} \\ \delta\varepsilon_{\eta\eta} \\ \delta\varepsilon_{\xi\eta} \\ \delta\varepsilon_{\varsigma\xi} \\ \delta\varepsilon_{\varsigma\eta} \end{pmatrix} \tag{2.45}$$

Substitutions of (2.43) and (2.45) into (2.38) and evaluation of the resulting variational operator then yield the desired internal force vector in terms of the shell-coordinate quantities. It should be noted that the strains, $\Delta\epsilon_s$, are equivalent to classical strain–displacement relations for an orthogonal shell-surface coordinate system, with one major difference. In classical shell theories, the unknowns are the covariant displacements ($\mathbf{a} \cdot \Delta\mathbf{u}$ and $\Delta\beta$), and their covariant derivatives. In the present formulation, the unknowns are the inertially-based displacements ($\Delta\mathbf{u}$ and $\Delta\hat{\mathbf{u}}$), and their covariant derivatives. This difference plays a crucial role in the finite element discretization of the resulting variational equations.

2.5 Resultant Form of Stiffness Force Operator

Using the above strain-displacement relations, the thin-shell counterpart to the stiffness force operator (2.38) can be expressed in a resultant-force form:

$$\delta\mathcal{F}^S = \int_S \delta\mathbf{e}_N^T \, \mathbf{f}_N^S \, dS \tag{2.46}$$

and the strain and stress resultant "vectors"[*], $\delta\mathbf{e}_N$ and $\mathbf{f}_N^S$, expressed in the natural

---

[*] We will continue to use the term "vector" for one-dimensional arrays, but note that the components of vectors such as $\delta\mathbf{e}_N$ and $\mathbf{f}_N^S$ actually transform as 2nd rank tensors.

10

(curvilinear) coordinate system, N, are defined as:

$$
\delta \mathbf{e}_N = \begin{Bmatrix} \delta \epsilon_{\xi\xi} \\ \delta \epsilon_{\eta\eta} \\ \delta \epsilon_{\xi\eta} \\ \delta \kappa_{\xi\xi} \\ \delta \kappa_{\eta\eta} \\ \delta \kappa_{\xi\eta} \\ \delta \gamma_{\xi} \\ \delta \gamma_{\eta} \end{Bmatrix} , \quad \mathbf{f}_N^S = \begin{Bmatrix} n^{\xi\xi} \\ n^{\eta\eta} \\ n^{\xi\eta} \\ m^{\xi\xi} \\ m^{\eta\eta} \\ m^{\xi\eta} \\ q^{\xi} \\ q^{\eta} \end{Bmatrix}
\tag{2 · 47}
$$

While the covariant strain measures in $\delta \mathbf{e}_N$ were defined in (2.46), the corresponding membrane, bending and transverse-shear contravariant stress resultants, in $\mathbf{f}_N^S$, are defined by pre-integration of (2.38) through the thickness, as follows:

$$
n^{\alpha\beta} = \int_\varsigma \sigma^{\alpha\beta} \, d\varsigma , \qquad m^{\alpha\beta} = \int_\varsigma \sigma^{\alpha\beta} \varsigma \, d\varsigma , \qquad q^\alpha = \int_\varsigma \sigma^{\varsigma\alpha} \, d\varsigma
\tag{2 · 48}
$$

where again α and β range from 1–2.

The last quantity to be explained in (2.46) is the differential *reference* surface area, dS. It arises by employing the thin-shell hypothesis to the volume integral in (2.38), i.e.,

$$
\int_V (\,) \, dV = \int_\varsigma \int_{S(\varsigma)} (\,) \, dS(\varsigma) \, d\varsigma \approx \int_S \int_\varsigma (\,) \, d\varsigma \, dS
\tag{2 · 49}
$$

3. Strain Interpolations

In Park and Stanley (1986) and Stanley(1985), a procedure for constructing shell elements whose strains were approximated along the natural-coordinate strain lines were presented. We shall refer to it as the *old construction procedure*. Our motivation for developing the old shell element procedure was to render the locking-free and mechanism-free features into the resulting shell elements.

In the old procedure, first, we projected the displacements and unit normals onto the natural-coordinate lines to obtain their covariant natural-coordinate quantities. Second, we interpolated the resulting covariant displacements and covariant unit normals. Third, we obtained the natural-coordinate derivatives of these covariant quantities along the element edges and the two natural-coordinate lines (or along the Hrennikoff lines). Finally, the strains in the interior of the element were obtained by interpolating the quantities along the Hrennikoff lines. It is important to note that the nodal displacements in the old construction were expressed in the covariant system, whereas they are expressed in the

11

inertial system in the new element construction. This difference plays a key role in the subsequent element construction.

The first key feature of the present construction is the way in which we obtain the product form of the strain-displacement relations, viz, $\epsilon_{\xi\xi}^o$ along any ξ-line from (2.23)

$$\epsilon_{\xi\xi}^o = t_\xi^T \cdot \frac{\partial u}{\partial S_\xi} \qquad (3 \cdot 1)$$

in which the variational operator, δ, and the finite incremental operator, Δ, are omitted for presentation clarity, and t_ξ^T and $\frac{\partial u}{\partial S_\xi}$ are recalled from (2.10) and (2.32):

$$t_\xi^T = \frac{1}{A_\xi}(x_{,\xi} \quad y_{,\xi} \quad z_{,\xi}) \qquad (3 \cdot 2)$$

$$\frac{\partial u}{\partial S_\xi} = \frac{1}{A_\xi}(\frac{\partial u}{\partial \xi} \quad \frac{\partial v}{\partial \xi} \quad \frac{\partial w}{\partial \xi})^T \qquad (3 \cdot 3)$$

Hence, in the new construction, first we interpolate the displacements that are fixed in the inertial coordinate system and the unit normals, t_ξ^T, that vary along the ξ and η-lines. We then obtain their derivatives along the natural-coordinate lines. Third, we project the interpolated quantities and the derivatives onto the appropriate natural-coordinate lines to yield the necessary covariant derivatives. By combining them, we obtain the desired covariant natural-coordinate strains.

The second key feature is the way in which we represent the natural–coordinate strains at any interior point of the element. In the old construction, we obtained the natural-coordinate strains along the Hrennikoff reference lines. The natural-coordinate strains at an interior of the element were then obtained by interpolating these reference-line strains. In the new construction, we do not make use of the Hrennikoff reference-line strains. Instead, at each integration point the necessary interpolations are performed along the two natural-coordinate lines that pass through the integration point.

The third key feature – perhaps the most significant of all – of the present procedure is the way the natural-coordinate inplane strain and twist, $\epsilon_{\xi\eta}$ and $\kappa_{\xi\eta}$, are interpolated. We have abandoned the directionally reduced integration approach that was adopted in the old procedure. Instead, we sample these strains at the Barlow points, which are then tensorially transformed and interpolated at each integration point. We believe that this enhanced interpolations of $\epsilon_{\xi\eta}$ and $\kappa_{\xi\eta}$ are largely responsible for overcoming pathological 4-ANS element behavior for doubly curved shell surfaces. We now describe the present construction of the assumed natural-coordinate strains for both 4-node and 9-node ANS shell elements.

3.1. Natural–Coordinate Strains for 4-ANS Element

The incremental forms of the natural-coordinate strains derived in (2.23)–(2.31) are to be implemented with care if the resulting element is to be free from locking and mechanisms. For 4-node elements (see Fig. 2 for its nodal designations), we have the following interpolation function:

$$
\begin{aligned}
NEN &= 4 \\[4pt]
N_a(\xi,\eta) &= \sum_{r=1}^{2}\sum_{s=1}^{2} N_r(\xi)\, N_s(\eta) \\[4pt]
N_1(\xi^\alpha) &= \frac{1}{2}(1 - \xi^\alpha) \\[4pt]
N_2(\xi^\alpha) &= \frac{1}{2}(1 + \xi^\alpha) \\[4pt]
a &= 2(s-1) + r \\[8pt]
NB &= 1 \\[4pt]
w_1(\xi^\alpha) &= 1 \\[4pt]
\xi_1^\alpha &= 0.
\end{aligned}
\tag{3.4}
$$

Full integration for this element corresponds to a 2×2 Gauss quadrature rule.

We now describe the interpolation procedures for the natural-coordinate strains, (2.23)–(2.31) for 4-ANS shell elements.

3.1.1 Interpolations of $\epsilon_{\xi\xi}$, $\epsilon_{\eta\eta}$, $\kappa_{\eta\eta}$, and $\kappa_{\xi\xi}$.

Let us recall from (2.23) the membrane strain

$$
\epsilon_{\xi\xi}^\circ = t_\xi^T \frac{\partial u}{\partial S_\xi}
\tag{3.5}
$$

Observe that, along an η-constant line, $u_{,\xi}$ and $x_{,\xi}$ remain constant whereas, along a ξ-constant line, $u_{,\eta}$ and $x_{,\eta}$ remain constant. Therefore, A_ξ and t_ξ remain constant along any η-constant line whereas A_η and t_η remain constant along any ξ-constant line. These simple observations provide basic properties of the product form of the natural-coordinate strains (2.23)–(2.31).

Hence, the axial membrane strain, $\epsilon_{\xi\xi}^\circ$, remains constant along any ξ-line, since t_ξ, A_ξ and $u_{,S_\xi}$ are constant along any ξ-line. Similarly, $\epsilon_{\eta\eta}^\circ$ remains constant along any η-line. Hence, the two membrane strains maintain a constant strain state along the two natural-coordinate lines, thereby satisfying the patch test requirement.

Interpolations of $\kappa_{\eta\eta}$ and $\kappa_{\xi\xi}$ are thus constructed in the same way as in the case of $\epsilon_{\xi\xi}$ and $\epsilon_{\eta\eta}$.

13

In other words, these four strains are obtained in a straightforward manner by substituting into (2.23), (2.25), (2.28) and (2.31) the standard isoparametric coordinates and displacements, and their derivatives via the shape functions given in (3.4).

3.1.2 Interpolation of Transverse Shear Strains, $\epsilon_{\xi\varsigma}$ and $\epsilon_{\eta\varsigma}$

Since there are several important features associated with the present interpolations of these two strains, we recall the two strains from (2.26) and (2.27):

$$\gamma_\xi = t_\varsigma^T \frac{\partial \mathbf{u}}{\partial S_\xi} + t_\xi^T \hat{\mathbf{u}} \qquad (2.26)$$

$$\gamma_\eta = t_\varsigma^T \frac{\partial \mathbf{u}}{\partial S_\eta} + t_\eta^T \hat{\mathbf{u}} \qquad (2.27)$$

In the above equations, the variational operator, δ, or the finite incremental operator, Δ, has been omitted for presentation clarity.

First, let us address the well-known transverse shear locking problem (Zienkiewicz, Taylor and Too, 1971; Pawsey and Clough, 1971; MacNeal, 1978): that is, the interpolation of the second terms, $t_\xi^T \hat{\mathbf{u}}$ and $t_\eta^T \hat{\mathbf{u}}$, that appear in the above two transverse shear strains. In the context of the present construction, in order for the term, $t_\xi^T \hat{\mathbf{u}}$, to be constant along the ξ-line, we must have $\hat{\mathbf{u}}$ constant since t_ξ^T remains constant along the ξ-line. This can be accomplished by adopting the following interpolation for $\hat{\mathbf{u}}$:

$$\hat{\mathbf{u}} = \sum_{r=1}^{2} \sum_{s=1}^{2} N_r(0)\, N_s(\eta) \cdot \hat{\mathbf{u}}_{(r,s)} \qquad (3\cdot6)$$

Similarly, we adopt for interpolation of $t_\eta^T \hat{\mathbf{u}}$:

$$\hat{\mathbf{u}} = \sum_{r=1}^{2} \sum_{s=1}^{2} N_r(\xi)\, N_s(0) \cdot \hat{\mathbf{u}}_{(r,s)} \qquad (3\cdot7)$$

so that it remains constant along the η-line.

The net effect of the above two modifications is the same as the widely adopted reduced integration procedure used to avoid the transverse shear locking phenonenon which is discussed in (Hughes, Taylor and Kanoknukulchai, 1977; MacNeal, 1978; Lee and Pian, 1978; Pugh, Hinton and Zienkiewicz, 1978; Hughes and Tedzduyar, 1981; Wempner, Talasiidis and Huang, 1982; Crisfield, 1983; Park and Flaggs, 1985; Park, Stanley and Flaggs, 1985; Park, 1984), among others. However, no rank deficiency is introduced as a consequence of the present modifications in $\hat{\mathbf{u}}$ for both γ_ξ and γ_η. This is because the η-dependency in $\hat{\mathbf{u}}$ for γ_ξ and and the ξ-dependency in $\hat{\mathbf{u}}$ for γ_η are *not* compromised as a result of the

14

foregoing modifications. Further discussions on rank deficiency vs (ξ, η)-dependency may be found in Park (1984).

Second, we will address the first term in γ_ξ, viz, $t_\varsigma^T \frac{\partial \mathbf{u}}{\partial S_\xi}$. Since we must have, for consistency, a constant value for this term along the ξ-line, the unit normal, t_ς^T, must remain constant along the ξ-line.

Observe that, if t_ς^T is to remain constant along the ξ-line, $\{x_{,\eta}\quad y_{,\eta}, \quad z_{,\eta}\}$ and A_η must be evaluated at $\xi = 0$ for each integration point while still substituting the appropriate value for η. To be specific, we evaluate

$$t_\varsigma^T(\xi = 0, \ \eta_j) \cdot \frac{\partial \mathbf{u}}{\partial S_\xi}(\xi_i, \ \eta_j) \tag{3 \cdot 8}$$

where the coordinates, $(\xi_i, \ \eta_j)$, denote spatial (2×2)-integration points.

For γ_η, we evaluate in the opposite way, viz,

$$t_\varsigma^T(\xi_i, \ \eta = 0) \cdot \frac{\partial \mathbf{u}}{\partial S_\eta}(\xi_i, \ \eta_j) \tag{3 \cdot 9}$$

3.1.3 Interpolations of $\epsilon_{\xi\eta}$ and $\kappa_{\xi\eta}$

The derivatives in the inplane bending strain, $\epsilon_{\xi\eta}^\circ$, and the twist, $\kappa_{\xi\eta}$, must be evaluated to preserve constant strain states along each of the natural-coordinate lines. It is noted that $\epsilon_{\xi\eta}^\circ$ consists of two product terms: $t_\xi^T \cdot \frac{\partial \mathbf{u}}{\partial S_\eta}$ and $t_\eta^T \cdot \frac{\partial \mathbf{u}}{\partial S_\xi}$. The first term implies that the parameteric derivative, $\frac{\partial \mathbf{u}}{\partial S_\eta}$, is projected on the vector component, t_ξ, that is parallel to the ξ-line. In the first term, $\frac{\partial \mathbf{u}}{\partial S_\eta}$ remains a constant along η-line. Hence, if the first term is to maintain a constant strain state, so must t_ξ.

To maintain such constant strain states with minimum mesh sensitivity, we introduce the following approximations. We sample $\epsilon_{\xi_0\xi_0}$, $\epsilon_{\xi_0\eta_0}$ and $\epsilon_{\eta_0\eta_0}$ at the element centroid (ξ_0, η_0). At each integration point (ξ, η), we introduce a rotation vector, $\mathbf{n}$, such that

$$\mathbf{n} = (\mathbf{a}_{\varsigma_0} \times \mathbf{a}_\varsigma)/|\mathbf{a}_{\varsigma_0} \times \mathbf{a}_\varsigma| \tag{3 \cdot 10}$$

which rotates the normal vector $\mathbf{a}_{\varsigma_0}$ at the centroid to coincide with the normal vector $\mathbf{a}_\varsigma$ at the integration point. The projection of $(\mathbf{a}_{\xi_0}, \mathbf{a}_{\eta_0})$ at the centroid onto the shell surface at the integration point is thus obtained by (Gibbs, 1960):

$$\mathbf{a}_{\xi_0'} = (\mathbf{a}_{\varsigma_0} \cdot \mathbf{a}_\varsigma)\mathbf{a}_{\xi_0} + (1 - \mathbf{a}_{\varsigma_0} \cdot \mathbf{a}_\varsigma)(\mathbf{n} \cdot \mathbf{a}_{\xi_0})\mathbf{n} - (\mathbf{a}_\varsigma \cdot \mathbf{a}_{\xi_0})\mathbf{a}_{\varsigma_0} \tag{3 \cdot 11}$$

$$\mathbf{a}_{\eta_0'} = (\mathbf{a}_{\varsigma_0} \cdot \mathbf{a}_\varsigma)\mathbf{a}_{\eta_0} + (1 - \mathbf{a}_{\varsigma_0} \cdot \mathbf{a}_\varsigma)(\mathbf{n} \cdot \mathbf{a}_{\eta_0})\mathbf{n} - (\mathbf{a}_\varsigma \cdot \mathbf{a}_{\eta_0})\mathbf{a}_{\varsigma_0} \tag{3 \cdot 12}$$

where $(\mathbf{a}_{\xi_0'}, \mathbf{a}_{\eta_0'})$ represent the projection of $(\mathbf{a}_{\xi_0}, \mathbf{a}_{n_0})$ on the shell surface at the integration point (ξ, η).

15

Hence, from (3.10)- (3.12) and (2.14) one obtains

$$\left\{ \begin{array}{c} a_\xi \\ a_\eta \end{array} \right\} = \left[\begin{array}{cc} t_{11} & t_{12} \\ t_{21} & t_{22} \end{array} \right] \left\{ \begin{array}{c} a_{\xi'_0} \\ a_{\eta'_0} \end{array} \right\} \qquad (3 \cdot 13)$$

The inplane bending strain at the integration point is obtained via the following tensorial transformation:

$$\epsilon_{\xi\eta} = 2t_{11}t_{21}\epsilon_{\xi_0\xi_0} + 2t_{12}t_{22}\epsilon_{\eta_0\eta_0} + (t_{11}t_{22} + t_{12}t_{21})\epsilon_{\xi_0\eta_0} \qquad (3 \cdot 14)$$

The projected inplane strain, $\epsilon_{\xi\eta}$ given by (3.14), thus maintains a constant strain state at each integration point.

Remark 3.1: When the shell surface is flat, the preceding treatment of the inplane strain interpolation appears to be akin to the Pian and Sumihara transformation (1984) of the tensor stress τ^{ij} to the physical stress component σ^{ij} for which they used the isoparametric Jacobian matrix evaluated at the element centroid. For the finite element discretization based on the natural-coordinate system, the present interpolation of $\epsilon_{\xi\eta}$ as given by (3.14) and the assumed stress interpolation of $\sigma^{\xi\eta}$ as given by Eq. (34) of Pian and Sumihara (1984) are different. The present interpolation replaces the inplane bending strain at each integration point with the one at the centroid via the centroid-to-integration point *shell surface* coordinate transformation. On the other hand, a straightforward application of the Pian and Sumihara transformation would require that the strains at each integration point are first transformed to the corresponding ones in terms of the centroid natural-coordinate system. The transformed inplane bending component at the integration point is then replaced by the centroidal one. Both approaches are easily implementable for 4-node elements. However, for 9-node elements, extension of the present interpolation for 9-node becomes easier than the Pian and Sumihara approach as we will discuss in Section 3.2.3.

3.2 Strain Interpolation for Nine-Noded ANS Element

When the shell surfaces are approximated by the isoparametric curved shape functions (see, e.g., Zienkiewicz, 1971 or Irons and Ahmad, 1980), the limitation principle (Fræjis de Veubeke, 1965) states that the strains should vary linearly for 9-node elements. From the theoretical viewpoints, the mitigation of element locking and spurious mechanisms resulting from reduced integration can be considered as efforts to adhere to Fræjis de Veubeke's limitation principle. Efforts to mitigate both locking and spurious mechanisms for 9-node elements can be found in Wempner, Oden and Kross (1968), Ergatoudis, Irons and Zienkiewicz (1968), Ahmad, Irons and Zienkiewicz (1970), Irons (1976), MacNeal (1982), Parisch (1979), Park (1985), Park and Stanley (1986), Bathe (1987), Salmon(1987) and Juang (1987).

In essence, the new 9-ANS shell element is based on the independent approximations of the two fields in terms of the nodal variables: the displacement and the strain field within

16

an element interior. The choice of the *nodal* displacements and rotations as the nodal variables for the present 9-ANS shell element presents only a special case; they can be stresses or strains, as well. Thus, it is this philosophy that is adopted in the discrete (finite element) version of the thin shell equations (2.23)-(2.31) for a 9-node shell element.

However, while those two fields are interdependent (through the strain-displacement relations), the *assumed strain* approach takes the liberty of selecting the approximations independently — each in terms of the nodal displacement variables. This is similar to what is done for "hybrid" elements via a mixed variational principle, except that there an element-level matrix inversion is required to achieve the linkage between strains and nodal displacements, while in the assumed-strain approach this linkage is made explicit.

This allows most of the usual element requirements (e.g., continuity of the displacement field, completeness of the strain field, convergence, locking-free behavior, etc.) to be met a priori. However, in particular, the assumed *natural-coordinate* strain (ANS) approach focuses on the *physical covariant* components of the strain field to reduce element sensitivity to mesh distortion. We will now describe the construction of a new 9-ANS shell element in detail.

3.2.1   Interpolation of $\epsilon^0_{\xi\xi}$

In the old construction, the curvilinear membrane strain along the ξ-line for a fixed η-line employed the formula

$$\tilde{\epsilon}^0_{\xi\xi} = \frac{\partial u_\xi}{\partial S_\xi} = \frac{1}{A_\xi}\frac{\partial u_\xi}{\partial \xi} \qquad (3\cdot15)$$

wherein u_ξ is the covariant displacement defined by:

$$u_\xi = \frac{\xi}{2}(\xi-1)\tilde{u}_1 + (1-\xi^2)\tilde{u}_2 + \frac{\xi}{2}(\xi+1)\tilde{u}_3 \qquad (3\cdot16)$$

in which $\tilde{u}_i$ are the covariant components at the nodal points, i, that are tangent along the ξ-line. Substituting (3.16) into (3.14) and making use of the relations (2.13), one can derive an explicit form for $\tilde{\epsilon}^0_{\xi\xi}$. It was shown in Park and Stanley (1986) that the strain $\tilde{\epsilon}^0_{\xi\xi}$, thus derived, introduces inconsistencies. The complicated interpolations offered therein can thus be viewed as corrective measures to improve $\tilde{\epsilon}^0_{\xi\xi}$.

To illustrate the the present membrane-strain construction, let us consider a 9-node shell surface as shown in Fig. 3. Both the coordinates and the displacements are interpolated

by the bi-quadratic Lagrange shape functions as given by

$$
\begin{aligned}
NEN &= 9 \\
N_a(\xi, \eta) &= \sum_{r=1}^{3} \sum_{s=1}^{3} N_r(\xi)\, N_s(\eta) \\
N_1(\xi^\alpha) &= \frac{1}{2}\xi^\alpha(\xi^\alpha - 1) \\
N_2(\xi^\alpha) &= (1 - (\xi^\alpha)^2) \\
N_3(\xi^\alpha) &= \frac{1}{2}\xi^\alpha(\xi^\alpha + 1) \\
a &= 3(s-1) + r \\[4pt]
NB &= 2 \\
\mathbf{w}_1(\xi^\alpha) &= \frac{1}{2}(1 - \sqrt{3}\,\xi^\alpha) \\
\mathbf{w}_2(\xi^\alpha) &= \frac{1}{2}(1 + \sqrt{3}\,\xi^\alpha) \\
\xi_1^\alpha &= -1/\sqrt{3} \\
\xi_2^\alpha &= +1/\sqrt{3}
\end{aligned}
\tag{3.17}
$$

It is noted that the most one can realize for the covariant natural-coordinate strain, $\epsilon^o_{\xi\xi}$, when interpolated by (3.1), is a linearly varying field along the ξ-line. It was shown in Park (1985) that the strains based on the quadratic polynomials yields an equivalent of the desired linearly varying field only if sampled at the two Barlow points, $\xi_b = \pm 1/\sqrt{3}$. Hence, a linearly varying strain field along the ξ-coordinate line can be constructed by the following strain interpolation:

$$
\epsilon^o_{\xi\xi} = \frac{1}{2}\{\epsilon^o_{\xi\xi}(\xi_b) + \epsilon^o_{\xi\xi}(-\xi_b)\} + \frac{\xi}{2\xi_b}\{\epsilon^o_{\xi\xi}(\xi_b) - \epsilon^o_{\xi\xi}(-\xi_b)\}, \qquad \xi_b = 1/\sqrt{3}
\tag{3.18}
$$

which was extensively used in Park and Stanley (1986).

We now come to the second key aspect of the present construction: that is, the way we obtain the natural-coordinate strains at any point in the element interior. Notice that the covariant membrane strain, $\epsilon_{\xi\xi}$, given by (3.18) can directly represent the natural-coordinate strain at any point in the element since the directional derivatives with respect to ξ, i.e., x_ξ and u_ξ, represent its values at any η-line. This is an important improvement over the old construction wherein the strains in the element interior were obtained by interpolating the strains along the six Hrennikoff lines.

For computer implementation ease, we reexpress (3.18) in the following form:

18

$$\epsilon_{\xi\xi}^{o} = \sum_{a=1}^{NEN} \mathbf{b}_{u_a}^{\xi\xi\xi} u^a \qquad (3 \cdot 19)$$

where

$$\mathbf{b}_{u_a}^{\xi\xi\xi} = \sum_{i=1}^{NB} \mathbf{w}_i(\xi) \left[N_{a,dS_\xi} t_{n_g}^{T}(\xi) \right]_{\xi_i, \eta} \qquad (3 \cdot 20)$$

where $w_i(\xi)$ are the weighting functions as give in (3.17).

Remark 3.2: The above explicit form for $\epsilon_{\xi\xi}^{o}$ given in (3.19) constitutes a key contribution of the present 9-ANS construction as it is valid everywhere in the element; it is linearly varying along the ξ-line. Hence, we have circumvented the strain interpolation of $\epsilon_{\xi\xi}^{o}$ by utilizing the strains along the three Hrennikoff lines, viz, $\eta = (-1, 0, +1)$, as previously employed in Park and Stanley (1986).

Remark 3.3: The strain interpolation along the ξ-line for $\epsilon_{\xi\xi}$, as derived in (3.18), does not require reduced integration as it exactly satisfies the constant and linearly varying strain states, thus causing no element locking. A similar approach was adopted in Crisfield (1984), Stolarski and Belytschko (1982, 1983) and Huang and Hinton (1986). It is this locking-free property of the present element construction that is distinct from the family of curved shell elements based on the standard isoparametric construction. In addition, as long as one invokes 9-point integration, the resulting element possesses its full rank, thus no spurious mechanism occurs. A symbolic analysis that illuminates this characteristic is given in Park (1984).

Reamrk 3.4: In the assumed covariant strain approach (Juang and Pinsky, 1987), one interpolate a nonphysical strain

$$\epsilon_{\xi\xi}^{cov} = \mathbf{t}_{\xi}^{T} \cdot \frac{\partial \mathbf{u}_{\xi}}{\partial \xi} \qquad (3 \cdot 21)$$

Hence, the difference between the present physical-component strain (3.1) and the covariant strain is the absence of A_ξ in its denominator. If $\epsilon_{\xi\xi}^{cov}$ is interpolated to vary linearly along the ξ-line, then the two formulations coinside only if A_ξ is constant along the ξ-line. This happens only for a constant curvature, viz, when the ξ-lines lie on a circle. For distorted meshcs, even though the elements may lie on a cylinder or sphere, the ξ-line does not necessarily lie on a constant curvature trajectory. This difference may play a crucial role on element performance for distorted meshes.

Interpolations of $\epsilon_{\eta\eta}$, $\kappa_{\xi\xi}$ and $\kappa_{\eta\eta}$ follow a similar procedure for interpolating $\epsilon_{\xi\xi}$ as described above.

3.2.2 Interpolation of Transverse Shear Strains, $\epsilon_{\xi\varsigma}$ and $\epsilon_{\eta\varsigma}$

19

We recall again the two strains from (2.26) and (2.27):

$$\gamma_{\xi} = \mathbf{t}_{\zeta}^{T} \frac{\partial \mathbf{u}}{\partial S_{\xi}} + \mathbf{t}_{\xi}^{T} \hat{\mathbf{u}} \tag{2.26}$$

$$\gamma_{\eta} = \mathbf{t}_{\zeta}^{T} \frac{\partial \mathbf{u}}{\partial S_{\eta}} + \mathbf{t}_{\eta}^{T} \hat{\mathbf{u}} \tag{2.27}$$

In order to avoid locking due to inconsistent interpolations of the transverse shear strains, one must employ the same interpolation procedure adopted for $\epsilon_{\xi\xi}$ in the preceding section. The resulting expression for the two interpolated transverse shear strains become:

$$\gamma_{\xi} = \frac{1}{2}\{\gamma_{\xi}(\xi_{b}) + \gamma_{\xi}(-\xi_{b})\} + \frac{\xi}{2\xi_{b}}\{\gamma_{\xi}(\xi_{b}) - \gamma_{\xi}(-\xi_{b})\}, \qquad \xi_{b} = 1/\sqrt{3} \tag{3·22}$$

$$\gamma_{\eta} = \frac{1}{2}\{\gamma_{\eta}(\xi_{b}) + \gamma_{\eta}(-\xi_{b})\} + \frac{\xi}{2\xi_{b}}\{\gamma_{\eta}(\xi_{b}) - \gamma_{\eta}(-\xi_{b})\}, \qquad \xi_{b} = 1/\sqrt{3} \tag{3·23}$$

For computer implementation ease, we reexpress the above equations in the following form:

$$\gamma_{\xi} = \sum_{a=1}^{NEN} \mathbf{b}_{u_{a}}^{\epsilon\xi\zeta} u^{a} + \sum_{a=1}^{NEN} \mathbf{b}_{\hat{u}_{a}}^{\epsilon\xi\zeta} \hat{u}^{a} \tag{3·24}$$

where

$$\mathbf{b}_{u_{a}}^{\epsilon\xi\zeta} = \sum_{i=1}^{NB} \mathbf{w}_{i}(\xi) \left[N_{a,dS_{\xi}} \mathbf{t}_{\zeta}^{T} \right]_{\xi_{i},\eta} \tag{3·25}$$

$$\mathbf{b}_{\hat{u}_{a}}^{\epsilon\xi\zeta} = \sum_{i=1}^{NB} \mathbf{w}_{i}(\xi) \left[N_{a} \mathbf{t}_{\xi}^{T} \right]_{\xi_{i},\eta} \tag{3·26}$$

Similarly, an explicit implementable expression for γ_{η} can be obtained by interchanging (ξ_{i}, η) with (ξ, η_{i}) into the preceding equation.

3.2.3 Interpolations of $\epsilon_{\xi\eta}$ and $\kappa_{\xi\eta}$

Essentially, we extend the procedure outlined for the 4-ANS case to the 9-ANS element as follows. We sample $\epsilon_{\xi\xi}$, $\epsilon_{\xi\eta}$ and $\epsilon_{\eta\eta}$ at the four Barlow points, $(\xi = \pm1/\sqrt{3}, \eta = \pm1/\sqrt{3})$. At each integration point (ξ, η), we transform the four inplane bending strains evaluated at the four Barlow points via the same tensorial transformation as was done for the 4-ANS case (3.14):

$$\epsilon_{\xi\eta}^{b} = 2t_{11}^{b}t_{21}^{b}\epsilon_{\xi_{b}\xi_{b}} + 2t_{12}^{b}t_{22}^{b}\epsilon_{\eta_{b}\eta_{b}} + (t_{11}^{b}t_{22}^{b} + t_{12}^{b}t_{21}^{b})\epsilon_{\xi_{b}\eta_{b}} \tag{3·27}$$

where the superscript and the subscript, b, refers to one of the four Barlow points and the matrtix components, t_{ij}^b, have the same geometrical meaning as the one derived in (3.13) except they relate the projection on the shell surface from a Barlow point to the integration point.

The inplane strain, $\epsilon_{\xi\eta}$, at the integration point is then obtained by interpolating $\epsilon_{\xi\eta}^b$ as follows:

$$\epsilon_{\xi\eta} = \sum_{b=1}^{4} W_b(\xi, \eta) \cdot \epsilon_{\xi\eta}^b \qquad (3 \cdot 28)$$

where

$$\begin{aligned} W_a(\xi, \eta) &= \sum_{r=1}^{2} \sum_{s=1}^{2} \mathbf{w}_r(\xi)\, \mathbf{w}_s(\eta) \\ \mathbf{w}_1(\xi^\alpha) &= \frac{1}{2}(1 - \sqrt{3}\xi^\alpha) \\ \mathbf{w}_2(\xi^\alpha) &= \frac{1}{2}(1 + \sqrt{3}\xi^\alpha) \\ a &= 2(s-1) + r \end{aligned} \qquad (3 \cdot 29)$$

Similarly, the twist, $\kappa_{\xi\eta}$, are obtained by interchaning $\epsilon_{\xi\eta}^b$.

4. Preliminary Evaluation of Present ANS Shell Elements

We present a theoretical analysis of 9-ANS element for an inextensional bending case, for a cylinder subjected to uniform pressure, and a comparison of the present 9-ANS element with the so-called covariant-strain elements (Dvorkin and Bathe, 1984; Pinsky and Jang, 1986). We will then give a priliminary performance of both the present 4-ANS and 9-ANS elements for two simple shell problems: a pinched cylinder and a pinched sphere.

4.1. Inextensional Bending of Arch

The linearly varying strains derived in the preceding section should yield a locking-free and mechanism-free curved shell element for most applications. For thin shells, however, accurate solution of inextensional bending problems remains an important part of shell analysis for many applications such as sheet metal forming. For an arch in Fig. 3, the present strain-displacement interpolations for the membrane strain (3.19), the bending strain that is obtained by replacing $(u\ v\ w)$ in (3.19) with $(\hat{u},\ \hat{v},\ \hat{w})$, and the transverse shear strain (3.24), respectively, yield the following results:

$$\epsilon_{\xi\xi}^{\circ} = \frac{1}{A_1^2}\{-R\sin\phi\,u_0 + \frac{4}{3}R(1 - \cos\phi)\,w_0\} \qquad (4 \cdot 1)$$

21

$$\kappa_{\xi\xi} = \frac{\phi/\sin\phi \cdot \{1 + \frac{8}{3}(\frac{1-\cos\phi}{\sin\phi})^2\}}{\{1 + \frac{4}{3}(\frac{1-\cos\phi}{\sin\phi})^2\} \cdot \{1 + 4(\frac{1-\cos\phi}{\sin\phi})^2\}^{\frac{1}{2}}} \cdot (\frac{1}{R'} - \frac{1}{R}) \qquad (4 \cdot 2)$$

$$\gamma_\xi = \frac{\xi R \sin\phi}{2A_1}(\phi' - \phi)f(\phi) \quad , \qquad (4 \cdot 3)$$

where

$$f(\phi) = 1 - \left[1 + \frac{4}{3}\left(\frac{1-\cos\phi}{\sin\phi}\right)^2\right]^{\frac{1}{2}} \frac{2(1-\cos\phi)}{\phi\sin\phi} \frac{1}{1 + \frac{1}{3}(1-\cos\phi)} \qquad (4 \cdot 4)$$

The theoretical solutions for the above inextensional bending case are

$$\epsilon^o_{\xi\xi} = 0 \quad , \quad \kappa_{\xi\xi} = (\frac{1}{R'} - \frac{1}{R}) \quad , \quad \gamma_\xi = 0 \qquad (4 \cdot 5)$$

It is easily verified that the membrane strain (4.1) remains zero due to the small strain-increment assumption invoked in the present formulation. Hence, the two remaining measures of accuracy for the present strain approximations for this inextensional bending case are: the error in the curvature itself, $e_{bending}$, and the error in the transverse shear relative to the curvature change, e_{shear}:

$$e_{bending} = 1 - \frac{\phi/\sin\phi \cdot \{1 + \frac{8}{3}(\frac{1-\cos\phi}{\sin\phi})^2\}}{\{1 + \frac{4}{3}(\frac{1-\cos\phi}{\sin\phi})^2\} \cdot \{1 + 4(\frac{1-\cos\phi}{\sin\phi})^2\}^{\frac{1}{2}}} \qquad (4 \cdot 6)$$

$$e_{shear} \approx O\left[\frac{\int \gamma_\xi^2 d\xi}{\int(\varsigma\kappa_{\xi\xi})^2 d\varsigma}\right]^{\frac{1}{2}} \simeq \frac{R}{h}f(\phi) \qquad (4 \cdot 7)$$

Figure 4 shows the errors in the present approximation of the bending strain in terms of the element size, ϕ. For $\phi = 60°$ which corresponds to the element arc length of $2R\phi$, the error remains within one percent. In Fig. 5, the errors in the relative transverse shear as defined in (4.7) are plotted against the shell parameter R/h for one-tenth of a percent and one percent error. Only for extremely thin shells–for example, $R/h \sim 1000$, which is not shown in the figure–one needs $\phi \leq 20°$ if the ratio in the two energy components, e_{shear}, is to remain less than one percent. Hence, we conclude that the present formulation can capture inextensional bending deformations with adequate accuracy, provided the element size is not too large.

4.2 Cylinder under Uniform Internal Pressure

For the case of a cylinder subjected to uniform internal pressure, we obtain from (3.19) and (3.24)

$$\epsilon^o_{\xi\xi} = \frac{w_0}{R} \quad , \quad \gamma_\xi = 0 \qquad (4 \cdot 8)$$

22

which is exact. Hence, the present formulation yields the exact solution for this classical problem.

4.3 Comparison with Covariant-Strain Formulations

As an additional error analysis, it is noteworthy to compare the present formulation with the so-called covariant-strain formulation (Dvorkin and Bathe, 1984; Pinsky and Jang, 1986). For this purpose we recall the *physical* membrane strain by the present formulation from (3.23):

$$\epsilon_{\xi\xi}^{ans} = \frac{1}{A_\xi^2}(x,_\xi u,_\xi + y,_\xi v,_\xi + z,_\xi w,_\xi) \tag{4·9}$$

The membrane stress is then computed by

$$\sigma_{\xi\xi} = E\epsilon_{\xi\xi}^{ans} \tag{4·10}$$

which varies linearly along the arch.

In contrast, in the covariant-strain formulation one must obtain the following non-physical quantity

$$\epsilon_{\xi\xi}^{cov} = (x,_\xi u,_\xi + y,_\xi v,_\xi + z,_\xi w,_\xi) \tag{4·11}$$

Notice that the above interpolated covariant strain is nothing but the denominator of the present interpolated form of the assumed natural-coordinate strain (4.9). The computation of stress based on the covariant strains for the arch, however, must adopt the following non-physical constitutive matrix:

$$\sigma_{\xi\xi} = E^{cov}\epsilon_{\xi\xi}^{cov}, \quad \text{or} \quad \sigma_{\alpha\beta} = C_{\alpha\beta\gamma\delta}^{cov}\epsilon_{\gamma\delta}^{cov} \tag{4·12}$$

where

$$C_{\alpha\beta\gamma\delta}^{cov} = \frac{\partial S_\alpha}{\partial x_i}\frac{\partial S_\beta}{\partial x_j}C_{ijkl}\frac{\partial S_\gamma}{\partial x_k}\frac{\partial S_\delta}{\partial x_l} \tag{4·13}$$

in which $C_{\alpha\beta\gamma\delta}^{cov}$ is the non-physical material tensor that corresponds to the covariant strain $\epsilon_{\gamma\delta}^{cov}$ and

$$\{\partial S_1 \ \partial S_2 \ \partial S_3\} = \{\partial S_\xi \ \partial S_\eta \ \partial S_\varsigma\}, \quad \{x_1 \ x_2 \ x_3\} = \{x \ y \ z\} \tag{4·14}$$

The expression for $C_{\alpha\beta\gamma\delta}^{cov}$ shows that it is a complex function of the appropriate components of the Jacobian matrix:

$$J = \begin{bmatrix} x,_\xi & x,_\eta & x,_\varsigma \\ y,_\xi & y,_\eta & y,_\varsigma \\ z,_\xi & z,_\eta & z,_\varsigma \end{bmatrix} \tag{4·15}$$

Hence, even though the covariant strains $\epsilon_{\gamma\delta}^{cov}$ are interpolated to vary linearly, the corresponding non-physical contravariant stresses for the covariant-strain formulation will in

23

general not be the case. For example, the covariant membrane stress for the arch case is seen to destroy the linearly varying stress field unless E^{cov} is forced to be a constant (see (4.13)). For general applications, such arbitrary adjustments of the covariant material tensor so that its components become constant, present themselves as a task.

4.4 Preliminary Numerical Results

The present four and nine-node ANS-shell elements have been implemented and tested for two simple shell cases, viz., cylinder under a concentrated load and a pinched hemisphere. Figure 6 shows the performance of both 4-ANS and 9-ANS elements for the pinched cylinder problem which was also studied in Park and Stanley (1986). The present 4-ANS and 9-ANS elements are designated as 4-ANS^n and 9-ANS^n. We note that the new 9-ANS element $(9 - ANS^n)$ element overshoots the solution. For the 4-ANS element, both the old and new 4-ANS manifest about the same convergence rate. This, however, is not the case for the hemisphere problem. As shown in Fig. 7, the new 9-ANS shell element (designated as $9 - ANS^n$) converges at the second grid (9×9) whereas the old 9-ANS element converges at the refined grid (17×17). As for the new 4-ANS element, the new element maintains the performance as the one obtained by the old 4-ANS element in conjunction with a rigid-mode projection designated as $4 - ANS/P$. This is a signigicant improvement over the old 4-ANS element and over the 4-STG/P element that is also compared in Park and Stanley (1986) and Stanley (1985).

It should be noted that a significant change in the construction of the new family ANS elements has been in the way the inplane bending strain and twist $(\epsilon_{\xi\eta}, \kappa_{\xi\eta})$ are interpolated even though interpolations of the rest of the strain compoments have been somewhat improved from the old construction. We will report in the coming months on the improved performance of the new 4-ANS and 9-ANS elements via production-level shell analysis.

5. Discussion

In this Part, we have presented in detail the construction of both 4-ANS and 9-ANS shell elements based upon the formulation presented in Part I (Park and Stanley, 1987) that is suitable for assumed-strain shell elements. Major emphasis of that formulation has been to incorporate as much shell behavior as possible into the basic formulation. One important consequence of this emphasis is the modification of the in-plane bending strain in the spirit of Sanders (1959). Other possibilities exist in the basic formulation, which may be further improved to better capture shell behavior, as a complete hierarchical approximation of the basic formulation has not yet been carried out.

It should be noted that, while we have endeavored to preserve the well-known *first-order* thin shell theory with transverse shear effects, the present element construction has avoided two related difficulties that stem from a direct application of the classical thin shell equations: rigid-body motions and the derivatives of the two fundamental surface coefficients,

24

A_ξ and A_η. Avoidance of these two deleterious effects by the present element construction has been accomplished by the use of the inertially fixed translational displacements and of the corotationally based two-rotational variables.

Even though we construct the basic element attributes–the strain-displacement matrix (known in the literature as B-matrix)–based on the natural-coordinate system, we proceed the evaluation of the internal stiffness force based on the orthogonal shell-surface coordinates. Hence, the present element can be easily *plugged into* any existing shell analyzer for both geometrical and material nonlinear problems. This is in contrast with the so-called covariant shell elements (Dvorkin and Bathe, 1984; Pinsky and Jang, 1986) wherein one works with a set of non-physical strains, which amounts to embedding the fundamental shell-surface coefficients into their corresponding constitutive matrix. For example, years of experience in the solution procedures for plasticity analysis based essentially on the amount of physical strain increments may not be of use in the solution of plasticity problems based on the covaraint strain elements, since the amount of covariant strain increments is dependent on the element size.

Although not elaborated in this Part, the strain increments need not be infinitesimal. In particular, the displacement and rotation increments for large rigid motions can be arbitrarily large. This will be corroborated in Part III, which will report on the performance of the present elements. Specifically, for nonlinear elasticity problems without bifurcation possibility, the present element together with an element-independent corotational algorithm need not accumulate stresses, since the displacement and rotation increments can be measured from the initial state to the current state.

An error analysis of the present element for uniform membrane strain state and inextensional bending state (Fig. 5) illustrates that the present 9-ANS element possesses improved transverse shear modeling and membrane modeling compared with the old 9-ANS element. For example, in no case does the error in the computed inextensional bending exceed one percent, for up to a 90^0-span. This is reported in Fig. 6. The mean square error in the transverse shear energy, though, restricts the allowable element size as the shell becomes thinner as illustrated in Fig. 7. A preliminary numerical test of the new 4-ANS and 9-ANS shell elements on the pinched cylinder and pinched hemisphere indicates that the new elements improve significantly for shell surfaces with double curvature. We will examine in more detail their potential improvements through production-level computations.

As for improving the accuracy of the transverse shear strains, this is where a rigorous three-dimensional analysis should shed light on the reliability of C^0-type thin shell elements. We intend to follow up this aspect in Part III. It should be noted, however, that such errors are consistent with the bounds of errors in most thin shell theories.

25

Acknowledgements.

References

Ahmad, S., Irons, B. M. and Zienkiewicz, O. C., 1970, "Analysis of Thick and Thin Shell Structures by Curved Elements," *Int. J. Num. Meth. Engr.*, 2, 419-451.

Barlow, J., 1976, "Optimal Stress Locations in Finite Element Models," *Int. J. Num. Meth. Engr.* 10, 243-251.

Crisfield, M. A., 1983, "A Four-Noded Thin-Plate Element Using Shear Constraints-A Modified Version of Lyons' Element," *Comp. Meth. Appl. Mech. Engr.*, 38, 93-120.

Crisfield, M. A., 1984, "A Quadratic Mindlin Element Using Shear Constraints," *Comp. Meth. Appl. Mech. & Engr.*, 18, 833-852.

Dvorkin, E. N. and Bathe, K.J., 1984, "A Continuum Mechanics Based Four-Node Shell Element for General Nonlinear Analysis," *Int. J. for Computer-Aided Engr. & Software*, 1, 77-88.

Ergatoudis, I., Irons, B. M. and Zienkiewicz, O. C., 1968, "Curved Isoparametric Quadrilateral Elements for Finite Element Analysis," *International Journal of Solids and Structures*, 4, 31-42.

Fræijs de Veubeke, B., 1965, "Displacement and Equilibrium Models in the Finite Element Method", in *Stress Analysis*, O. C. Zienkiewicz and G. Holister (eds.), John Wiley, 145-197.

Gibbs, J. W., *Vector Analysis*, Dover, 1960, New York, N. Y., Chapt. 6.

Hrennikoff, A., 1941, "Solution of Problems of Elasticity by the Framework Method," *Journal of Applied Mechanics*, 8, A169-175.

Huang, H.C. and Hinton, E., 1986, "A New Nine Node Degenerated Shell Element with Enhanced Membrane and Shear Interpolation, *Int. J. Num. Meth. Engr.*, 22, 73-92.

Hughes, T. J. R., Taylor, R. C. and Kanoknukulchai, W., 1977, "A Simple and Efficient Finite Finite Element for Plate Bending," *Int. J. Num. Meth. Engr.*, 11, 1529-1547.

Hughes, T. J. R. and Tedzduyar, T. E., 1981, "Finite Elements Based on Mindlin Plate Theory with Particular Reference to the Four-node Bilinear Isoparametric Elements," *Journal of Applied Mechanics* , 587-596.

Irons, B., 1966, "Engineering Application of Numerical Integration in Stiffness methods," *AIAA J.*, 4, 2035-2037.

Irons, B. M., 1976, "The Semiloof Shell Element," in *Finite Elements for Thin Shells and Curved Members*, Eds. D. G. Ashwell and R. H. Gallagher, John Wiley & Sons, London, 197-222.

Irons, B. and Ahmad, S., 1980, *Techniques for Finite Elements*, John Wiley and Sons, New York.

Lee, S. W. and Pian, T. H. H., 1978, "Improvement of Plate and Shell Finite Elements by Mixed Formulations," *AIAA J.*, 16, 29-34.

MacNeal, R. H., 1978, "A Simple Quadrilateral Shell Element," *Comp. & Struct.*, 8, 175-183.

MacNeal, R. H., 1982, "Derivation of Element Stiffness Matrices by Assumed Strain Distribution," *Nuclear Eng. Design*, 70, 3-12.

Parisch, H., 1979, "A Critical Survey of the 9-Node Degenerated Shell Element with Special Emphasis on Thin Shell Application and Reduced Integration," *Comp. Meth. Appl. Mech. Engr.*, 20, 323-350.

Park, K. C., 1984, "Symbolic Fourier Analysis Procedures for C^0 Finite Elements," in *Innovative Methods for Nonlinear Analysis*, Pineridge Press, Swansea, 269-293.

Park, K. C., 1985, "An Improved Strain Interpolation for Curved C^0 Elements," to appear in the Bruce Irons Memorial Issue of *Int. J. Num. Meth. Engr.*.

Park, K. C., 1987, "The ANS Shell Elements: Part I – Formulation," Center for Space Structures and Controls, University of Colorado, Report CU-CSSC-87-06.

Park, K. C. and Flaggs, D. L., 1985, "A Symbolic Fourier Synthesis of a One-Point Integrated Quadrilateral Plate Element," *Comp. Meth. Appl. Mech. Engr.*, 48, 203-236.

Park, K. C., Stanley, G. M. and Flaggs, D. L., 1985, "A Uniformly Reduced, Four-Noded C^0-Shell Element with Consistent Rank Corrections," *Comp. & Struct.*, 20, 129-139.

Park, K.C. and Stanley, G.M., 1986, "A Curved C^0 Shell Element Based on Assumed Natural-Coordinate Strains," *Journal of Applied Mechanics*, 108, 278-290.

Park, K.C. and Stanley, G.M. and Cabiness, H., 1986, "A Family of $C°$ Shell Elements Based on Generalized Hrennikoff's Method and Assumed Natural-Coordinate Strains," in: *Finite Element Methods for Nonlinear Problems*, Bergan. P. et al(Editors), Springer-Verlag, Berlin, 265-282.

Pawsey, S. F. and Clough, R. W., 1971, "Improved Numerical Integration of Thick Shell Finite Elements," *Int. J. Num. Meth. Engr.*, 3, 575-586.

Pian, T. H. H. and Sumihara, K., 1984, "Rational Approach for Assumed Stress Finite Elements," *Int. J. Num. Meth. Engr.*, 20, 1685-1695.

Pinsky, P.M. and Jang, J., 1986, "A 9-Node Assumed Covariant Strain Element," presented at the First World Congress on Computational Mechanics, Sept. 22-26, Austin, Texas.

Pugh, E. D. L., Hinton, E. and Zienkiewicz, O. C., 1978, "A Study of Quadrilateral Plate Bending Elements with Reduced Integration," *Int. J. Num. Meth. Engr.*, 12, 1059–1079.

Rankin, C. C. and Brogan, F. A., 1984, "An Element-Independent Corotational Procedure for the Treatment of Large Rotations," in : *Collapse Analysis of Structures* (eds. L.H. Sobel and K. Thomas), ASME, New York, 85-100.

Reissner, E., 1945, "The Effect of Transverse Shear Deformation on the Bending of Elastic Plates, *J. Appl. Mech., Trans. ASME*, A69–A77.

Sanders, J.L, 1959, "An Improved First Approximation Theory for Thin Shells," NASA-TR-R24.

Salmon, D. C., 1987, *Large Change-of-Curvature Effects in Quadratic Finite Elements for CAD of membrane Structures*, PhD Thesis, Cornell University, Ithaca, N. Y.

Stanley, G. M., 1985, *Continuum-Based Shell Analysis*, PhD Thesis, Stanford University, Stanford, Calif.

Stolarski, H. and Belytschko, T., 1982, "Membrane Locking and Reduced Integration for Curved Elements," *J. Appl. Mech.*, 49, 172–176.

Stolarski, H. and Belytschko, T., 1983, "Shear and Membrane Locking in Curved C^0 Elements," *Comp. Meth. Appl. Mech. Engr.*, 41, 279-296.

Wempner, G. A., Oden, T. J. and Kross, D. A., 1968, "Finite Element Analysis of Thin Shells," *J. Eng. Mech. Div.*, ASCE, 1273-1294.

Wempner, G., Talaslidis, D. and Huang, C. - M., 1982, "A Simple and Efficient Approximation of Shells via Finite Quadrilateral Elements," *Journal of Applied Mechanics*, 49, 115-120.

Zienkiewicz, O. C., 1971, *The Finite Element Method in Engineering Science*, McGraw-Hill Book Co., New York.

Zienkiewicz, O. C., Taylor, R. C. and Too, J. M., 1971, "Reduced Integration Technique in General Analysis of Plates and Shells," *Int. J. Num. Meth. Engr.*, 3, 275-290.

Fig. 1 Deformed Shell Geometries in Terms of Inertial (e), Shell Surface (s),
Natural-Coordinate (a) and Deformed Normal (b_3) Vectors.

29
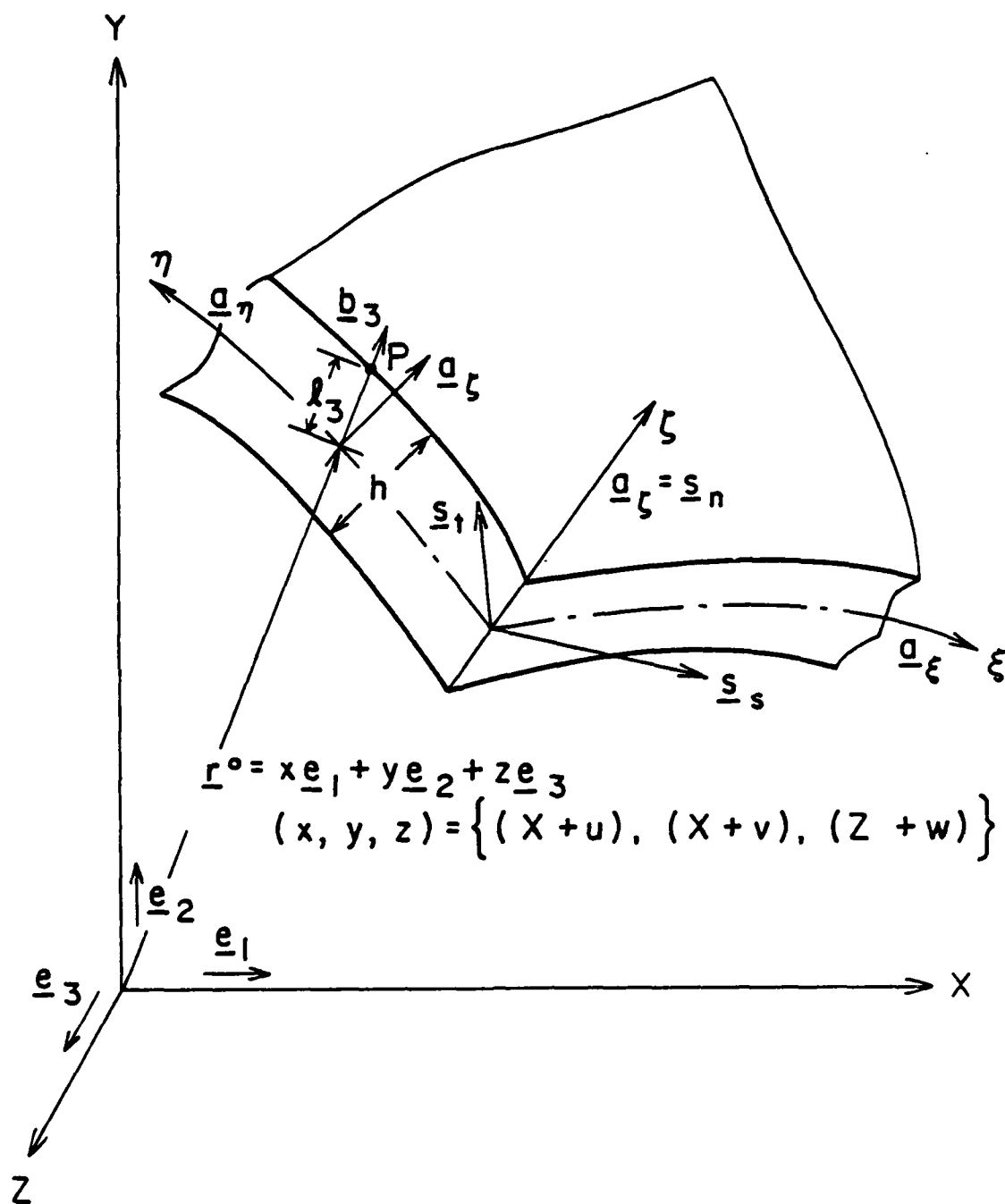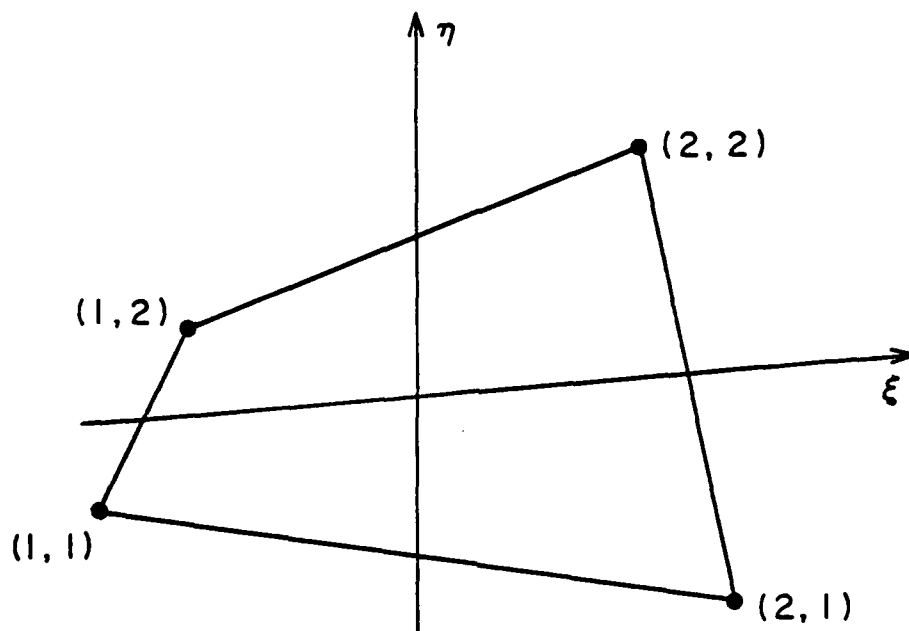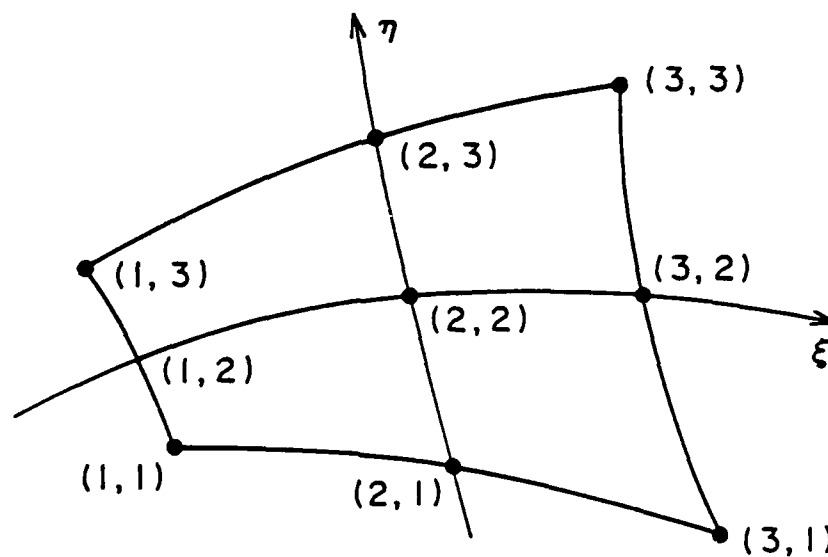
a) 4-NODE ELEMENT

b) 9-NODE ELEMENT

Fig. 2 Nodal Designations for Shell Elements

30
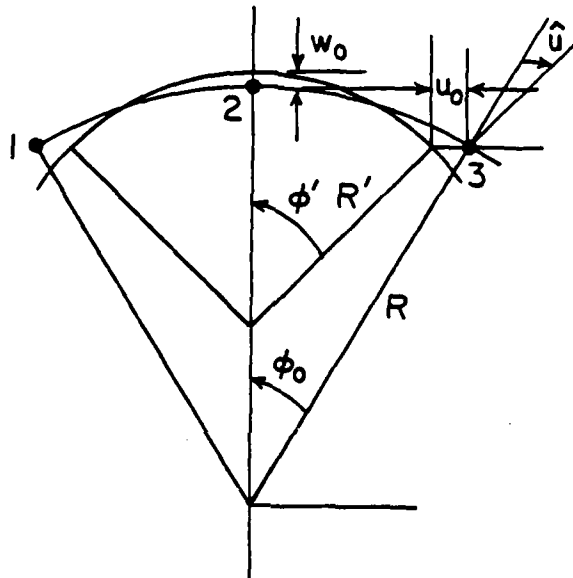
ARCH LENGTH, $S = 2R\phi = 2R'\phi'$

ROTATION, $\hat{u} = \phi' - \phi = \left(\dfrac{1}{R'} - \dfrac{1}{R}\right)\dfrac{S}{2}$

Fig. 3 Inextensional Deformation of an Arch

31
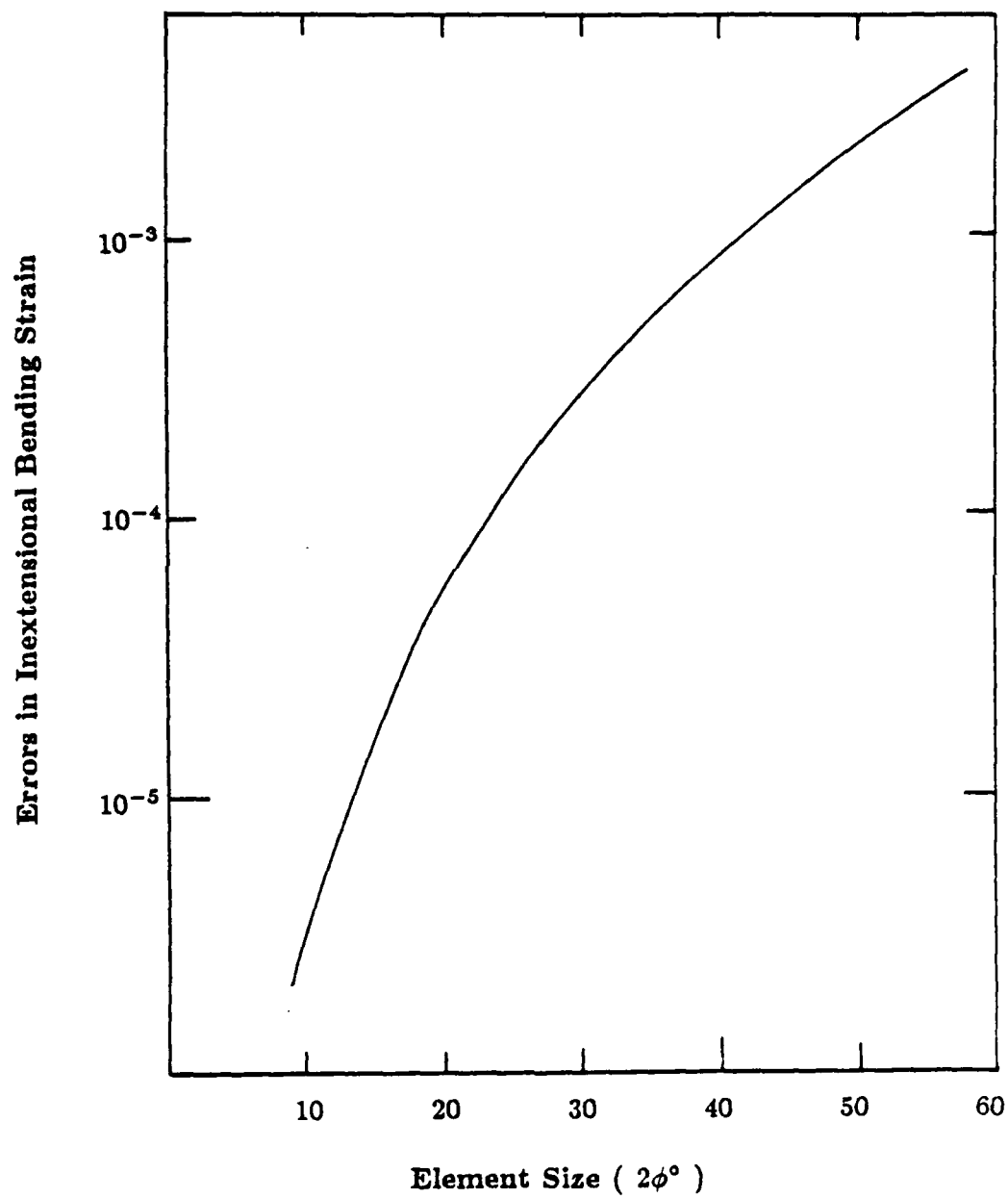
Fig. 4 Errors in the Bending Strain for Inextensional Bending of Arch
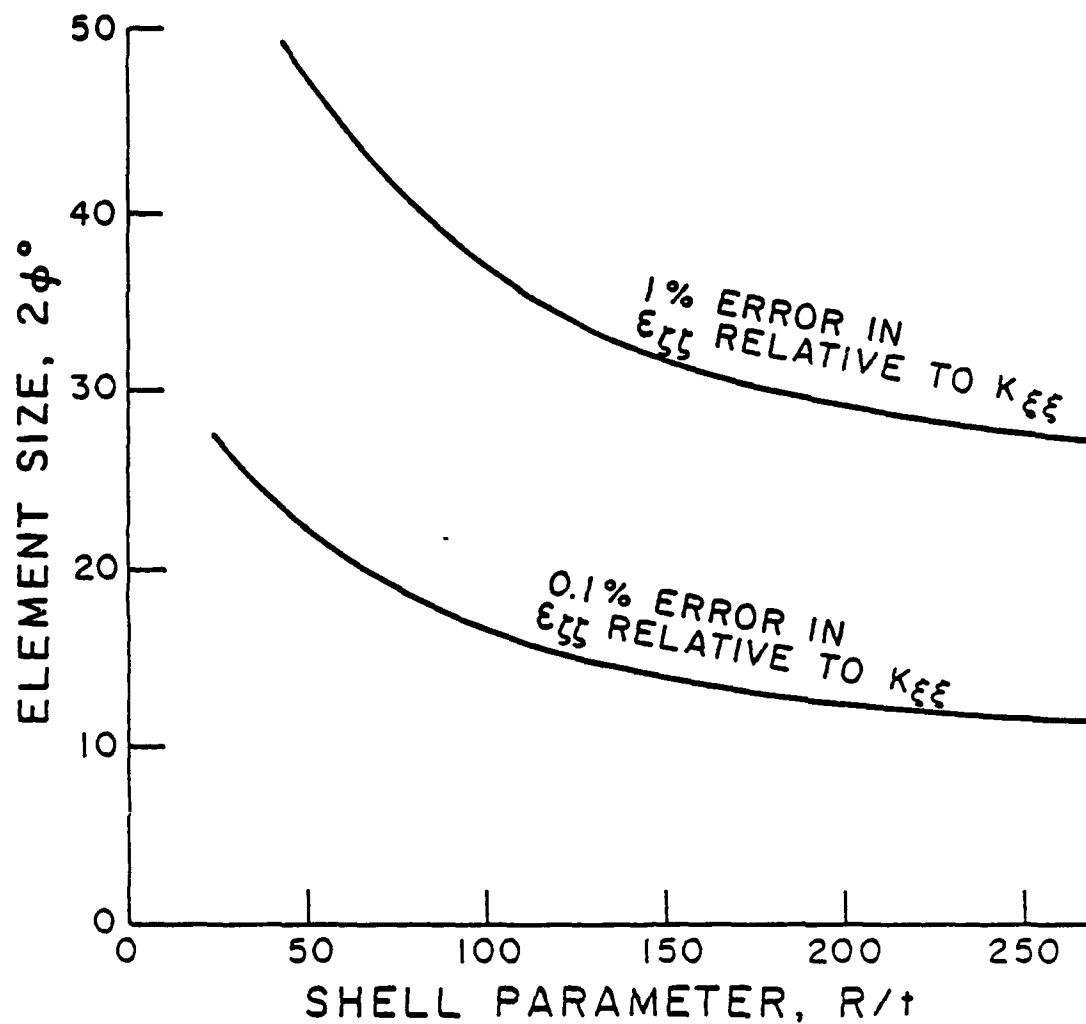
Fig. 5   Errors in Transverse Shear for Inextensional Bending of an Arch

Fig. 6 Pinched Cylinder with Open Ends

Normalized Maximum Displacement

$E = 10.5 \times 10^6$
$\nu = .3125$
$R = 4.053$
$L = 10.35$

$R/h = 50$

SYM

P/4

SYM

w^P

SYM

FREE

SYM

$L/2$

q_ANS^n

q_ANS

u_ANS^n

u_ANS, 4-LAG

Nodes Per Side

Displacement

1.1

1.0

0.9

0.8

0.7

0.6

3   4   5   6   7   8   9

34

Fig. 7 Pinched Shpere

Normalized Maximum Displacement

Appendix D

PARAMETRIZED MULTIFIELD VARIATIONAL PRINCIPLES IN ELASTICITY: I. MIXED FUNCTIONALS, II. HYBRID FUNCTIONALS AND THE FREE FORMULATION

by

C. A. Felippa

Parametrized Multifield Variational
Principles in Elasticity. I: Mixed Functionals
II: Hybrid Functionals and the Free Formulation

Carlos A. Felippa

Department of Aerospace Engineering Sciences and
Center for Space Structures and Controls
University of Colorado
Boulder, Colorado 80309-0429, USA

March 1988

Report No. CU-CSSC-88-01

PARAMETRIZED MULTIFIELD VARIATIONAL PRINCIPLES IN ELASTICITY: I. MIXED FUNCTIONALS

CARLOS A. FELIPPA

*Department of Aerospace Engineering Sciences
and Center for Space Structures and Controls
University of Colorado
Boulder, Colorado 80309-0429, USA*

SUMMARY

A one-parameter family of mixed variational principles for linear elasticity is constructed. This family includes the generalized Hellinger-Reissner and total potential energy principles as special cases. The presence of the free parameter offers an opportunity for the systematic derivation of energy-balanced finite elements that combine displacement and stress assumptions. It is shown that Fraeijs de Veubeke's stress-assumption limitation principle takes a particularly elegant expression in terms of the parametrized discrete form. Other possible parametrizations are briefly discussed.

GOVERNING EQUATIONS

Consider a *linearly elastic body* under static loading that occupies the volume V. The body is bounded by the surface S, which is decomposed into $S : S_d \cup S_t$. Displacements are prescribed on S_d while surface tractions are prescribed on S_t. The outward unit normal on S is denoted by $\mathbf{n} \equiv n_i$. The presence of internal natural or artificial interfaces is not treated in this paper.

The three unknown volume fields are displacements $\mathbf{u} \equiv u_i$, infinitesimal strains $\mathbf{e} \equiv e_{ij}$, and stresses $\boldsymbol{\sigma} \equiv \sigma_{ij}$. The problem data include: the body force field $\mathbf{b} \equiv b_i$ in V, prescribed displacements $\hat{\mathbf{d}}$ on S_d, and prescribed surface tractions $\hat{\mathbf{t}} \equiv \hat{t}_i$ on S_t.

The relations between the volume fields are the strain-displacement equations

$$\mathbf{e} = \tfrac{1}{2}(\nabla \mathbf{u} + \nabla^T \mathbf{u}) = \mathbf{D}\mathbf{u} \qquad \text{or} \qquad e_{ij} = \tfrac{1}{2}(u_{i,j} + u_{j,i}) \quad \text{in } V, \tag{1}$$

the constitutive equations

$$\boldsymbol{\sigma} = \mathbf{E}\mathbf{e} \qquad \text{or} \qquad \sigma_{ij} = E_{ijkl}e_{kl} \quad \text{in } V, \tag{2}$$

and the equilibrium (balance) equations

$$-\text{div}\,\boldsymbol{\sigma} = \mathbf{D}^*\boldsymbol{\sigma} = \mathbf{b} \qquad \text{or} \qquad \sigma_{ij,j} + b_i = 0 \quad \text{in } V, \tag{3}$$

in which $\mathbf{D}^* = -\text{div}$ denotes the adjoint operator of $\mathbf{D} = \tfrac{1}{2}(\nabla + \nabla^T)$.

The stress vector with respect to a direction defined by the unit vector $\mathbf{v}$ is denoted as $\boldsymbol{\sigma}_v = \boldsymbol{\sigma}.\mathbf{v}$, or $\sigma_{vi} = \sigma_{ij}v_j$. On S the surface-traction stress vector is defined as

$$\boldsymbol{\sigma}_n = \boldsymbol{\sigma}.\mathbf{n}, \qquad \text{or} \quad \sigma_{ni} = \sigma_{ij}n_j. \tag{4}$$

With this definition the traction boundary conditions may be stated as

$$\boldsymbol{\sigma}_n = \hat{\mathbf{t}} \qquad \text{or} \qquad \sigma_{ij}n_j = \hat{t}_i \qquad \text{on } S_t, \tag{5}$$

and the displacement boundary conditions as

$$\mathbf{u} = \hat{\mathbf{d}} \qquad \text{or} \qquad u_i = \hat{d}_i \qquad \text{on } S_d. \tag{6}$$

NOTATION

Field Dependency. In variational methods of approximation we do not work of course with the exact fields that satisfy the governing equations (1-3,5-6), but with *independent* (primary) fields, which are subject to variations, and *dependent* (secondary, associated, derived) fields, which are not. The approximation is determined by taking variations with respect to the independent fields.

An *independently varied* field will be identified by a superposed tilde, for example $\tilde{u}$. A dependent field is identified by writing the independent field symbol as superscript. For example, if the displacements are independently varied, the derived strain and stress fields are

$$\mathbf{e}^u = \tfrac{1}{2}(\nabla + \nabla^T)\tilde{\mathbf{u}} = \mathbf{D}\tilde{\mathbf{u}}, \qquad \boldsymbol{\sigma}^u = \mathbf{E}\mathbf{e}^u = \mathbf{E}\mathbf{D}\tilde{\mathbf{u}}. \tag{7}$$

An advantage of this convention is that $\mathbf{u}$, $\mathbf{e}$ and $\boldsymbol{\sigma}$ may be reserved for the *exact* fields.

Integral Abbreviations. Volume and surface integrals will be abbreviated by placing domain-subscripted parentheses and square brackets, respectively, around the integrand. For example:

$$(f)_V \overset{\text{def}}{=} \int_V f\, dV, \quad [f]_S \overset{\text{def}}{=} \int_S f\, dS, \quad [f]_{S_d} \overset{\text{def}}{=} \int_{S_d} f\, dS, \quad [f]_{S_t} \overset{\text{def}}{=} \int_{S_t} f\, dS. \tag{8}$$

If $\mathbf{f}$ and $\mathbf{g}$ are vector functions, and $\mathbf{p}$ and $\mathbf{q}$ tensor functions, their inner product over V is denoted in the usual manner

$$(\mathbf{f}, \mathbf{g})_V \overset{\text{def}}{=} \int_V \mathbf{f}.\mathbf{g}\, dV = \int_V f_i g_i\, dV, \qquad (\mathbf{p}, \mathbf{q})_V \overset{\text{def}}{=} \int_V \mathbf{p}.\mathbf{q}\, dV = \int_V p_{ij}q_{ij}\, dV, \tag{9}$$

and similarly for surface integrals, in which case square brackets are used.

Domain Assertions. Finally, the notation

$$(a = b)_V, \qquad [a = b]_S, \qquad [a = b]_{S_d}, \qquad [a = b]_{S_t}, \tag{10}$$

is used to assert that the relation $a = b$ is valid at each point of V, S, S_d and S_t, respectively.

I-2

THE HU-WASHIZU PRINCIPLE

There are several essentially equivalent statements of the Hu-Washizu functional of linear elasticity. The starting form used in this paper is the four-field functional presented in Washizu[1]

$$\Pi_W^t(\tilde{u}, \tilde{e}, \tilde{\sigma}, \tilde{t}) = \tfrac{1}{2}(\sigma^e, \tilde{e})_V + (\tilde{\sigma}, e^u - \tilde{e})_V - P^t \tag{11}$$

where P^t is the "forcing" potential

$$P^t(\tilde{u}, \tilde{t}) = (b, \tilde{u})_V + [\tilde{t}, \tilde{u} - \hat{d}]_{S_d} + [\hat{t}, \tilde{u}]_{S_t}. \tag{12}$$

The functional (11) will be called t-generalized (traction-generalized) in the sense that the volume fields $\tilde{u}, \tilde{e}, \tilde{\sigma}$ *and* the surface field $\tilde{t}$ are subject to independent variations, whereas in the conventional form of the principle the relation $[t = \tilde{\sigma}_n]_{S_d}$ is enforced *a priori*. The superscript t is used to distinguish it from the d-generalized variant

$$\Pi_W^d(\tilde{u}, \tilde{e}, \tilde{\sigma}, \tilde{d}) \tag{13}$$

in which the surface displacements $\tilde{d}$ are varied independently from the volume displacement field u. Functionals of the form (13) require the introduction of internal interfaces and are studied more extensively in a sequel paper.[2]

Application of the divergence theorem

$$(\sigma, e^u)_V = -(\text{div }\sigma, u)_V + [\sigma_n, u]_S \tag{14}$$

to transform the $(\tilde{\sigma}, \delta e^u)$ term yields the first variation of (11)

$$\delta\Pi_W^t = (\sigma^e - \tilde{\sigma}, \delta\tilde{e})_V + (e^u - \tilde{e}, \delta\tilde{\sigma})_V - (\text{div }\tilde{\sigma} + b, \delta\tilde{u})_V \\ - [\hat{t} - \tilde{\sigma}_n, \delta\tilde{u}]_{S_t} - [\tilde{u} - \hat{d}, \delta\tilde{t}]_{S_d} - [\tilde{t} - \tilde{\sigma}_n, \delta\tilde{u}]_{S_d}. \tag{15}$$

Setting $\delta\Pi_W^t = 0$ yields the Euler field equations and boundary conditions satisfied by the *exact* solution:

$$(\sigma = Ee)_V, \quad (e = e^u)_V, \quad (\text{div }\sigma + b = 0)_V, \quad [\sigma_n = \hat{t}]_{S_t}, \quad [\sigma_n = t]_{S_d}, \quad [u = \hat{d}]_{S_d}. \tag{16}$$

A PARAMETRIZED MIXED VARIATIONAL PRINCIPLE

Constraining the Hu-Washizu functional by selectively enforcing field equations and boundary conditions *a priori* yields six functionals listed in Ch. 4 of Oden and Reddy's monograph[3]. Of particular interest for the present study are the t-generalized Hellinger-Reissner functional

$$\Pi_R^t(\tilde{u}, \tilde{\sigma}, \tilde{t}) = -\tfrac{1}{2}(\tilde{\sigma}, e^\sigma)_V + (\tilde{\sigma}, e^u)_V - P^t, \tag{17}$$

the t-generalized potential energy functional

$$\Pi_P^t(\tilde{u}, \tilde{t}) = \tfrac{1}{2}(\sigma^u, e^u)_V - P^t, \tag{18}$$

In addition, Oden and Reddy[3] list an "unnamed" functional whose t-generalized version is

$$\Pi_U^t(\tilde{u}, \tilde{\sigma}, \tilde{t}) = (\sigma^u, e^u)_V - \tfrac{1}{2}(\tilde{\sigma}, e^\sigma)_V - (\tilde{\sigma}, e^u)_V - P^t. \tag{19}$$

These three functionals are special cases of the following parametrized form

$$\Pi_\gamma^t(\tilde{u}, \tilde{\sigma}, \tilde{t}) = \tfrac{1}{2}(1-\gamma)(\sigma^u, e^u)_V - \tfrac{1}{2}\gamma(\tilde{\sigma}, e^\sigma)_V + \gamma(\tilde{\sigma}, e^u)_V - P^t, \tag{20}$$

where γ is a scalar. If $\gamma = 1, 0, -1$ we obtain the functionals Π_R^t, Π_P^t and Π_U^t, respectively. The first variation of (20) is

$$\delta\Pi_\gamma^t = \gamma(e^u - e^\sigma, \delta\tilde{\sigma})_V - (\operatorname{div}\sigma^\gamma + b, \delta\tilde{u})_V$$
$$- \left[\hat{t} - \sigma_n^\gamma, \delta\tilde{u}\right]_{S_t} - \left[\tilde{t} - \sigma_n^\gamma, \delta\tilde{u})\right]_{S_d} - \left[u - \hat{d}, \delta\tilde{t}\right]_{S_d}, \tag{21}$$

in which σ^γ and σ_n^γ denote the γ-weighted stresses

$$\sigma^\gamma \stackrel{\text{def}}{=} \gamma\tilde{\sigma} + (1-\gamma)\sigma^u, \quad \sigma_n^\gamma \stackrel{\text{def}}{=} \gamma\tilde{\sigma}_n + (1-\gamma)\sigma_n^u. \tag{22}$$

If $\gamma \neq 0$, the Euler equations and natural boundary conditions are

$$(e^u = e^\sigma)_V, \quad (\operatorname{div}\sigma^\gamma + b = 0)_V, \quad [\sigma_n^\gamma = \hat{t}]_{S_t}, \quad [\sigma_n^\gamma = \tilde{t}]_{S_d}, \quad [u = \hat{d}]_{S_d}. \tag{23}$$

The constitutive equations do not appear since they are enforced *a priori* in Π_γ^t. If $\gamma = 0$, the first Euler equation drops out.

ENERGY BALANCING

Distances. Let $U(\epsilon) = \tfrac{1}{2}(E\epsilon, \epsilon)_V$ denote the strain energy associated with field ϵ. We may rewrite (20) as a potential-energy deviator

$$\Pi_\gamma^t = \Pi_P^t - \gamma U(e^u - e^\sigma), \tag{24}$$

because

$$\frac{\Pi_\gamma^t - \Pi_P^t}{\gamma/2} = (\tilde{\sigma}, e^\sigma - e^u) - (\tilde{\sigma} - \sigma^u, e^u)_V =$$
$$(\sigma^u - \tilde{\sigma}, e^u - e^\sigma)_V = (Ee^u - Ee^\sigma, e^u - e^\sigma)_V. \tag{25}$$

If E is positive definite, $U(e^u - e^\sigma) \geq 0$ and consequently

$$\Pi_\gamma^t \leq \Pi_P^t \quad \text{if} \quad \gamma > 0. \tag{26}$$

If $\tilde{u}$ is kinematically admissible, Π_P^t exceeds the exact potential energy as shown below. It follows that to improve solutions in energy we expect to take $\gamma \geq 0$. Thus principles associated with $\gamma < 0$ have limited practical interest.

Let $\Pi(\mathbf{u})$ denote the exact potential energy

$$\Pi(\mathbf{u}) = \tfrac{1}{2}(\boldsymbol{\sigma},\mathbf{e})_V - (\mathbf{b},\mathbf{u})_V - [\hat{\mathbf{t}},\mathbf{u}]_{S_t} \tag{27}$$

where $\boldsymbol{\sigma}$ and $\mathbf{e}$ denotes the exact stress and strain field, respectively. If $\tilde{\mathbf{u}}$ is kinematically admissible and thus satisfies $[\mathbf{u} = \hat{\mathbf{d}}]_{S_d}$, then the energy distance from $\Pi_P^t(\tilde{\mathbf{u}})$ to the exact functional (27) is (see $e.g.$ §34 of Gurtin[4])

$$\Pi_P^t - \Pi = \tfrac{1}{2}(\boldsymbol{\sigma}^u - \boldsymbol{\sigma},\mathbf{e}^u - \mathbf{e})_V = U(\mathbf{e}^u - \mathbf{e}) \tag{28}$$

Optimal Approximation. To derive an "energy balanced" approximation we impose the condition $\Pi_\gamma^t = \Pi$, which yields

$$\gamma_{opt} = \frac{U(\mathbf{e}^u - \mathbf{e})}{U(\mathbf{e}^u - \mathbf{e}^\sigma)} = \frac{(\boldsymbol{\sigma}^u - \boldsymbol{\sigma},\mathbf{e}^u - \mathbf{e})}{(\boldsymbol{\sigma}^u - \tilde{\boldsymbol{\sigma}}^u,\mathbf{e}^u - \mathbf{e}^\sigma)}. \tag{29}$$

For example, if we assume that the exact stresses and strains lie halfway between the approximate fields,

$$\boldsymbol{\sigma} = \tfrac{1}{2}(\boldsymbol{\sigma}^u + \tilde{\boldsymbol{\sigma}}), \qquad \mathbf{e} = \tfrac{1}{2}(\mathbf{e}^\sigma + \mathbf{e}^u), \tag{30}$$

then $\gamma_{opt} = \tfrac{1}{4}$.

THREE-FIELD FINITE ELEMENT DISCRETIZATION

To construct a 3-field finite element approximation based on Π_γ^t, globally assume[*]

$$(\tilde{\mathbf{u}} = \mathbf{Nq})_V, \qquad (\tilde{\boldsymbol{\sigma}} = \mathbf{Aa})_V, \qquad [\tilde{\mathbf{t}} = \mathbf{Ss}]_{S_d} \tag{31}$$

Here matrices $\mathbf{N}$, $\mathbf{A}$ and $\mathbf{S}$ collect generalized displacement shape functions, internal stress modes and boundary traction modes, respectively, whereas column vectors $\mathbf{q}$, $\mathbf{a}$ and $\mathbf{s}$ collect generalized displacements[†], stress mode amplitudes, and surface traction amplitudes, respectively. The derived fields are

$$(\mathbf{e}^u = \mathbf{DNq} = \mathbf{Bq})_V, \qquad (\boldsymbol{\sigma}^u = \mathbf{EBq})_V, \qquad (\mathbf{e}^\sigma = \mathbf{E}^{-1}\tilde{\boldsymbol{\sigma}} = \mathbf{E}^{-1}\mathbf{Aa})_V. \tag{32}$$

Inserting these expressions into Π_γ^t we obtain the algebraic form

$$\Pi_\gamma^t(\mathbf{a},\mathbf{q},\mathbf{s}) = \tfrac{1}{2}(1-\gamma)\mathbf{q}^T\mathbf{K}_u\mathbf{q} - \tfrac{1}{2}\gamma\mathbf{a}^T\mathbf{Ca} + \gamma\mathbf{q}^T\mathbf{Qa} - \mathbf{q}^T\mathbf{f}_d - \mathbf{s}^T\mathbf{Rq} - \mathbf{s}^T\mathbf{f}_s. \tag{33}$$

---

[*] Following usual practice in finite element work, the components of $\boldsymbol{\sigma}$ and $\mathbf{e}$ will be arranged as column vectors whereas the moduli in $\mathbf{E}$ will be arranged as a square symmetric matrix.

[†] If $\mathbf{q}$ are nodal displacements, $\mathbf{N}$ contains conventional shape functions. But for the present study we need not specialize to that level.

The matrices K_u, C, Q and R that appear in (31) are called displacement-stiffness, compliance, leverage and boundary-dislocation matrices, respectively, and are given by

$$K_u = (B^T E B)_V, \quad C = (A^T E^{-1} A)_V, \quad Q = (B^T A)_V, \quad R = [S^T N]_{S_d} \qquad (34)$$

Both K_u and C are symmetric. The forcing vectors are

$$f_q = (N^T b)_V + [N^T \hat{t}]_{S_t}, \qquad f_s = -[S^T \hat{d}]_{S_d} \qquad (35)$$

Vector f_q contains generalized forces (conjugate to q) whereas f_s contains generalized displacements. Making (33) stationary yields the linear system

$$\begin{bmatrix} -\gamma C & \gamma Q^T & 0 \\ \gamma Q & (1-\gamma)K_u & -R^T \\ 0 & -R & 0 \end{bmatrix} \begin{Bmatrix} a \\ q \\ s \end{Bmatrix} = \begin{Bmatrix} 0 \\ f_q \\ f_s \end{Bmatrix} \qquad (36)$$

The first matrix equation is the discrete analog of $(e^u = e^\sigma)_V$ in (23) and expresses internal compatibility. The second one is the discrete analog of the next three relations, and expresses equilibrium. The last relation is the discrete analog of $[u = \hat{u}]_{S_d}$ and enforces boundary compatibility.

Since there is no force term on the first matrix equation, the stress amplitude vector a can be readily condensed out if C is nonsingular, and we get

$$\begin{bmatrix} K & -R^T \\ -R & 0 \end{bmatrix} \begin{Bmatrix} q \\ s \end{Bmatrix} = \begin{Bmatrix} f_q \\ f_s \end{Bmatrix} \qquad (37)$$

where

$$K = (1-\gamma)K_u + \gamma Q C^{-1} Q^T = (1-\gamma)K_u + \gamma K_\sigma \qquad (38)$$

is the *effective stiffness matrix*. This is a γ-weighted combination of the displacement-assumed stiffness matrix K_u and the stress-assumed stiffness matrix $K_\sigma = Q C^{-1} Q^T$. If the assumed displacements satisfy $[\tilde{u} = \hat{d}]_{S_d}$, the contribution from $(\tilde{t}, \tilde{u} - \hat{d})$ drops out and we simply have the conventional stiffness equations

$$Kq = f_q \qquad (39)$$

LIMITATION PRINCIPLE

The famous limitation principle of Fraeijs de Veubeke[5] takes on a particularly striking algebraic representation in terms of the parametrized matrix system (36). This principle applies when the derived stress field σ^u is contained in the assumed stress field $\tilde{\sigma}$:

$$\tilde{\sigma} \ni \sigma^u = E D \tilde{u} \qquad (40)$$

This inclusion can be expressed in matrix form as

$$\tilde{\sigma} = A a = E B a_q + A_x a_x = [EB \quad A_x] \begin{Bmatrix} a_q \\ a_x \end{Bmatrix} \qquad (41)$$

I-6

Here a_q contains the same number of entries as q whereas A_x contains "excess" stress modes. Inserting (41) into (36) and calling $Q_x = (B^T A_x)_V$ and $C_{xx} = (A_x^T E^{-1} A_x)_V$ we get

$$\begin{bmatrix} -\gamma K_u & -\gamma Q_x & \gamma K_u & 0 \\ -\gamma Q_x^T & -\gamma C_{xx} & \gamma Q_x^T & 0 \\ \gamma K_u & \gamma Q_x & (1-\gamma)K_u & -R^T \\ 0 & 0 & -R & 0 \end{bmatrix} \begin{Bmatrix} a_q \\ a_x \\ q \\ s \end{Bmatrix} = \begin{Bmatrix} 0 \\ 0 \\ f_q \\ f_s \end{Bmatrix} \tag{42}$$

The first two matrix equations give $a_q = q$ and $a_x = 0$. Dropping the equations associated with the extra stress modes reduces (42) to

$$\begin{bmatrix} -\gamma K_u & \gamma K_u & 0 \\ \gamma K_u & (1-\gamma)K_u & -R^T \\ 0 & -R & 0 \end{bmatrix} \begin{Bmatrix} q \\ q \\ s \end{Bmatrix} = \begin{Bmatrix} 0 \\ f_q \\ f_s \end{Bmatrix} \tag{43}$$

which obviously condenses to (37) with $K = K_u$ for any γ. The solution (q, a, s) becomes independent of γ. In other words, it is useless to inject additional degrees of freedom in the stresses beyond σ^u if the three-field variational principle is used. Furthermore, if $\sigma^u \equiv \tilde{\sigma}$ there is no point in using anything else than the potential energy principle $\gamma = 0$.

In fact the limitation principle expresses nothing more than the algebraic identity, valid for any γ,

$$\begin{bmatrix} -\gamma X & -\gamma Y & \gamma X \\ -\gamma Y^T & -\gamma Z & \gamma Y^T \\ \gamma X & \gamma Y & (1-\gamma)X \end{bmatrix} \begin{Bmatrix} x \\ 0 \\ x \end{Bmatrix} = \begin{Bmatrix} 0 \\ 0 \\ Xx \end{Bmatrix} \tag{44}$$

where X is symmetric and Y, Z arbitrary.

Constant Stress Assumption. If the derived field σ^u varies over V, assuming a constant stress field $\bar{\sigma}$ for $\tilde{\sigma}$ is a safe way to get around the limitation principle. In this case it is convenient to take $a \equiv \bar{\sigma}$ and $A = I$ (the identity matrix) in (31) so that $(\tilde{\sigma} = \bar{\sigma})_V$. Then the stress-assumed stiffness matrix is

$$\overline{K}_\sigma = v \overline{B}^T \overline{E}\, \overline{B} \tag{45}$$

where v denotes the total volume $v = (1)_V$, and $\overline{B}$ and $\overline{E}$ are the over-the-volume averages

$$\overline{B} = (B)_V / v, \qquad \overline{E}^{-1} = (E^{-1})_V / v \tag{46}$$

The effective stiffness matrix (38) is a weighted average of K_u and $\overline{K}_\sigma$. Since $\overline{K}_\sigma$ is typically rank deficient, $\gamma = 1$ is excluded.

TWO-FIELD FINITE ELEMENT DISCRETIZATION

If the relation $[t = \sigma_n]_S$ is imposed *a priori* as an essential boundary condition, t is no longer an independently varied field, and Π_γ^t becomes a two-field functional. The last finite element assumption of (31) is replaced by

$$[t^\sigma = \sigma_n = A_n a]_{S_d}, \tag{47}$$

where $\mathbf{A}_n$ denotes the normal projection of $\mathbf{A}$ on S_d, and the finite element equations become

$$\begin{bmatrix} -\gamma\mathbf{C} & \gamma(\mathbf{Q}+\mathbf{P})^T \\ \gamma(\mathbf{Q}+\mathbf{P}) & (1-\gamma)\mathbf{K_u} \end{bmatrix} \left\{ \begin{matrix} \mathbf{a} \\ \mathbf{q} \end{matrix} \right\} = \left\{ \begin{matrix} \mathbf{f}_a \\ \mathbf{f}_q \end{matrix} \right\}, \tag{48}$$

with

$$\mathbf{P} = [\mathbf{N}^T\mathbf{A}_n]_{S_d} \qquad \mathbf{f}_a = [\mathbf{N}^T\hat{\mathbf{d}}]_{S_d}. \tag{49}$$

A range analysis such as performed in the previous subsection reveals that the limitation principle does not generally apply if $[\mathbf{u} \neq \hat{\mathbf{d}}]_{S_d}$. The effect of the additional stress modes is to improve somewhat the satisfaction of boundary compatibility. But if the assumed displacements satisfy $[\mathbf{u} \neq \hat{\mathbf{d}}]_{S_d}$, $\mathbf{P}$ and $\mathbf{f}_a$ drop out and the limitation principle again holds.

TRACTION-CONNECTED ELEMENTS

The preceding results are relevant to the construction of conventional mixed elements, simply by treating each element as a body of volume V, and the element boundary as S. Continuity of displacements across interfaces is still required and results in traction/displacement element connectors s and *qbold*. If this continuity is relaxed by adding an additional boundary term, traction-connected mixed-hybrid elements result, for which displacement connectors (or simply generalized displacement amplitudes) q can be eliminated at the element level. As this type of hybrid elements is not so interesting as the displacement-connected ones, the topic is not pursued here.

OTHER PARAMETRIZATIONS

A one-parameter family of strain-displacement mixed variational principles derived from the Hu-Washizu functional (11) by eliminating the stress field can be represented as

$$\Pi_\beta^t(\tilde{\mathbf{u}},\tilde{\mathbf{e}},\tilde{\mathbf{t}}) = \tfrac{1}{2}(1-\beta)(\sigma^u,\mathbf{e}^u) - \tfrac{1}{2}\beta(\sigma^e,\tilde{\mathbf{e}})_V + \beta(\sigma^u,\mathbf{e}^u)_V - P^t, \tag{50}$$

where β is a scalar. For $\beta = 0$ we recover again Π_P^t whereas if $\beta = 1$ we obtain the Reissner-type strain-displacement principle listed in Oden and Reddy[3] generalized with an independent $\tilde{\mathbf{t}}$:

$$\Pi_S^t(\tilde{\mathbf{u}},\tilde{\mathbf{e}},\tilde{\mathbf{t}}) = -\tfrac{1}{2}(\sigma^e,\tilde{\mathbf{e}})_V + (\sigma^u,\mathbf{e}^u)_V - P^t. \tag{51}$$

Continuing along this path, a two-parameter, four-field family that embeds both Π_γ^t and Π_β^t is easily constructed as

$$\begin{aligned} \Pi_{\beta\gamma}^t(\tilde{\mathbf{u}},\tilde{\mathbf{e}},\tilde{\sigma},\tilde{\mathbf{t}}) = &\tfrac{1}{2}(1-\beta-\gamma)(\sigma^u,\mathbf{e}^u)_V + (1-\beta)\gamma\{(\tilde{\sigma},\mathbf{e}^u)_V - \tfrac{1}{2}(\tilde{\sigma},\mathbf{e}^\sigma)_V\} \\ &+ (1-\gamma)\beta\{(\sigma^e,\mathbf{e}^u)_V - \tfrac{1}{2}(\sigma^e,\tilde{\mathbf{e}})_V\} - P^t. \end{aligned} \tag{52}$$

This functional yields stress-displacement principles for $\beta = 0$ and strain-displacement principles for $\gamma = 0$. Finally, the Hu-Washizu principle itself may be embedded in a three-parameter form

$$\Pi_{\alpha\beta\gamma}^t = (1-\alpha)\Pi_W^t + \alpha\Pi_{\beta\gamma}^t \tag{53}$$

which obviously reduces to Π_W^t for $\alpha = 1$ and to $\Pi_{\beta\gamma}^t$ for $\alpha = 0$.

The superiority of one parametrized form variational principle over another as regards the construction of energy-balanced finite elements is not clear at this time.

CONCLUDING REMARKS

The parametrization (20) of the stress-displacement variational principles provide a unifying framework for the development of finite elements. This framework embodies the potential energy and Hellinger-Reissner principles. and encompasses displacement-assumed elements, conventional mixed elements and traction-connected hybrid elements. But it does not cover developments such as displacement-connected hybrid finite elements, incompatible elements and the free formulation[6] To accomplish that one has to continue the process by introducing a d-generalized version of (20), internal boundaries, internal-field energy-orthogonal splitting, and selective kinematic constraints. These extensions are covered in a sequel paper.[2]

ACKNOWLEDGEMENTS

REFERENCES

1. K. Washizu, *Variational Methods in Elasticity and Plasticity*, Pergamon Press, Oxford, 1968

2. C. A. Felippa, 'Parametrized Multifield Variational Principles in Elasticity: II. Hybrid Functionals and the Free Formulation,' following in this report.

3. J. T. Oden and J. N. Reddy, *Variational Methods in Theoretical Mechanics*, 2nd ed., Springer-Verlag, Berlin, 1983

4. M. Gurtin, 'The Linear Theory of Elasticity,' in Volume VIa/2 of *Encyclopedia of Physics*, ed. by C. Truesdell, Springer-Verlag, Berlin, 1972

5. B. M. Fraeijs de Veubeke, 'Displacement and Equilibrium Models in the Finite Element Method,' Ch. 9 in *Stress Analysis*, ed. by O. C. Zienkiewicz and G. Hollister, Wiley, London, 1965

6. P. G. Bergan and M. K. Nygård, 'Finite elements with increased freedom in choosing shape functions,' *Int. J. Num. Meth. Engrg.*, **20**, 1984, pp. 643–664

PARAMETRIZED MULTIFIELD VARIATIONAL PRINCIPLES IN ELASTICITY: II. HYBRID FUNCTIONALS AND THE FREE FORMULATION

CARLOS A. FELIPPA

Department of Aerospace Engineering Sciences
and Center for Space Structures and Controls
University of Colorado
Boulder, Colorado 80309-0429, USA

SUMMARY

A one-parameter family of d-generalized hybrid/mixed variational principles for linear elasticity is constructed following a domain subdivision. The family includes the d-generalized Hellinger-Reissner and potential energy as special cases. The parametrized principle is discretized by independently varied internal displacements, stresses, and boundary displacements. The resulting finite element equations are studied following a physically motivated decomposition of the stress and internal displacement fields. The free formulation of Bergan and Nygård is shown to be a special case of this element type, and is obtained by assuming a constant internal stress field. The parameter appears as a scale factor of the higher order stiffness.

INTRODUCTION

This paper continues a study, initiated in Part I[1], of parametrized stress-displacement variational principles in linear elastostatics. The boundary value problem is as follows. We consider an elastic body of volume V and surface $S : S_t \cup S_d$. Surface tractions $\hat{t}$ are prescribed on S_t whereas displacements $\hat{d}$ are prescribed on S_d. The internal (volume) fields are displacements u, stresses σ, strains e and given body forces b. The internal field equations are $e = Du$, $\sigma = Ee$ and $D^*\sigma = b$ in V, where $D = \frac{1}{2}(\nabla + \nabla^T)$, $D^* = -\text{div}$, and   is the elastic modulus operator. The boundary conditions are $u = \hat{d}$ on S_d and $\sigma_n = t$ on S.

The reader is referred to Part I[1] for additional notational conventions. Therein the following parametrized functional was introduced:

$$\Pi_\gamma^t(\tilde{u}, \tilde{\sigma}, \tilde{t}) = \tfrac{1}{2}(1-\gamma)(\sigma^u, e^u)_V - \tfrac{1}{2}\gamma(\tilde{\sigma}, e^\sigma)_V + \gamma(\tilde{\sigma}, e^u)_V - P^t, \qquad (1)$$

where γ is a scalar, and P^t is the forcing potential

$$P^t(\tilde{u}, \tilde{t}) = (b, \tilde{u})_V + [\tilde{t}, \tilde{u} - \hat{u}]_{S_d} + [\hat{t}, \tilde{u}]_{S_t}. \qquad (2)$$

In this functional the volume fields $\tilde{u}$, $\tilde{e}$, $\tilde{\sigma}$, and the surface field $\tilde{t}$ are subject to independent variations.

This functional "interpolates" the t-generalized Hellinger-Reissner and total potential energy functionals Π_R^t and Π_P^t, which are obtained for $\gamma = 1$ and $\gamma = 0$, respectively. The qualifier "t-generalized" means that the surface traction field $\tilde{t}$ is varied independently

whereas in the conventional form of those principles, the constraint $[t = \sigma_n]_S$ is enforced *a priori*.

INTERNAL INTERFACES

In the following subsection an alternative version of (1) is constructed, in which boundary displacements d can be varied independently rather than boundary tractions t. These displacement play the role of Lagrange multipliers that relax internal displacement continuity. Variational principles of this form will be called *d-generalized*.

The choice of d as independent field is *not* variationally admissible on S_d or S_t. We must therefore extend the definition of boundary to include *internal interfaces* collectively designated as S_i. Thus

$$S : S_d \cup S_t \cup S_i \tag{3}$$

On S_i neither displacements nor tractions are prescribed. A simple case is illustrated in Figure 1, in which the interface S_i divides V into two subvolumes: V^+ and V^-.
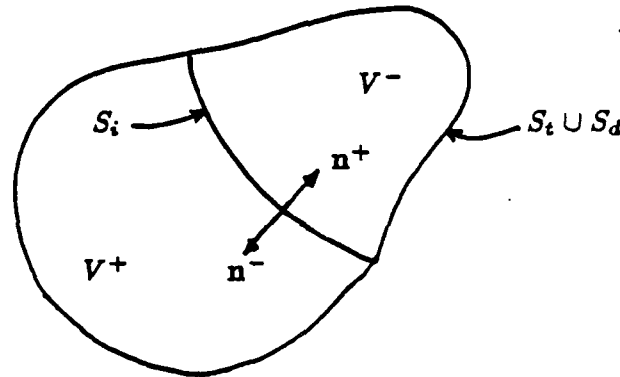
Figure 1. Internal interface example.

An interface such as S_i on Figure 1 has two "sides" called S_i^+ and S_i^-, which identify S_i viewed as boundary of V^+ and V^-, respectively. At smooth points of S_i the unit normals n^+ and n^- point in opposite directions.

The integral abbreviations of Part I generalize as follows, using Figure 1 for definiteness. A volume integral is the sum of integrals over the subvolumes:

$$(f)_V \stackrel{\text{def}}{=} \int_{V^+} f\, dV + \int_{V^-} f\, dV. \tag{4}$$

An integral over S_i includes two contributions:

$$[g]_{S_i} \stackrel{\text{def}}{=} \int_{S_i^+} g^+\, dS + \int_{S_i^-} g^-\, dS, \tag{5}$$

where g^+ and g^- denotes the value of the integrand g on S_i^+ and S_i^-, respectively. These two values may be different if g is discontinuous or involves a projection on the normals.

PARAMETRIZED d-GENERALIZED MIXED PRINCIPLE

Variational Principle. The d-generalized counterpart of Π_γ^t is

$$\Pi_\gamma^d(\tilde{u}, \tilde{\sigma}, \tilde{d}) = \tfrac{1}{2}(1-\gamma)(\sigma^u, e^u)_V - \tfrac{1}{2}\gamma(\tilde{\sigma}, e^\sigma)_V + \gamma(\tilde{\sigma}, e^u)_V - P^d. \tag{6}$$

This agrees with (1) except for the forcing potential, which is

$$P^d(\tilde{u}, \tilde{\sigma}, \tilde{d}) = (b, \tilde{u})_V + [\tilde{\sigma}_n, \tilde{u} - \hat{d}]_{S_d} + [\hat{t}, \tilde{u}]_{S_t} + [\tilde{\sigma}_n, \tilde{u} - \tilde{d}]_{S_i}. \tag{7}$$

Defining the γ-weighted stresses

$$\sigma^\gamma \overset{\text{def}}{=} \gamma\tilde{\sigma} + (1-\gamma)\sigma^u \quad \text{in } V, \qquad \sigma_n^\gamma \overset{\text{def}}{=} \gamma\tilde{\sigma}_n + (1-\gamma)\sigma_n^u \quad \text{on } S. \tag{8}$$

the first variation can be written

$$\begin{aligned}
\delta\Pi_\gamma^d = {} & \gamma\,(e^u - e^\sigma, \delta\tilde{\sigma})_V - (\operatorname{div}\sigma^\gamma + b, \delta\tilde{u})_V - \left[\hat{t} - \sigma_n^\gamma, \delta\tilde{u}\right]_{S_t} \\
& - [\tilde{\sigma}_n - \tilde{\sigma}_n^\gamma, \delta\tilde{u}]_{S_d} - \left[u - \hat{d}, \delta\tilde{\sigma}_n\right]_{S_d} \\
& - [\tilde{\sigma}_n - \tilde{\sigma}_n^\gamma, \delta\tilde{u}]_{S_i} - \left[\tilde{u} - \tilde{d}, \delta\tilde{\sigma}_n\right]_{S_i} - \left[\tilde{\sigma}_n, \delta\tilde{d}\right]_{S_i}
\end{aligned} \tag{9}$$

Since d is unique on S_i whereas $\check{u}$ and $\tilde{\sigma}$ are generally discontinuous on it, the interface integrals in (9) split as follows:

$$\begin{aligned}
\left[\tilde{\sigma}_n - \tilde{\sigma}_n^\gamma, \delta\tilde{u}\right]_{S_i} &= \left[\tilde{\sigma}_n^+ - \tilde{\sigma}_n^{\gamma+}, \delta\tilde{u}^+\right]_{S_i^+} + \left[\tilde{\sigma}_n^- - \tilde{\sigma}_n^{\gamma-}, \delta\tilde{u}^-\right]_{S_i^-} \\
\left[\tilde{u} - \tilde{d}, \delta\tilde{\sigma}\right]_{S_i} &= \left[\tilde{u}^+ - \tilde{d}, \delta\tilde{\sigma}_n^+\right]_{S_i^+} + \left[\tilde{u}^- - \tilde{d}, \delta\tilde{\sigma}_n^-\right]_{S_i^-} \\
\left[\tilde{\sigma}_n, \delta\tilde{d}\right]_{S_i} &= \left[\tilde{\sigma}_n^+, \delta\tilde{d}\right]_{S_i^+} + \left[\tilde{\sigma}_n^-, \delta\tilde{d}\right]_{S_i^-} = \left[\tilde{\sigma}_n^+ - \tilde{\sigma}_n^-, \delta\tilde{d}\right]_{S_i}
\end{aligned} \tag{10}$$

Setting the first variation to zero and taking (10) into account, the Euler equations and natural boundary conditions for $\gamma \neq 0$ are found to be

$$\begin{aligned}
& (e^u = e^\sigma)_V, \quad (\operatorname{div}\sigma^\gamma + b = 0)_V, \quad [\sigma_n^\gamma = \hat{t}]_{S_t}, \quad [\sigma_n = \sigma_n^\gamma]_{S_d}, \quad [u = \hat{d}]_{S_d}, \\
& [\sigma_n^{\gamma+} + \sigma_n^+ = 0]_{S_i}, \quad [\sigma_n^{\gamma-} + \sigma_n^- = 0]_{S_i}, \quad [u^+ = u^- = d]_{S_i}, \quad [\sigma_n^+ + \sigma_n^- = 0]_{S_i}.
\end{aligned} \tag{11}$$

If $\gamma = 0$ the first equation, $(e^u = e^\sigma)_V$, drops out.

Modified Forcing Potential. Substituting d in lieu of u in the potential (7)

$$P^d(\tilde{u}, \tilde{\sigma}, \tilde{d}) = (b, \tilde{u})_V + [\tilde{\sigma}_n, \tilde{d} - \hat{d}]_{S_d} + [\hat{t}, \tilde{d}]_{S_t} + [\tilde{\sigma}_n, \tilde{u} - \tilde{d}]_{S_i}. \tag{12}$$

is *not* variationally admissible because incorrect Euler equations result. This form has appeared, however, in publications dealing with mixed-hybrid methods. A correct potential

that resembles (12) can be obtained in two stages. First, surface terms $[\tilde{\sigma}_n, \tilde{u} - \check{d}]_{S_t}$ and $[\tilde{\sigma}_n, \tilde{u} - \check{d}]_{S_d}$ are added and subtracted to produce

$$P^d(\tilde{u}, \tilde{\sigma}, \check{d}) = (b, \tilde{u})_V + [\tilde{\sigma}_n, \check{d} - \hat{d}]_{S_d} + [\tilde{\sigma}_n - \hat{t}, \tilde{u}]_{S_t} + [\hat{t}, \check{d}]_{S_t} + [\tilde{\sigma}_n, \tilde{u} - \check{d}]_S. \qquad (13)$$

Second, $\hat{t}$ is assumed to be in the range of $\tilde{\sigma}_n$ and the condition $[\tilde{\sigma}_n = \hat{t}]_{S_t}$ satisfied *a priori*, reducing (13) to

$$P^d(\tilde{u}, \tilde{\sigma}, \check{d}) = (b, \tilde{u})_V + [\tilde{\sigma}_n, \check{d} - \hat{d}]_{S_d} + [\hat{t}, \check{d}]_{S_t} + [\tilde{\sigma}_n, \tilde{u} - \check{d}]_S. \qquad (14)$$

This expression differs from (12) in that the all-important surface dislocation integral is taken over S rather than S_i. Further simplification results if the displacement boundary conditions $[\check{d} = \hat{d}]_{S_d}$ are exactly satisfied:

$$P^d(\tilde{u}, \tilde{\sigma}, \check{d}) = (b, \tilde{u})_V + [\hat{t}, \check{d}]_{S_t} + [\tilde{\sigma}_n, \tilde{u} - \check{d}]_S. \qquad (15)$$

This expression of P^d is used in the sequel, as modifications required to account for the case $[\check{d} \neq \hat{d}]_{S_d}$ are of minor importance.

FINITE ELEMENT APPROXIMATIONS

In this section the finite element discretization of Π_γ^d is studied. Assume formally

$$(\tilde{u} = Nq)_V, \qquad (\tilde{\sigma} = Aa)_V, \qquad [\check{d} = Vv]_S. \qquad (16)$$

Here matrices N, A and V collect generalized-displacement shape functions, internal stress modes and interface displacement modes, respectively, whereas column vectors q, a and v collect generalized internal displacements, stress mode amplitudes, and generalized interface displacements, respectively. The assumed volume fields need not be continuous across S. The derived fields are

$$(e^u = DNq = Bq)_V, \quad (\sigma^u = EBq)_V, \quad (e^\sigma = E^{-1}\tilde{\sigma} = E^{-1}Aa)_V. \qquad (17)$$

Inserting these expressions into Π_γ^d with the forcing potential (15), we obtain the algebraic form

$$\Pi_\gamma^d(a, q, s) = \tfrac{1}{2}(1 - \gamma)q^T K_u q - \tfrac{1}{2}\gamma a^T Ca + \gamma q^T Qa - q^T Pa + v^T La - q^T f_q - v^T f_v. \qquad (18)$$

where

$$\begin{aligned} K_u &= (B^T EB)_V = K_u^T, \qquad C = (A^T E^{-1} A)_V = C^T, \qquad Q = (B^T A)_V, \\ L &= [V^T A_n]_S, \qquad P = [N^T A_n]_S, \qquad f_q = (N^T b)_V, \qquad f_v = [N^T \hat{t}]_{S_t}. \end{aligned} \qquad (19)$$

The matrices K_u, C, Q, L and P are called internal-displacement-stiffness, compliance, leverage, force-lumping, and boundary dislocation matrices, respectively. Making (18) stationary yields the linear system

$$\begin{bmatrix} -\gamma C & \gamma Q^T - P^T & L^T \\ \gamma Q - P & (1 - \gamma)K_u & 0 \\ L & 0 & 0 \end{bmatrix} \begin{Bmatrix} a \\ q \\ v \end{Bmatrix} = \begin{Bmatrix} 0 \\ f_q \\ f_v \end{Bmatrix} \qquad (20)$$

The first matrix equation is the discrete analog of the first, fifth and eight relations in (11), and expresses internal and boundary compatibility. The third equation is the discrete analog of the last relation, and expresses equilibrium across S_i. The second one is the discrete analog of the remaining relations, and expresses internal and boundary equilibrium.

Stress Condensation. If C is nonsingular, the stress amplitude vector a can be statically condensed from (20), giving

$$\begin{bmatrix} \mathbf{K}_q & \mathbf{K}_{qv}^T \\ \mathbf{K}_{qv} & \gamma^{-1}\mathbf{K}_v \end{bmatrix} \begin{Bmatrix} \mathbf{q} \\ \mathbf{v} \end{Bmatrix} = \begin{Bmatrix} \mathbf{f}_q \\ \mathbf{f}_v \end{Bmatrix} \tag{21}$$

in which

$$\mathbf{K}_q = (1-\gamma)\mathbf{K}_u + \gamma \mathbf{Q}\mathbf{C}^{-1}\mathbf{Q}^T - (\mathbf{P}\mathbf{C}^{-1}\mathbf{Q}^T + \mathbf{Q}\mathbf{C}^{-1}\mathbf{P}^T) + \gamma^{-1}\mathbf{P}\mathbf{C}^{-1}\mathbf{P}^T$$
$$\mathbf{K}_{qv} = \mathbf{L}\mathbf{C}^{-1}\left(\mathbf{Q}^T - \gamma^{-1}\mathbf{P}^T\right), \qquad \mathbf{K}_v = \mathbf{L}\mathbf{C}^{-1}\mathbf{L}^T. \tag{22}$$

The coefficient submatrices will be identified as follows: $\mathbf{K}_q$ is the internal stiffness matrix, $\mathbf{K}_b$ is the boundary stiffness matrix, and $\mathbf{K}_{qv}$ is a internal-boundary coupling stiffness. The internal stiffness is similar but not identical to the effective stiffness matrix of t-generalized mixed principles[1]. We now proceed to reinterpret these results in terms of hybrid elements.

HYBRID ELEMENTS

Approach. The preceding treatment is relevant to the construction of *displacement-connected hybrid elements*. Hybrid elements based on more restricted assumptions were originally constructed by Pian and coworkers[2-4]. The principal features of the hybrid approach are:

(I) The domain is subdivided into elements *before* the variational principle is established.

(II) Continuity requirements across element boundaries are relaxed by introducing boundary tractions or boundary displacements as Lagrange multiplier fields.

(III) All stress and internal-displacement degrees of freedom are eliminated (by either static condensation or kinematic constraints) at the *element level.*

Feature (I) says that hybrid functionals are effectively *mesh-dependent*, since the domain subdivision process introduces element boundaries which must be treated as *internal interfaces*, and therefore become part of the boundary portion S_i. Previous developments remain valid if we reinterpret "body" as "individual element," "volume" as "element volume," and "surface" as "interelement boundary."

Continuity and Connectors. The internal fields $\tilde{\sigma}$ and $\tilde{\mathbf{u}}$ may be discontinuous across elements. The boundary displacement field $\tilde{\mathbf{d}}$, however, must be continuous on S_i, *i.e.* it must have the same value on adjacent elements. This conditions may be satisfied if $\tilde{\mathbf{d}}$ on an interface separating two elements *is uniquely interpolated by nodal values on that interface.* It is natural to take such nodal values as entries of $\mathbf{v}$, which automatically becomes the vector of *connected node displacements* or *connectors*.

FIELD DECOMPOSITION

In this and subsequent sections we work with an *individual element* unless otherwise noted. The element volume is V and the element surface is $S : S_d \cup S_t \cup S_i$. The $\mathbf{v}$ subvector contains the element-connector degrees of freedom, whereas $\mathbf{q}$ and $\mathbf{a}$ contain internal freedoms. To gain further insight into the structure of the element equations and to link up eventually with the free formulation, we proceed to decompose both internal element fields as follows.

Stress Decomposition. The assumed stress field, $\tilde{\sigma}$, is decomposed into a mean value, $\bar{\sigma}$, and a deviator:

$$\tilde{\sigma} = \bar{\sigma} + \sigma_h = \bar{\sigma} + \mathbf{A}_h \mathbf{a}_h, \tag{23}$$

in which

$$\bar{\sigma} = (\tilde{\sigma})_V / v, \qquad (\mathbf{A}_h)_V = 0, \tag{24}$$

where $v = (1)_V$ denotes the element volume. The second relation in (24) is obtained by integrating (23) over V and noting that $\mathbf{a}_h$ is arbitrary.

Internal Displacement Decomposition. Next, the $\tilde{\mathbf{u}}$ assumption is decomposed into rigid body, constant strain, and higher order displacements:

$$\tilde{\mathbf{u}} = \mathbf{N}_r \mathbf{q}_r + \mathbf{N}_c \mathbf{q}_c + \mathbf{N}_h \mathbf{q}_h. \tag{25}$$

Applying the strain operator $\mathbf{D} = \frac{1}{2}(\nabla + \nabla^T)$ to $\tilde{\mathbf{u}}$ we get the associated strain field:

$$\mathbf{e}^u = \mathbf{D}\mathbf{N}_r \mathbf{q}_r + \mathbf{D}\mathbf{N}_c \mathbf{q}_c + \mathbf{D}\mathbf{N}_h \mathbf{q}_h = \mathbf{B}_r \mathbf{q}_r + \mathbf{B}_c \mathbf{q}_c + \mathbf{B}_h \mathbf{q}_h. \tag{26}$$

But $\mathbf{B}_r = \mathbf{D}\mathbf{N}_r$ vanishes because $\mathbf{N}_r$ contains only rigid-body modes. We are also free to select $\mathbf{B}_c = \mathbf{D}\mathbf{N}_c$ to be the identity matrix $\mathbf{I}$ if the generalized coordinates $\mathbf{q}_c$ are identified with the mean (volume-averaged) strain values $\bar{\mathbf{e}}^u$. Then (26) simplifies to

$$\mathbf{e}^u = \bar{\mathbf{e}}^u + \mathbf{e}_h^u = \bar{\mathbf{e}}^u + \mathbf{B}_h \mathbf{q}_h, \tag{27}$$

in which

$$\mathbf{q}_c = \bar{\mathbf{e}}^u = (\mathbf{e}^u)_V / v, \qquad (\mathbf{B}_h)_V = 0. \tag{28}$$

Equation Partitioning. Assume that all elastic moduli in $\mathbf{E}$ are *constant* over the element. The degree of freedom partition

$$\mathbf{a} = \left\{ \begin{array}{c} \bar{\sigma} \\ \mathbf{a}_h \end{array} \right\}, \qquad \mathbf{q} = \left\{ \begin{array}{c} \mathbf{q}_r \\ \bar{\mathbf{e}}^u \\ \mathbf{q}_h \end{array} \right\}, \tag{29}$$

II-6

induces the following partition of the element equations

$$
\begin{bmatrix}
-\gamma v \mathbf{E}^{-1} & 0 & -\overline{\mathbf{P}}_r^T & \gamma v \mathbf{I} - \overline{\mathbf{P}}_c^T & -\overline{\mathbf{P}}_h^T & \overline{\mathbf{L}}^T \\
0 & -\gamma \mathbf{C}_h & -\mathbf{P}_{hr}^T & -\mathbf{P}_{hc}^T & \gamma \mathbf{Q}_h^T - \mathbf{P}_{hh}^T & \mathbf{L}_h^T \\
-\overline{\mathbf{P}}_r & \mathbf{P}_{hr} & 0 & 0 & 0 & 0 \\
\gamma v \mathbf{I} - \overline{\mathbf{P}}_c & \mathbf{P}_{hc} & 0 & (1-\gamma)v\mathbf{E} & 0 & 0 \\
-\overline{\mathbf{P}}_h & \gamma \mathbf{Q}_h - \mathbf{P}_{hh} & 0 & 0 & (1-\gamma)\mathbf{K}_{qh} & 0 \\
-\overline{\mathbf{L}} & -\mathbf{L}_h & 0 & 0 & 0 & 0
\end{bmatrix}
\begin{Bmatrix}
\bar{\sigma} \\ \mathbf{a}_h \\ \mathbf{q}_r \\ \bar{\mathbf{e}}^u \\ \mathbf{q}_h \\ \mathbf{v}
\end{Bmatrix}
=
\begin{Bmatrix}
0 \\ 0 \\ \mathbf{f}_{qr} \\ \mathbf{f}_{qc} \\ \mathbf{f}_{qh} \\ \mathbf{f}_v
\end{Bmatrix}
$$

(30)

where

$$
\mathbf{C}_h = (\mathbf{A}_h^T \mathbf{E}^{-1} \mathbf{A}_h)_V, \qquad \mathbf{Q}_h = (\mathbf{B}_h^T \mathbf{A}_h)_V, \qquad \mathbf{K}_{qh} = (\mathbf{B}_h^T \mathbf{E} \mathbf{B}_h)_V,
$$

$$
\overline{\mathbf{P}}_x = \left[\mathbf{N}_{xn}^T\right]_S, \quad x = r,c,h, \qquad \mathbf{P}_{hx} = \left[\mathbf{N}_x^T \mathbf{A}_{hn}\right]_S, \quad x = r,c,h
$$

(31)

$$
\overline{\mathbf{L}} = [\mathbf{V}_n^T]_S, \qquad \mathbf{L}_h = [\mathbf{V}^T \mathbf{A}_{hn}]_S, \qquad \mathbf{f}_{qx} = (\mathbf{N}_x^T \mathbf{b})_V, \quad x = r,c,h
$$

Integral transformations. Application of the divergence theorem to the work of the mean stress on $\mathbf{e}^u$ yields

$$
(\bar{\sigma}, \mathbf{e}^u)_V = (\bar{\sigma}, \bar{\mathbf{e}}^u + \mathbf{B}_h \mathbf{q}_h)_V = v \bar{\sigma}^T \bar{\mathbf{e}}^u + \bar{\sigma}^T (\mathbf{B}_h)_V \mathbf{q}_h = v \bar{\sigma}^T \bar{\mathbf{e}}^u
$$
$$
= [\bar{\sigma}_n, \tilde{\mathbf{u}}]_S = [\bar{\sigma}_n, \mathbf{N}_r \mathbf{q}_r + \mathbf{N}_c \bar{\mathbf{e}}^u + \mathbf{N}_h \mathbf{q}_h]_S = \bar{\sigma}^T (\overline{\mathbf{P}}_r \mathbf{q}_r + \overline{\mathbf{P}}_c \bar{\mathbf{e}}^u + \overline{\mathbf{P}}_h \mathbf{q}_h).
$$

(32)

Hence,

$$
\overline{\mathbf{P}}_r = 0, \qquad \overline{\mathbf{P}}_c = v\mathbf{I}, \qquad \overline{\mathbf{P}}_h = 0.
$$

(33)

A similar analysis of the stress-deviator work $(\sigma_h, \mathbf{e}^u)_V$ does not yield simple forms for the $\mathbf{P}_{hx}$ matrices unless σ_h is *divergence-free*, in which case

$$
\mathbf{P}_{hr} = 0, \qquad \mathbf{P}_{hc} = 0, \qquad \mathbf{P}_{hh} = \mathbf{Q}_h.
$$

(34)

Assuming (34) to hold, the element equations (30) simplify to

$$
\begin{bmatrix}
-\gamma v \mathbf{E}^{-1} & 0 & 0 & -(1-\gamma)v\mathbf{I} & 0 & \overline{\mathbf{L}}^T \\
0 & -\gamma \mathbf{C}_h & 0 & 0 & -(1-\gamma)\mathbf{Q}_h^T & \mathbf{L}_h^T \\
0 & 0 & 0 & 0 & 0 & 0 \\
-(1-\gamma)v\mathbf{I} & 0 & 0 & (1-\gamma)v\mathbf{E} & 0 & 0 \\
0 & -(1-\gamma)\mathbf{Q}_h & 0 & 0 & (1-\gamma)\mathbf{K}_{qh} & 0 \\
-\overline{\mathbf{L}} & -\mathbf{L}_h & 0 & 0 & 0 & 0
\end{bmatrix}
\begin{Bmatrix}
\bar{\sigma} \\ \mathbf{a}_h \\ \mathbf{q}_r \\ \bar{\mathbf{e}}^u \\ \mathbf{q}_h \\ \mathbf{v}
\end{Bmatrix}
=
\begin{Bmatrix}
0 \\ 0 \\ \mathbf{f}_{qr} \\ \mathbf{f}_{qc} \\ \mathbf{f}_{qh} \\ \mathbf{f}_v
\end{Bmatrix}
$$

(35)

The stress freedoms $\bar{\sigma}$ and $\mathbf{a}_h$ may be eliminated by static condensation as before. To eliminate $\mathbf{q}_r$, a kinematic transformation that uniquely determines the rigid body motion from the element interface motion is constructed:

$$
\mathbf{q}_r = \mathbf{H}_r \mathbf{v}
$$

(36)

II-7

where $\mathbf{H}_r$ is a rectangular matrix derived in Appendix 1. Elimination of $\bar{\sigma}$, a_h and q_r gives

$$\begin{bmatrix} \frac{1-\gamma}{\gamma} v\mathbf{E} & \mathbf{0} & -\frac{1-\gamma}{\gamma}\mathbf{E}\overline{\mathbf{L}}^T \\ \mathbf{0} & (1-\gamma)\mathbf{K}_{qh} + \gamma\mathbf{K}_{\sigma h} & \mathbf{K}_{qvh}^T \\ -\frac{1-\gamma}{\gamma}\overline{\mathbf{L}}\mathbf{E} & \mathbf{K}_{qvh} & \gamma^{-1}\mathbf{K}_v \end{bmatrix} \begin{Bmatrix} \bar{\mathbf{e}}^u \\ \mathbf{q}_h \\ \mathbf{v} \end{Bmatrix} = \begin{Bmatrix} \mathbf{f}_{qc} \\ \mathbf{f}_{qh} \\ \mathbf{f}_v + \mathbf{H}_r^T\mathbf{f}_{qr} \end{Bmatrix} \tag{37}$$

where

$$\mathbf{K}_{\sigma h} = \mathbf{Q}_h\mathbf{C}_h^{-1}\mathbf{Q}_h^T, \quad \mathbf{K}_{qvh} = \mathbf{L}_h\mathbf{C}_h^{-1}\mathbf{Q}_h^T, \quad \mathbf{K}_v = \overline{\mathbf{K}}_v + \mathbf{K}_{vh},$$
$$\overline{\mathbf{K}}_v = v^{-1}\overline{\mathbf{L}}\mathbf{E}\overline{\mathbf{L}}^T, \qquad \mathbf{K}_{vh} = \mathbf{L}_h\mathbf{C}_h^{-1}\mathbf{L}_h^T \tag{38}$$

Mean Strain Elimination. Subvector $\bar{\mathbf{e}}^u$ may be eliminated in two ways. Static condensation produces

$$\begin{bmatrix} (1-\gamma)\mathbf{K}_{qh} + \gamma\mathbf{K}_{\sigma h} & \mathbf{K}_{qvh}^T \\ \mathbf{K}_{qvh} & \overline{\mathbf{K}}_v + \gamma^{-1}\mathbf{K}_{vh} \end{bmatrix} \begin{Bmatrix} \mathbf{q}_h \\ \mathbf{v} \end{Bmatrix} = \begin{Bmatrix} \mathbf{f}_{qh} \\ \mathbf{f}_v + \mathbf{H}_r^T\mathbf{f}_{qr} + v^{-1}\overline{\mathbf{L}}^T\mathbf{f}_{qc} \end{Bmatrix} \tag{39}$$

On the other hand, if $\bar{\mathbf{e}}^u$ is eliminated through the kinematic constraint $\bar{\mathbf{e}}^u = \mathbf{H}_c\mathbf{v}$ derived in Appendix 1,

$$\begin{bmatrix} (1-\gamma)\mathbf{K}_{qh} + \gamma\mathbf{K}_{\sigma h} & \mathbf{K}_{qvh}^T \\ \mathbf{K}_{qvh} & \mathbf{K}_v' + \gamma^{-1}\mathbf{K}_{vh} \end{bmatrix} \begin{Bmatrix} \mathbf{q}_h \\ \mathbf{v} \end{Bmatrix} = \begin{Bmatrix} \mathbf{f}_{qh} \\ \mathbf{f}_v + \mathbf{H}_r^T\mathbf{f}_{qr} + \mathbf{H}_c^T\mathbf{f}_{qc} \end{Bmatrix} \tag{40}$$

where

$$\mathbf{K}_v' = \gamma^{-1}\overline{\mathbf{K}}_v + \frac{1-\gamma}{\gamma}\left(v\mathbf{H}_c^T\mathbf{E}\mathbf{H}_c - \mathbf{H}_c^T\mathbf{E}\overline{\mathbf{L}}^T - \overline{\mathbf{L}}\mathbf{E}\mathbf{H}_c\right) \tag{41}$$

The two methods produce identical results if

$$\mathbf{H}_c = v^{-1}\overline{\mathbf{L}}^T \tag{42}$$

As discussed in Appendix 1, this relation may be obtained from the first matrix equation in (35) if either $\gamma = 0$, or $\mathbf{e}^u = \bar{\mathbf{e}}^\sigma = \mathbf{E}^{-1}\bar{\sigma}$. The last condition is obtained in the limit of a converged solution as the patch test analysis of Appendix 2 shows. In practice any difference between (39) and (40) for $\gamma \neq 0$ is not practically significant, and (39) is preferable on grounds of simplicity.

THE FREE FORMULATION

The free formulation of Bergan and Nygård[5] was originally constructed as an incompatible displacement model that passes a cancelling-tractions version of the patch test which Bergan and Hanssen called the individual patch test[6]. Here the formulation is reinterpreted in the context of a displacement-connected hybrid variational principle.

II-8

First, assume that the internal stress field is *constant*, so there are no a_h parameters. Then (39) reduces to

$$\begin{bmatrix} (1-\gamma)\mathbf{K}_{qh} & \mathbf{0} \\ \mathbf{0} & \overline{\mathbf{K}}_b \end{bmatrix} \begin{Bmatrix} \mathbf{q}_h \\ \mathbf{v} \end{Bmatrix} = \begin{Bmatrix} \mathbf{f}_{qh} \\ \mathbf{f}_v + \mathbf{H}_r^T \mathbf{f}_{qr} + \upsilon^{-1}\overline{\mathbf{L}}\mathbf{f}_{qc} \end{Bmatrix} \quad (43)$$

The equations for $\mathbf{q}_h$ uncouple. Consequently static condensation of $\mathbf{q}_h$ will not change the solution. We have run into a displacement limitation principle. This leads to the second assumption: the higher order internal displacement modes are eliminated by kinematic constraints that link $\mathbf{q}_h$ to the boundary displacements:

$$\mathbf{q}_h = \mathbf{H}_h\mathbf{v} \quad (44)$$

Matrix $\mathbf{H}_h$ is derived in Appendix 1. Application of this constraint to (43) produces the final stiffness equations

$$\mathbf{K}\mathbf{v} = [\mathbf{K}_b + (1-\gamma)\mathbf{K}_h]\,\mathbf{v} = \mathbf{f} \quad (45)$$

where

$$\mathbf{K}_b = \overline{\mathbf{K}}_v, \qquad \mathbf{K}_h = \mathbf{H}_h^T\mathbf{K}_{qh}\mathbf{H}_h, \qquad \mathbf{f} = \mathbf{f}_v + \mathbf{H}_r^T\mathbf{f}_{qr} + \upsilon^{-1}\overline{\mathbf{L}}\mathbf{f}_{qc} + \mathbf{H}_h\mathbf{f}_{qh}. \quad (46)$$

In the free formulation, $\mathbf{K}_b$ and $\mathbf{K}_h$ receive the name *basic* and *higher order* stiffness matrices, respectively. A $\frac{1}{2}$ scaling derived from energy-balancing studies of $\mathbf{K}_h$ was recommended by Bergan and Felippa[7] for a plane stress element This corresponds to taking $\gamma = \frac{1}{2}$.

CONCLUDING REMARKS

It has been known[7] that the *basic-stiffness* part of the free formulation can be interpreted as a constant-stress hybrid element. But the interpretation of the higher order stiffness within a variational framework has been difficult. A key result of this paper is that this can be accomplished by a *parametrized* mixed-hybrid variational principle. Note that the free formulation cannot be obtained within the conventional Hellinger-Reissner principle ($\gamma = 1$), since then the higher-order stiffness vanishes and $\mathbf{K} = \overline{\mathbf{K}}_v$ is generally rank-deficient. And taking $\gamma = 0$ does not account for the fact that the higher order stiffness can be scaled by a nonzero coefficient.

The variational framework is important because it allows consistent extensions of the free formulation that are not obvious from a physical standpoint. For example: allowing more internal displacement degrees of freedom than boundary freedoms, i.e. $m = \dim(\mathbf{q}) - \dim(\mathbf{v}) > 0$. A glance at (39) shows that m additional higher-order divergence-free stress fields have to be retained so that the coupling stiffness $\mathbf{K}_{qvh}$ does not vanish. The reduction of $\mathbf{q}_h$ can be then performed by a combination of static condensation and kinematic constraints.

ACKNOWLEDGEMENTS

REFERENCES

1. C. A. Felippa, 'Parametrized Multifield Variational Principles in Elasticity: I. Mixed Functionals,' preceding in this report.

2. T. H. H. Pian, 'Derivation of element stiffness matrices by assumed stress distributions,' *AIAA Journal*, 2, pp. 1333–1336, 1964

3. T. H. H. Pian and P. Tong, 'Basis of finite element methods for solid continua,' *Int. J. Numer. Meth. Engrg.*, 1, pp. 3–29, 1969

4. T. H. H. Pian, 'Finite element methods by variational principles with relaxed continuity requirements,' in *Variational Methods in Engineering*, Vol. 1, (ed. by C. A. Brebbia and H. Tottenham), Southampton University Press, 1973

5. P. G. Bergan and M. K. Nygård, 'Finite elements with increased freedom in choosing shape functions,' *Int. J. Num. Meth. Engrg.*, 20, 1984, pp. 643–664

6. P. G. Bergan and L. Hanssen, A new approach for deriving "good" finite elements, MAFE-LAP II Conference, Brunel University, 1975, in *The Mathematics of Finite Elements and Applications – Volume II*, ed. by J. R. Whiteman, Academic Press, London, 1976

7. P. G. Bergan and C. A. Felippa, 'A Triangular Membrane Element with Rotational Degrees of Freedom,' *Computer Methods in Applied Mechanics & Engineering*, 50, 1985, pp. 25–69

8. P. G. Bergan, "Finite Elements Based on Energy Orthogonal Functions," *Int. J. Num. Meth. Engrg.*, 15, 1980, pp. 1141–1555

9. B. M. Fraeijs de Veubeke, 'Variational Formulation and the Patch Test,' *Int. J. Num. Meth. Engrg*, 8, pp. 783–801, 1974

APPENDIX 1: KINEMATIC CONSTRAINTS

One of the principal assumptions invoked in the free formulation is that the dimension of q is the same as that of v and that the latter are physical node displacements. If so, evaluation of the expansion $\tilde{u} = Nq$ on the element boundary S establishes the transformation

$$v = Gq \tag{47}$$

where matrix G is square. Furthermore, suppose that G is *nonsingular* and can be inverted:

$$q = G^{-1}v = Hv, \tag{48}$$

or, in partitioned form

$$q = \left\{ \begin{array}{c} q_r \\ q_o \\ q_h \end{array} \right\} = \left[\begin{array}{c} H_r \\ H_o \\ H_h \end{array} \right] v. \tag{49}$$

The first matrix equation (the discrete compatibility equation) in (20) can be presented as

$$\gamma(e^* - e^\sigma, A)_V = L^T v - Q^T q = (L^T - Q^T H)v = (L^T G - Q^T)q. \tag{50}$$

Setting $\gamma = 0$ forces the constraint

$$L^T = Q^T H \quad \text{or} \quad L^T G = Q^T \tag{51}$$

to be satisfied. The same constraint emerges if $\gamma \neq 0$ and the finite element solution has converged in the sense that $e^* = e^\sigma$ is constant over the element. Now carrying out the freedom partition (29) and assuming divergence-free higher order stresses so that (34) holds, the constraint (51) partitions as

$$\begin{bmatrix} \overline{\mathbf{L}}^T \\ \mathbf{L}_h^T \end{bmatrix} = \begin{bmatrix} 0 & v\mathbf{I} & 0 \\ 0 & 0 & \mathbf{Q}_h^T \end{bmatrix} \begin{bmatrix} \mathbf{H}_r \\ \mathbf{H}_c \\ \mathbf{H}_h \end{bmatrix} \quad \text{or} \quad \begin{bmatrix} \overline{\mathbf{L}}^T \\ \mathbf{L}_h^T \end{bmatrix} [\mathbf{G}_r \quad \mathbf{G}_c \quad \mathbf{G}_h] = \begin{bmatrix} 0 & v\mathbf{I} & 0 \\ 0 & 0 & \mathbf{Q}_h^T \end{bmatrix}. \tag{52}$$

from which follow the relations

$$\begin{array}{llll} \overline{\mathbf{L}}^T \mathbf{G}_r = 0, & \overline{\mathbf{L}}^T \mathbf{G}_c = v\mathbf{I}, & \overline{\mathbf{L}}^T = v\mathbf{H}_c, & \overline{\mathbf{L}}^T \mathbf{G}_h = 0, \\ \mathbf{L}_h^T \mathbf{G}_r = 0, & \mathbf{L}_h^T \mathbf{G}_c = 0, & \mathbf{L}_h^T = v\mathbf{H}_h, & \mathbf{L}_h^T \mathbf{G}_h = \mathbf{I}. \end{array} \tag{53}$$

The first four were obtained through other means by Bergan[8] and Bergan and Nygård[5], who called them the *force orthogonality* conditions on account of the physical interpretation of $\overline{\mathbf{L}}$ as a "boundary nodal force lumping" matrix.

APPENDIX 2: THE CANCELLING-TRACTIONS PATCH TEST

It is not apparent whether this element class passes the patch test for an arbitrary γ. To investigate this question we use the sketch of Figure 1 and view the subvolumes V^+ and V^- as *two elements* connected along S_i with an external traction boundary S_t. Both elements are in a state of *constant stress* σ_0. The prescribed surface tractions are $[\hat{t} = \sigma_{0n}]_{S_t}$ and the body forces b vanish. We take (35) to be the governing equations for the two-element assembly. The only nonzero forces are $f_v = [\mathbf{V}^T \hat{t}]_{S_t}$. The key observation is that

$$\overline{\mathbf{L}} = [\mathbf{V}_n^T]_S = [\mathbf{V}_n^T]_{S_t}, \tag{54}$$

because the integral over S_i vanishes because $\mathbf{V}$ is identical for both elements on account of interface compatibility conditions, and $n^+ = -n^-$. Similarly for L_h. One may verify that for any γ the solution of (35) is

$$\bar{\sigma} = \sigma_0 = \bar{\sigma}^*, \qquad a_h = 0, \qquad \bar{e}^* = v^{-1}\overline{\mathbf{L}}^T v, \qquad q_h = 0. \tag{55}$$

The connector node displacement vector v satisfies

$$v\overline{\mathbf{L}}\mathbf{E}\overline{\mathbf{L}}^T v = f_v \tag{56}$$

and consistency with the third of (55) is easily verified fi ..1 (54). If the rigid body modes are eliminated, $v = G_c\bar{e}^*$. Since the constant stress solution is _ecovered, the patch test is passed for any value of γ.

The physical meaning of this form of the patch test is that the *interface virtual work is zero* when the element patch is in a constant stress state[9].

END

DATE

FILMED

9-88

DTIC